



HAL
open science

Measurement of the van der Waals interaction between two Rydberg atoms

Lucas Beguin

► **To cite this version:**

Lucas Beguin. Measurement of the van der Waals interaction between two Rydberg atoms. Other [cond-mat.other]. Institut d'Optique Graduate School, 2013. English. NNT: 2013IOTA0004 . pastel-00936072

HAL Id: pastel-00936072

<https://pastel.hal.science/pastel-00936072>

Submitted on 24 Jan 2014

HAL is a multi-disciplinary open access archive for the deposit and dissemination of scientific research documents, whether they are published or not. The documents may come from teaching and research institutions in France or abroad, or from public or private research centers.

L'archive ouverte pluridisciplinaire **HAL**, est destinée au dépôt et à la diffusion de documents scientifiques de niveau recherche, publiés ou non, émanant des établissements d'enseignement et de recherche français ou étrangers, des laboratoires publics ou privés.



INSTITUT D'OPTIQUE GRADUATE SCHOOL
ÉCOLE DOCTORALE ONDES ET MATIERE

DISCIPLINE Physique

THÈSE

pour l'obtention du grade de Docteur en science de l'Institut d'Optique
Graduate School

préparée au Laboratoire Charles Fabry

soutenue le 13/12/2013

par

Lucas BÉGUIN

Measurement of the van der Waals interaction between
two Rydberg atoms

Directeur de thèse : Antoine BROWAEYS – Laboratoire Charles Fabry

Composition du jury :

Président du jury : Pierre PILLET – Laboratoire Aimé Cotton
Rapporteurs : Frédéric CHEVY – Laboratoire Kastler-Brossel
James. V. PORTO – National Institute of Standards and Technology
Examineurs : Tilman PFAU – Universität Stuttgart
Membres invités : Thierry LAHAYE – Laboratoire Charles Fabry

Remerciements

Les travaux présentés dans ce manuscrit de thèse ont été effectués dans le groupe expérimental d'Optique Quantique du laboratoire Charles Fabry de l'Institut d'Optique, entre octobre 2010 et décembre 2013. Ces travaux sont le fruit d'une équipe formidable avec laquelle j'ai pris énormément de plaisir à travailler, et à laquelle je souhaite adresser par ces modestes lignes mes plus sincères remerciements.

Je tiens pour commencer à exprimer ma profonde gratitude à l'équipe ChadoQ initiale. Tout d'abord à mon directeur de thèse Antoine Browaey, qui m'a ouvert la porte du monde de la recherche il y a maintenant cinq ans. Antoine, j'aimerais pouvoir te dire combien ces années d'initiation à tes côtés ont été enrichissantes. La confiance que tu sais témoigner aux gens qui t'entourent, ton énergie si communicative, et ton immense culture scientifique ont été chaque jour, et resteront, une profonde source d'inspiration. Je te remercie de m'avoir donné la chance de participer à la naissance d'un projet expérimental aussi passionnant. Ce projet, tu l'as porté avec ton dynamisme exceptionnel, ta disponibilité, et tes précieux conseils.

Je souhaite ensuite remercier chaleureusement Thierry Lahaye, mon co-encadrant de thèse, qui a rapidement rejoint l'équipe, et pris d'assaut le projet. Si l'on a jamais douté de tes qualités exceptionnelles, l'assaut promis a stoppé net le doute ! C'était un vrai privilège de travailler à tes côtés; merci pour ta patience, ton incroyable richesse d'esprit, et ta disponibilité au quotidien. J'aimerais pouvoir apporter à quelqu'un autant que toi et Antoine m'avez apporté ces dernières années. Les discussions de bureau vont me manquer, mais ça y est, tu vas peut-être pouvoir recommencer à travailler normalement.

Enfin, un immense merci à Aline Vernier, partenaire de labo exceptionnelle. Ces deux ans et demi coincés dans le noir, à 1h15 de chez nous, franchement je ne les ai pas vus passer. Travailler avec toi, c'était pas vraiment travailler. Et cette thèse, c'est un peu notre thèse, même si j'aurais bien échangé notre rôle respectif dans son écriture. Merci pour les pauses thé, les pauses pas thé, l'initiation à l'esca, le Vexin, le yodeling, la guitare, et tout le reste.

Je tiens évidemment à témoigner une pensée toute particulière à l'ensemble des autres membres du groupe. Tout d'abord à Yvan Sortais, qui m'a accueilli en stage bien avant le début de la thèse, et qui m'a initié à tous les métiers de l'expérimentation; du bricolage à l'art de la métrologie. Merci pour tous tes précieux conseils, ton souci des personnes, et ton modèle de pédagogie. Et pour les goûters rillettes du Mans particulièrement salvateurs. Je souhaiterais ensuite remercier profondément Florence Nogrette pour sa précieuse assistance aux différentes étapes clés du montage de l'expérience. Enfin, j'ai une pensée chaleureuse pour tous les compagnons de galère. Aux plus anciens, qui m'ont fait découvrir ce domaine qui m'a tant plu : Alpha Gaëtan, Charles Tuchendler, Charles Evellin, Andreas Fuhrmanek et Radu Chicireanu. Puis aux moins Anciens, avec qui j'ai vécu l'aventure tout du long : Ronan Bourgain, acolyte officiel et road-tripper américain de choix, et Joseph Pellegrino le jeunot ; à nos voisin(e)s plus photoniques : Philippe Grangier, Rosa Tualle-Brouri, Marco Barbieri, Franck Ferreyrol, Rémi Blandino, Jean Etesse, Bhaskar Kanseri ; aux autres joueurs de Rydberg : Alexei Ourjountsev, Valentina Parigi, Rajiv Boddeda, Imam Usmani et Erwan Bimbard. Et finalement aux nouveaux arrivants : Sylvain Ravets, Henning Labuhn, Daniel Barredo, et Stephan Jennewein. J'ai eu énormément de plaisir à travailler à vos côtés.

Mon immense gratitude va également à André Guilbaud et Patrick Roth de l'atelier de mécanique, qui ont énormément contribué à la conception, au montage, et aux succès de notre expérience. Merci pour votre patience et votre disponibilité même dans la plus grande urgence. Il en va évidemment de même pour les hommes de l'art du couloir voisin, Gilles Colas et Christian Beurthe, qui ont affûté nos optiques comme nulle part ailleurs. Merci pour l'usinage de céramiques merdiques, pour toutes les visites de l'atelier, pour le rhum de la réunion... Et continuez de résister ! L'Atelier d'Optique doit garder ses portes ouvertes, et son savoir-faire intact. Un grand merci aussi aux électroniciens Frédéric Moron et André Villing, qui font tourner l'essentiel de l'électronique des labos, et qui sont toujours disponibles pour répondre aux questions naïves des petits ignorants.

Je souhaite également remercier les directeurs Christian Chardonnet et Pierre Chavel pour leur accueil chaleureux et leur grande disponibilité au sein du laboratoire. Merci de même à Jacky Robin et Jean-Luc Cadore du service technique, ainsi qu'à Nathalie Baudry, Nicoles Esteves-Mangeon, Ghislaine Canale, Isabelle Soury, Aziz Aboulahyane, que j'ai énormément sollicités au cours de ces trois années, et qui assurent en amont avec tous les membres du service administratif le bon fonctionnement de la recherche au sein du laboratoire.

Je tiens à exprimer ma reconnaissance à tous les enseignants avec qui j'ai pris beaucoup de plaisir à apprendre, puis à enseigner, en particulier à Lionel Jacobowicz, Fabienne Bernard, Thierry Avignon, Cédric Lejeune, Jean-Marie Feybesse, et Raymond Mercier.

Je remercie chaleureusement les membres de mon jury : Trey Porto, Frédéric Chevy, Tilman Pfau et Pierre Pillet, qui m'ont fait l'immense honneur d'accepter de juger ce travail de thèse.

Enfin, mes derniers remerciements vont à ma famille et à tous mes proches pour leur soutien indéfectible, et tous les bons moments partagés. Un spécial merci aux jeunes mariés, au power rangers, au 4bC crew, à toutes les colocs denfert, d'issy et d'ailleurs ! À Quintino, sans qui j'aurais peut-être jamais fait de thèse, à Delphine et Cédric, Mimi, Olivier, pour m'avoir si bien logé et nourri dans la dernière ligne droite ! À Faust, Fred, Sharps, Marion, Co, Anne-So, Claudia, Doudi, pour toutes les soirées Villa Marguerite ! À Toinou, Max, Adib, Chris, Ressort, Vince, Pépé, et Léon de LKL, à Mapi et à mes colocs Chach, Peyo, et Guims, le détail serait trop long. Vous savez combien vous m'êtes précieux.

Contents

Introduction	1
1 New apparatus for single Rydberg atoms manipulation	7
1.1 Experimental requirements	8
1.1.1 Single atom trapping and imaging	8
1.1.2 Rydberg states manipulation	16
1.2 UHV compatible experimental apparatus design	19
1.2.1 Custom aspheric lens	19
1.2.2 Lens holders assembly inside vacuum	25
1.2.3 Control electrodes and MCP charge detector	27
1.2.4 MOT coils under vacuum	30
1.3 Vacuum system	31
1.3.1 Vacuum chamber	31
1.3.2 Effusive oven and Zeeman slower	33
1.3.3 Reaching UHV conditions	33
1.4 Trapping and imaging single atoms	34
1.4.1 Laser systems at 780 nm	34
1.4.2 Laser system at 850 nm	37
1.4.3 Detection systems: CCD camera and single photon counting modules	37
1.4.4 Single atom trapping	40
2 Trap characterization using a single atom	45
2.1 Trapping ^{87}Rb atoms using the dipole force	46
2.1.1 State-dependent light shifts	46
2.1.2 Trap profile for a gaussian trapping laser beam	48
2.2 Typical experimental sequences and computer control system	49
2.2.1 Typical experimental sequences	50
2.2.2 Computer control system	53
2.3 Characterization of the single atoms in the ODT	54
2.3.1 Lifetime in the trap	55
2.3.2 Single Atom Temperature	58
2.3.3 Trap oscillation frequencies	59
2.3.4 Measurement of the trap depth	61
3 Manipulation of ^{87}Rb internal ground states	67
3.1 Zeeman effect: an overview	68
3.2 Cancellation of residual magnetic fields with microwave spectroscopy	69

3.2.1	Magnetic dipole transitions between hyperfine ground states	69
3.2.2	Hyperfine ground states detection scheme	70
3.2.3	Setup for the microwave generation	71
3.2.4	Zeeman shifts measurements	72
3.3	Stimulated Raman transitions	75
3.3.1	Choice of the qubit	75
3.3.2	Two-photon electric-dipole transitions	76
3.3.3	Laser system at 795 nm	77
3.3.4	Raman spectra of the transition $ F = 2, m_F = 2\rangle \rightarrow F = 1, m_F = 1\rangle$	79
3.3.5	Optical pumping optimization	83
3.3.6	Conclusion	84
4	Coherent excitation of a single atom towards Rydberg states	85
4.1	Rydberg states $ nD_{3/2}, m_j = 3/2\rangle$	86
4.2	Excitation scheme	87
4.2.1	Two-photon transition	87
4.2.2	Laser systems	90
4.2.3	Transfer cavity lock	91
4.2.4	Rydberg pulse parameters	93
4.3	Experimental realization	95
4.3.1	Alignment of the beam at 795 nm	95
4.3.2	Alignment of the beam at 474 nm	96
4.3.3	Rydberg state detection	99
4.3.4	Spectra of Rydberg excitations	99
4.4	Cancellation of residual electric fields	101
4.4.1	Preliminary results without the ITO coating	101
4.4.2	Stark spectroscopy with single atoms	103
4.4.3	Coherent Rabi oscillations in compensated electric field	106
4.4.4	Conclusion	110
5	Direct measurement of the van der Waals interaction between two Rydberg atoms	111
5.1	Van der Waals interactions between Rydberg atoms: an overview	112
5.2	Experimental investigation of the blockade	114
5.2.1	Two-trap setup and calibration of R	115
5.2.2	Experimental sequences and typical data	117
5.2.3	Fully independent regime: $n = 62$ and $R = 15.5 \mu\text{m}$	119
5.2.4	Blockade regime: $n = 62$ and $R = 4 \mu\text{m}$	120
5.2.5	Cancellation of electric field matters!	122
5.2.6	Partial blockade regime	123
5.3	Modeling of partial blockade	127
5.3.1	Schrödinger equations in the effective 3-level system	127
5.3.2	Bloch equations in the 4-level system	128
5.3.3	Extraction of $ \Delta E /h$ and error bars analysis	129
5.3.4	Measurements of the van der Waals interaction	132
5.4	Theoretical calculations of the interaction ΔE	134
5.4.1	Construction of the basis	135
5.4.2	Calculation of dipole matrix elements $\langle n', l', j', m'_j \hat{d}_q n, l, j, m_j \rangle$	136

5.4.3	C_6 calculations from second-order perturbation theory	137
5.4.4	Diagonalization of the interaction hamiltonian	139
5.4.5	Conclusion	141
Conclusion and outlook		143
A Fundamental constants and main properties of ^{87}Rb		149
A.1	Fundamental constants	149
A.2	Properties of ^{87}Rb	149
B Properties of Rydberg states in alkali atoms		153
B.1	Effective approach: quantum defect theory	154
B.1.1	Quantum defects	154
B.1.2	Fine and hyperfine structure splittings	155
B.1.3	State-selective ionization	156
B.1.4	Numerical calculations of Rydberg radial wavefunctions	157
B.1.5	Rydberg states lifetime	159
B.1.6	Stark effect	160
B.2	Förster resonances	161
B.2.1	Quasi-Förster resonances	163
B.2.2	Tuning pure Förster resonances with external electric fields	163
C Custom aspheric lens: drawings, specifications and characterization		165
D Design and characterization of the Zeeman slower coils and the MOT coils		171
D.1	Zeeman slower coils	171
D.2	MOT coils	173
E Published article		177
Bibliography		183

Introduction

During the last four decades, significant advances in atomic physics and optics opened new ways to manipulate quantum systems — electrons, atoms, photons — at the single particle level. A number of thought experiments questioning the basis of quantum mechanics could be actually realized in the laboratory (Haroche and Raimond, 2006). In 2012, these advances were recognized by the Nobel prize in Physics awarded jointly to S. Haroche and D. Wineland. With this new level of control, quantum systems can now be used not only to test fundamental issues, but also for practical applications. As an example, we can mention the use of single aluminium ions (Chou *et al.*, 2010), or of a few thousands of trapped ytterbium atoms (Hinkley *et al.*, 2013), as frequency standards providing unprecedented stability, below 1×10^{-17} .

Quantum systems are also at the heart of the rapidly developing field of *Quantum Information Processing* (Nielsen and Chuang, 2000), triggered mainly by two conceptual revolutions in the 1980s and 1990s. The first one occurred in 1984 when C. Bennett and G. Brassard reported on a quantum cryptography protocol (Bennett and Brassard, 1984) that could be used to exchange a secret key securely. Quantum cryptography is now mature, and commercial devices enable to implement quantum key distribution over tens of kilometers in standard optical fibers. The second revolution came with the discovery of quantum algorithms allowing to solve some problems faster than the best-known classical algorithms (Shor, 1994; Grover, 1997): quantum computing was born. This field of research focuses on the new perspectives offered when information is not encoded into binary digits, but in a two-level quantum system: a qubit. Several approaches allowing to achieve universal computation were developed theoretically. In the quantum circuit approach, it was proven that any algorithm can be decomposed in a sequence of one-qubit gates, and universal two-qubit gates, such as C-NOT or phase gates (DiVincenzo, 1995). These gates generate multi-particle entanglement that is very sensitive to decoherence due to the environment (Zurek, 1991). Protecting experimental systems against decoherence is thus challenging.

In the last ten years, significant advances have been achieved in this direction with trapped ions (Blatt and Wineland, 2008), from the implementation of the two qubits C-NOT gate, to the realization of the quantum Fourier transform (at the heart of Shor's algorithm) or the creation of Greenberger-Horne-Zeilinger (GHZ) states with up to 14 entangled ions (Monz *et al.*, 2011). However, scaling up the entanglement to larger numbers of ions is not straightforward. In such systems, entanglement is mediated through the collective quantized motion of the Coulomb chain. The larger the number of interacting ions, the harder it gets to protect the system from electric noise and other decoherence mechanisms. This constrains in practice the ability to produce the desired final quantum state. Recent promising experiments have thus developed more sophisticated trap geometries with

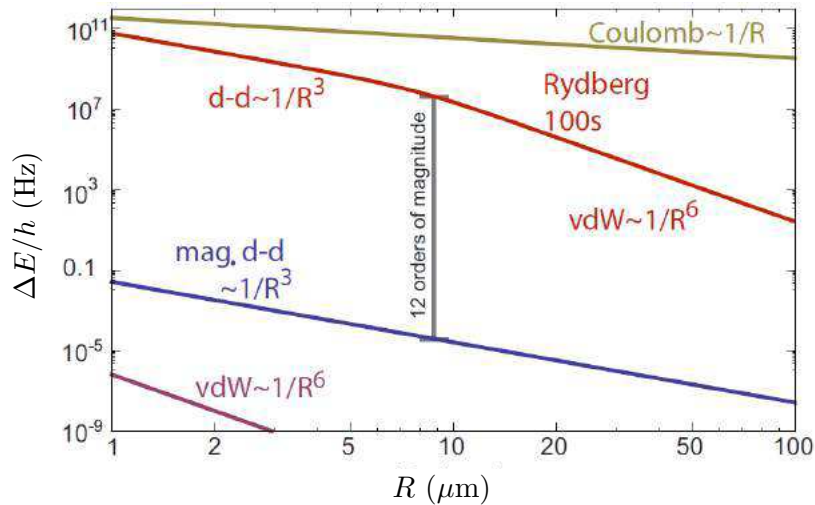


Figure 1: Two-body interaction strength (in frequency units) for ground-state ^{87}Rb atoms, ^{87}Rb atoms excited to the $100S_{1/2}$ level, and singly charged ions. (taken from Saffman and Molmer (2010)).

shuttling ions (Home *et al.*, 2009; Walther *et al.*, 2012).

Alternatively, systems using optically trapped neutral atoms could be more robust to decoherence and offer the possibility to test new schemes of entanglement (Bloch, 2008). Registers containing many atomic qubits can be realized by loading a Bose-Einstein condensate into a 2D optical lattice in the Mott insulator regime (Greiner *et al.*, 2002). The designs of deterministic gates require then to make these qubits interact, which is challenging for neutral species. Early theoretical proposals made use of controlled cold collisions as coherent interactions (see e.g. Jaksch *et al.* (1999)). Such interactions can be used to investigate other approaches of quantum computation than the circuit model, such as the measurement-based model (reviewed in Briegel *et al.* (2009)). The group of I. Bloch could demonstrate the creation of a cluster state using spin-dependent s-wave scattering in a 2D lattice (Mandel *et al.*, 2003). Four years later, the team of W. Philipps and J. V. Porto realized parallelized $\sqrt{\text{SWAP}}$ gates operations by using the exchange interaction in a double-well optical lattice (Anderlini *et al.*, 2007). However, implementing such gates requires a careful control of the center of mass wavefunction of the atoms. This involves in particular ultra-cold gases and is thus experimentally demanding. As an alternative, another gate design was proposed by Jaksch *et al.* (2000). This gate uses the large interaction energy provided by the long-range dipole-dipole interaction between atoms excited to Rydberg states.

Rydberg states of an atom are electronically excited states with large principal quantum number n , where one electron orbits far away from the ionic core (Gallagher, 1994). These states have exaggerated properties such as large orbital radius increasing as $a_0 n^2$, so large dipole moments increasing as $ea_0 n^2$. Two Rydberg atoms can thus exhibit a strong dipole-dipole interaction. As an illustration, Fig. 1 (from Saffman and Molmer (2010)) shows the strength of the two-particle interaction as a function of the separation R , for singly charged ions, ground-state neutral atoms, and Rydberg atoms $100S$ of ^{87}Rb .

A prerequisite for the implementation of the two-qubit gate from Jaksch *et al.* (2000) is to work with the two atomic qubits in the Rydberg blockade regime. The principle of the

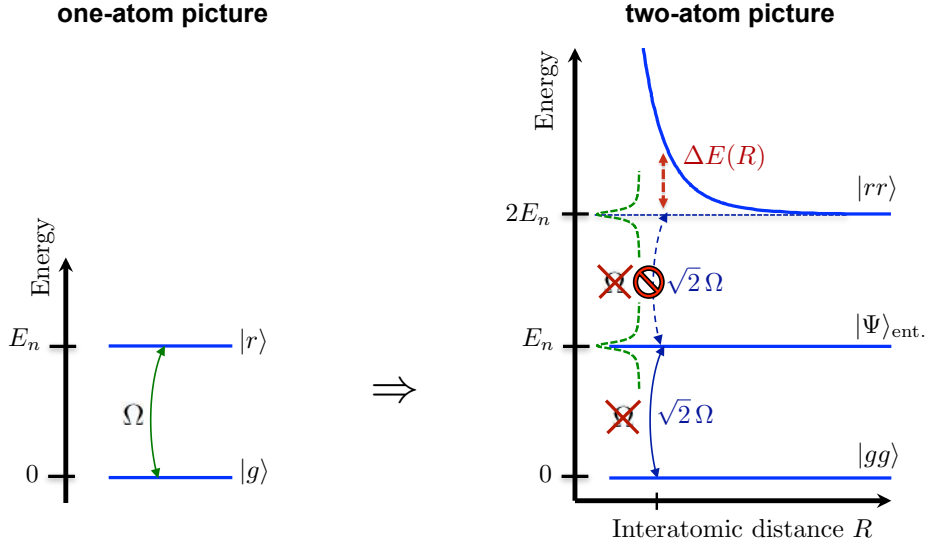


Figure 2: Principle of the Rydberg blockade.

blockade is shown in Fig.2. Let us consider two atoms that can be either in the ground state $|g\rangle$ of energy zero, or excited towards a Rydberg state $|r\rangle$ of energy E_n . At interatomic distances $R \rightarrow \infty$, the eigenstates of the two-atom system $|gg\rangle$, $|rg\rangle$, $|gr\rangle$, and $|rr\rangle$ have respectively the energies 0, E_n , E_n and $2E_n$. However, when the two atoms are brought closer from each other, the energy of the doubly excited state $|rr\rangle$ is shifted by a quantity $\Delta E(R)$ which results from the dipole-dipole interactions. Now, let us assume that a laser source is used to drive the transition $|g\rangle \rightarrow |r\rangle$ with a Rabi coupling Ω . In the limit

$$\Omega \ll \Delta E(R)/\hbar, \quad (1)$$

$|gr\rangle$ and $|rg\rangle$ are resonantly coupled to $|gg\rangle$, but the doubly excited state $|rr\rangle$ is off-resonance, and can not be populated. This is called Rydberg blockade. Such a scheme is interesting in itself as it generates entanglement. Indeed, the two states $|rg\rangle$ and $|gr\rangle$ being degenerate, the ground state $|gg\rangle$ couples to the symmetric state $|\Psi_{\text{ent.}}\rangle = (|rg\rangle + |gr\rangle)/\sqrt{2}$, with a collective Rabi frequency $\sqrt{2}\Omega$. Furthermore, this scheme can be extended to a system of N atoms in a straightforward way. As long as the system is blockaded, the same laser excitation couples the ground state to the collective symmetric state containing only one delocalized Rydberg excitation. In this case, the collective Rabi frequency is enhanced by a factor of \sqrt{N} .

In Lukin *et al.* (2001), the authors developed an approach inspired from Jaksch *et al.* (2000) that uses the blockade to manipulate quantum information stored in such collective states of mesoscopic ensembles. The blockade has been then investigated in various experiments using laser cooled atomic ensembles (Comparat and Pillet, 2010): in magneto-optical traps, starting from 2004 (Tong *et al.*, 2004; Singer *et al.*, 2004; Liebisch *et al.*, 2005; Vogt *et al.*, 2007), and more recently in BECs (Heidemann *et al.*, 2008; Löw *et al.*, 2009; Balewski *et al.*, 2013), and in optical lattices (Viteau *et al.*, 2011; Schauss *et al.*, 2012). Cold atomic ensembles are also a versatile tool to store, manipulate and retrieve quantum states of light Lvovsky, Sanders, and Tittel (2009). In such systems, the blockade induces large optical non-linearities which can be effective at the single photon level and yield strong effective photon-photon interactions (Weatherill and Adams, 2012). Recent experimental

advances offer promising perspectives for all-optical quantum information processing (Dudin and Kuzmich, 2012; Peyronel *et al.*, 2012; Maxwell *et al.*, 2013), even in room temperature atomic vapors (Baluktsian *et al.*, 2013).

The Rydberg blockade can also be investigated with a small number of single atoms in arrays of microscopic optical dipole traps, separated by a few microns. The main advantages of such systems are that the geometry and the atom-atom separation can be very well controlled, while ensuring the optical addressability. This is the approach that was followed in our team at the Institut d'Optique. Pioneering experiments with single atoms in microscopic optical tweezers have been investigated since 2001 (Schlosser *et al.*, 2001; Darquié *et al.*, 2005; Beugnon *et al.*, 2006). The Rydberg project started in 2008, and shortly after, the team observed the blockade between two individual atoms almost simultaneously with the group of M. Saffman (Gaëtan *et al.*, 2009; Urban *et al.*, 2009). Very rapidly, it could be used to generate entanglement (Wilk *et al.*, 2010) and to implement a C-NOT gate (Isenhower *et al.*, 2010). These results offered exciting perspectives for the study of multi-particle entanglement in arrays of single atoms held in microscopic dipole traps.

However, the blockade observed in our group at that time was not perfect. Uncontrolled drifting electric fields in the environment of the atoms were strongly suspected to cause significant Rydberg states mixing (Evellin, 2011). These can decrease the strength of the expected interaction and thus degrade the quality of the blockade. The apparatus, originally built in 1999, was not equipped with a control of external electric fields. Furthermore, recent advances in molding technology enabled the design of cheap, high-NA and vacuum compatible aspheric lenses. A pioneering single-atom experiment using such lenses had recently demonstrated adequate optical performances (Sortais *et al.*, 2007). When I joined the group in 2010, it was decided to build a new single-atom experiment using molded aspheric lenses. This setup would be specified mainly to ensure a stable electrostatic environment around the atoms, and to implement a control of external electric fields, allowing to achieve well-controlled Rydberg excitations. In the long run, it would allow us to explore multi-atom configuration using holographically-generated arrays of microscopic traps.

Organization of the thesis

During this thesis, I was thus in charge of designing, building, and characterizing a new experimental apparatus to trap single atoms from a magneto-optical trap, and to excite them towards Rydberg states. I implemented a trapping setup composed of two individual optical tweezers separated by a controlled distance R . With this setup, I could demonstrate an improved control over the dipole-dipole interaction and observe almost perfect blockade of the atom pair, which is very promising for future studies of multi-particle entanglement. Finally, by working with partially blocked pairs of atoms in the van der Waals regime, I developed a method to directly measure the $\Delta E = C_6/R^6$ dependence of the van der Waals interaction energy.

The thesis is divided into five chapters.

- In chapter 1, I describe in detail the specifications and the design of the new experimental apparatus. Single atom trapping is demonstrated at the end.
- In chapter 2, I present four experiments to characterize our microscopic optical dipole traps using single atoms.

- In chapter 3, I show that we can prepare and manipulate the internal ground states of our single atoms using either microwaves or two-photon Raman transitions. The quality of the preparation is discussed at the end.
- In chapter 4, coherent Rydberg excitations of single atoms are presented. In particular, I explain how we compensated for residual electric field using Stark spectroscopy.
- In chapter 5, I present Rydberg excitation experiments of a pair of atoms yielding almost perfect blockade at short distance. Then, partial blockade configurations are investigated in the van der Waals interaction regime. Operating in this regime allowed us to directly measure the interaction energy, in very good agreement with ab-initio calculations.

Chapter 1

New apparatus for single Rydberg atoms manipulation

Contents

1.1	Experimental requirements	8
1.1.1	Single atom trapping and imaging	8
1.1.2	Rydberg states manipulation	16
1.2	UHV compatible experimental apparatus design	19
1.2.1	Custom aspheric lens	19
1.2.2	Lens holders assembly inside vacuum	25
1.2.3	Control electrodes and MCP charge detector	27
1.2.4	MOT coils under vacuum	30
1.3	Vacuum system	31
1.3.1	Vacuum chamber	31
1.3.2	Effusive oven and Zeeman slower	33
1.3.3	Reaching UHV conditions	33
1.4	Trapping and imaging single atoms	34
1.4.1	Laser systems at 780 nm	34
1.4.2	Laser system at 850 nm	37
1.4.3	Detection systems: CCD camera and single photon counting modules	37
1.4.4	Single atom trapping	40

The experimental apparatus built during this thesis was designed to investigate quantum information processing protocols with single neutral atoms. These protocols involve quantum gates operations that require a control of long range dipole-dipole interactions, in 2D systems of single ^{87}Rb Rydberg atoms. The atoms will be held in 2D arrays of microscopic optical dipole traps produced by a spatial light modulator similar to [Bergamini *et al.* \(2004\)](#) (see Sec. 1.1.1). With this approach, it is possible to study various 2D configurations of N interacting atoms, where N can be increased step by step, as represented in Fig. 1.1.

In such 2D systems, the typical distance between neighboring trapped atoms is limited by the resolution of the imaging system which is on the order of a few microns. At these

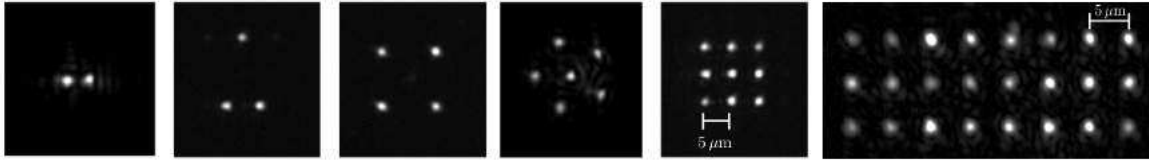


Figure 1.1: Holographically generated 2D patterns of optical dipole traps. From left to right, we show various 2D trapping geometries with increasing number of traps.

distances, the interaction energy between two ground-state atoms is too weak to be observed with laser spectroscopy. However, atomic interactions can be enhanced by exciting the atoms to Rydberg states with high principal quantum number n , for which the excited electron is in a large, loosely bound orbit. These states exhibit large dipole moments which can induce strong dipole-dipole interactions between the atoms. These interactions increase dramatically with the quantum number n of the targeted Rydberg states. By tuning the frequency of laser excitations, one can aim at various Rydberg states with n ranging from thirty to a few hundreds, which then allows to tune the strength of the interactions in the system. This project is motivated by previous experimental investigations on such interactions between two trapped single atoms which started in 2008 during Alpha Gaetan's PhD thesis. They successfully led to the observations of the Rydberg blockade between two single Rydberg atoms simultaneously with the group of M. Saffman (Gaëtan *et al.*, 2009; Urban *et al.*, 2009). Studies of the entanglement induced by the blockade effect (Wilk *et al.*, 2010) were pursued during Charles Evellin's PhD thesis, who clearly demonstrated several technical limitations of the experimental apparatus (Evellin, 2011). Besides imperfections and aging of the existing equipment, the main limitation lied in the complete absence of control over the electrostatic environment surrounding the trapped atoms. The experimental setup was unsuitable for the implementation of the experimental tools needed to diagnose and control stray electric fields. Thus, it was decided to start a new experiment from scratch to overcome the identified limitations with a more compact and up-to-date design.

In the first part of this chapter, we discuss the experimental requirements needed to combine single atom trapping and imaging in 2D patterns of optical dipole traps with careful Rydberg states manipulation. In the second part, we focus on the design of the various elements that were combined under ultra-high vacuum conditions to fulfill these requirements. A brief overview of the design and the performances of the complete vacuum system is given in the third part. Finally, we describe the laser systems used for cooling, trapping and imaging of the single atoms.

1.1 Experimental requirements

For the new experimental apparatus, we aimed at combining a compact setup already developed in our group for single atom trapping and imaging with the standard tools for Rydberg states manipulation and detection.

1.1.1 Single atom trapping and imaging

The first main experimental challenge is to be able to prepare N microscopic optical dipole traps (ODTs) with one single atom in each, where N ranges from one to a few tens. Generating the traps and imaging the trapped atoms are nowadays easy tasks, but implementing deterministic schemes to load the single atoms into the traps is experimentally challenging

even to date. A possibility is to start with a Bose-Einstein condensate (BEC) with repulsive interactions, held in a three-dimensional optical lattice potential. At low potential depth, the system of N atoms is in a superfluid phase where each atom wavefunction is spread out over the entire lattice. By increasing the potential depth, the system undergoes a quantum transition to a Mott insulator phase for which exact numbers of atoms are localized at individual lattice sites. Observed for the first time in I. Bloch's group in Munich in 2002 (Greiner *et al.*, 2002), this mechanism allows to load a large number of optical traps with single atoms with a very good efficiency as soon as the condensate contains less atoms than the available number of lattice sites. The only disadvantages of such an elegant method are the rather slow duty cycle required to prepare the system (about 1 min) and the necessity to implement a wide range of complex and rather costly experimental techniques.

An easier loading procedure of a single atom in one ODT relies on a stochastic process that we are going to describe below. By using a real time imaging system, it is possible to know exactly when a single atom has entered the trap and use this information to trigger one-atom experiments with typically 1 s duty cycle. We will also show how the same method can be extended to trigger N -atom experiments with N up to three. During this thesis, we investigated such a scheme with a preliminary version of the experimental apparatus which allowed us to study fundamental interactions between two isolated single atoms.

However, loading and imaging more than three traps using a stochastic loading scheme is not experimentally realistic. Indeed, the average time one has to wait before the N traps are filled simultaneously increases exponentially with N . With the final version of the new experimental apparatus, we will show how we plan to implement a flexible way to generate and to image 2D patterns of more than three ODTs within which we intend to investigate deterministic loading schemes.

Loading an ODT with a single atom

It was shown in Schlosser *et al.* (2001) that a red-detuned laser beam focused down to a few microns in a cloud of cold atoms from a standard magneto-optical trap (MOT) setup can be used as an optical tweezer for trapping single atoms. Indeed, the dipole force resulting from a strong light intensity gradient is attractive, and thus produces a tiny trap of a μm^3 volume. A schematic of such an experiment is depicted in Fig. 1.2. According to detailed studies by Kuppens *et al.* (2000) and Schlosser (2001), the number of atoms $N(t)$ inside the optical dipole trap results from a competition between a loading mechanism and various loss processes. Its evolution can be modeled by a differential equation of the form:

$$\frac{dN}{dt} = R - \gamma_{\text{vac.}}N - \frac{\beta_0}{V_{\text{trap}}} \frac{N(N-1)}{2}, \quad (1.1)$$

where $\gamma_{\text{vac.}}$, and β_0/V_{trap} are respectively one-body and two-body loss terms, and R is a loading term.

One-body losses are due to collisions with residual gas. In ultra-high vacuum environments with a pressure below 10^{-10} mbar, $\gamma_{\text{vac}} \leq 1 \text{ s}^{-1}$. The two-body losses are mostly due to inelastic light-assisted collisions between two atoms and near-resonant light of the MOT beams. In Fuhrmanek *et al.* (2012), the constant β_0 was measured to be surprisingly large, on the order of $10^4 \mu\text{m}^3/\text{s}$. The trapping volume V_{trap} can be estimated considering a Gaussian trapping beam of wavelength λ focused on a waist w_0 with a Rayleigh range $Z_R = \pi w_0^2/\lambda$:

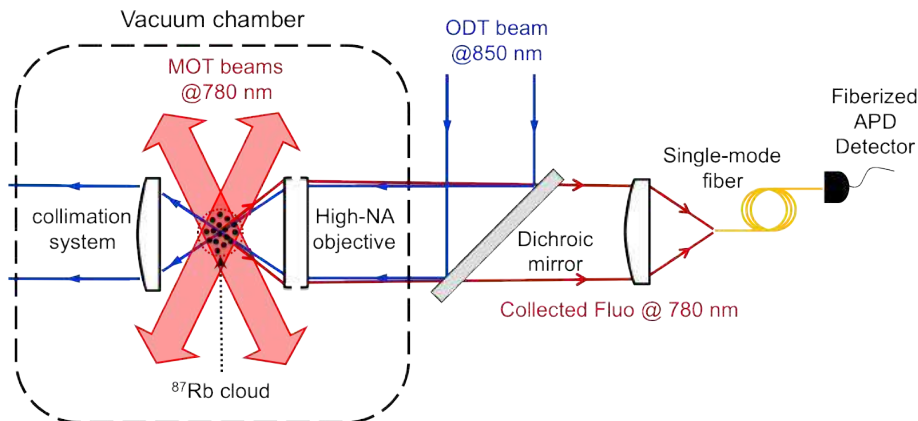


Figure 1.2: Sketch of a single atom experiment. A cloud of cold ^{87}Rb atoms is produced in a vacuum chamber with a standard MOT setup. Inside, a red-detuned optical dipole trap (ODT) beam is strongly focused ($1/e^2$ radius of about $1\ \mu\text{m}$) using an optical system with a large numerical aperture (NA) operating under vacuum. The atoms are trapped at the peak intensity of the ODT beam while scattering near-resonant photons from the MOT beams. The same optical system collects up to 10% of these photons and a dichroic mirror allows to separate them from the 850 nm trapping light. A standard imaging system can then be used to couple the fluorescence light towards a sensitive detector. In our experiment, we have been using fiberized avalanche photodiode detectors (APDs).

$$V_{\text{trap}} \simeq w_0^2 Z_R \simeq \frac{\lambda^2}{4NA^2} \frac{\pi\lambda}{2NA^2} = \frac{\pi\lambda^3}{8NA^4}, \quad (1.2)$$

where NA is the numerical aperture of the optical system focusing the optical dipole trap beam. The loading rate R increases linearly with the atomic density in the MOT cloud and thus can be tuned by adjusting the current flowing in the MOT coils. When the condition $\gamma_{\text{vac.}} \ll R \ll \beta_0/V_{\text{trap}}$ is fulfilled, the trap can only contain either zero or one individual atom, with equal probability. This non-Poissonian loading regime is called the 'collisional blockade regime', or the 'single atom regime', for which single atoms can remain trapped for an average time $1/R$. As $\gamma_{\text{vac.}}$ is determined by the purity of the vacuum and cannot be much smaller than $0.1\ \text{s}^{-1}$, the way to extend the validity range of this condition is to work with trapping volume $V_{\text{trap}} \propto \lambda^3/NA^4$ as small as possible. The wavelength of rather high power lasers is within $400\ \text{nm} - 1.5\ \mu\text{m}$ (except for CO_2 lasers, which require inconvenient specific optics) so this parameter can not be varied too much. Then, the numerical aperture NA has to be on the order of 0.4 to 0.5 to reach high two-body collision rates $\beta_0/V_{\text{trap}} \geq 1000\ \text{s}^{-1}$. Let us see now shortly how to choose the parameters for the trapping laser.

Parameters of the trapping laser

The operating parameters for the trapping laser are chosen to minimize the spontaneous emission rate while providing deep enough trapping potentials with reasonable laser power. Let us consider a ^{87}Rb atom with transition frequencies $\omega_{1/2}$ (D1 line $|5S_{1/2}\rangle \rightarrow |5P_{1/2}\rangle$ at 795 nm) and $\omega_{3/2}$ (D2 line $5S_{1/2} \rightarrow 5P_{3/2}$ at 780 nm). It is illuminated by a far-detuned trapping laser of intensity $I(\vec{r})$ and frequency ω_L . We define the detunings $\delta_{1/2} = \omega_L - \omega_{1/2}$ and $\delta_{3/2} = \omega_L - \omega_{3/2}$. With the rotating wave approximation (RWA), the dipolar trapping potential reads (Cohen-Tannoudji, Grynberg, and Dupont-Roc, 1998; Grimm, Weidemüller, and Ovchinnikov, 2000; Schlosser, 2001):

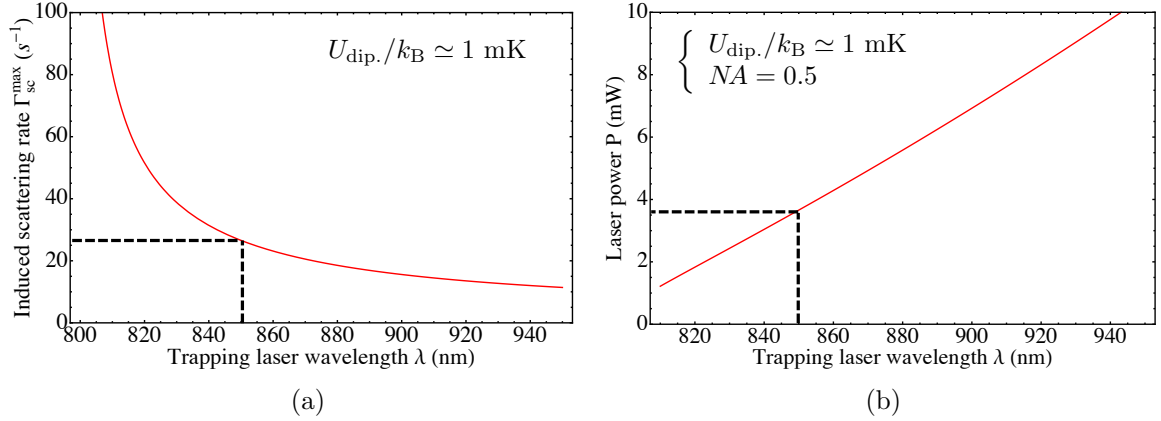


Figure 1.3: Choosing the wavelength of the trapping laser. (a) and (b) show respectively relevant orders of magnitude of the variation of the spontaneous emission rate induced by the dipole trap and the laser power needed for one dipole trap, as a function of the dipole trap wavelength (calculated using the rotating wave approximation).

$$U_{\text{dip}}(\vec{r}) \simeq \frac{\hbar\Gamma^2}{8I_{\text{sat}}} \frac{I(\vec{r})}{\Delta_{\text{eff}}}, \quad (1.3)$$

where I_{sat} is the saturation intensity of the D1 and D2 transitions, and Δ_{eff} is an effective trapping laser detuning from the atomic resonances D1 and D2, defined by:

$$\frac{1}{\Delta_{\text{eff}}} = \frac{1}{3\delta_{1/2}} + \frac{2}{3\delta_{3/2}}. \quad (1.4)$$

For red-detuned trapping laser ($\Delta_{\text{eff}} < 0$), the potential is attractive towards the laser intensity maxima. Efficient trapping is achieved when the potential depth is large compared to the kinetic energies of the atoms inside the MOT cloud characterized by a typical temperature $T_{\text{MOT}} \simeq 100 \mu\text{K}$. For a typical operating value of efficient trapping energy $|U_{\text{dip}}^{\text{max}}|/k_{\text{B}} \simeq 1 \text{ mK}$, the ratio $I^{\text{max}}/|\Delta_{\text{eff}}|$ is thus fixed and can be estimated using Eq. 1.3 with the parameters of the D1 and D2 lines of ^{87}Rb (see Appendix A):

$$\frac{I^{\text{max}}}{|\Delta_{\text{eff}}|} \simeq 10^{-5} \text{ W}/(\text{m}^2 \cdot \text{rad} \cdot \text{s}^{-1}). \quad (1.5)$$

Finally, the trapping laser wavelength λ is chosen to minimize the scattering rate Γ_{sc} responsible for undesired decoherence in the two-level atomic system. In the limit of a low saturation of the atomic transition, Γ_{sc} can be written:

$$\Gamma_{\text{sc}} = \frac{I(\vec{r})}{8I_{\text{sat}}} \Gamma^3 \left(\frac{1}{3\delta_{1/2}^2} + \frac{2}{3\delta_{3/2}^2} \right). \quad (1.6)$$

Keeping $I^{\text{max}}/|\Delta_{\text{eff}}|$ constant, $\Gamma_{\text{sc}}^{\text{max}}$ decreases as λ increases. At the same time, the required trapping laser power $P = \pi w_0^2 I/2$ for a Gaussian beam of peak intensity $I = I^{\text{max}}$ and waist $w_0 \simeq 1.22\lambda/NA$ increases with the trapping laser wavelength λ . The evolutions of Γ_{sc} and P as a function of λ are shown in Fig. 1.3(a) and (b). On our experiment, it was decided to operate with $\lambda = 850 \text{ nm}$ for which $\Gamma_{\text{sc}} \simeq 26 \text{ s}^{-1}$ and $P_{\text{trap}} \simeq 3.8 \text{ mW}$ using a focusing setup with $NA = 0.5$.

So far, we have described the physical processes allowing the existence of the single

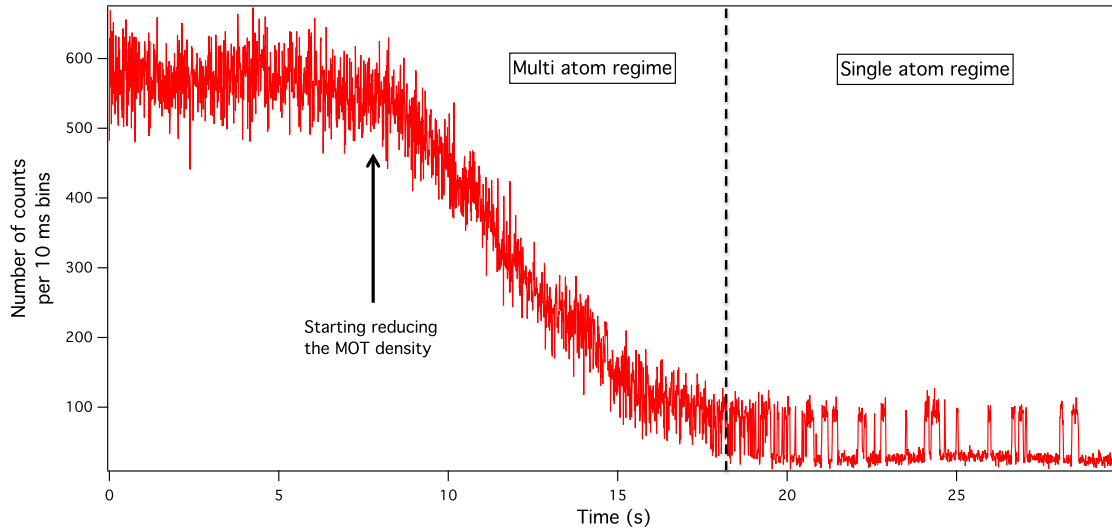


Figure 1.4: Reaching the single atom regime. A fraction of the fluorescence light scattered by the trapped atoms is collected into a fiberized avalanche photodiode detector (APD) connected to a photon counting module. The number of counts per 10 milliseconds time bins is plotted as a function of time. At $t=0$ ms, the atomic density in the MOT cloud is adjusted such that the loading rate R of the trap is bigger than the two-body loss rate. In this so called multi-atom regime, the trap can contain several atoms which scatter many photons. On the plot, the corresponding average detection rate on the APD detector is ~ 580 counts/(10 ms time bins). At $t=7500$ ms, the current flowing in the MOT coils is ramped down; the atomic density in the MOT cloud and so the loading rate of the trap R start to decrease. Less and less atoms get trapped inside the tweezer, so the photons scattering rate detected onto the APD also decreases. By $t \simeq 19000$ ms, the signal can only take two main discrete values. This is the typical experimental signature that the single atom regime has been reached. We checked that the low fluorescence level corresponds only to background and dark counts detection. When the fluorescence signal is high, a single atom has been trapped in the tweezer.

atom regime and what were the corresponding constraints on the trapping laser parameters to reach it. The next step is to find a way to 'see' when such a regime has been reached experimentally.

Imaging trapped single atoms

Inside the optical tweezer, trapped atoms continuously scatter many photons from the near-resonant cooling beams used for the magneto-optical trap (MOT). Those photons are collected on a photon counting detector to get an estimate of the trapped atoms number as a function of time. Then, starting with a high atomic density in the MOT cloud and reducing it slowly, one can monitor the fluorescence signal collected from the dipole trap in real time. As the loading term R of the tweezer decreases, the average number of trapped atoms also decreases until it reaches the single atom regime. Such a procedure is represented in Fig. 1.4. The collection efficiency of the imaging system has to be large enough such that one can detect and count enough photons scattered by a single atom on a timescale small compared to the average time $1/R$ during which the single atom remains in the trap. A clever solution originally implemented in [Schlosser, Reymond, and Grangier \(2002\)](#) is to use the same optical system operating under vacuum to focus the ODT beam and to collect the fluorescence light emitted by the trapped atoms, as shown in Fig. 1.2. A dichroic mirror is

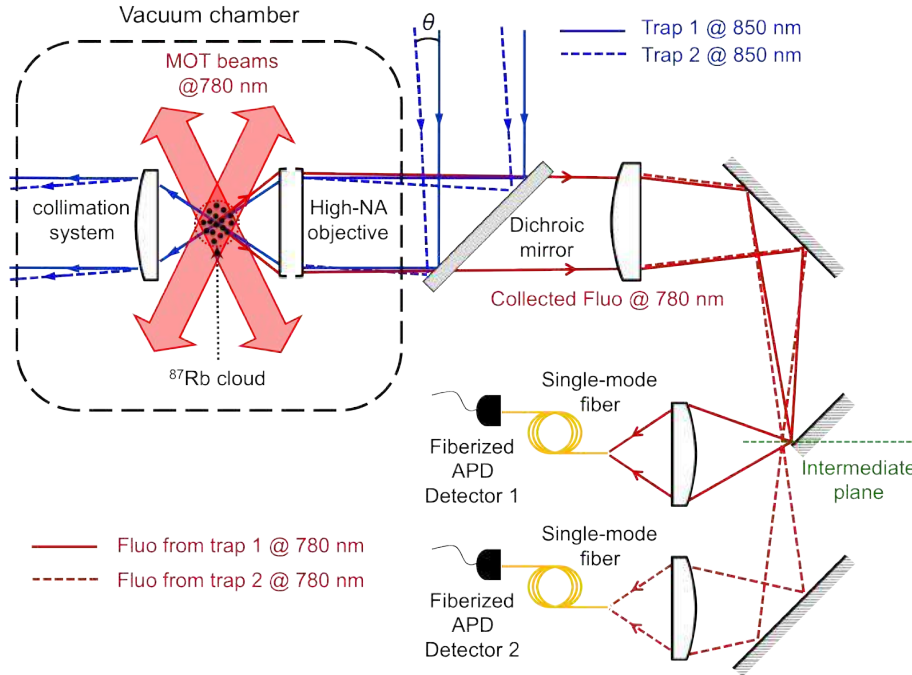


Figure 1.5: Sketch of a two-atom experiment. A second ODT beam is combined with the first one with a small angle θ before entering the large NA objective of focal length f . In the focal plane, they create two distinct traps separated by the distance $R \simeq f\theta$ as small as a few microns. Using a confocal imaging setup with a magnification ≥ 25 , it is then possible to use a mirror in the intermediate plane to separate the fluorescence scattered from of each trap and couple it into two distinct APD detectors.

used to separate the two wavelengths and the fluorescence can be coupled into a fiberized avalanche photodiode detector (APD). Single atom experiments can be triggered as soon as a rising edge of the fluorescence signal is detected.

From one to two-atom experiments

This trapping and imaging scheme can easily be scaled up for two-atom experiments. Two distinct ODT beams can be combined with a small angle θ before being sent through the imaging system of focal length f , and focused into the MOT cloud. At the focal plane, they create two distinct traps separated by a distance $R \simeq f\theta$ of a few microns. It is then possible to separate the fluorescence signals emitted by two distinct single atoms in each trap by using a confocal imaging setup, as represented on 1.5. With a magnification of a few tens between the atoms plane and the intermediate plane, the distance between the two images is about one hundred microns. A mirror can be used to separate the fluorescence light scattered from each trap which can then be coupled to two distinct APD detectors. Thus, two-atom experiments can be triggered as soon as the two fluorescence signals are simultaneously above a given threshold.

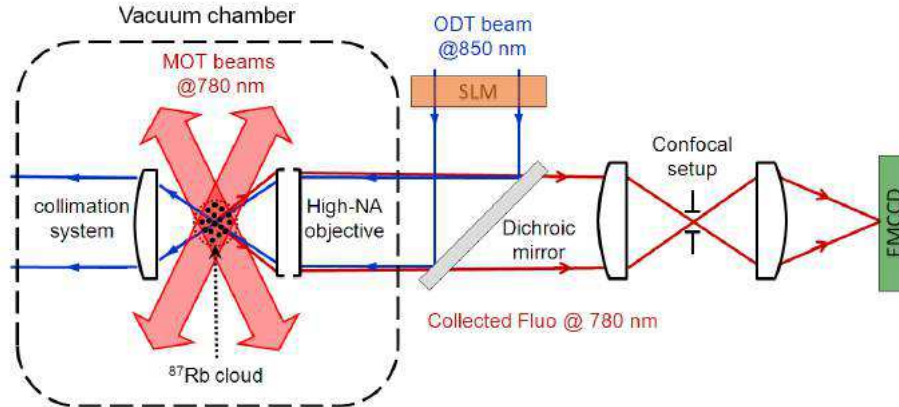


Figure 1.6: Sketch of the new compact setup for N -atom experiment. A spatial light modulator (SLM) imprints various 2D phase patterns on the incoming ODT beam. In the focal plane of the large NA objective, the light intensity profile is approximately the modulus square of the Fourier Transform (FT) of the initial incoming field. Almost arbitrary 2D intensity profiles can be engineered by calculating the right phase pattern to apply onto the ODT beam. Then, any 2D trapping geometry can be imaged onto an Electron Multiplying Charge Coupled Device (EMCCD) camera used in a confocal imaging setup for filtering unwanted background light.

Towards 2D patterns of single atoms

Increasing the number of traps by combining more and more beams quickly becomes expensive and cumbersome. Many research groups have investigated other ways to generate 2D arrays of dipole traps using arrays of microlenses (Dumke *et al.*, 2002), optical lattices (Nelson, Li, and Weiss, 2007), or diffractive optics (Piotrowicz *et al.*, 2013) working with various interatomic distances, depth and volume of the traps.

Promising studies based on holographic techniques were conducted in our group during B. Darquié's thesis around 2004 (Bergamini *et al.*, 2004; Darquié, 2005). A programmable spatial light modulator (SLM) was used to create arbitrary intensity patterns in the focal plane of the large NA imaging system, in which the single atom loading regime could be achieved. This device operates outside the vacuum chamber and allows to take advantage of the full numerical aperture of the trapping setup. Thanks to their rather low optical losses, standard SLM devices should allow us to produce up to fifty traps with an initial laser power of about 1 W. This scheme is currently under investigation but has already allowed us to produce up to 3×8 arrays of microscopic dipole traps as shown in Fig. 1.1. Once the 2D patterns of traps are created, one still needs to find a way to image the trapped atoms. It is very inconvenient to separate spatially the fluorescence light of more than two or three traps with confocal setups and mirrors. Instead, the SLM can be used in combination with an EMCCD camera. A sketch of the setup is represented in Fig. 1.6.

A major limitation to the scalability of the system is due to the stochastic process used so far for loading the traps. Deterministic loading schemes based on inelastic blue-detuned light-assisted collisions (Grünzweig *et al.*, 2010) or taking advantage of the Rydberg blockade mechanism (Beterov *et al.*, 2011) will be investigated. A first step in this last direction has been demonstrated recently in Ebert *et al.* (2013).

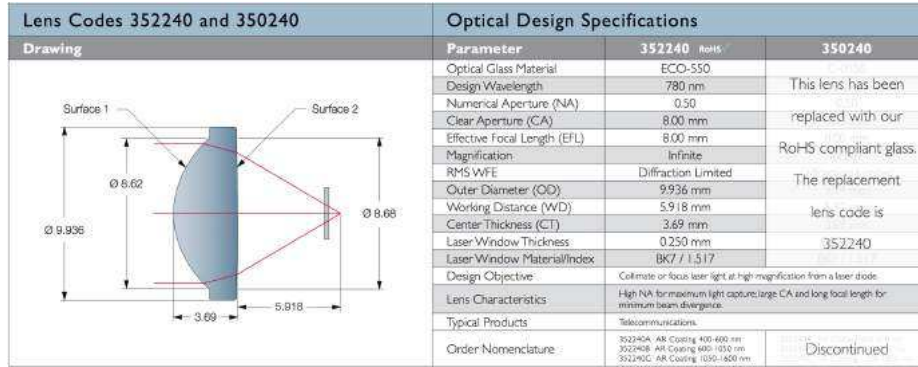


Figure 1.7: Molded aspheric lens from LightPathTechnologies[®] implemented by Sortais *et al.* It is diffraction limited at both 850 nm and 780 nm up to $NA = 0.5$, and has a working distance of almost 6 mm which enables the crossing of small MOT cooling beams (see Fig. 1.11 for a clearer schematic).

Aspheric lenses for compact setup

The design of the large NA objective implemented on the pioneering experiment of (Schlosser, Reymond, and Grangier, 2002) consisted of a vacuum compatible assembly of nine spherical lenses with stringent mechanical constraints on their alignment. Similar optical performances can now be reached with cheap off-the-shelf aspheric lenses. Previous experiments in our group (Sortais *et al.*, 2007), and now in many other groups (Grünzweig *et al.*, 2010) have implemented similar setups using a single aspheric lens to focus the trapping light and to image the trapped atoms. This achievement follows on recent advances in molding technology enabling the design of diffraction-limited and vacuum compatible aspheric lenses with large numerical aperture. These lenses are now available on the market for only a few hundreds of euros and can be found in a wide range of parameters such as focal, working distance, or operating wavelength. Among them, some exhibit large enough working distances to allow for the crossing of small MOT cooling beams. Drawing and design specifications of the aspheric lens from LightPathTechnologies[®] implemented by Sortais *et al.* is shown in Fig. 1.7.

Conclusion

In order to create the 2D arrays of single atoms, the experimental requirements concerning the optical system are mainly twofold:

- First, a large numerical aperture (typically $NA > 0.4$) is needed to produce small traps with high two-body collision rates;
- Second, a large detection efficiency is required to detect the presence of the trapped atoms as quickly as possible.

A convenient compact solution is to use the same large NA molded aspheric lens to focus the ODT beams and to collect the fluorescence light emitted by the trapped single atoms. This provides large optical access for internal states manipulation of the trapped atoms. We will see below that the simplicity and the compactness of the setup is also crucial to implement the tools needed to control the electrostatic environment seen by the trapped atoms excited towards Rydberg states.

1.1.2 Rydberg states manipulation

The second main challenge is to achieve the control of the dipole-dipole interactions between atoms excited to Rydberg states. These states exhibit large dipole moments which make them very sensitive to external electric fields.

Indeed, they are so sensitive that they can even be ionized in rather weak external electric fields. Taking advantage of this property, high-lying Rydberg states have been used as probes for compensating residual electric fields down to tens of microvolts per centimeter (Neukammer *et al.*, 1987). They have also been used in spectroscopy setups as local sensitive electric field sensors to probe patch charges effect on conducting surfaces (Tauschinsky *et al.*, 2010).

However, in our experiment, the atom-atom interactions strength depends strongly on the purity of the Rydberg states which could be contaminated by other unwanted states via Stark mixing. We will see how to avoid uncontrolled states mixing by implementing both a passive stable electrostatic environment and an accurate active experimental control of the static electric fields surrounding the atoms.

Avoiding patch charges effect from the lenses

On typical single atom trapping setups described in the previous section, the atoms electrostatic environment can be affected by the proximity of dielectric surfaces exhibiting patch charges. Indeed, for a given large aperture angle needed for small trapping volume, the working distance between the trapped atoms and the closest dielectric surface of the imaging system depends only on the 'clear aperture' diameter ϕ_{ca} of the last optical element (see Fig. 1.11). Custom large diameter optics with large NA are hard to make so their price is prohibitively high; this was the main reason to use cheaper diffraction limited aspheric lenses with typical working distances on the order of 5 mm. Unfortunately, at such short distances, previous studies led by Alpha Gaetan and Charles Evellin (Gaetan, 2009; Evellin, 2011) on the former Rydberg apparatus clearly showed the parasitic effect of patch charges accumulating on the last dielectric surface of a lens, only few millimeters away from the trapped atoms.

Indeed, patch charges are responsible for stray electric fields which induce energy shifts of the atomic Rydberg states via DC Stark effect. Those shifts can fluctuate over time while the charges rearrange slowly onto the dielectric surface. To be able to perform and read out a coherent optical transition between an initial ground state and a targeted Rydberg state, the induced Stark shift fluctuations have to remain much smaller than the laser excitation width during all the acquisition time of the coherent Rabi oscillations. On the former apparatus, the first experimental realizations of coherent transition between the ground state $5S_{1/2}$ and the targeted Rydberg state $58D_{3/2}$ exhibited a maximal Rabi frequency $\Omega = 2\pi \times 3$ MHz. The polarizability of the ground state can be neglected. The excited Rydberg state polarizability α is on the order of $300 \text{ MHz}/(\text{V}/\text{cm})^2$ (see details in Appendix B). So we can estimate the static electric field F leading to a Stark effect ΔU_{Stark} shifting the atomic transition out of resonance with respect to the excitation lasers:

$$\Omega \simeq \frac{\Delta U_{\text{Stark}}}{\hbar} = \frac{1}{2} \alpha F^2 \implies F \simeq \sqrt{\frac{2\Omega}{\alpha}} \simeq \sqrt{\frac{6}{300}} \simeq 150 \text{ mV}/\text{cm}. \quad (1.7)$$

The distance between the atom and the closest dielectric surface was 4 mm. By applying Coulomb's law, an elementary charge q creates a field with amplitude F_q at distance $r =$

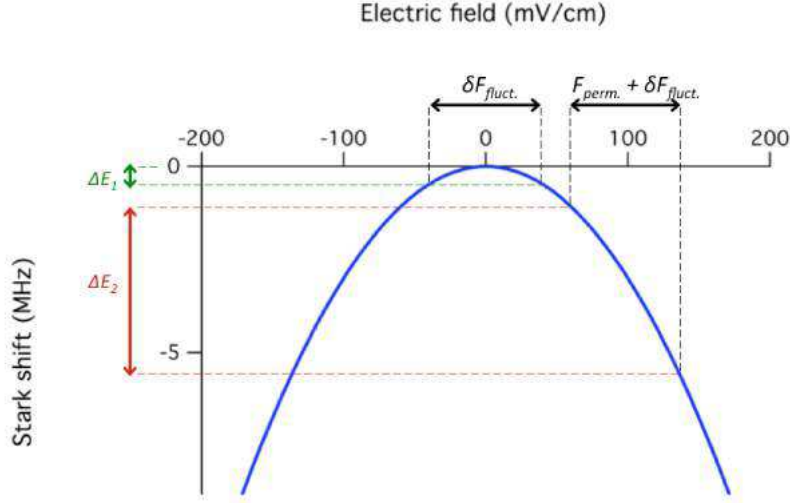


Figure 1.8: Influence of uncompensated residual DC fields on the Stark effect of the state $58D_{3/2}$. For a given fluctuation amplitude of stray fields $\delta F_{\text{fluct.}}$ along a chosen axis, the stark shift fluctuation ΔE_1 (green) related to the zero-DC field case is much smaller than ΔE_2 (red) where a permanent field $F_{\text{perm.}} = 100$ mV/cm is present.

4 mm:

$$F_q = \frac{q}{4\pi\epsilon_0 r^2} \sim 10^{-8} \text{ V/cm.} \quad (1.8)$$

The number of elementary charges responsible for decreasing the contrast of coherent Rabi oscillations would then be about $\Delta N_{\text{charges}} = F/F_q \simeq 10^7$. We will see in chapter 3 that we could observe the effect of such charges on the new apparatus, before correcting for it. The charges were most likely at the origin of drifting electric fields with amplitudes as high as 150 mV/cm. For Rydberg states with $n \geq 50$, such high stray fields can lead to neighboring states mixing which would completely prevent us from well controlling the atom-atom interactions.

One way to shield the atoms from these slowly drifting electric fields is to use a grid connected to the ground placed in front of the fields sources on the dielectric surface. Behind the grounded grid, the parasite field amplitude decreases exponentially with the distance towards the trapped atoms, with a decay length on the order of the grid spacing. However, it may affect the optical properties of the lens.

Another way is to use a conductive coating also connected to the ground on the lens itself. In our case, we used a transparent and colorless thin layer of indium tin oxide (ITO) coating¹. The film is 200 nm thin and it has a transmission $T_{\text{ITO}} \geq 90$ % for the operating wavelengths 780 nm and 850 nm.

Active control of the electrostatic environment

Though stray fields fluctuations should be passively minimized as well as possible, it is also crucial to implement an active and accurate control of the electric environment surrounding the excited Rydberg atoms.

¹ITO is often used to make transparent conductive coatings for devices such as liquid crystal displays, flat panel displays, plasma displays, or touch panels.

First, the Stark effect is quadratic for low angular moment states of Alkali atoms. So, the effect of residual charge fluctuations gets even worse if the ^{87}Rb atoms are trapped in a region where a permanent DC field $F_{\text{perm.}}$ created by another steady source is already present and cannot be compensated for, as shown in Fig. 1.8. By grounding most of the material surrounding the atoms, the amplitudes of these permanent fields are expected to be small but not negligible. Canceling them is a preliminary and necessary step towards the control of atomic interactions.

Second, the strength of the dipole-dipole interactions can be tuned up or down by using so called Förster resonances (see Sec. B.2). Those resonances occur in systems of two atoms A and B when two-Rydberg-atom states $|\Psi_1\rangle = |r, r\rangle$ and $|\Psi_2\rangle = |r', r''\rangle$ of energies E_1 and E_2 are coupled by the dipole-dipole interaction. By applying an external electric field, these states can get Stark shifted differently such that for a certain amplitude $F_{\text{res.}}$ a perfect degeneracy can be reached: $E_1 = E_2$. This leads to an avoided level crossing for which the strength of the dipole-dipole interaction is enhanced. For the resonances we can investigate in our experiment, the field amplitudes required to reach such a resonance are small, in the 10-100 mV/cm range. A well chosen set of at least four electrodes close to the atoms can be used to impose finely controlled electric fields in any given direction matching the resonance condition. These electrodes can be used to apply both compensation electric fields in the permanent regime, and add weak controlled pulsed fields to tune the system to a Förster resonance in a given time window.

Selective ionization and positive detection of Rydberg states

Finally, Rydberg states have low binding energies (~ 1 THz) so they can be ionized by rather weak static electric fields. A sensitive charge detector based on avalanche processes can then be used to detect the single ion or the single electron with detection efficiency up to 50 %. An estimate of the electric field $F_{\text{ioniz.}}$ required to ionize a given Rydberg state with an effective principal quantum number $n_{n,l,j}^*$ can be obtained with a classical calculation (see Sec. B.1.3), and reads:

$$F_{\text{ioniz.}} = \frac{F_0}{16 n_{n,l,j}^*{}^4}, \quad (1.9)$$

with

$$F_0 \simeq \frac{16\pi\epsilon_0 Ry^2}{q^3} \simeq 5 \times 10^9 \text{ V/cm}, \quad (1.10)$$

where Ry is the Rydberg unit of energy. For $n \geq 40$, the amplitudes of the fields required to ionize the Rydberg states do not exceed 150 V/cm. Furthermore, the precision required to discriminate between two nearby Rydberg states is reasonable. It is related to the typical spread in $n_{n,l,j}^*$. Around $n = 40 - 80$ and for low orbital moment $l = 0, 1, 2$, the typical spread $\Delta n_{n,l,j}^*$ is 0.5 so the precision for the field amplitude can be estimated using Eq. 1.9:

$$\frac{\Delta F_{\text{ioniz.}}}{F_{\text{ioniz.}}} = 4 \frac{\Delta n_{n,l,j}^*}{n_{n,l,j}^*} \sim 4\%. \quad (1.11)$$

The voltage controlled power supply used to apply $F_{\text{ioniz.}}$ thus has to be accurate to about a volt in the range 100–1000 V.

Conclusion

To achieve a fine control over the dipole-dipole interactions between single Rydberg atoms, we have identified the following experimental requirements:

- First, the electrostatic environment of the trapped atoms has to be passively stable to avoid Rydberg states mixing. In our specific setup, patch charges at the surface of the lenses are the main source of fluctuating uncontrolled fields. These fields can be shielded by using a conductive ITO coating connected to ground;
- Second, an active control of static electric fields pointing in any chosen direction has to be implemented to compensate for stray DC stray fields, to manipulate Förster resonances and to apply pulses of ionizing fields. It is achievable by using controlled electrodes close to the atoms. Their design has to be vacuum compatible and take into account optical access needed for all the laser beams. A large dynamical range for the fields amplitude of about 10 mV/cm to 200 V/cm is required with a relative accuracy and repeatability $\leq 1\%$ both for fine tuning of Förster resonances (low fields), and for selective Rydberg states detection (high fields);
- Last, a sensitive charge detector combined with the pulses of ionizing fields can be used to implement a positive detection scheme of Rydberg states. This latter should not block the path of the laser beams and F -field lines must be carefully engineered so that single charged particles can be guided towards its detection area.

1.2 UHV compatible experimental apparatus design

The crucial requirements needed for designing the new apparatus have been discussed in the previous section. We will now describe how the parts inside the science chamber were designed to reach the specifications. As we saw previously, the first step towards the study of interactions between single atoms is to create a cloud of cold rubidium 87 atoms. We have chosen to implement a standard MOT setup with three pairs of counterpropagating beams in a $\sigma_+ - \sigma_-$ configuration and a pair of anti-Helmholtz coils. Then the tools required for Rydberg states manipulation of single atoms had to be incorporated. A sketch of a compact solution comprising the aspheric lenses, the electrodes, the MCP detector and the MOT coils is shown in Fig. 1.9. To begin with, we designed the optical system consisting of the pair of identical aspheric lenses which sets the mechanical constraints for the other parts.

1.2.1 Custom aspheric lens

The specifications of the optical system are directly related to the atomic physics requirements discussed in the previous section:

Optical specifications

High two-body losses rates, necessary to achieve the single atom regime, require the trapping volume to be as small as possible (see Eq 1.1). Thus, the optical system has to be diffraction limited up to $NA = 0.5$ at the trapping wavelength $\lambda = 850$ nm. This can be quantitatively characterized by the Strehl ratio $S = I_{\text{real}}/I_{\text{stig.}}$, where I_{real} is the peak intensity of the point spread function (PSF) of the real system with aberrations, and $I_{\text{stig.}}$ is the theoretical

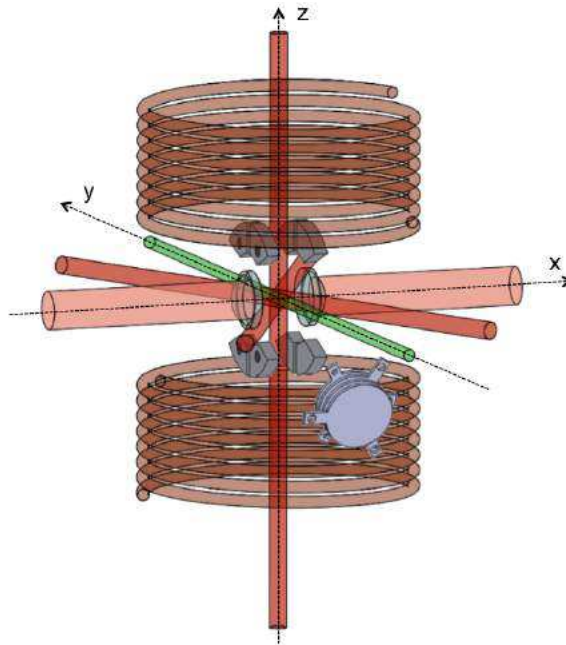


Figure 1.9: Sketch of the setup inside the science chamber. An incoming atomic beam (green) is propagating in the y direction while it is being slowed down by a Zeeman slower laser beam to be loaded in a MOT. Two horizontal pairs (in the xy plane) and one vertical pair (along the z axis) of MOT beams (red) cross each other at the center of the reference frame. Two MOT coils (brown) used in anti-Helmholtz configuration are coaxial with the vertical axis z . A pair of two aspheric lenses (transparent blue) centered on the x axis are symmetrically positioned with respect to the MOT cloud. A collimated ODT beam (pink) propagating backward along the x axis is focused by the first aspheric lens on the right and gets collimated back after going through the second aspheric lens on the left. A set of four cloverleaf shaped electrodes (grey) encircles each aspheric lens. As we will see in more details in Sec. 1.2.3, it is a simple geometry to apply static electric fields in arbitrary directions. A micro-channel plate (MCP) detector (purple) stands below the incoming atomic beam. Its detection surface points towards the focal point of the ODT beam at the center of the diagram.

intensity of the same system without aberration (Born and Wolf, 2003). The Strehl ratio S is a quantity which lies between 0 and 1. It can be related to the quality of the real wavefront with respect to the stigmatic case. Let us define Δ the wavefront deviation from the stigmatic reference over the aperture of the optical system, and $\sigma_{\Delta}^2 = \langle (\Delta - \bar{\Delta})^2 \rangle$ the root mean square of the wavefront deviation. In the limit $\sigma_{\Delta} \ll \lambda$, one shows that:

$$S \simeq \exp\left(\frac{-4\pi^2\sigma_{\Delta}^2}{\lambda^2}\right) \simeq 1 - \frac{4\pi^2\sigma_{\Delta}^2}{\lambda^2}. \quad (1.12)$$

An arbitrary criterion commonly used in optics is to verify that $S \geq 0.8$ at the operating numerical aperture, which corresponds to $\sigma_{\Delta} = \lambda/14$. A practical consequence is that the larger S , the deeper the optical trapping potential seen by the atoms will be for a given trapping laser power.

The same system is then used to collect fluorescence light emitted by the trapped atoms at $\lambda_{\text{im.}} = 780$ nm. For this wavelength, the collection efficiency has to be as large as possible. In this configuration, the position of the object (the single atom) with respect to the optical system is determined by the focal point at 850 nm. The system can be affected by axial

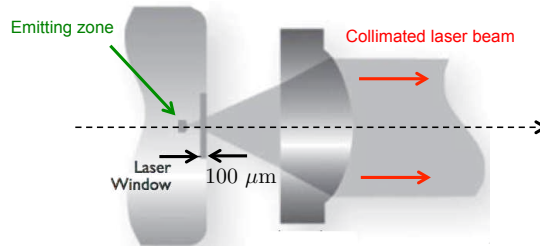


Figure 1.10: Typical aspheric lens used for laser diode collimation. The radial profiles of aspheric lenses used for laser diode collimation are calculated to compensate for the residual spherical aberration due to $100\ \mu\text{m}$ -slab of glass covering the emitting zone in standard diode packages.

chromatism such that the collected beam at $780\ \text{nm}$ does not exit the vacuum chamber with the same divergence as the incoming trapping beam at $850\ \text{nm}$. This is not an issue as long as the angle is small enough such that a common imaging setup can be implemented. Finally, the long-term goal is to study N -single atom interactions trapped in 2D arrays of ODTs such as the patterns shown in Fig. 1.1 up to about 9 by 9 traps with a typical separation of $5\text{-}6\ \mu\text{m}$. Thus, the system has to exhibit good optical performances off-axis up to fields of about $\pm(9-1)/2 \times 6\ \mu\text{m} = \pm 24\ \mu\text{m}$. Quantitatively, the Strehl ratio S has to remain bigger than 0.8 within a field of about $\pm 24\ \mu\text{m}$ for both the trapping and the imaging wavelength.

Previous studies conducted in the group by Sortais *et al.* (2007) demonstrated that a single aspheric lens could achieve these specifications. However, at the time they built the first experiment, they directly bought the lens from LightPathTechnologies[®] catalogue. So the lens was not originally intended to be used for an atomic physics experiment and it had to be adapted to work as initially specified. When this project started in October 2010, LightPathTechnologies[®] assisted us for custom aspheric lens design. We took this opportunity to try a new design, specifically adapted to our needs, and which could improve slightly the optical performances of the former lens.

Looking for improvements

We identified three points that could be improved by designing the lens profile ourselves:

- First of all, a large proportion of large NA aspheric lenses produced in the industry is used to collimate light emitted by laser diodes. These diodes are generally sold in standard packages where an active zone emits the laser light through a thin glass window as shown in Fig. 1.10. This slab of glass introduces spherical aberration as soon as the diode is working beyond the paraxial regime. The profile of the aspheric lens operating the collimation is then calculated to correct for this spherical aberration. In our case, when such a lens is used to focus a trapping laser beam under vacuum, there is no thin glass window anymore and a 'negative' spherical aberration due to the lens shape itself appears. The way around used in Sortais *et al.* (2007) was to use the lens with finite conjugate ratio. It is possible to find an incident convergence angle for which the lens becomes aberration free. But then, one needs to control both the incoming beam diameter and the incident convergence angle on the lens, which further constrains the optical layout. By designing the aspheric profile ourselves, we could preserve the flexibility to work with a collimated incoming trapping beam.
- The working distance WD between the last surface of the aspheric lens and the focal plane where the atoms are trapped (see Fig. 1.11) could be improved. This is interest-

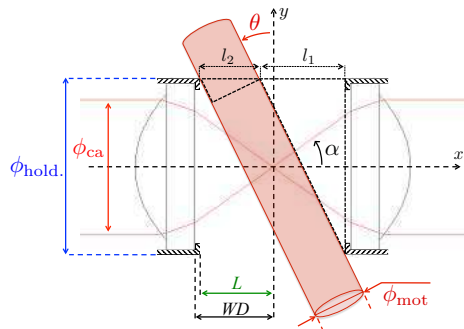


Figure 1.11: Geometry constraints on the MOT beam diameter. This sketch shows the two aspheric lenses facing each other in our experiment. The dashed parts correspond to the mechanical pieces needed to hold the lenses. Their thickness were reduced as much as possible with standard machining specifications down to $500 \mu\text{m}$.

ing for two reasons. First, it also allows to increase the MOT beams diameter, which makes the alignment of the MOT setup a lot easier². Second, once the MOT diameter is fixed, increasing WD allows to avoid scattering light on the lens holders.

- Finally, the numerical aperture $NA = \sin \alpha$ of the imaging system at 780 nm (see Fig. 1.11) could be larger, which increases the collection efficiency of the fluorescence emitted by the trapped atoms.

The two last points rely on the ability to mold diffraction limited aspheric lenses with large 'clear aperture' diameter while keeping very good optical performances.

Design procedure with OSLO[®]

Our contribution to the design of the custom aspheric lens was conducted with the software Optics Software for Layout and Optimization (OSLO[®]). This software implements a method of sequential ray tracing between an object and an image plane through several interfaces based on Snell's law of refraction. Each medium i is defined with an effective index n_i , a thickness t_i and the interfaces are cylindrically symmetric surfaces around the propagation axis x described by a set of equations $x_i = f_i(r)$, where x_i is the surface coordinate along the rotation axis, and r the distance to the x axis. Fig. 1.12(a) shows OSLO[®] environment for such interface specification. The goal was to define the equations of the two aspheric surfaces of the custom lens to minimize optical aberrations.

The general shape of the lens was the first parameter to decide on. In ray optics, for any conjugate ratio between an object and its image, there exists a certain lens shape that minimizes the 3rd order spherical aberration, which is the main aberration in our system working almost only on-axis. In the case of infinite conjugate ratio and with a typical glass spherical singlet, the plano-convex shape with convex side towards the collimated incoming

²The MOT beam diameter is constrained by the opto-mechanical geometry involving the diameter of the mechanical lens holders ϕ_{hold} (almost equal to the clear aperture diameter ϕ_{CA}), the distance between the holder and the focal point L , and the angle θ between an horizontal MOT beam and the atomic beam axis y , as represented in Fig. 1.11. They are related as follows:

$$2L = l_1 + l_2 = \phi_{\text{hold}} \tan \theta + \frac{\phi_{\text{mot}}}{\cos \theta}. \quad (1.13)$$

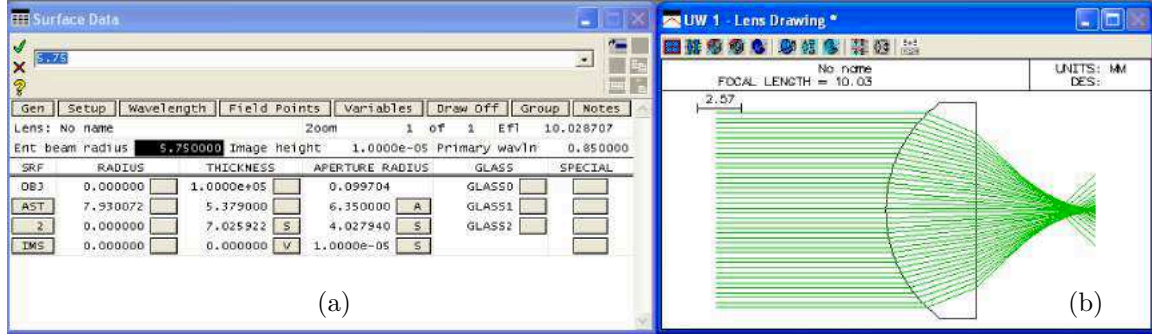


Figure 1.12: OSLO[®] environment. (a) shows the design environment interface. (b) represents a set of 40 incoming rays parallel to the optical axis passing through the optical system in 2D. The system is not yet optimized, and the operating numerical aperture is large, on the order of 0.5, so the spherical aberration is colossal. The caustic curve of the spherical aberration can even be observed at this scale. In the paraxial focal plane, the resulting geometrical spot diameter is about 2 mm.

trapping beam performs nearly as well as the best-form spherical lens. It is a quite popular shape, because a plano-convex lens costs much less to manufacture than an asymmetric biconvex singlet.

Once the general shape was chosen, we chose the clear aperture diameter ϕ_{ca} to be as large as possible. With tooling diameter limited to 20 mm used for the molding process, lenses with maximum outer diameter up to 15 mm could be achieved. Then, a 1 mm thick flat bored flange required to tighten the molds together during the process limits the maximum effective outer diameter down from 15 mm to 13 mm. Last, a blending radius due to releasing of molds during fabrication eventually fixes the upper bound for the clear aperture diameter $\phi_{ca} = 12.5$ mm up to which theoretical aspheric profiles with diffraction limited performances could be guaranteed.

Then, for an infinite conjugate ratio configuration with a numerical aperture $NA \geq 0.5$ at 850 nm, the effective focal length is upper bounded as: $f_{\text{eff}} \leq \phi_{ca}/(2\alpha) \simeq 10.8$ mm. We fixed this value to 10 mm to keep a large enough working distance WD . Assuming the central thickness CT of the lens to be small enough such that thin lens approximation is valid, the curvature radii of the lens could be estimated using the lens-maker's formula:

$$\frac{1}{f} = (n_{850} - 1) \left(\frac{1}{R_1} - \frac{1}{R_2} \right), \quad (1.14)$$

where f is the focal length, n_{850} is the refractive index of the lens material at 850 nm, and $R_{1,2}$ are the algebraic radii of curvature of the two lens surfaces measured from the front surfaces towards their centers of curvature. The chosen plano-convex shape implies $R_2 = \infty$. The glass used for molding is D-ZLAF52LA with a refraction index $n_{850} = 1.7902$ so we could estimate $R_1 = 7.9$ mm. With a reasonable value of the central thickness $CT \simeq 5.4$ mm, OSLO[®] could be used to check the expected behaviour of the initial system. At this point, the spherical aberration of the system was colossal, and led to a geometrical spot with a radius on the order of $900 \mu\text{m}$ as shown in Fig. 1.12(b).

The following step was to make the surface aspheric. Rotationally symmetric aspheric surfaces passing through the origin are commonly described by the equation:

$$x = \frac{r^2}{R \left(1 + \sqrt{1 - (1 + \kappa) \frac{r^2}{R^2}} \right)} + A_4 r^4 + A_6 r^6 + A_8 r^8 + A_{10} r^{10} + A_{12} r^{12} + \dots, \quad (1.15)$$

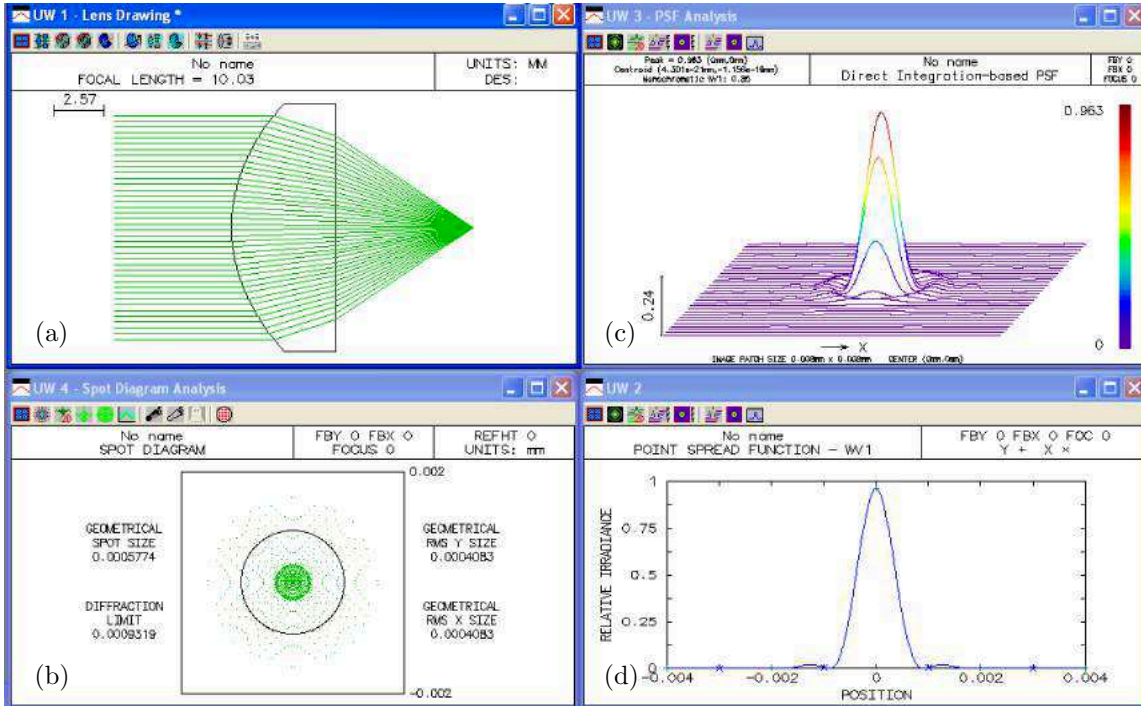


Figure 1.13: OSLO[®] diagnostic tools. (a) represents a set of 40 incoming rays parallel to the optical axis passing through the optical system in 2D after optimization of the aspheric profile. (b) shows an the corresponding on-axis spot diagram computed in the best focal plane of the lens. On the left, standard deviation of the geometric rays radial position distribution σ_R and the radius of the Airy disk corresponding to the diffraction limit of the system are given in mm. The expected PSF can be plotted in 3D with the Strehl ratio in the top right corner (c), or with a 2D cut passing through the global maximum (d).

where R and κ are respectively the curvature radius and the conic constant³ of the surface, and the coefficients A_{2i} are aspheric surface corrections of higher even orders. OSLO[®] allows to perform multi-variable optimization algorithms to find good values for the A_{2i} coefficients. One of them is based on minimizing the spot diagram standard deviation σ_R of the optical system; after choosing a good set of geometrical rays j covering the full entrance pupil, OSLO[®] calculates the impact radial position r_j of each of these rays in a chosen imaging plane, such as represented in Fig. 1.13(b). A comparison between the width of this distribution and the radius of the Airy disk (in dark) associated to a virtual equivalent stigmatic optical system gives information about how much the real system is affected by geometrical aberrations. Getting this width as low as possible can be used as a good error function for optical system optimization. In our case, we started to apply such optimizing procedures with CT , κ , and the A_{2i} coefficients, with i up to 6, as free parameters in the case of an incoming collimated trapping beam at 850 nm. The expected point spread function (PSF) of the system can be calculated with OSLO[®] and be used to compute the Strehl ratio S . An example of such a PSF obtained after optimization with a Strehl ratio $S \simeq 0.96$ is shown in Fig. 1.13(c) and (d).

This way, we found good first estimates for all the aspheric parameters, and it fixed the working distance WD at which the atoms are trapped. Then, we returned the system to

³The lens surface has the shape of a conic section rotated about the optical axis which form depends on the conic constant as follows: $\kappa < -1 \rightarrow$ hyperbola; $\kappa = -1 \rightarrow$ parabola; $-1 < \kappa < 0 \rightarrow$ ellipse; $\kappa = 0 \rightarrow$ sphere.

Parameters	Lens 352240	Custom lens
Conjugate ratio @ 850 nm	Finite	Infinite
Working distance WD	5.70 mm	7.03 mm
MOT beam diameters ϕ_{mot} ($\theta = 26^\circ$)	4.2 mm	4.8 mm
Operating NA ($S \geq 0.8$ for $y \pm 25 \mu\text{m}$)		
$\lambda_{\text{trap}} = 850 \text{ nm}$:	0.45	0.45
$\lambda_{\text{fluo}} = 780 \text{ nm}$:	0.50	0.53

Table 1.1: Comparison of the main features of the former and the new optical system.

simulate an atom emitting light at 780 nm while keeping the value of WD fixed. The beam at 780 nm is not collimated, it is focused about 2.7 m after the lens where it is also possible to perform a spot diagram minimization. We finely optimized the aspheric coefficients A_{2i} to get the best theoretical performances of the lens at 780 nm in this configuration. At last, we checked that the final aspheric coefficients A_{2i} led also to good theoretical performances for focusing the 850 nm trapping laser. All the parameters obtained after complete optimization are summed up in Appendix C which includes all the technical drawings, specifications and tolerances of the custom lens.

Optical performances

Ten similar custom lenses were received and a subset was tested before coating them with a 200 nm thick ITO layer and operating them in a vacuum environment. A point source illumination method was used to characterize experimental point spread functions (PSFs) for various operating numerical apertures and various transverse fields (see Appendix C for characterization details). As expected, the lenses performed a bit better at 780 nm than at 850 nm. The table 1.1 sums up the comparison between the main features of the former and the new optical system. In the end, the custom new lens is only slightly better, except for the real benefit to work with an infinite conjugate ratio configuration.

1.2.2 Lens holders assembly inside vacuum

Once the geometry of the optical setup was defined, we designed the corresponding opto-mechanical system to guarantee good relative spacing and centering of the lenses inside the main vacuum chamber, providing optimal operating conditions. This was done with the software SolidWorks®.

Concerning the centering of the system, we saw previously that the field of view of the lenses is about $\pm 25 \mu\text{m}$. To be able to use simultaneously the two lenses for trapping or imaging (even if one is enough to begin with), the centering tolerances are smaller than $25 \mu\text{m}$. To achieve this, we implemented a solution based on a single machined amagnetic A4 stainless steel block screwed to the bottom flange of the vacuum chamber, as represented in grey in Fig. 1.14. This piece is almost cut in two in the yz -plane to allow for the crossing of the MOT beams as well as to create space close to the atoms that will be useful to position the electrodes (see Sec. 1.2.3). It is drilled along the x -axis with ISO H6g7-boring tolerances with respect to the yellow lens holder part. The hole diameter is 22 mm for a depth of 12.5 mm, so H6g7-boring tolerances of about $12.5 \mu\text{m}$ could be held. The lens

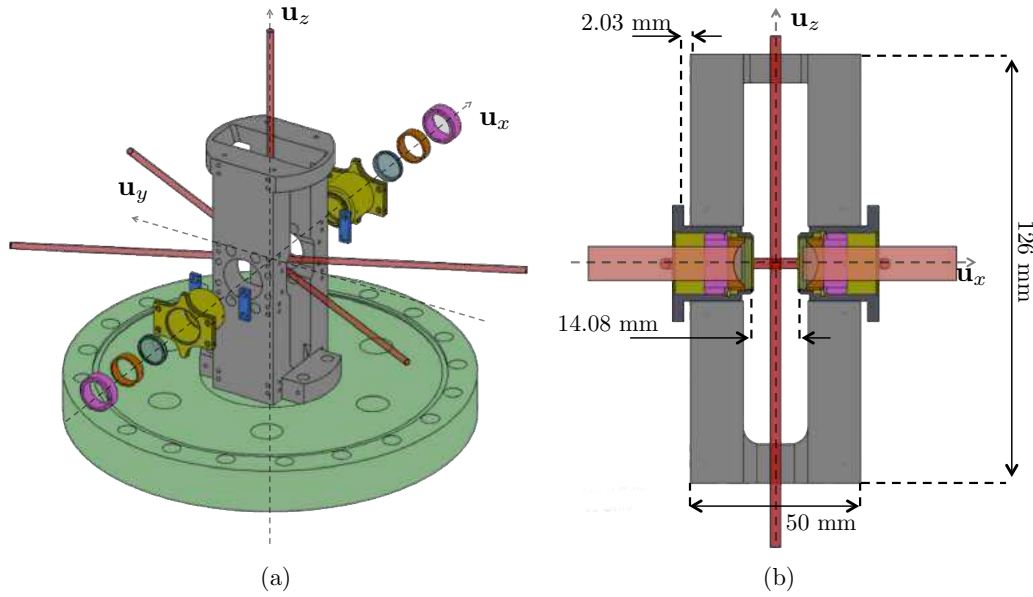


Figure 1.14: Lens holders assembly inside vacuum. (a) Disassembled view of the lens holders assemblies into the central A4 stainless steel piece. The lens holders (yellow) are also made out of A4 stainless steel. Each lens (transparent blue) is held inside by a peek washer (orange) and an A4 stainless steel threaded ring (purple). The distance between the two aspheric lenses is adjusted by A4 stainless steel spacers (blue). (b) Cut of the assembled system along the zx -plane. The A4 stainless steel spacers are hidden behind the lens holders.

holders are also made out of A4 stainless steel. The lens is held inside by a PEEK washer⁴ and a M18 A4 stainless steel threaded ring. PEEK is softer than steel and it is used to compensate for possible mechanical expansion constraints during the bake out to protect the lenses.

Finally, the spacing between the two lenses is controlled by the thickness of two pairs of A4 stainless steel spacers. They were carefully adjusted in situ with the great help of the Optics Workshop at the Institut d'Optique. The thickness of the spacers was purposely machined too large so that the lenses were initially too far apart. Then, the optical engineers polished them in multiple steps to remove each time about $20 \mu\text{m}$ of steel on all of them at the same time. At each polishing iteration, the distance between the two lenses was decreased by about $40 \mu\text{m}$ before we operated the complete opto-mechanical system under primary vacuum conditions. A collimated trapping beam was sent through the two lenses, and we measured where it was focused after the system. We could then estimate the spacing accuracy between the two lenses with respect to the theoretical specifications using the thin lens equation for the second lens:

$$\overline{FA} \times \overline{F'A'} = -f^2, \quad (1.16)$$

where A and A' are respectively the object and the image points of the trapped atoms with respect to the second lens, F and F' are the focal points, and $f = 10 \text{ mm}$ is the focal length of the second lens. For a perfectly symmetric system, the beam is collimated back by the second

⁴Polyether ether ketone (PEEK) is a colourless organic polymer thermoplastic used in various engineering applications. It has a glass-liquid transition temperature of 143°C and a melting point temperature of about 343°C .

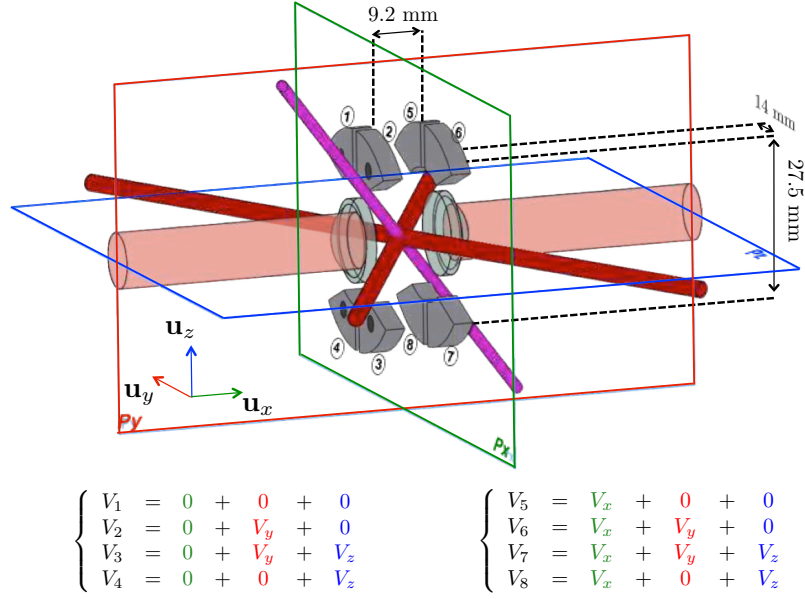


Figure 1.15: Octopole configuration of control electrodes. The three symmetry planes P_x , P_y and P_z are drawn in green, red and blue respectively.

lens such that $\overline{F'A'} = \infty$. In practice, we stopped the process when $\overline{F'A'} \geq 30f \simeq 3000$ mm, which corresponds to a spacing mismatch $|\overline{FA}| \leq f/30 \simeq 30 \mu\text{m}$. The height of the central piece was designed such that it can also be used for mounting the MOT coils, as we will see in more details in Sec. 1.2.4.

1.2.3 Control electrodes and MCP charge detector

Based on the opto-mechanical assembly described in Fig. 1.14, we designed the electrodes used to apply controlled electric fields together with the charge detector following the specifications described in Sec. 1.1.2.

Octopole electrodes configuration

We took advantage of the natural symmetries of the setup to implement a symmetrical octopolar configuration of the control electrodes, as represented in Fig. 1.15. This configuration allows to control both the amplitude and the direction of a desired external electric field in a simple way. Indeed, the three planes P_x , P_y and P_z are symmetry planes of the electrodes system. A given field $\mathbf{F}_i = F_i \mathbf{u}_i$ in direction $i = x, y, z$ is obtained by applying the electric potentials V_i^+ on the four electrodes on one side of plane P_i , and V_i^- on the four electrodes on the other side of plane P_i such that $\Delta V_i = V_i^+ - V_i^-$. At the center (where the atoms are trapped), the symmetry of the charge distribution ensures that voltage ΔV_i corresponds to a field normal to the plane P_i , of the form $F_i \mathbf{u}_i$. The superposition principle of electrostatics states that a given field $\mathbf{F} = F_x \mathbf{u}_x + F_y \mathbf{u}_y + F_z \mathbf{u}_z$ is obtained by adding the electric potentials used to create the three independent electric tensions ΔV_x , ΔV_y and ΔV_z which respectively create the orthogonal fields $F_x \mathbf{u}_x$, $F_y \mathbf{u}_y$ and $F_z \mathbf{u}_z$. By imposing electrode 1 to be grounded, $V_i^- = 0$ V and $\Delta V_i = V_i^+$, and the required potential is worked out as shown in Fig. 1.15. In practice, only the three parameters V_x , V_y and V_z have to be controlled. The corresponding field amplitudes F_i are then of the form: $F_i = V_i/l_i$, where

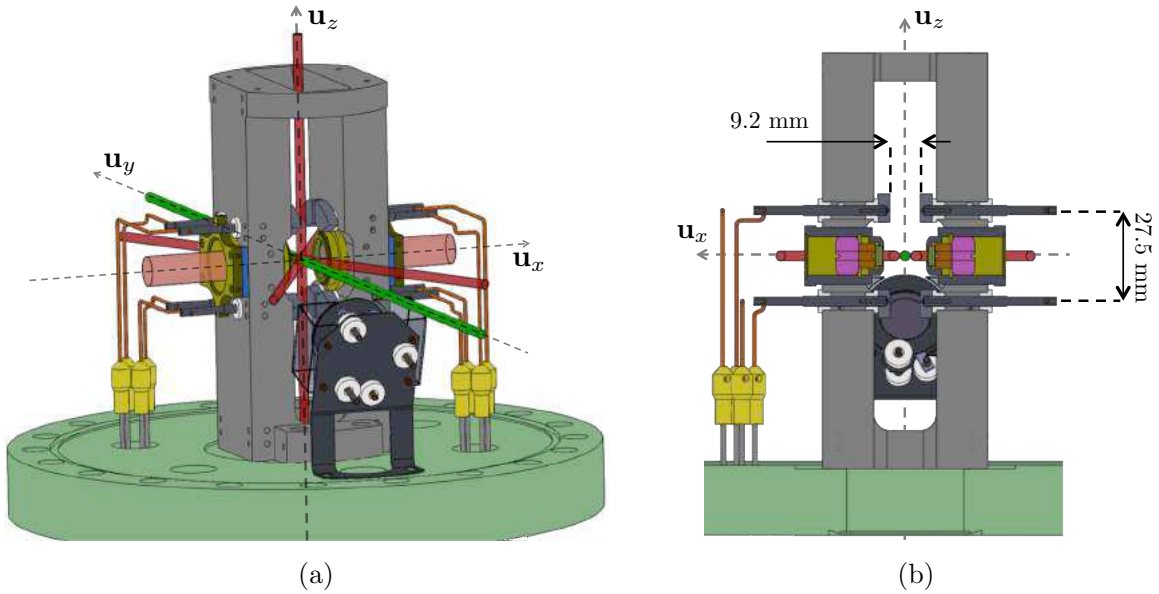


Figure 1.16: Electrodes and charge detector assembly inside vacuum. (a) Isometric view of the electrodes (dark grey) mounted on the central stainless steel piece (light grey) with pairs of isolating ceramic spacers (white) and threaded rods (dark grey) going through the central piece. The electrodes are contacted to medium voltage electrical feedthroughs with thin copper wires screwed to the other end of the rods at one side, and connected to crimp connectors (yellow) on the other side. The MCP detector is mounted just below the incoming atomic beam and points towards the position of the MOT. (b) Cut of the assembled system along a plane parallel to the zx -plane and passing through the set of four rods placed on the MCP detector side.

the coefficients l_i are effective lengths. In a first step, we estimated these parameters by performing 3D numerical simulations of the electric fields with boundary conditions as realistic as possible. This will be described later in this section.

Mechanical mounts for the electrodes

To be able to apply ionizing fields on the order of 200 V/cm with reasonable voltage power supply ($\sim 1 \text{ kV}$), it was crucial to position the electrodes as close to the atoms as possible while keeping all the optical access available. The cloverleaf shape was the result of a tradeoff between having large plates simulating quasi-infinite plane capacitors and keeping available the optical axis up and down by 19° of each of the four horizontal MOT viewports (see Fig. 1.20). One beam going along one of these axes is also depicted in purple in Fig. 1.15. The surfaces of the electrodes were mechanically polished to an average roughness $R_a = 0.8 \mu\text{m}$. Arc discharges are not likely in ultra high vacuum conditions ($P \simeq 10^{-10} \text{ mbar}$), however good surface finish might help having smooth fields structures at short distances. The eight electrodes were mounted using threaded rods going through the central stainless steel piece and electrically isolated using ceramic spacers, as shown in Fig. 1.16. The rods are threaded outside towards the electrodes and in their middle so their assembly can be screwed to the central piece. At their other end, they are threaded inside and drilled perpendicular to their axis with a 1 mm diameter through-hole such that thin copper wires can be inserted

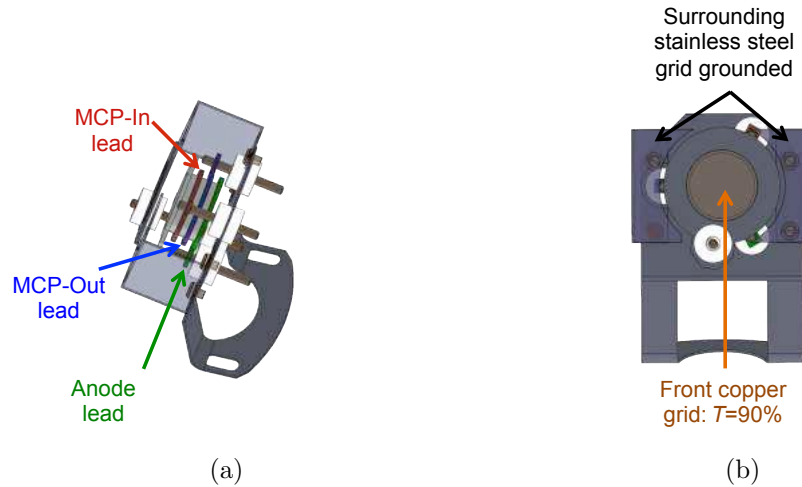


Figure 1.17: Hamamatsu MCP detector F4655. (a) Side view of the MCP assembly showing MCP connections and grids. (b) Front view of the MCP assembly. A stainless steel grid shaped like 'ears' around the detector is connected to ground in order to shield the MCP operating high voltage which could induce parasitic fields and prevent Rydberg states manipulation. In front of the detector, an independent copper grid with a transmission of 90 % can be connected to positive or negative potentials to guide electric field lines and thus the charged particles from the optical trap towards the MCP effective area.

and screwed on. These wires are then cramped to medium voltage electrical feedthroughs⁵ (~ 1 kV).

MCP detector assembly

The sensitive charge detector implemented in combination with ionizing fields to selectively detect Rydberg states is a micro-channel plate (MCP) detector F4655 from Hamamatsu, represented in Fig. 1.17. It is a compact circular-shaped two-stage detector with a 2.5 kV voltage drop across its electrodes. The electron avalanche process taking place in the device leads to a gain on the order of $5 \cdot 10^7$ with a detection efficiency (from the datasheet) of about 50 % for particles energies of 1-2 keV.

The MCP detector was mounted on a stainless steel assembly using threaded rods and isolating ceramic spacers which can be seen in Fig. 1.17(a). Around the detector, an outside steel grid shaped like 'two ears' (see Fig. 1.17(b)) is connected to ground to shield high voltages between the MCP plates producing the charge avalanche process. An independent copper grid with a transmission of 90% is mounted in a steel ring in front of the detector. Arbitrary low voltages (± 15 V) can be applied on this grid in order to guide the electric field lines from the optical trapping region to the MCP.

3D electric fields simulations

In order to check that we could apply external electric fields in controlled directions and amplitudes, we simulated the full opto-mechanical system with the software Simion[®]. This software performs a numerical evaluation of the Poisson equation with user defined bound-

⁵The electrical feedthrough reference is FHM-A4-16CF multipin power from LewVac with maximal DC voltage per pin of 700 V.

ary conditions, and can simulate time of flight of charged particles by computing classical trajectories based on the field lines calculations.

The system was modeled with a rather simplified geometry for the central piece. The outer spherical chamber, the central steel piece and the two ITO-coated surfaces of the aspheric lenses facing the atoms were defined as ground. The electrodes and the front grid of the MCP were connected to arbitrary voltages depending on each simulation. Calculations were performed with a mesh $201 \text{ mm} \times 201 \text{ mm} \times 201 \text{ mm}$, with 1 mm step.

A first set of tests consisted in checking that the voltage configurations ΔV_i with $i = x, y, z$ led indeed to fields pointing along axis i , with a non negligible amplitude F_i . For each configuration, we compared the amplitude F_i^{\parallel} in a given direction to the amplitude F_i^{\perp} in the orthogonal plane. We show in Eq. 1.17 the results of the simulations at the position of the trapped atoms, which exhibit the expected symmetries:

$$\begin{aligned}
 \Delta V_x = 1 \text{ V}, \quad |F_x^{\parallel}| &= 0.052 \text{ V/cm} & \Rightarrow & \quad |F_x^{\parallel}| \simeq \frac{\Delta V_x}{19.2 \text{ cm}}, \\
 |F_x^{\perp}/F_x^{\parallel}| &\leq 1\%, \\
 \\
 \Delta V_y = 1 \text{ V}, \quad |F_y^{\parallel}| &= 0.23 \text{ V/cm} & \Rightarrow & \quad |F_y^{\parallel}| \simeq \frac{\Delta V_y}{4.4 \text{ cm}}, \\
 |F_y^{\perp}/F_y^{\parallel}| &\leq 0.4\%, & & \quad (1.17) \\
 \\
 \Delta V_z = 1 \text{ V}, \quad |F_z^{\parallel}| &= 0.27 \text{ V/cm} & \Rightarrow & \quad |F_z^{\parallel}| \simeq \frac{\Delta V_z}{3.7 \text{ cm}}, \\
 |F_z^{\perp}/F_z^{\parallel}| &\leq 0.3\%,
 \end{aligned}$$

The results show that $F_{\perp}/F_{\parallel} \leq 1\%$ along x , y and z . We also checked that the variations of the field amplitude remain below 0.1% inside a sphere of radius $25 \mu\text{m}$. In Sec. 4.4.2, we present preliminary electric field calibrations based on Stark spectroscopy that we performed directly using single Rydberg atoms.

A second set of tests were performed to confirm the possibility to guide ionized charged particles from the center of the chamber to the MCP detection area. Without providing accurate results, this kind of simulations allowed us to realize the importance of having a grid in front of the MCP detector. Field lines could reach the detection area only by applying to this grid voltages on the order of 15 V . This remains to be tested on the experiment.

1.2.4 MOT coils under vacuum

The last elements included in the UHV design are the anti-Helmholtz (AH) coils producing the magnetic field gradients of about 10 G/cm required for the ^{87}Rb MOT. It is useful for certain experiments to commute very quickly from anti-Helmholtz configuration to Helmholtz (H) configuration, in which a static B -field imposes a given quantization axis. By having a pair of coils as close to the atoms as possible, we implemented a simple helical design where the required magnetic field gradients is reached with a small number of loops, as depicted in Fig. 1.18. The inductance of the coils is then be small enough ($L \simeq 36 \mu\text{H}$) to achieve short switching times (on the order of $1\text{-}10 \mu\text{s}$ with reasonable electronics). In our case, the dimensions of N -atom arrays are below $25 \mu\text{m} \times 25 \mu\text{m}$, so a static quantization B -field is

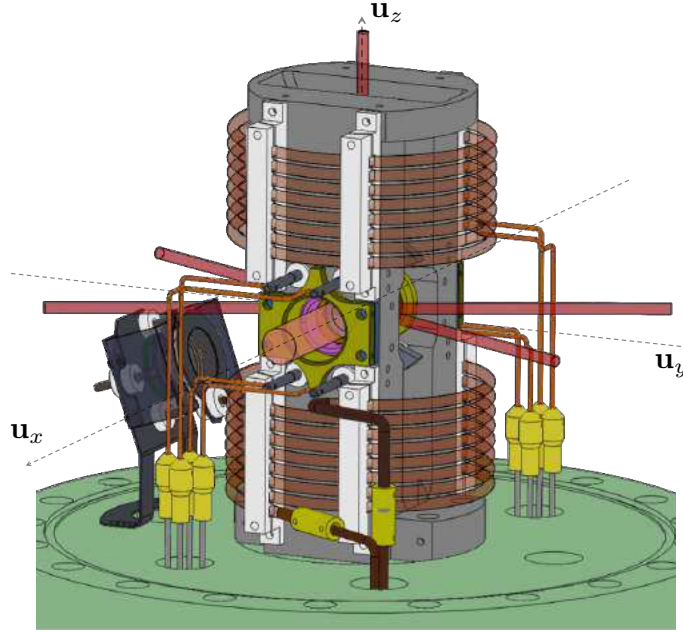


Figure 1.18: Complete assembly inside vacuum. Two circular helical coils are mounted into the central stainless steel support using MACOR[®] ceramic holders.

almost homogenous over the system without great effort. Furthermore, field amplitudes of only a few gauss are usually sufficient to remove Zeeman degeneracy and perform standard optical pumping. The geometry and the characterization of these coils are described in Appendix D, providing the following operating parameters, with current up to 30 A:

$$\text{Anti-Helmholtz configuration: } \begin{aligned} |B'_z/I| &= 0.4 \text{ G/cm/A,} \\ B'_x &= B'_y = -B'_z/2, \end{aligned}$$

$$\text{Helmholtz configuration: } \begin{aligned} |B_z/I| &= 1.1 \text{ G/A,} \\ |B_{\perp}/I| &\leq 10 \text{ mG/A.} \end{aligned}$$

1.3 Vacuum system

The complete vacuum system shown in Fig. 1.19 was then also designed with the help of SolidWorks. We started by designing the vacuum chamber itself mainly to match the geometry of the lasers beams.

1.3.1 Vacuum chamber

The main vacuum chamber was made out of 316L stainless steel to minimize material-induced stray magnetic fields with an outer diameter ϕ_{ch} of 246 mm. A sketch highlighting the two aspheric lenses and the horizontal MOT beams crossing at the center of the chamber is represented in Fig. 1.20. We used an angle $2\theta = 52^\circ$ between the horizontal crossing MOT beams. The maximum MOT beam diameter ϕ_{mot} was then 4.7 mm (see Eq.1.13). We used CF40 viewports along the y axis providing an optical access with a rather large solid

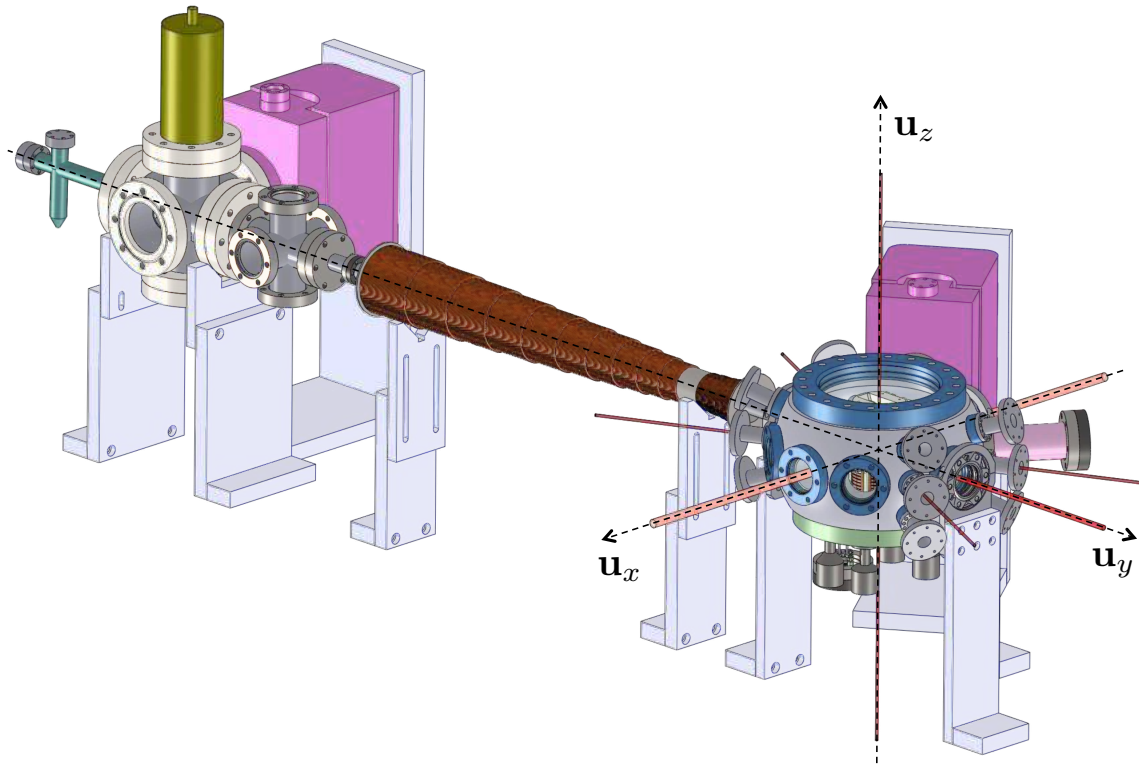


Figure 1.19: Overview of the complete vacuum system. From left to right. A rubidium effusive oven (turquoise) heated up to $T = 400$ K produces an atomic beam along the y -axis of the experiment. A cold nitrogen reservoir (gold) is used to condense and thus pump the residual rubidium vapor. ^{87}Rb atoms are decelerated using a standard Zeeman slower setup (coils are in reddish brown) and load the MOT trap inside the main science chamber (grey). A mechanical valve (not represented) is placed just before the entrance of the Zeeman slower and splits the vacuum system in two parts. A first ion pump (purple, on the left) allows to lower the pressure in the left part down to $P_{\text{oven}} \simeq 10^{-9}$ mbar. A second ion pump (purple, on the right) is connected to the main science chamber. Last, a small NEG pump (in pink inside a tube) is also connected to the chamber where the residual pressure is measured to be about $P_{\text{chamb}} \simeq 10^{-10}$ mbar around the trapped atoms.

angle⁶. The MOT beams are sent through small CF16 viewports in the horizontal plane. The chamber designed so far was large enough to sustain eight extra CF16 viewports, one up and one down by 19° of each of the four horizontal MOT viewports. The three main planes xy , yz and zx are symmetry planes of the chamber. In total, it comprises $12 \times \text{CF16}$ ports, $8 \times \text{CF40}$ ports (4 providing optical access), and $2 \times \text{CF160}$ ports, one on the top and one on the bottom.

Last, a mechanical piece in 2017 A (aluminium) and shaped like a ‘double tee’ was screwed directly to each CF16 port to allow for mounting 30 mm standard cage systems, as shown in Fig. 1.19.

⁶Both the Zeeman slower beams at 780 nm and the Raman beams at 795 nm are sent through this optical access, as shown respectively in Fig. 1.21 and Fig. 3.7.

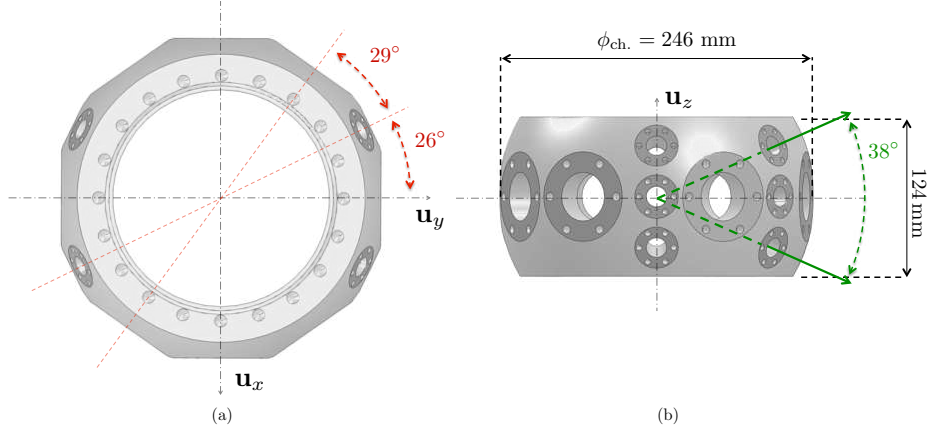


Figure 1.20: Geometry of the main vacuum chamber. (a) View from the top. (b) View from the side, through one horizontal MOT beam viewport.

1.3.2 Effusive oven and Zeeman slower

The magneto-optical trap is loaded from a standard Zeeman slower represented in Fig. 1.19. An effusive oven is filled with about 1 g of solid rubidium. When the experiment is run, heating wires wound around the oven heat it up to $T = 400$ K such that the liquid rubidium is in equilibrium with its vapor at the saturated vapor pressure $P_{\text{sat}} \simeq 3 \times 10^{-2}$ Pa. An effusive atomic beam is extracted from the oven and collimated using a 5 mm diameter hole in a copper plate placed between the oven reservoir and the Zeeman slower entrance, at a distance of about 70 mm from the exit of the oven nozzle. An effusive atomic beam with a calculated flux $\Phi \simeq 10^{12}$ atoms/s enters the Zeeman slower with a beam divergence of 35 mrad. The capture efficiency of our Zeeman slower is estimated to 0.25 over the full effusive velocity distribution (see Appendix D for details about the characterization of the Zeeman slower apparatus). In the end, an effective atomic flux $\Phi_{\text{eff}} \simeq \times 10^9$ atoms/s is expected to load the MOT.

1.3.3 Reaching UHV conditions

We describe briefly in this section the set of pumps used to operate in UHV conditions and to give a few details about how the non-evaporable getter (NEG) pump was activated.

Ion vacuum pumps

We already mentioned previously that the vacuum system is composed of two parts, isolated by a mechanical valve placed between the CF40 six-way crosses and the entrance of the Zeeman slower tube. Left part and right part have a volume of 5 L and 15 L respectively (see Fig. 1.19). On the oven side, residual pressure in permanent regime is controlled by an ion pump (Diode40 from Varian Inc.) connected to the CF63 six-way crosses with a pumping speed of 40 L/s. On the main science chamber side, two pumping systems are connected to the chamber via CF40 ports. The first one is an active ion pump (45S-4V from Gamma Vacuum) with also a pumping speed of 40 L/s. The second one is a passive getter pump (GP50 2F St707 from SAES Getter Company) which needs to be activated once under vacuum conditions.

NEG pump activation during bake-out

On each part of the vacuum system, a tee-tube with a mechanical valve in the middle allows to insert an external pumping system to reach a preliminary low pressure regime. In a first step, with ion pumps switched off, each part was connected one after the other to such an external pumping device composed of a primary diaphragm pumping stage combined with a secondary turbomolecular pumping stage, which could reach a residual pressure of about 10^{-7} mbar. During this, a first activation of the NEG pump was performed on the chamber side. The passive adsorbing surface of the NEG pump is protected by an oxide layer which needs to be evaporated by heating at 450°C during at least 45 minutes. Then, we performed a rather standard one-week bake-out at a temperature of 150°C ⁷. At the end of the week, the passive getter pump was re-activated (with ion pump switched off) a second time to clean the adsorbing surface after possible contamination due to the baking.

Residual pressure

From the ion pump current on the oven side, the residual pressure is measured to be about $3\text{--}4 \times 10^{-9}$ mbar when the oven is not heated up. The Zeeman slower tube ensures a differential pressure reduced by a factor of about 50-100 between the oven side and the trapped atoms side, where the residual pressure is measured below 10^{-10} mbar (3×10^{-11} mbar measured by the ion pump).

At the end, the pressure level achieved corresponds to an average lifetime of the atoms in the microscopic dipole traps τ on the order of 7 s measured directly as described in Sec. 2.3.1.

1.4 Trapping and imaging single atoms

In this section, we start by summing up the main parameters used for the ^{87}Rb cooling and repumping lasers at 780 nm and for the trapping laser at 850 nm. Then, the two imaging systems comprising respectively a CCD camera and single photons detectors are described; we give a brief overview of the procedures implemented to align both the cold atomic cloud of the MOT and the microscopic optical dipole trap on these two imaging systems. Finally, we analyse the typical experimental signature of the single atom loading regime.

1.4.1 Laser systems at 780 nm

Two laser systems are commonly used in atomic physics experiment involving ^{87}Rb . A primary laser at 780 nm is used to cool the ^{87}Rb atoms down by making them undergo many absorption and re-emission processes on the closed atomic transition $(5S_{1/2}, F=2) \rightarrow (5P_{3/2}, F'=3)$, with linewidth $\Gamma \simeq 2\pi \times 6$ MHz, during which spontaneous decay takes away part of the kinetic energy. This main cooling laser is frequency-locked onto the crossover transition $(5S_{1/2}, F=2) \rightarrow (5P_{3/2}, \text{cross} - \text{over}1' - 3')$ of ^{87}Rb D2 transition by using standard Doppler-free saturation spectroscopy (the hyperfine structure of ^{87}Rb and the laser frequency-locks details are given in App. A). During the cooling cycles, the atoms have a low but non-zero probability to decay to the other hyperfine ground state $F=1$ via off-resonance excitation of $F'=2$. A secondary repumping laser system at 780 nm, almost resonant on the transition $(5S_{1/2}, F=1) \rightarrow (5P_{3/2}, F'=2)$, is used to bring these atomic

⁷We did not operate with a higher temperature to avoid evaporating the 200 nm-thin layer of ITO coating deposited on the aspheric lenses

states back on the cooling transition. This secondary repumping laser is frequency-locked onto the crossover transition ($5S_{1/2}, F=1$) \rightarrow ($5P_{3/2}, \text{cross} - \text{over} 1' - 2'$) also by using standard Doppler-free saturation spectroscopy. The two systems are grating-stabilized external cavity diode lasers (DL100 from Toptica) with output power of about 100 mW. A built-in 35 dB optical isolator allows to suppress possible back reflections into the laser that could lead to multi-mode behavior. The quality of the outcoming mode is good enough to get typically 50 % coupling in polarization maintaining fibers (PM fibers) without using mode-matching telescopes.

All the distinct laser beams at 780 nm involved in cooling and trapping, probing, pumping or repumping ^{87}Rb atoms are derived from these two laser diode systems. Acousto-optical modulators (AOMs) from AA Opto-electronic[®] are used to shift their frequency from the crossover to an atomic transition of interest. Switching on and off the AOMs driving RF power also provides an easy way to switch on and off a laser beam, by decoupling them spatially from the PM fibers. For each laser beam, the switching times depend on how much they are focused inside the AOM crystals, but these times are typically below 1 μs for 40 dBm extinction. The different laser beams operating parameters (frequency, power, beam diameter) are set up on an auxiliary optical table where the beams are coupled into polarization maintaining (PM) optical fibers and sent to the science chamber table. When a complete extinction is required, an additional mechanical shutter (controlled by TTL electronics) is implemented just before the PM fiber, with switching times on the order of 5 ms.

Zeeman slower beams

The Zeeman slower provides the first cooling stage of the experiment, in which a hot effusive atomic beam of initial temperature 400 K is cooled down to a few kelvin and loads the magneto-optical trap. A 780 nm laser beam resonant with ^{87}Rb closed atomic transition $|5S_{1/2}, F=2, m_F=2\rangle \rightarrow |5P_{3/2}, F'=3, m'_F=3\rangle$ with σ^+ polarization is shone in the direction opposite to the atomic beam's motion and applies a radiation pressure force on the atoms (see Fig. 1.21). The longitudinal magnetic field profile produced by the Zeeman coils is calculated to operate this laser with a detuning $\delta/2\pi = -133$ MHz with respect to the atomic transition at rest (more details are given in App. D); cold atoms captured in the MOT are thus off-resonance by more than 22Γ and do not feel any radiation pressure effect related to the Zeeman laser beam. The detuning is controlled with a single-pass AOM. A Zeeman repumper beam, resonant with the transition $|5S_{1/2}, F=1\rangle \rightarrow |5P_{3/2}, F'=2\rangle$, is combined with the Zeeman cooling beam and projected onto the same polarization using half-waveplates and PBS cubes, before coupling them into the same PM fiber. This beam is also red-detuned by $-2\pi \times 133$ MHz with respect to the transition in the absence of magnetic field using a simple passage in an AOM. The two beams are brought to the main chamber via the PM fiber and aligned on the y -axis of the experiment by centering them on the entrance viewport and on the hole in the copper plate placed at the rubidium oven exit (see the full schematic in Fig. D.1 in App. D). A telescope is used to tune their initial diameter to 10 mm and to make them slightly converging such that two meters away, they match the 5 mm diameter of the hole in the copper plate. The power in the cooling beam and the repumping beam are respectively about 4 mW (leading to a saturation parameter $s \simeq 3$) and 1 mW.

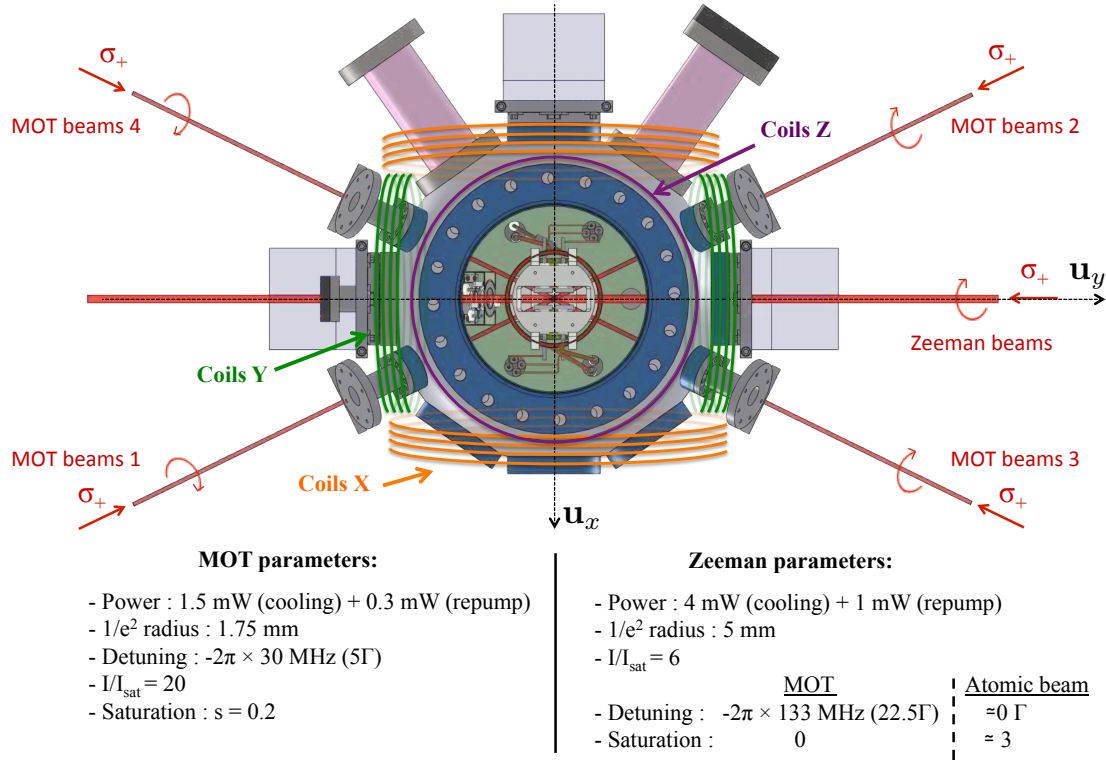


Figure 1.21: MOT and Zeeman slower setup. Schematic view (from the top) and useful parameters of the cooling lasers configuration. The vertical MOT beams going out of plane (not represented in this sketch) are σ^- -polarized.

MOT beams

The molasses cooling laser beams are red-detuned from ^{87}Rb closed atomic transition ($5S_{1/2}, F = 2$) \rightarrow ($5P_{3/2}, F' = 3$) by about -5Γ , controlled by a double-pass AOM. The molasses repumping beams frequency is almost resonant with the transition ($5S_{1/2}, F = 1$) \rightarrow ($5P_{3/2}, F' = 2$). A fiberized light splitter (2 inputs-6 outputs, from OzOptics) is used to produce and to bring the six MOT beams to the science chamber table via PM fibers. Each beam has a waist of 1.75 mm and has about 1.5 mW of cooling light (leading to a saturation parameter $s \simeq 0.2$) and 0.3 mW of repumping light. As shown in Fig. 1.21, the horizontal beams are σ^+ -polarized with respect to the magnetic fields produced by the MOT coils operated in anti-Helmholtz configuration. As the magnetic field gradients in the xy plane and along the z -axis have opposite signs, the vertical MOT beams are σ^- -polarized. The balance between the output powers remained stable over months.

Switching compensation coils

Three independent pairs of coils, centered on the three main axes x , y and z , are operated in Helmholtz configuration to produce static magnetic fields up to 3 G in arbitrary directions. They are powered by High Finesse power supplies (with a relative stability of 10^{-4}) which can be switched between two current values. The first setting of the three power supplies provides the set of values I_x^1 , I_y^1 , and I_z^1 which allow to create a magnetic field \mathbf{B}_{comp} canceling out the residual magnetic field from the environment at the crossing of the MOT beams. Then, tuning finely these three parameters allows to move the point of zero magnetic

field and thus to adjust the position of the MOT cloud with about $10\ \mu\text{m}$ accuracy. The second setting of the three power supplies is then used during a sequence when the internal state of an atom is manipulated. It provides a second set of values I_x^2 , I_y^2 , and I_z^2 allowing to produce a controlled magnetic field along the z -direction while cancelling out transverse magnetic fields in the xy plane. Two accurate experimental realizations of the cancellation of the transverse magnetic fields based respectively on micro-waves and on optical Raman spectroscopy are described in more details in Chapter 2.

1.4.2 Laser system at 850 nm

As we saw in section 1.1.1, a far red-detuned laser system allows to create the microscopic optical tweezers used to trap the single ^{87}Rb atoms. Here we describe briefly the main parameters of this laser system and we describe the preliminary configuration of optical dipole traps which does not involve the spatial light modulator.

Operating parameters

The laser system at 850 nm is a single-mode free running laser diode⁸ controlled in temperature ($\pm 0.1\ ^\circ\text{C}$) and in current ($\pm 0.01\ \text{mA}$) in order to avoid multi-mode behaviour. The diode output power is about 150 mW delivered in a spatially elliptic mode with aspect ratio 4:1. The laser beam goes through an anamorphic prism pair with about 90 % transmission (improving the ratio to 2:1) followed by a 35 dB optical isolator with also about 90 % transmission. Then, a single-pass AOM in which the beam is focused to about $70\ \mu\text{m}$ (75 % transmission) provides a rather fast light switch (on the order of 100 ns from 5 % to 95 % extinction). Finally, the beam is coupled into a PM fiber with 40 % coupling efficiency and sent to the breadboard used for the trapping and imaging setup close to the vacuum chamber. In the end, the power available at the output of the fiber is about 35 mW.

Two-atom trapping setup

The preliminary setup implemented at the beginning of this project allows to produce two distinct microscopic dipole traps separated by a few microns in order to study the fundamental dipole-dipole interactions between two single ^{87}Rb Rydberg atoms. As shown in Fig. 1.22, the trapping beam coming out of the fiber is separated in two beams of equal power using a half-wave plate and a polarizing beam splitter (PBS). Then, the two beams are recombined with a small angle ($\theta \simeq 1\ \text{mrad}$) and projected on the same vertical linear polarization using half-wave plates and two PBS cubes (half of the power is lost). In the end, about 17 mW can be used for the two traps. We will see in Chapter 2 that each trap requires only about 5 mW. The work presented in this thesis is always based on this experimental configuration unless otherwise stated.

1.4.3 Detection systems: CCD camera and single photon counting modules

The 780 nm resonant light scattered by the trapped atoms and collected by the aspheric lens is sent to two different detection systems implemented on the same breadboard that supports the dipole trap beams, as shown in Fig. 1.22. The primary detection system is

⁸The laser diode was M9-852-0150 from Thorlabs, Inc.

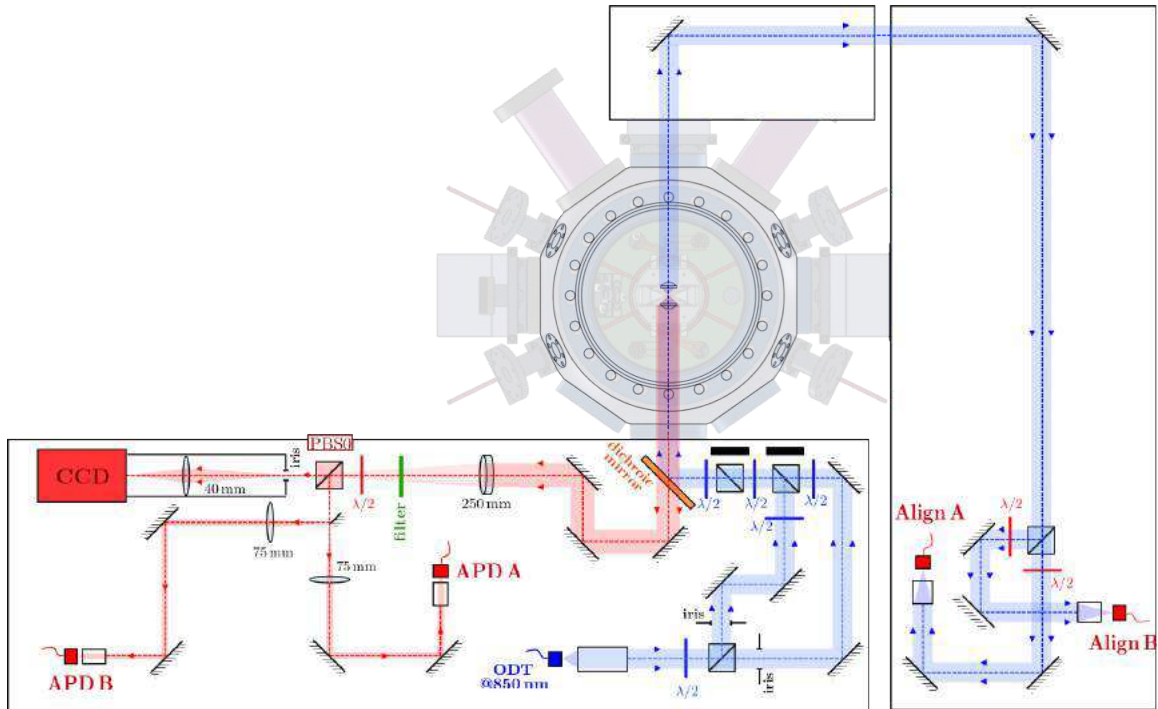


Figure 1.22: Trapping and imaging setup. The blue paths correspond to the trapping beams at 850 nm. The red paths correspond to the imaging beams at 780 nm.

a charge-coupled device (CCD) camera mainly used for pre-alignment of the microscopic traps. Then single photon counting modules are used to detect the single trapped atoms.

CCD camera

The CCD camera is a 12-bits PixelFly-QE camera from PCO. The resolution is 1392×1024 with a pixel size of $6.45 \mu\text{m} \times 6.45 \mu\text{m}$. It was operated with a horizontal and a vertical binning 2×2 pixels, such that the effective pixel size was $12.9 \mu\text{m} \times 12.9 \mu\text{m}$. The quantum detection efficiency is about 20% at 780 nm when it operates in low light mode, with a typical readout noise of $7 e^-$ RMS.

We used this camera for preliminary imaging the cloud of cold atoms in the magneto-optical trap and to visualize the microscopic dipole trap focused inside. The light collected at 780 nm (in red in Fig. 1.22) is almost collimated by the aspheric lens with effective focal length of 10 mm and goes through the chamber CF40 viewport and the dichroic mirror. Then, we use a doublet with focal length of 250 mm to image the real plane containing the atoms onto an intermediary plane where an iris acting as a confocal pinhole is used to filter background light. The effective magnification is about 25. Just before the intermediary plane, an interference filter from Semrock allows to block residual 850 nm light scattered inside the vacuum chamber or on the optics and to let the 780 nm fluorescence light go through with 90% transmission. Then, a PBS cube divides the light⁹ in two paths. In the direction of the CCD camera, a 40 mm plano-convex lens operating with a conjugate ratio of $1/3$ is used to image the intermediary plane onto the CCD sensor. The iris and the

⁹The fluorescence light coming from the atoms has been measured to be elliptically polarized. The percentage of light in each path can be changed between 50% – 50% and 30% – 70% by turning the $\lambda/2$ -plate.

40 mm plano-convex lens are both mounted into a tube screwed onto the C-mount port of the CCD camera. The total magnification between the atoms plane and the CCD sensor plane is then about 8 such that the image of a $2\ \mu\text{m}$ diameter microscopic dipole trap is almost matched to a square of 2 by 2 real pixels of $13\ \mu\text{m}$ size.

Single photon counting modules (SPCMs)

The secondary and main imaging system is composed of fiberized single photon counting modules (SPCM-ARQH-14) from PerkinElmer using a single silicon avalanche photodiode (APD) with a circular active area of $180\ \mu\text{m}$ diameter. The photodiode is thermoelectrically cooled to reduce dark counts and temperature controlled to ensure stabilized performances. The module can achieve counting speed exceeding 20 million counts per second. For each detected photon, a TTL pulse of 2.5 V in a $50\ \Omega$ load and 28 ns wide is output via a BNC connector. The latter is connected to a TTL counter unit operating on a standard acquisition card from National Instruments¹⁰ which allows to measure the fluorescence signal averaged out on a chosen time scale. The acquisition program is described in more details in Sec. 2.2. The dead time between two detection events is about 35 ns and the typical dark count rate is 100/s.

The optical path is derived from the CCD path using the cube PBS0 (see Fig. 1.22). After the reflection on the cube, a knife-edge mirror placed in the intermediate image plane is used to separate the fluorescence of the two atoms. As the magnification is about 25 ($1\ \mu\text{m}$ separation in real space corresponds to $25\ \mu\text{m}$ in the intermediary plane), it is possible to image two atoms as close as about $3\ \mu\text{m}$ without crosstalks between the fluorescence signals. Then, a plano-convex lens with focal length 75 mm is used on each path to the fluorescence light into a 1 m multi-mode fiber connected to a fiberized photon counting module. Using a fiber provides a very efficient spatial filtering of the background light emitted by the atoms in the MOT.

Detection efficiency η_d

Based on the description of the imaging system towards the SPCM detectors, we can estimate the total detection efficiency of the system at 780 nm. The collection efficiency $\Omega/4\pi$ of the aspheric lens is 6.7%. The transmission through the chamber¹¹ was calibrated by measuring input and output power of a 780 nm laser. It is estimated to 75%. Assuming that the two sets of aspheric lens and CF40 viewport through which the light is transmitted are identical, we estimate the transmission of one set to be $\sqrt{0.75} = 87\%$. The dichroic mirror and the interference filter have similar transmissions of about 90% at 780 nm. Then, the PBS cube¹² splits the light in two paths with a transmission of about 50%. The coupling into the fiber connected to the SPCM is not easy to measure, it is about $50\% \pm 20\%$. As we mentioned before, the quantum detection efficiency of the silicon APD inside the SPCM detector is 60% at 780 nm. Finally, all glass surfaces due to mirrors and lenses make up 98% of the transmission. The total detection efficiency η_d is estimated at $0.7 \pm 0.2\%$.

¹⁰Reference: NI PCI 6713.

¹¹This transmission coefficient takes into account the transmission through two IR-coated viewports and the two aspheric lenses with ITO and IR coatings.

¹²Up to the PBS separating the fluorescence in two paths we capture 3.8% of the total amount of fluorescence emitted from the center of the dipole trap.

Loss	Efficiency (%)
Solid angle $\Omega/4\pi$	6.7
Asph. lens and viewport (ITO+IR coatings)	87
Dichroic mirror	90
Interference filter	90
PBS cube	50
APD multi-mode fiber coupling	50 ± 20
APD quantum efficiency @780 nm	60
Various optics (mirrors and doublet)	98
Total	0.70 ± 0.2

Table 1.2: Detection efficiency budget of the SPCM at 780 nm.

1.4.4 Single atom trapping

This last section describes shortly the alignment procedure allowing to visualize experimentally the single atom loading regime. Finally, a brief analysis of the sub-Poissonian statistics of this loading regime is given.

Alignment procedure of the imaging system

We briefly describe the alignment procedure implemented on our setup for coupling the fluorescence light emitted by the atoms trapped in one microscopic optical tweezer into a SPCM input fiber. The exact same procedure was performed for the other trap.

We start by aligning the trapping beam onto the optical system axis operating inside the vacuum chamber. The mechanical constraints of the setup inside the chamber ensure that a preliminary good alignment is already achieved as soon as the beam exits the system with a good cylindrical shape. A temporary imaging system composed of an aberration-free objective and a cheap CCD camera is placed at the exit of the optical system. Fine alignment is then performed by walking the beam with two mirrors and optimizing the peak intensity at the center of the image spot while keeping a symmetric cylindrical shape.

Once this is done, the axis of the trapping and imaging system is defined. After passing through the chamber, the trapping beam is coupled into a fiber coupler 2 m away (see Fig. 1.22). This fiber coupler allows to send back a low power 780 nm beam through the optical system which is already pretty well aligned on the main optical axis. This beam at 780 nm goes through the dichroic mirror and is used to prealign the CCD sensor in the transverse xy plane. The beam convergence after passing through the chamber is adjusted such that it matches OSLO[®] simulations (theoretical focal point at 2700 mm after the viewport). The longitudinal position of the filtering confocal pinhole with respect to the 250 mm doublet is also pre-adjusted based on OSLO[®] simulations. Then, the MOT cloud is centered on the CCD images thanks to the compensation coils. The atomic density around the trap is thus increased as well as the loading. By working with a vertical magnetic field gradient on the order of 6 G/cm, the MOT is dense and therefore the dipole trap operates in multi-atom loading regime, such that a bright pixel appears near the center of the CCD sensor as shown in Fig. 1.23.

The last step consists in coupling the collected fluorescence light into the SPCM input fiber. For this, we also use the beam at 780 nm propagating backward. Operated with

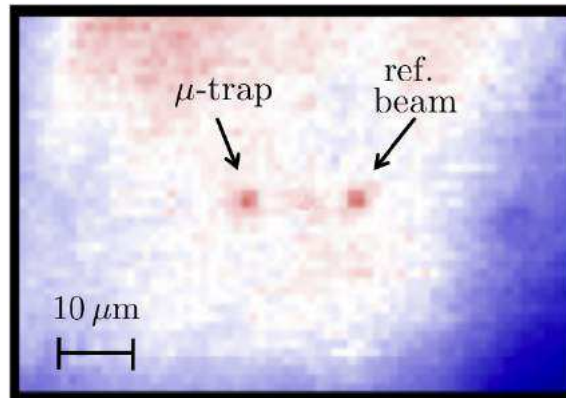


Figure 1.23: Typical CCD picture of the MOT. Two hot spots stand out from the background MOT fluorescence. They correspond respectively to the microscopic optical dipole trap in the multi-atom regime and to the reference beam at 780 nm used for alignment. The real space length scale is indicated.

very low power, this beam also produces a bright pixel onto the CCD images as shown in Fig. 1.23. By superimposing this bright pixel with the bright pixel corresponding to the tweezer, this beam acts as an artificial atom which would emit 780 nm light within the same solid angle. Then we can operate the beam with high power and couple it into the SPCM fiber with the output connected to a power meter. Finally, this reference beam is blocked and we look at the level of real fluorescence detected onto the SPCM photodiode. It can be already quite high (on the order of 800-1000 counts/(10 ms) as the vertical magnetic field gradient is high and the MOT cloud is dense. However, a clear decrease of about at least 300 counts/(10 ms) is observed by switching off the optical trap beam, meaning that a large fraction of the fluorescence signal is due to atoms trapped in the microscopic tweezer. By reducing slowly the magnetic field gradients, the loading decreases until the single atom regime is reached and observed, as already shown in Fig. 1.4.

SPCM signal in single atom loading regime

The single atom fluorescence signal collected and detected on SPCM detectors in single atom regime have been extensively studied and discussed in the theses of N. Schlosser, G.O. Raymond, and B. Darquié (Schlosser, 2001; Reymond, 2002; Darquié, 2005). Here, we only briefly present the similar experimental results we obtained on the new apparatus and we refer to the works of our former colleagues for more detailed investigations.

A typical single atom signature is shown in Fig. 1.24(a). A counter unit operating on a National Instruments acquisition card (NI-PCI 6713) allows to plot in real time the number of counts detected onto the SPCM detector during time bins ranging from 1 μ s to 1 s. In our case, we used 10 ms time bin which was proven to be an optimal integration time (Schlosser, 2001). About twenty-six steps can be identified during a total duration of 20 s so the loading rate R was about 1.3 s^{-1} , which satisfies the condition required to work in the single atom regime as discussed in Sec. 1.1.1. The step height corresponds to the average number of detected photons that were emitted by a single atom during a time of 10 ms and collected by the imaging system. During this acquisition, the dipole trap power inside the chamber was 4 mW, which corresponds to a lightshift of the ground states of about 25 MHz (see Sec 2.3.4). Inside the dipole trap, the MOT cooling lasers are thus red-detuned by about

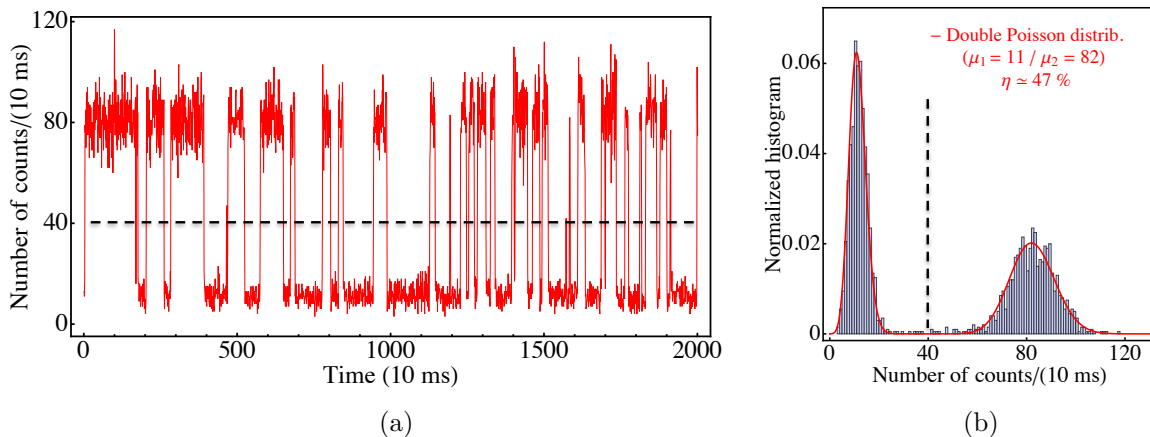


Figure 1.24: Single atom signature. (a) shows the time evolution of the number of counts per bins of 10 ms detected onto one SPCM module during a period of about 20 s. (b) is the corresponding normalized histogram with a 1 count/(10 ms) resolution. The red solid line is a fit by the sum of two Poisson distributions with mean values $\mu_1 = 11$ counts/(10 ms) and $\mu_2 = 82$ counts/(10 ms). The ratio of the area below the single atom fluorescence level over the total area is 47%.

$\delta_{\text{eff.}} = 2\pi \times (30 + 25 = 55)$ MHz with respect to the atomic transition. Assuming two-level atoms, the effective scattering rate can be estimated by:

$$s_{\text{eff.}} = \frac{I/I_{\text{sat}}}{1 + 4\delta_{\text{eff.}}^2/\Gamma^2} = 0.05, \quad (1.18)$$

$$\Gamma_{\text{sc.}} = \frac{\Gamma}{2} \frac{s_{\text{eff.}}}{1 + s_{\text{eff.}}} \simeq 1 \times 10^6 \text{ photons/s,}$$

where $s_{\text{eff.}}$ is an estimate of the saturation parameter inside the tweezer (in this calculation, we assume that the trapped atoms feel the intensity of only one MOT beam on average). With a total detection efficiency of 0.0069, one can expect to detect about 7500 counts/s, so 75 counts/(10 ms), which is approximately what we observed in the histogram of the signal shown in Fig. 1.24(b). This histogram exhibits two peaks corresponding respectively to the background level and to the single atom fluorescence level, separated by a step height of 71 counts/s. The background level was about 11 counts/(10 ms) and was much higher than the dark count rate of the SPCM detectors ($\simeq 1$ count/(10 ms)) or residual molasses fluorescence (below 5 counts/(10 ms)). We found that it came from residual reflections of the horizontal MOT beams 1 and 3 on the aspheric lens holders under vacuum (see Fig. 1.21). This background level could be lowered occasionally by adding pinholes on the path of these two MOT beams.

However, even with such a background level, a clear threshold can be set to discriminate the single atom fluorescence level. One-atom experiments are triggered as soon as a rising edge of the fluorescence signal has an amplitude bigger than half of the fluorescence step height corresponding to the presence of a single atom in the trap. Jérôme Beugnon showed in his thesis (Beugnon, 2007) that with typical single atom signature as the one presented in Fig. 1.24, such a triggering scheme has an efficiency better than 99%. In the same spirit, two-atom experiments can be triggered as soon as rising edges on signals from both SPCM A and SPCM B (corresponding to traps A and B) have been detected before a falling edge occurs. Such detection events are used to trigger various experimental sequences allowing to

manipulate the internal states of the atoms. These sequences are computer designed using a LabWindows software and realized with rather standard acquisition cards from National Instruments. The architecture of the computer control system is described in Sec. [2.2](#).

Chapter 2

Trap characterization using a single atom

Contents

2.1	Trapping ^{87}Rb atoms using the dipole force	46
2.1.1	State-dependent light shifts	46
2.1.2	Trap profile for a gaussian trapping laser beam	48
2.2	Typical experimental sequences and computer control system	49
2.2.1	Typical experimental sequences	50
2.2.2	Computer control system	53
2.3	Characterization of the single atoms in the ODT	54
2.3.1	Lifetime in the trap	55
2.3.2	Single Atom Temperature	58
2.3.3	Trap oscillation frequencies	59
2.3.4	Measurement of the trap depth	61

The apparatus described in Chapter 1 allows to trap and to detect single atoms in arrays of microscopic optical traps within a controlled electrostatic environment suitable for Rydberg excitations. Before investigating complex 2D configurations of N interacting atoms, a simpler preliminary trapping system providing either one or two microscopic traps was implemented, as shown in Fig. 1.22.

In this chapter, we present the main characterization measurements of the new apparatus that were performed with the preliminary trapping system. We start by briefly reminding the main theoretical results about trapping multi-level ^{87}Rb atoms using the dipole force. Then, we describe the architecture of the computer control system developed to realize versatile experimental sequences as well as acquire, store, and analyse experimental data. Finally, we present four standard experiments implemented at the beginning of the project to characterize useful parameters related to one microscopic optical trap and to the external state of the single atoms trapped inside.

2.1 Trapping ^{87}Rb atoms using the dipole force

Dipole forces acting on neutral atoms are conservative forces resulting from the interaction between the atomic dipoles and strong light field gradients which eventually lead to shift the eigenenergies of the internal atomic states proportionally to the light intensity. In the general case, the corresponding potential energy depends both on the light field polarization and on the internal state of the atom¹.

2.1.1 State-dependent light shifts

We briefly review the light-matter interaction following the dressed atom formalism from [Cohen-Tannoudji, Grynberg, and Dupont-Roc \(1998\)](#). Consider an atom at rest with internal states $|e_i\rangle$ of energies $\hbar\omega_i$. The atomic hamiltonian reads:

$$\hat{H}_{\text{at}} = \sum_i \hbar\omega_i |e_i\rangle \langle e_i|. \quad (2.1)$$

It interacts with a laser field $\vec{\mathcal{E}}(\vec{r}, t)$ of frequency ω_L which can be expressed at the position of the atom:

$$\vec{\mathcal{E}} = \mathcal{E}_0 \cos(\omega_L t) \vec{\epsilon}. \quad (2.2)$$

After the standard quantization procedure, the field operator reads:

$$\hat{\vec{E}} = \sqrt{\frac{\hbar\omega_L}{2\epsilon_0 V}} (\hat{a} + \hat{a}^\dagger) \vec{\epsilon} = \mathcal{E}_L (\hat{a} + \hat{a}^\dagger) \vec{\epsilon} = \hat{E} \vec{\epsilon}, \quad (2.3)$$

where V is the quantization volume, and \hat{a} and \hat{a}^\dagger are respectively the annihilation and creation operators of one photon in the laser mode. The hamiltonian of the laser field is then:

$$\hat{H}_L = \hbar\omega_L \left(\hat{a}^\dagger \hat{a} + \frac{1}{2} \right). \quad (2.4)$$

The eigenstates of the system described by the hamiltonian $\hat{H}^0 = \hat{H}_L + \hat{H}_{\text{at}}$ without interaction are of the form $\{|e_i, N\rangle\}$, where N is the number of photons in the laser mode. Finally, under the electric dipole approximation ($\lambda_L \gg \langle \hat{r}_e \rangle$, where \hat{r}_e is the position operator of the valence electron with respect to the nucleus) the interaction is described by the electric dipole hamiltonian:

$$\hat{H}_{\text{ED}} = -\hat{\vec{D}} \cdot \hat{\vec{E}}, \quad (2.5)$$

where $\hat{\vec{D}}$ is the atom dipole operator. The energy shifts of the atomic states due to the presence of the light can be computed using time-independent perturbation theory. The dipole operator has odd parity such that the first order perturbation term vanishes. At second order, the light shift of a state $|\psi\rangle$ due to the interaction hamiltonian \hat{H}_{ED} reads:

¹In Sec. 1.1.1 of Chapter 1, we gave the expression of such a potential derived from a semi-classical approach of light-matter interaction where the atom is treated as a two-level system (Eq.1.3). Such an approach was useful to estimate relevant trapping laser parameters but it can not take into account the complexity of the internal atomic structure of real ^{87}Rb atoms.

$$\Delta E_\psi = \sum_{\phi \neq \psi} \frac{|\langle \phi | \hat{H}_{\text{ED}} | \psi \rangle|^2}{E_\psi - E_\phi}. \quad (2.6)$$

In our case, the laser light we use at 850 nm is near-resonant for a restricted number of transitions. To compute the energy shifts of the states involved in these transitions, the sum in Eq. 2.6 can be evaluated by keeping only the resonant terms for which $E_\psi \simeq E_\phi$. Then, under the rotating-wave approximation (RWA), the interaction hamiltonian \hat{H}_{ED} couples only the states $\{|e_i, N+1\rangle, |e'_i, N\rangle\}$, with $i \neq i'$, where e_i and e'_i correspond respectively to the ground state and the excited state manifolds. The state of the laser light field is a coherent state and its decomposition onto the Fock basis $\{|N\rangle\}$ has non negligible components only over a range $\Delta N \propto \sqrt{\langle N \rangle}$ small compared to the mean number of photons $\langle N \rangle$. The terms $\langle N | \hat{E} | N+1 \rangle = \mathcal{E}_L \sqrt{N+1}$ are all very well approximated by $\mathcal{E}_L \sqrt{\langle N \rangle}$. Then, by equating the volumetric energy densities of the quantum field and the classical field:

$$\frac{\langle N \rangle \hbar \omega_L}{V} = \frac{1}{2} \epsilon_0 \mathcal{E}_0^2, \quad (2.7)$$

we can write the terms appearing in the sum of Eq. 2.6:

$$\langle \phi | \hat{H}_{\text{ED}} | \psi \rangle = \langle e'_i, N | -\hat{\vec{D}} \cdot \hat{\vec{E}} | e_i, N+1 \rangle = -\frac{\mathcal{E}_0}{2} \langle e'_i | \hat{\vec{D}} \cdot \vec{\epsilon} | e_i \rangle. \quad (2.8)$$

In the fine basis, the internal states are written $|n, l, j, m_j\rangle$, where n is the principal quantum number, l is the angular momentum, j is the total spin of the state, and m_j is the quantized projection of j onto the quantization axis. We can use the Wigner-Eckart theorem to compute the dipole matrix elements using the spherical polarization basis:

$$\begin{aligned} \langle e'_i | \hat{\vec{D}} \cdot \vec{\epsilon} | e_i \rangle &= \langle n', l', j', m'_j | e r_q | n, l, j, m_j \rangle \\ &= \langle j' | | e \hat{r} | | j \rangle \cdot \langle j, m_j; 1, q | j', m'_j \rangle, \end{aligned} \quad (2.9)$$

where:

- $\langle j' | | e \hat{r} | | j \rangle$ is a reduced matrix element of the transition $|n, l, j\rangle \rightarrow |n', l', j'\rangle$, independent of m_j, m'_j and q ;
- $q = 0, \pm 1$ respectively for the light polarization $\vec{\epsilon} = \pi, \sigma^\pm$;
- $\langle j, m_j; 1, q | j', m'_j \rangle$ is a Clebsch-Gordan coefficient.

Using this approach and some linear algebra to go from the fine basis $|n, l, j, m_j\rangle$ to the hyperfine basis $|j, i; f = |i \pm j|, m_f\rangle$ which takes into account both ls -coupling and ij -coupling, one can derive (Darquié, 2005) the energy shifts of each Zeeman sub-level of the ^{87}Rb ground states ($5S_{1/2}, F=1$) and ($5S_{1/2}, F=2$), as well as the ones of the excited states ($5P_{3/2}, F'=3$). The figures 2.1(a) and (b) show these energy shifts in the case of a π -polarized trap or a σ^+ -polarized trap respectively.

By using a trap with a linear polarization, all Zeeman sub-levels of a given hyperfine state of the ground state $5S_{1/2}$ are shifted by the same quantity, which can be expressed by the general form:

$$\Delta E(F, m_F) = \frac{\hbar I}{8I_{\text{sat}}} \Gamma^2 \left(\frac{1}{3 \delta_{1/2}(F)} + \frac{2}{3 \delta_{3/2}(F)} \right), \quad (2.10)$$

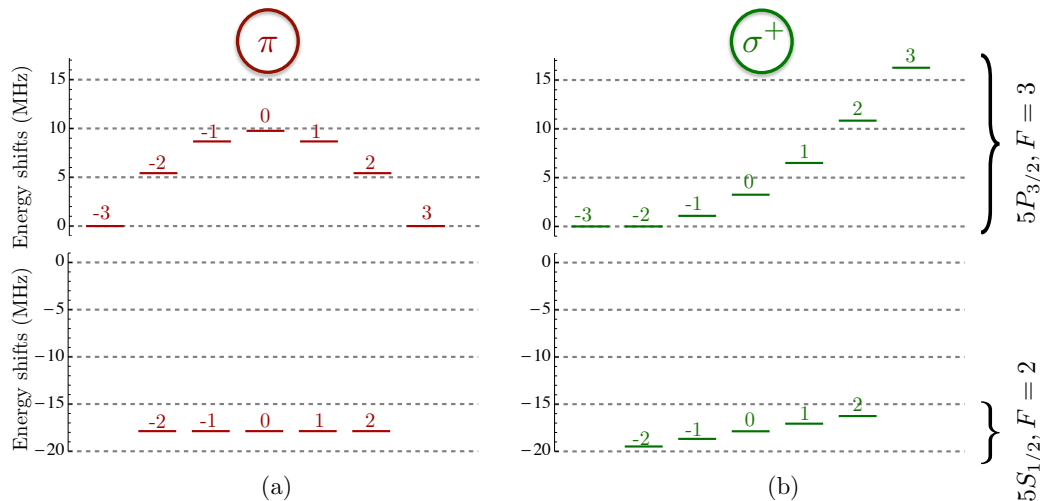


Figure 2.1: Light-induced energy shifts of the Zeeman sub-levels of the transition ($5S_{1/2}, F=2 \rightarrow 5P_{3/2}, F'=3$). (a) π -polarized trap. (b) σ^+ -polarized trap. The shifts were calculated by taking into account only the states $5S_{1/2}$, $5P_{1/2}$ and $5P_{3/2}$. Including also the states $5D_{3/2}$, $5D_{5/2}$ and $7S_{1/2}$ leads to relative corrections smaller than 10%.

where I is the trapping light intensity, I_{sat} is the saturation intensity of the transition $5S \rightarrow 5P$, Γ is the decay rate of the excited state $5P$, and $\delta_{1/2}(F)$ and $\delta_{3/2}(F)$ are respectively the trapping laser detuning from the transition ($5S_{1/2}, F \rightarrow 5P_{1/2}$) and ($5S_{1/2}, F \rightarrow 5P_{3/2}$)². When the atom is in an arbitrary superposition of states $|\psi\rangle = \sum_i \alpha_i |e_i\rangle$, the effective trapping potential energy is the average $U_{\text{eff}} = \sum_i |\alpha_i|^2 \Delta E_{e_i}$.

Finally, the photon scattering rate Γ_{sc} due to the dipole trap at 850 nm can be calculated through the same reduced matrix elements and Clebsch-Gordan coefficients for the D1 and the D2 lines as for the dipole potential. For π -polarization, and in the limit $\delta_{1/2}, \delta_{3/2}$ large compared to the hyperfine splitting³, one explicitly obtains:

$$\Gamma_{\text{sc}} = \frac{I}{8I_{\text{sat}}} \Gamma^3 \left(\frac{1}{3\delta_{1/2}^2} + \frac{2}{3\delta_{3/2}^2} \right). \quad (2.11)$$

In our experiment with a power of 3 mW focused down to a $1/e^2$ radius spot size of $1 \mu\text{m}$, the rate is $\Gamma_{\text{sc}} \simeq 24 \text{ s}^{-1}$.

2.1.2 Trap profile for a gaussian trapping laser beam

In the case of a π -polarized trap, we saw above that the trapping potential U_0 explored by ground state atoms is identical for all Zeeman sub-levels and proportional to the light intensity I of the trapping laser beam. This beam is brought on the vacuum chamber table via a PM single-mode fiber, so the laser mode is almost a TEM_{00} gaussian mode. Then, it is focused by the aspheric lens with numerical aperture $NA=0.5$. Even with such a strong focusing, the beam intensity I in the focal plane of the lens is very well approximated by the cylindrically symmetric gaussian profile:

²In this context, it is a good approximation to consider that the states $5P_{1/2}$ and $5P_{3/2}$ have the same decay rates $\Gamma \simeq 2\pi \times 6 \text{ MHz}$ and the same saturation intensity $I_{\text{sat}} \simeq 1.67 \text{ mW/cm}^2$. More accurate values can be found in Steck (2008).

³With a 850 nm dipole trap, the detunings $|\delta_{1/2}|/2\pi$ and $|\delta_{3/2}|/2\pi$ are equal to 24.4 and 31.6 THz respectively, large compared to the ground state hyperfine splitting of 6.8 GHz.

$$I(r, z) = \frac{I_0}{1 + z^2/z_R^2} \exp\left(-2\frac{r^2}{w^2(z)}\right). \quad (2.12)$$

Thus, the trapping potential takes the form:

$$U(r, z, F) = \frac{U_0(F)}{1 + z^2/z_R^2} \exp\left(-2\frac{r^2}{w^2(z)}\right), \quad (2.13)$$

with the following definitions:

$$U_0(F) = \frac{\hbar\Gamma^2 I_0}{8I_{\text{sat}}} \left(\frac{1}{3\delta_{1/2}(F)} + \frac{2}{3\delta_{3/2}(F)} \right) \quad \text{and} \quad w(z) = w_0 \sqrt{1 + z^2/z_R^2}, \quad (2.14)$$

where w_0 is the waist of the gaussian beam, $z_R = \pi w_0^2/\lambda$ is the Rayleigh range and the peak intensity I_0 is related to the total power P of the gaussian beam by the expression:

$$I_0 = \frac{2P}{\pi w_0^2}. \quad (2.15)$$

The trap profile is thus gaussian in the transverse plane and lorentzian along the propagation axis of the trapping laser beam. We will check experimentally that the atoms explore mostly the bottom of the trap where the profile can be then very well approximated by the harmonic expression:

$$U_0(r, z, F) = U_0(F) + \frac{1}{2}m(\omega_r^2 r^2 + \omega_z^2 z^2), \quad (2.16)$$

with m the mass of the ^{87}Rb atoms. The expressions of ω_r and ω_z are obtained by developing Eq. 2.13 to first order and identifying the terms with Eq. 2.16:

$$\omega_r = \sqrt{\frac{4U_0}{m w_0^2}} \quad \text{and} \quad \omega_z = \sqrt{\frac{2U_0}{m z_R^2}}. \quad (2.17)$$

In our experiment, with an objective of numerical aperture $NA=0.5$ at 850 nm, we expect $w_0 \simeq 1 \mu\text{m}$ and thus $z_R = \pi w_0^2/\lambda \simeq 4 \mu\text{m}$. The corresponding oscillation frequencies estimated using Eq. 2.17 with a typical trap depth $U_0/h = 20 \text{ MHz}$ are $\omega_r \simeq 2\pi \times 110 \text{ kHz}$ and $\omega_z \simeq 2\pi \times 20 \text{ kHz}$.

2.2 Typical experimental sequences and computer control system

As we will see in the next sections, the internal state manipulation of single atoms requires to control many parameters on very short timescales; the information about the final state can then only be retrieved by performing many identical measurements of a chosen observable \hat{A} in order to reconstruct the probabilities corresponding to each outcome. Thus, a computer control system is necessary to achieve the required time resolution, to ensure accurate experimental repeatability and to store large amount of experimental data. Here, we start by depicting the typical experimental sequences realized on our single atom apparatus. Then we briefly describe the global architecture of the program allowing to generate these sequences and to store and analyse the experimental data.

2.2.1 Typical experimental sequences

Before launching an experimental sequence, the experiment is run in what we can call single atom 'continuous mode', in which the amplitudes of the fluorescence signals associated to the SPCM detector A and B (after integration over 10 ms time bins if no exception is specified) are read continuously by their corresponding counters. These signals exhibit two levels, as we saw in Sec. 1.4.4. The high-level corresponds to the presence of a single trapped atom and the low-level to the background noise. By keeping trace of the rising edges and falling edges events on such a signal in real time, we can associate a logic state of occupancy (0=empty; 1=occupied) for a given trap and for every 10 ms time slot. One-atom experimental sequences for trap A or trap B are triggered as soon as the corresponding counter enters in logic state 1.⁴ This triggering scheme is almost equivalent to set a triggering threshold, but it proved to be more robust against slow drifts of the background level⁵.

When a sequence s_j is triggered as shown in Fig. 2.2, the initial value of the counter is saved in the computer as a reference value f_j^{initial} measured at the beginning of this particular sequence. Because of the background level drifts, two initial fluorescence values f_j^{initial} and f_k^{initial} for two sequences s_j and s_k separated in time by more than few seconds could differ by more than the single atom step of fluorescence. However, the duration of most of the experimental sequences are shorter than 250 ms and the background level fluctuations are almost negligible on this time scale. Thus, at the end of a sequence s_j , we discriminate the presence of the atom from its absence by performing a final measurement of fluorescence f_j^{final} and comparing it to the initial value f_j^{initial} . If they differ by more than half of the single atom step of fluorescence on the counters, the atom is considered to be lost.

After a trigger event, a typical sequence is composed of three main steps, as shown in Fig. 2.2:

1. The first step starts by switching off all the beams at 780 nm as well as the magnetic field gradients while keeping the trapping laser on for a duration t_{disp} . This allows to disperse away the cold ^{87}Rb atoms of the MOT cloud surrounding the dipole trap in order to prevent any kind of collisional process with the main trapped atoms which could result in their loss. Atoms in the MOT have a temperature T_{MOT} of about 100 μK . Their thermal velocity can be estimated by:

$$\sigma_{v,\text{th}} = \sqrt{\frac{3k_B T_{\text{MOT}}}{m}} \simeq 0.17 \text{ m/s}, \quad (2.18)$$

where m is the mass of a ^{87}Rb atom and k_B is the Boltzmann constant. We wait for a duration $t_{\text{disp}} = 40$ ms after which most of the MOT atoms will have traveled a distance of $g \cdot t_{\text{disp}}^2 / 2 \simeq 8$ mm under gravity, and $\sigma_{v,\text{th}} t_{\text{disp}} \simeq 7$ mm due to thermal effects, which are both large compared to the initial size of the MOT cloud of several hundreds of microns. After this, the MOT beams are switched on again for $t_{\text{check,i}} = 40$ ms to check if the trapped atom is still present. The fluorescence signal obtained on the counter is an averaged out over four 10 ms time bins and compared to the initial reference value.

⁴Two-atom experiments are triggered as soon as both counters are in logic states 1. The same method described here is applied simultaneously to the two traps.

⁵Drifts of the background level were due to residual reflections of the MOT beams onto the lens holders under vacuum which happen to couple into the SPCM fibers. These drifts had various amplitudes from day to day. Sometimes, it could be almost on the order of the single atom fluorescence itself over five seconds. It was not possible to set a threshold value, though we could still operate using the rising edge method.

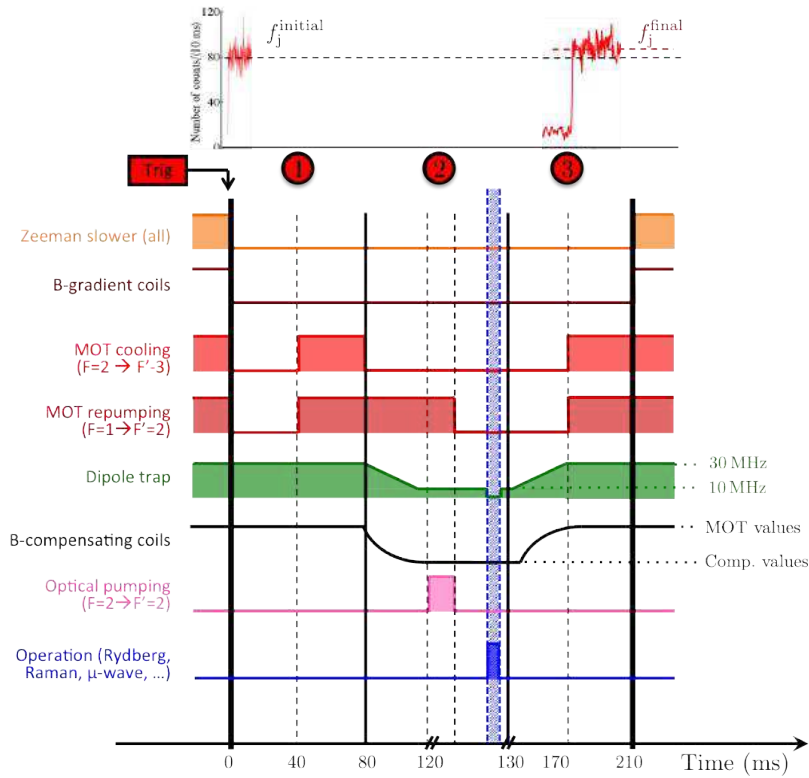


Figure 2.2: Typical experimental sequences.

If they differ by more than half of the single atom fluorescence step, the final result at the end of the sequence is discarded. This post selection scheme helps improve the quality of the data by only taking into account experiments where the atoms were really present at the beginning of the sequence.

2. Then the experiment itself begins. The three pairs of compensation coils along the main axes x , y and z are commuted to new current values optimized to compensate residual transverse magnetic fields. Depending on the experiment, the current in the z -coil can be adjusted to apply a vertical static magnetic field in order to impose a quantization axis and to remove the degeneracy between Zeeman sub-levels. When these coils are commuted, eddy currents are induced in the vacuum system, with a typical decay time of 4 ms (see Sec.3.3.4 for their characterization). Thus, we wait for about $t_{\text{mag.}} = 40 \text{ ms} \gg 4 \text{ ms}$ until the establishment of the chosen magnetic fields have reached a permanent regime in which the persistent currents have no measurable effect on the trapped atom. At the same time, the power of the trapping laser is ramped down linearly until it is decreased by a factor of approximately three. The trap depth is thus adiabatically reduced by a factor three and the temperature of the atom by $\sqrt{3}$ from $55 \mu\text{K}$ to $32 \mu\text{K}$.

After that, an optical pumping stage is performed to prepare the initial internal state of the atom. Sometimes, only a preparation in hyperfine state $|5S_{1/2}, F=1\rangle$ or $|5S_{1/2}, F=2\rangle$ is sufficient regardless the Zeeman sub-levels. This is performed by keeping only the molasses cooling beams or only the repumper beams for more than about 5 ms with more than 99% efficiency. For Raman or Rydberg sequences, a vertical

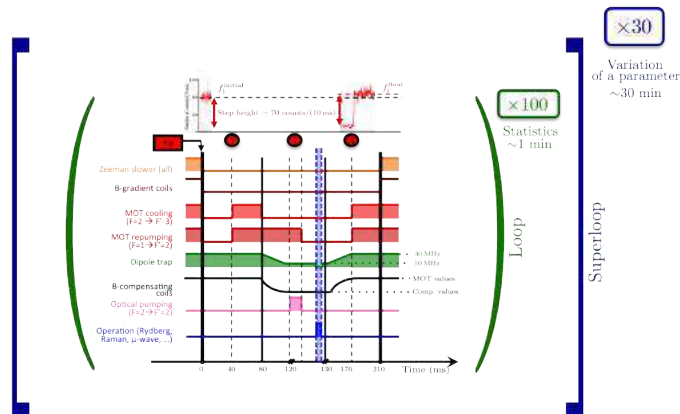


Figure 2.3: Construction of our experimental data

Sequence j	1	2	3	4	5	6	7	8	9	10	...	N_{tot}
Atom A	1	0	0	1	1	1	0	0	0	1	...	1
Atom B	0	0	1	1	0	1	1	0	1	0	...	1

$$P_{00} = \frac{N_{00}}{N_{\text{tot}}} \quad P_{11} = \frac{N_{11}}{N_{\text{tot}}} \quad P_{10} = \frac{N_{10}}{N_{\text{tot}}} \quad P_{01} = \frac{N_{01}}{N_{\text{tot}}}$$
Figure 2.4: Array of typical results out of N_{tot} sequences.

beam resonant on the transition $|5S_{1/2}, F=2\rangle \rightarrow |5P_{3/2}, F'=2\rangle$ with σ^+ polarization is used to optically pump the initial internal state of the atom into the Zeeman sub-state $|5S_{1/2}, F=2, m_F=2\rangle$. Once the state is well defined, all the lasers at 780 nm are usually switched off to avoid near-resonant scattering, and various operations can be performed using laser excitations, micro-waves pulses or ionizing pulses of static electric fields. These operations can be performed either inside the dipole trap, or in free space if they last typically less than $2 \mu\text{s}$.

- Finally, we perform a last fluorescence measurement by coming back to the initial values of currents of the compensation coils again ($t_{\text{mag.}} = 40 \text{ ms}$) and switching on all the MOT beams for a duration $t_{\text{check,f}} = 40 \text{ ms}$. The fluorescence signal obtained on the counter is again averaged out over four 10 ms time bins and compared to the initial reference value. If they differ by more than half of the single atom fluorescence step height, then the atom is considered to be lost.

For most of the experiments presented in this thesis, the result of one realization of a given sequence is binary for each atom: either it is present or lost at the end of the sequence. As shown in Fig. 2.3, we reconstruct the probability of the final atomic state – to be trapped or not – by repeating the same sequence many times (loop), and we get statistical results for each atom separately. At the end of a loop, for one given set of parameters, the typical data stored in the computer are shown in Fig. 2.4. The probability of the four possible outcomes labeled P_{00} , P_{01} , P_{10} and P_{11} can be computed. Usually, we built statistics over 100 sequences. The duty cycle of the experiment is slightly less than 1 Hz, so this took about 1 minute.

Then, we vary one parameter – pulse duration, frequency, delay – and we repeat the same procedure (superloop). Typical curves of Rabi oscillations or excitation spectra were obtained in about 30 minutes.

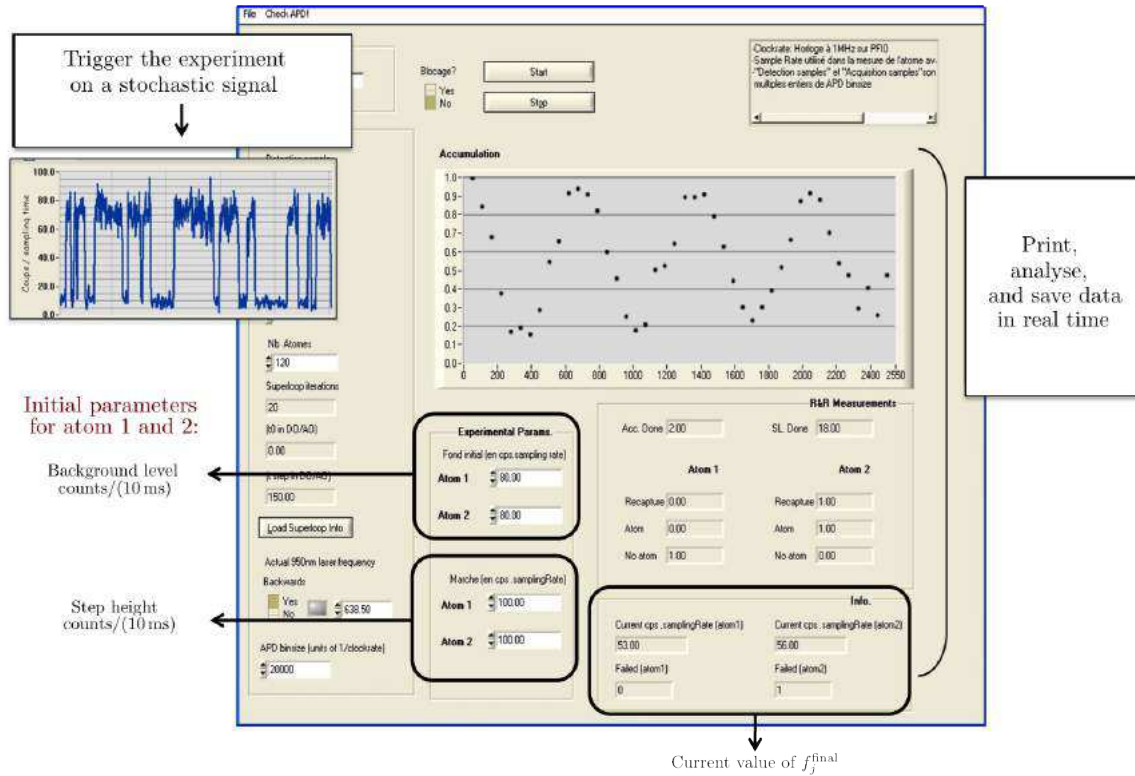


Figure 2.6: Layout of the measurement program.

laser frequency or to vary the duration of an excitation pulse automatically, improving thus the data acquisition rate. For each trigger received from the counters card, this program launches one full experimental sequence which ends by a final fluorescence measurement f^{final} (stage 3 in Fig. 2.2) before giving back the control to the measurement program.

Measurement program

The measurement program is shown in Fig. 2.6. It is the master program that controls the National Instruments PCI 6713 acquisition card, and records experimental data. It operates simultaneously two independent counter units connected to the output of the two SPCM detectors. As we saw in Sec. 1.4.3, a 28 ns wide TTL pulse followed by a 36 ns dead time is output by the photon counters via a BNC connector for each detected photon. This main program allows to choose the integration time of the counters (typically 10 ms) when they are run in 'continuous mode'. After a single atom detection event, this program saves the initial fluorescence level f^{initial} and sends a trigger to the NI PCI 6534 card, before entering into 'sequence mode' during which the slave control program generates the sequence. At the end, the measurement program takes over. With the final fluorescence measurement, it compares f^{final} with f^{initial} , determines if an atom was lost or not, saves the binary result in the computer and goes back to 'continuous mode' until the next detection event.

2.3 Characterization of the single atoms in the ODT

Single atom experiments have been investigated in the group since N. Schlosser started his PhD thesis in 1998. Over these last fifteen years, standard experimental sequences have

been developed to characterize the parameters of the microscopic optical dipole traps. In this section, we describe four experiments that we also performed to characterize our new apparatus when it became operational. For more details about them, we refer to the theses of our predecessors (Schlosser, 2001; Beugnon, 2007; Reymond, 2002; Darquié, 2005). These four characterization experiments allow to extract the atoms lifetime in the trap, the single atom temperature, the trap oscillation frequencies, and the trap depth for the typical trap power used on a daily basis for Rydberg experiments.

2.3.1 Lifetime in the trap

The very first characterization experiments consists in measuring the probability $P_{\text{trap}}(t)$ to keep a single atom trapped during a time t . This allows to access the crucial time scale determining for how long on average one can manipulate the state of the single atoms trapped in the tweezer before loosing them. As typical sequences last about 100 ms, the lifetime needs to be larger than 10 s to reach less than 1 % of losses.

A first method allowing to measure the survival probability $P_{\text{trap}}(t)$ was implemented after a first bake-out of the vacuum system, yielding a first value of the typical lifetime τ . Later during the project, we had to reopen the vacuum system and change the aspheric lenses, such that we had to characterize this parameter again. We did it using the second and third methods presented below. After the second bake-out, the pressure level indicated by the ion pump of the vacuum chamber was a factor of three lower, so we expected to observe a longer lifetime.

First method: survival probability

The experimental sequence shown in Fig. 2.7(a) allows to perform such a measurement in a rather simple direct way. As soon as a single atom is detected, all the 780 nm lasers beams are switched off for a certain time t . Then they are switched back on and we check if the atom is still there by fluorescence imaging. Such an experiment is repeated 100 times to extract the probability $P(t)$, and we repeat this procedure for values of t . The results obtained for a trap depth of about 30 MHz (1.5 mK) are shown in Fig. 2.7(b). At short times (< 0.5 s) the data points follow a 'plateau' before suddenly dropping down to zero, which indicates that at least two different timescales come into play.

The underlying physical process are now well known and consist in two main mechanisms. First, the trapped atoms can collide with molecules from the residual gas inside the vacuum chamber. This mechanism leads to a surviving probability $P_{\text{coll}}(t)$ after a time t which decays exponentially with a typical time τ :

$$P_{\text{coll}}(t) = e^{-t/\tau}. \quad (2.19)$$

A second loss mechanism is due to heating of the atoms inside the trap. By assuming that the heating is linear in time and that the trap is a truncated 3D isotropic harmonic trap, with depth U_0 , B. Darquié showed that the corresponding surviving probability $P_{\text{heat}}(t)$ reads:

$$P_{\text{heat}}(t) = 1 - \exp\left(-\frac{U_0}{k_B(T_0 + \alpha t)}\right) \left(1 + \frac{U_0}{k_B(T_0 + \alpha t)} + \frac{U_0^2}{2 k_B^2 (T_0 + \alpha t)^2}\right), \quad (2.20)$$

where T_0 is the initial temperature of the trapped atom, and α is the heating rate. The initial temperature was measured to be about 50 μ K (detailed in Sec. 2.3.2). As the two

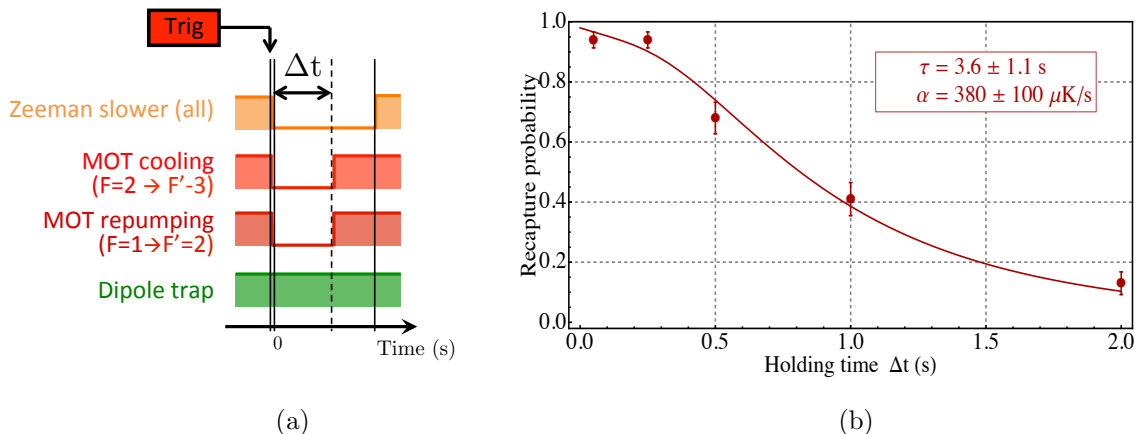


Figure 2.7: Lifetime measurement of a single atom in the trap. (a) Experimental sequence. The thick vertical black bar at $t = 0$ ms symbolizes the initial atom presence checking procedure (step 1 in Fig. 2.2). (b) Recapture probability vs duration Δt . Each data point is an average result over 100 experiments. The error bars show corresponding statistical uncertainties. The trap depth is about $U_0/h = 30$ MHz and the initial temperature of the atom is about 50 μK . The solid line is a fit by the function P_{tot} (described in the main text). We find $\tau = 3.6 \pm 1.1$ s.

processes are independent, the total survival probability $P_{\text{tot}}(t)$ is thus the product:

$$P_{\text{tot}}(t) = P_{\text{coll}}(t) \cdot P_{\text{heat}}(t). \quad (2.21)$$

The solid line in Fig. 2.7(b) is a fit of the experimental data using the function $P_{\text{tot}}(t)$ in which the free parameters are τ and α . The results $\tau = 3.6 \pm 1.1$ s and $\alpha = 380 \pm 100$ $\mu\text{K/s}$ are rather compatible with similar measurements performed on the former setup (error bars are standard deviations from the regression).

The heating rate can have different origins. One fundamental source of heating is due to spontaneous scattering of trap photons at 850 nm. The corresponding heating rate α_{trap} reads (Grimm, Weidemüller, and Ovchinnikov, 2000):

$$\alpha_{\text{trap}} = \frac{T_{\text{rec}}}{3} \Gamma_{\text{sc}} \simeq 5 \mu\text{K/s}, \quad (2.22)$$

where $T_{\text{rec}} = 349$ nK is the ^{87}Rb recoil energy, and Γ_{sc} is the photon scattering rate defined in Eq. 2.11, which is equal to 24 s^{-1} with our trap parameters (3 mW focused down to a $1/e^2$ radius of 1 μm). This heating rate α_{trap} is much smaller than the one we measure. There can be also technical heating induced by intensity fluctuations or pointing instabilities of the trapping laser beam (Savard, O'Hara, and Thomas, 1997), but they should also be negligible. At the time of this measurement, residual near-resonant light at 780 nm was probably responsible for most of the observed experimental heating. Besides, between the first and the second bake-out, a lot of effort was put into preventing any resonant light at 780 nm from scattering into the chamber using mechanical shutters. Further analysis of heating mechanisms might be performed in the future.

Second method: mean lifetime

An alternative method was implemented to extract an estimate of the decay time τ' after the second bake-out of the experiment, for which the getter pump was activated properly (see Sec. 1.3.3).

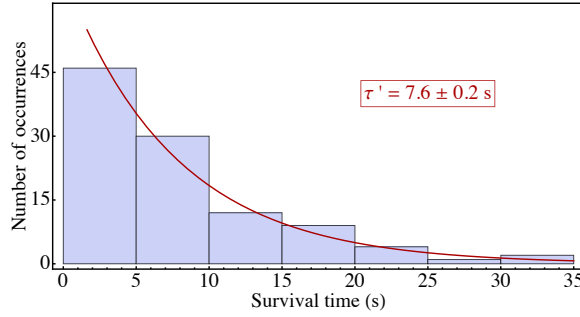


Figure 2.8: Histogram of survival time measurements. Histogram of 104 experiments for which we measured the survival time of a single atom, with 5 s time bins.

For this method, we worked with a molasses configuration with no magnetic gradient. The loading of the tweezer is not completely zero, and by looking at the fluorescence signal on the counter as shown in Fig. 1.24(a), we could capture atoms by blocking the Zeeman beams just after a rising edge of the fluorescence. From this moment, the atomic density of trapped atoms in the molasses decreases rapidly together with the loading term of the trap such that the lifetime of the single atom is almost only limited by collisions with molecules from the residual gas. For each try i , we measured the time t_i after which the atom was lost and we repeated the procedure 104 times. The histogram of the results with a binning of 5 s is shown in Fig. 2.8.

In this experiment, the heating processes are completely compensated for by the cooling provided by the MOT beams. However, light-assisted collisions with cold atoms from the molasses can also participate to the total loss. By assuming that these events remain negligible, the survival probability of an atom inside the trap is approximately $P'_{\text{coll}}(t) = \exp(-t/\tau')$, with a decay time τ' . The red solid line in Fig. 2.8 is a fit of the experimental data using such a probability distribution, with τ' as the only free parameter, and we found $\tau' = 7.6 \pm 0.2$ s.

The lifetime τ' obtained with this second method was thus larger than the lifetime measured before the second bake-out by a factor of about two, which confirmed the improvement of the vacuum performances. This was then confirmed by a third method measuring the lifetime of the MOT cloud.

Third method: MOT lifetime

After the second bake-out, we also tried to estimate the lifetime τ' of the single atoms in the trap by measuring the lifetime τ_{MOT} of the MOT cloud. The fluorescence of the MOT was collected with an objective and monitored in real time on a CCD camera. We considered only the integrated signal over a relevant region of interest. After a certain time t_1 , the Zeeman beams were switched off. As the MOT loading rate is then almost zero, the fluorescence signal decreases. In Fig. 2.9, the fluorescence is plotted semi-logarithmically (in a.u.) as a function of the time (in s). Two regimes can be identified:

- $t_1 < t < t_2$: the signal decays faster than an exponential. As the measurement was done with a rather large initial MOT density ($|B'| \simeq 8$ G/cm), this fast decay corresponds most probably to two-body collisions, assisted by the near-resonant light of the MOT beams. With time, the MOT density decreases, and these collisions become less and less significant.

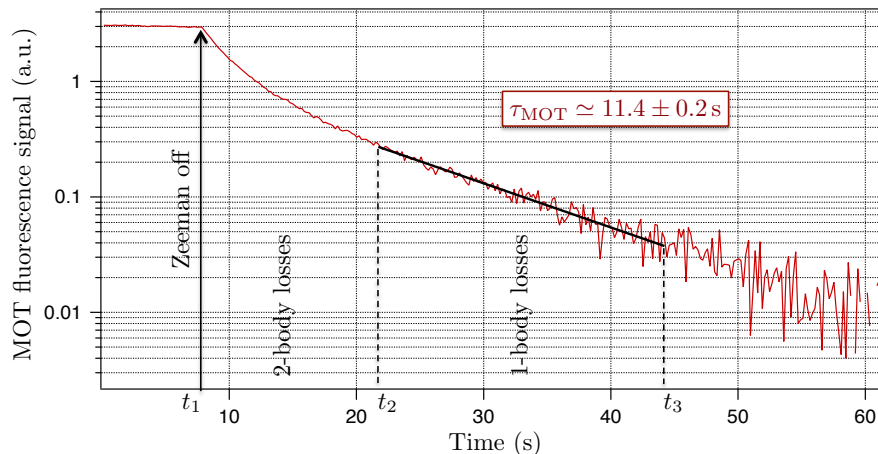


Figure 2.9: MOT lifetime. Fluorescence signal (in a.u.) of the MOT versus time (in s). At $t=t_1$, the Zeeman beams are switched off. A first regime dominated by two-body losses due to near-resonant light is observed for $t_1 < t < t_2$. After t_2 , the fluorescence signal decays exponentially, with a decay time $\tau_{\text{MOT}} = 11.4$ s.

- $t > t_2$: the decay is exponential.

By fitting the signal after $t=t_2$ by an exponential decay, we obtained a decay time $\tau_{\text{MOT}} \simeq 11.4 \pm 0.2$ s in good agreement with the value of τ' obtained previously.

2.3.2 Single Atom Temperature

We measured next the temperature of our single atoms inside the dipole traps. The concept of temperature concerning a single particle may appear inappropriate. Indeed, when a single atom experiment is triggered, an atom i trapped in the tweezer has a well determined total energy E_i . However, from one experiment to another, the energies $\{E_i\}_i$ follow a certain distribution which was proven to be a thermal Boltzmann distribution (Tuchendler *et al.*, 2008). The temperature T corresponding to this distribution can be measured by a standard release and recapture method.

The experimental sequence is shown in Fig. 2.10(a). After the detection of a single atom in the trap, the molasses beams are switched off. Then, the dipole trap is switched off for a variable duration Δt of several microseconds. During this time, an atom i escapes from its initial position \vec{r}_i near the center of the trap with a non-zero velocity \vec{v}_i . Then the trap is switched back on together with the molasses beams to perform a fluorescence measurement and check the presence of the atom. At this moment, if the kinetic energy of the atom $1/2m|\vec{v}_i|^2$ is larger than the remaining potential energy at the atom final position $U(\vec{r}_f)$, then the atom can leave the trap and it is lost at the end of the sequence. If the kinetic energy $1/2m|\vec{v}_i|^2$ is smaller than the remaining potential energy $U(\vec{r}_f)$, the atom starts to oscillate in the trap again while being cooled by the molasses beams, and it is recaptured at the end of the sequence. The probability to recapture the atom after a release time Δt_i is reconstructed by repeating the sequence for about 100 times. Then, the data obtained for several times Δt_i are compared to Monte-Carlo simulations (more details in Tuchendler *et al.* (2008)) where the input parameters are the initial trap power P , the waist w_0 of the trapping laser at 850 nm (leading to a trap depth U_0/h), and the free parameter is the

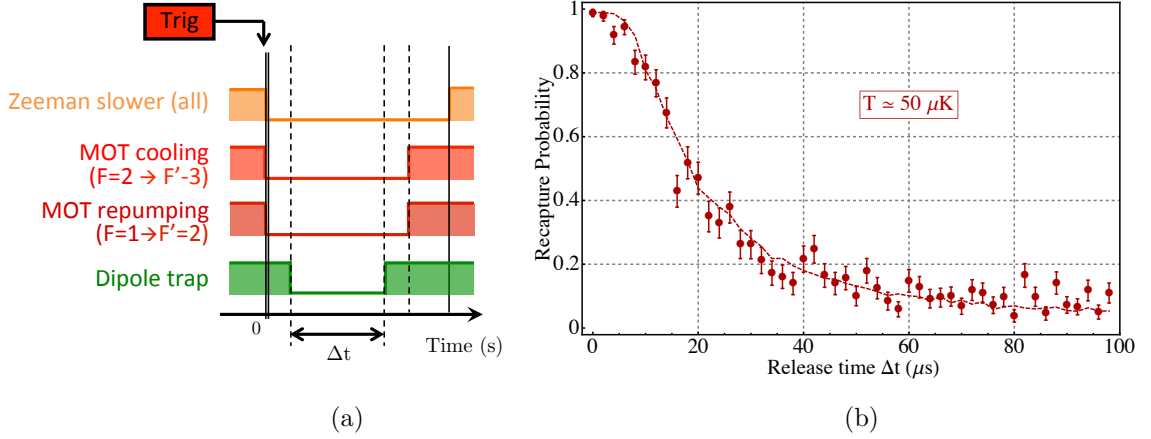


Figure 2.10: Release and recapture temperature measurements. (a) Experimental sequence. The thick vertical black bar at $t=0$ ms symbolizes the initial atom presence checking procedure (step 1 in Fig. 2.2). (b) Recapture probability vs release time Δt . Each data point is an average result over 100 sequences. The error bars show the corresponding statistical uncertainties. The trap depth is $U_0/h = 25$ MHz. The dashed line is a fit from Monte-Carlo simulations. We find $T = 50 \pm 2 \mu\text{K}$.

temperature T describing the initial energy distribution of the atoms from which the initial position \vec{r}_i and velocity \vec{v}_i are drawn at each realization.

The result illustrated in Fig. 2.10(b) was obtained for a trap power $P = 3.8$ mW. The corresponding trap depth is measured in Sec. 2.3.4 to be $U_0/h = 26$ MHz. The trapping beam waist was estimated to be about $w_0 = 0.96 \mu\text{m}$. The result of the Monte-Carlo simulations gave a temperature $T = 50 \mu\text{K} \pm 2 \mu\text{K}$ (the error bar is the standard deviation from the least square regression). This value is in the range of temperature observed in similar experiments with microscopic dipole traps (Kuhr *et al.*, 2001; Yavuz *et al.*, 2006; Weber *et al.*, 2006). On average, it means that an atom occupies $[k_B T / (\hbar \omega_r)]^2 \simeq 11^2$ radial vibrational states and $k_B T / (\hbar \omega_z) \simeq 57$ longitudinal vibrational states, which justifies afterwards the classical treatment of its motion inside the trap.

Such initial temperature combined with rather high trap oscillation frequencies is a good starting point to achieve ground state cooling and get free of temperature effects, as it was recently demonstrated by Kaufman, Lester, and Regal (2012) using polarization gradient cooling and Raman side-band cooling schemes.

2.3.3 Trap oscillation frequencies

A third standard characterization procedure consisted in measuring the oscillation frequencies of the trapped atoms in the microscopic optical trap. Expected values of the frequencies ω_\perp (transverse) and ω_\parallel (longitudinal) expected for such a cylindrical harmonic trap were derived in Sec. 2.1.2 for a typical power of 3 mW, focused down to a $1/e^2$ radius of $1 \mu\text{m}$, yielding a trap depth $U_0/h = 20$ MHz; they read:

$$\omega_\perp^{\text{expected}} = \sqrt{\frac{4U_0}{mw_0^2}} \simeq 2\pi \times 110 \text{ kHz} \quad \text{and} \quad \omega_\parallel^{\text{expected}} = \sqrt{\frac{2U_0}{mz_R^2}} \simeq 2\pi \times 22 \text{ kHz}. \quad (2.23)$$

It is also possible to measure directly the trap oscillation frequencies. A common technique is to generate parametric excitations in the system and to observe resonances at twice

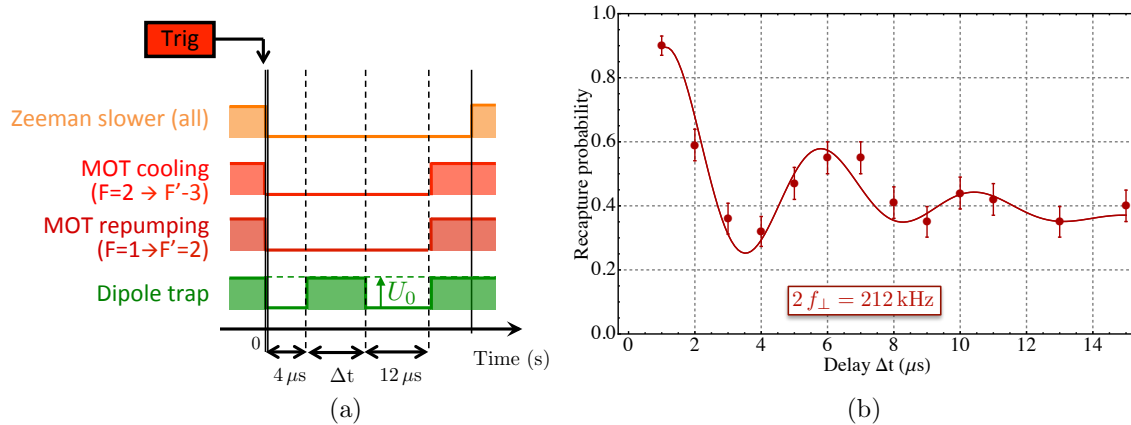


Figure 2.11: Measurement of the trap oscillation frequencies. (a) Experimental sequence. The thick vertical black bar at $t=0$ ms symbolizes the initial atom presence checking procedure (step 1 in Fig. 2.2). (b) Recapture probability vs delay Δt . Each data point is an average result over 100 sequences. The error bars show corresponding statistical uncertainties. The trap depth is $U_0/h = 24$ MHz. The solid line is a fit of the data with the function $y_0 + A \exp(-t/\tau) \sin(2\pi \times 2ft)$. We find $2f_{\perp} = 212$ kHz.

the oscillator resonance frequencies ω (Melde, 1860). With dipole traps, such excitations can be performed by modulating either the power or the position of the trap, respectively at ω and 2ω , and the resonances can be observed via a loss of atoms, such as it was done in numerous experiments (Barrett, Sauer, and Chapman, 2001; Zürn *et al.*, 2012).

However, G. O. Reymond showed during his thesis (Reymond, 2002) that another method inspired by Engler *et al.* (2000) was well suited to our single atoms apparatus. The experimental sequence is shown in Fig. 2.11(a) and consists in the following step:

1. After the detection of a single atom in the trap, all lasers beams at 780 nm are switched off. The atom oscillates at the bottom of the harmonic trap.
2. Then the dipole trap is switched off twice, for fixed durations t_1 and t_2 of several microseconds, separated by a variable duration Δt during which it is on.
3. Finally, the molasses beams are switched on again and we check if the atom is still present.

By repeating this sequence for about 100 times, we can reconstruct the probability to recapture the atom at the end as a function of the duration Δt . A typical curve obtained for $t_1 = 4 \mu\text{s}$ and $t_2 = 12 \mu\text{s}$ is shown in Fig. 2.11(b). It turns out that the oscillation frequency observed is about twice the trap radial oscillation frequency. An intuitive way to understand this is to picture the evolution of all the experimental realizations in phase space. The atoms are analogous to an ensemble of classical billiard balls oscillating in a harmonic trap. At $t=0 \mu\text{s}$, the initial distribution of atoms follows a gaussian distribution in position and velocity. A 1D representation of the phase diagram is shown in Fig. 2.12(a). During the first 'off' pulse, the trajectories of the atoms are ballistic such that the circular cloud of the phase diagram gets elongated along the position axis and becomes strongly elliptical, as shown in in Fig. 2.12(b). When the trap is switched back on, recaptured atoms resume their oscillation, which corresponds to a rotation of the ellipse in the phase diagram. These atoms then oscillate in phase in the trap during the variable duration Δt . The probability to loose

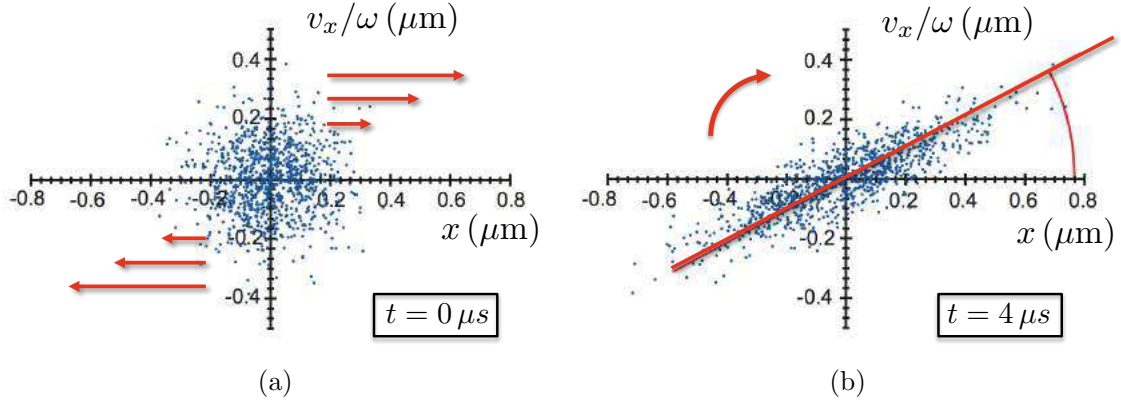


Figure 2.12: Evolution in phase space. (a) shows the phase diagram at $t = 0 \mu\text{s}$ composed of 1000 initial conditions chosen randomly according to gaussian distributions for the position x and the velocity v_x . (b) shows the same phase diagram after a free evolution of $4 \mu\text{s}$.

the atoms when the second 'off' pulse occurs is maximum when the long axis of the ellipse is vertical, which corresponds to a distribution of atoms near the bottom of the trap with large velocities. Similarly, the probability is minimum when the long axis of the ellipse is horizontal, which corresponds to a distribution of atoms almost at their maximal elongation in the trap, with low velocities. These two cases happen twice per ellipse revolution, such that the recapture probability oscillates at twice the oscillation frequency of the trap. Such a collective behaviour is commonly referred to as a monopole, or a breathing mode.

In principle, the same description could be given in 3D, and one could expect to see beat notes of the 3D trap oscillation frequencies ω_x , ω_y , and ω_z . However, with our realistic 3D trapping parameters, the transverse confinement is much larger than the longitudinal confinement. During the chosen time $t_1 = 4 \mu\text{s}$, the free expansion along the longitudinal axis x remains quite small compared to the initial size of the spatial distribution, and we can thus only excite the radial oscillation frequency ω_\perp . The experimental data shown in Fig. 2.12(b) were fitted by a damped sine function, and we measured:

$$\omega_\perp^{\text{measured}} \simeq 2\pi \times 106 \text{ kHz}, \quad (2.24)$$

which is compatible with the expected value of the radial oscillation frequency $\omega_\perp^{\text{expected}}$ within 5%. The relationship between the trap longitudinal and radial oscillation frequencies is obtained by replacing the definition of the Rayleigh distance z_R as a function of w_0 into Eq. 2.17, and the value of the longitudinal oscillation frequency ω_\parallel can be inferred from the previous measurement:

$$\omega_\parallel^{\text{inferred}} = \frac{\lambda}{\sqrt{2}\pi w_0} \omega_\perp^{\text{measured}} \simeq 2\pi \times 21 \text{ kHz}. \quad (2.25)$$

2.3.4 Measurement of the trap depth

Finally, we measured the trap depth seen by the atoms as a function of the trapping laser power $U_0 = f(P_{\text{trap}})$ for of a π -polarized trap.

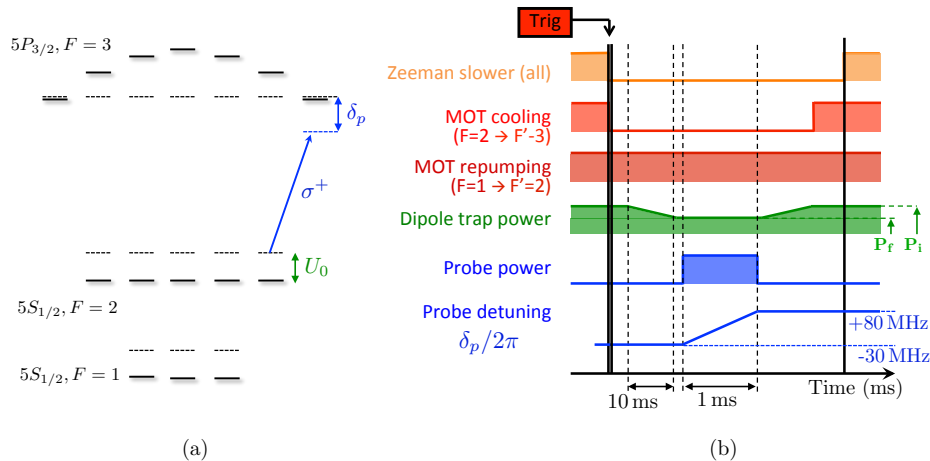


Figure 2.13: Spectroscopy of the cycling transition. (a) Internal structure of a ^{87}Rb atom where the energies of the states are shifted in the presence of the linearly polarized trap. (b) Experimental sequence. The thick vertical black bar at $t = 0$ ms symbolizes the initial atom presence checking procedure (step 1 in Fig. 2.2). After the detection of a single atom, the initial trap power $P_i = 3.8$ mW optimizing single atom loading is ramped to a chosen fixed value P_f ranging from 0.5 mW to 13 mW. The probe detuning $\delta_p/2\pi$ from the transition $|5S_{1/2}, F = 2, m_F = 2\rangle \rightarrow |5P_{3/2}, F' = 3, m_{F'} = 3\rangle$ is scanned during 1 ms from about -30 MHz to 80 MHz. Finally the trap power is switched back to its initial value. This sequence is repeated typically 1000 times to improve the signal to noise ratio.

Physical requirements

As we saw in Sec. 2.1.1, the focused trapping laser light at 850 nm induces energy shifts of the internal states of ^{87}Rb atoms that shift the transition frequencies between the ground states and the excited states (Fig. 2.13(a)). However, the spin-stretched state $|5P_{3/2}, F' = 3, m_{F'} = 3\rangle$ is almost unshifted by the presence of the trapping laser. It has been demonstrated since the thesis of G.O. Reymond (Reymond, 2002) that an accurate measurement of the trapping potential energy U_0 can be obtained by measuring the frequency of the transition $|5S_{1/2}, F = 2, m_F = 2\rangle \rightarrow |5P_{3/2}, F' = 3, m_{F'} = 3\rangle$.

The laser sequence we implemented is sketched in Fig. 2.13(b). After a single atom detection event, the molasses cooling beams are switched off while the repumping beams are kept on until the end of the sequence to prevent optical depumping into the hyperfine ground state $F = 1$. The initial trap power $P_i = 3.8$ mW is ramped to an arbitrary value P_f in the range 0 – 13 mW. Then, the probe detuning from the unshifted transition $\delta_p/2\pi$ is scanned from about -30 MHz to $+80$ MHz. A low probe saturation parameter $s_p = I_p/I_{\text{sat}} \leq 0.1$ is used to avoid power broadening. The duration of the scan is adjusted such that heating induced by the probe remains small while the atom scatters enough photons to be optically pumped into $|5S_{1/2}, F = 2, m_F = 2\rangle$ and cycles mostly on the transition of interest. A typical duration of 1 ms proved to be a good tradeoff, for which the total number of scattered photons can be estimated by integrating over the duration of the ramp the number of photons $N(t)dt$ scattered during a time dt :

$$N(t) dt = \frac{\Gamma}{2} \frac{I_p/I_{\text{sat}}}{1 + 4(\delta_p(t) - \delta_0(P_f))^2/\Gamma^2} dt \Rightarrow \int_{\text{ramp}} N(t) dt \simeq 100. \quad (2.26)$$

where $\delta_0(P_f)$ is the position of the resonance for a trap power P_f . The scattered photons are

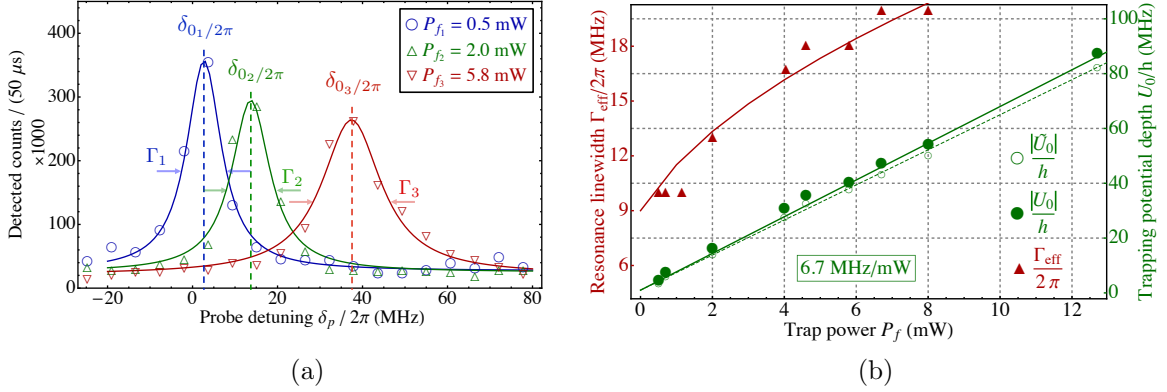


Figure 2.14: Measurement of the trapping potential depth $|U_0| = f(P_{\text{trap}})$. (a) Light shifted transition spectra obtained for various trap powers P_f . Solid lines are lorentzian fits from which the peak position $\delta_0/2\pi = |\tilde{U}_0|/h$ and linewidth Γ_{eff} of the resonances are extracted. (b) Double plot showing the trap depth (before and after the corrections due to finite temperature bias) and the width of the resonance Γ_{eff} as a function of the trap power P_f .

collected by the imaging system going to the SPCM detectors. For this specific measurement, the photon counter is gated during the scan of the probe and used with its full resolution with time bins of $1 \mu\text{s}$. Our detection efficiency η_d is about 0.68% (see Sec. 1.4.3) so we need to average over typically 1000 sequences to collect enough scattered photons and get a large signal to noise ratio. After averaging over many sequences, the profile of the fluorescence signal measured as a function of the probe detuning δ_p should be a lorentzian profile $\mathcal{L}(\delta_p - \delta_0)$ centered on a detuning $\delta_0 = -U_0/\hbar$ with a linewidth equal to Γ .

Experimental configuration and results

The linear polarization of the dipole trap is aligned with the vertical axis z of the experiment. A probe laser beam is derived from the main laser system at 780 nm, it goes through a double-pass AOM and is coupled into a PM fiber and brought to the vacuum chamber table. There, it is first combined on a PBS cube with one vertical beam of the molasses, then they both pass through the same quarter-wave plate such that the probe and the cooling beams become respectively σ^+ and σ^- -polarized, and they are sent along the vertical axis of the experiment. At the time of this measurement, the probe beam was slightly converging and the probe waist was about 0.5 mm at the position of the atom. The power was set to $0.5 \mu\text{W}$ corresponding to a saturation parameter on resonance $I/I_{\text{sat}} \simeq 0.07$. The probe frequency was scanned over a range of 110 MHz by tuning the AOM driver frequency while the driver RF power was adjusted⁶ such that power variations⁷ of the probe beam were maintained below 5%.

Experimental fluorescence signals detected on the photon counter are shown in Fig. 2.14(a) for various trap powers P_{f_i} . The signals obtained for each sequence are time resolved detected counts with a resolution of $1 \mu\text{s}$. Each curve is then an average over 1000 sequences where the number of counts was summed over time bins of $50 \mu\text{s}$. The total number of detected photons is compatible with the probe saturation parameter $s_p \simeq 0.07$ and a detection

⁶Both the RF frequency and the RF power are controlled by analog outputs of National Instruments PCI 6713.

⁷The variations of the probe power were monitored on a photodiode placed after the vacuum chamber.

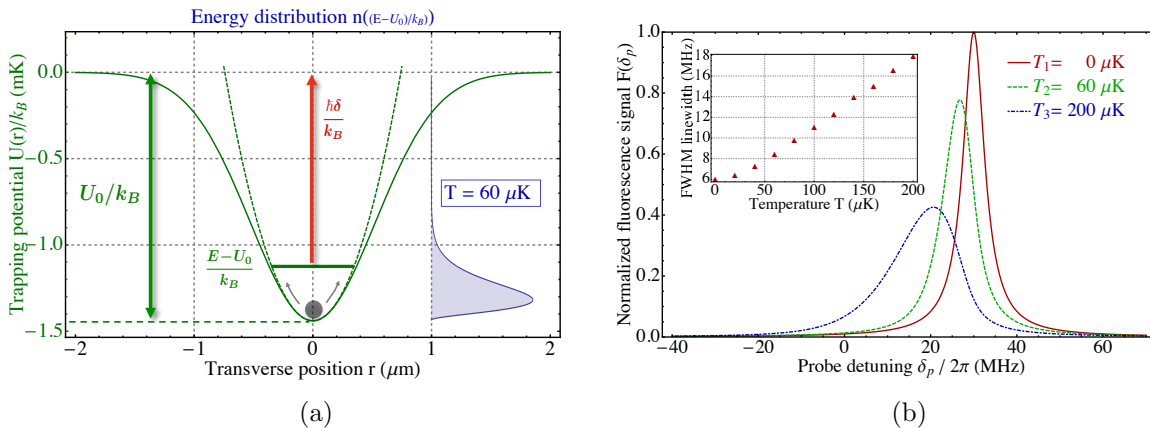


Figure 2.15: Finite temperature effects. (a) Transverse cross-section of a gaussian trap of depth $U_0/k_B = -1.4$ mK (green) and its approximation by a harmonic oscillator (dashed, green). The energy distribution in the 3D harmonic oscillator for a temperature $T = 50 \mu\text{K}$ is represented in blue. (b) Distortion of the fluorescence signals at high temperatures. The inset shows the evolution of the typical widths with the temperature.

efficiency $\eta_d = 0.68\%$. Finally, the variations of the trap depth \tilde{U}_0/h and the width of the resonance Γ_{eff} as a function of the trap power P_f are shown in Fig. 2.14(b). As expected, the trap depth \tilde{U}_0/h evolves linearly with the trap power P_f with the expected slope of about 6.5 MHz/mW.

Finite temperature effects

We can notice that the lorentzian shape broadens and gets distorted as the power of the trap increases. This can be well explained by finite temperature effects. Indeed, the single atoms are not cooled down to the ground state of the dipole trap. From one experiment to another, the energy of a trapped atom is not exactly the same, and it was shown that the energy distribution is well described by a thermal Boltzmann distribution with temperature T (Tuchendler *et al.*, 2008). Then, during a scan of the probe, each atom i with total energy E_i oscillates in the trap and explores not only the bottom of the trapping potential of depth U_0 , as shown in Fig. 2.15(a). A direct trap depth measurement \tilde{U}_0 is then an average over a range of positions in the trap corresponding to different energy shifts. We saw in Sec. 2.3.2 that the initial temperature T_i of the atom is on the order of $50 \mu\text{K}$ for an initial trap power $P_i = 3.8$ mW corresponding to a trap depth $|U_0|/k_B = 1.2$ mK. The condition $k_B T \ll |U_0|$ is well fulfilled, so the atoms explore mostly the quadratic part of the trap. The latter can be well approximated by a 3D harmonic trap for which the density of states $\rho(E)$ increases as E^2 . The bias in the trap depth measurement introduced by finite temperature effect can be evaluated in an approximate way by computing the convolution of a lorentzian profile $\mathcal{L}(\delta)$ of width Γ centered on $\delta = 0$ with the thermal detuning distribution $n(\delta)$, obtained from the energy distribution $n(E) = \rho(E) \exp(-E/k_B T)$ with the substitutions $E' = E + U_0$ (harmonic trap with minimum energy U_0) and $\hbar\delta = -E' > 0$ (see Fig. 2.15(a)). The signal of fluorescence $F(\delta_p)$ expected for a detuning δ_p is of the form:

$$F(\delta_p) = \int_{\delta'=-\infty}^{-U_0/\hbar} n(\delta') \mathcal{L}(\delta_p - \delta') d\delta'. \quad (2.27)$$

For non-zero temperature $T > 0$, the position of the maximum of $F(\delta_p)$ is red-shifted

from the initial position of the resonance δ_0 , and the lorentzian shape sinks and becomes asymmetric, with a larger full width at half maximum (FWHM), as shown in Fig. 2.15(b). Based on these results, we corrected the positions of the resonances that we measured for each trap power P_f . The initial temperature of the single atom thermal distribution is $T_i \simeq 57 \mu\text{K}$ for a power $P_i = 3.8 \text{ mW}$. The duration of the linear trap power ramp is long enough such that the trap oscillation frequency $\omega(t)$ follows an adiabatic evolution⁸. For each value of P_f , the corresponding temperature was estimated by $T_f = T_i \sqrt{P_f/P_i}$. According to the simulations, we computed the corrected value U_0 shifted from the direct measurement of the trap depth \tilde{U}_0 because of the finite temperature T_f . As predicted by Eq. 2.10, the trap depth U_0 evolves linearly with the trapping laser power P with a coefficient 6.7 MHz/mW.

Assuming that the trap has a gaussian shape, we can combine Eq. 2.14 and Eq. 2.15 to estimate the waist⁹ w_0 in the focal plane of the aspheric lens:

$$w_0 = \sqrt{\frac{\hbar\Gamma^2 P}{4\pi I_{\text{sat}} U_0} \left(\frac{1}{3\delta_{1/2}} + \frac{2}{3\delta_{3/2}} \right)} \simeq 0.96 \mu\text{m}. \quad (2.28)$$

Finally, one can notice that for very low values of P_f , the measured linewidths for temperatures T_f of less than $20 \mu\text{K}$ are still about 10 MHz which is much larger than the natural linewidth $\Gamma/2\pi = 6 \text{ MHz}$. One source of broadening could be due to heating by the probe laser during the measurements. Another could be attributed to the linewidth of the probe laser beam, which we did not measure accurately. Indeed, the probe beam is derived from the main laser diode at 780 nm of which the current is modulated to achieve a standard locking scheme onto a saturated absorption setup. However, this modulation should be on the order of 100-200 kHz.

⁸The adiabatic condition is: $\dot{\omega}(t) \ll \omega^2(t)/2\pi$.

⁹The waist w_0 can also be estimated from the same measurements without using the rotating wave approximation leading to Eq. 2.14. The terms $\delta_{1/2}^{-1}$ and $\delta_{3/2}^{-1}$ in Eq. 2.28 should then be replaced respectively by $(\omega_L - \omega_{D1})^{-1} - (\omega_L + \omega_{D1})^{-1}$ and $(\omega_L - \omega_{D2})^{-1} - (\omega_L + \omega_{D2})^{-1}$, where ω_L is the laser frequency, and $\omega_{D1, D2}$ are the frequencies of the D1 and the D2 transitions in ⁸⁷Rb. With this expression, one would obtain $w_0 \simeq 0.98 \mu\text{m}$.

Chapter 3

Manipulation of ^{87}Rb internal ground states

Contents

3.1 Zeeman effect: an overview	68
3.2 Cancellation of residual magnetic fields with microwave spectroscopy	69
3.2.1 Magnetic dipole transitions between hyperfine ground states	69
3.2.2 Hyperfine ground states detection scheme	70
3.2.3 Setup for the microwave generation	71
3.2.4 Zeeman shifts measurements	72
3.3 Stimulated Raman transitions	75
3.3.1 Choice of the qubit	75
3.3.2 Two-photon electric-dipole transitions	76
3.3.3 Laser system at 795 nm	77
3.3.4 Raman spectra of the transition $ F=2, m_F=2\rangle \rightarrow F=1, m_F=1\rangle$	79
3.3.5 Optical pumping optimization	83
3.3.6 Conclusion	84

We saw in Chapter 2 how to characterize the main parameters of one microscopic optical trap (size, depth) as well as useful parameters describing the single atoms external state inside such a trap (non-zero residual temperature, lifetime). Now, we plan to excite the single atoms towards Rydberg states using a two-photon coherent transition. However, the coupling strength of such a transition depends on the Zeeman sub-levels of the initial ground state and the final Rydberg state through a Clebsch-Gordan coefficient. In order to achieve excitation efficiencies close to 100 %, it is necessary to prepare the initial ground state into a well-chosen Zeeman sub-level. This is commonly achieved by performing optical pumping while applying a controlled static magnetic field along the quantization axis, thus breaking the Zeeman degeneracy. However, any magnetic fields transverse to the quantization axis can damage the state preparation by mixing different Zeeman sub-levels of the initial hyperfine state and need to be compensated for. In this chapter, we describe the set of experimental

tools that we implemented to manipulate the internal state of the trapped atoms and we characterize their efficiency.

In the first part of the chapter, we briefly recall the main properties of the Zeeman effect for ^{87}Rb atoms. Then, we show how we measured and compensated for residual transverse magnetic fields by performing Zeeman spectroscopy on the hyperfine ground states with microwave transitions. In a third part, we describe the Raman lasers system at 795 nm allowing to manipulate the state of a qubit encoded into the internal states $|5S_{1/2}, F=1, m_F=1\rangle = |0\rangle$ and $|5S_{1/2}, F=2, m_F=2\rangle = |1\rangle$, as required for the implementation of quantum information protocols. As we will see in Chapter 4, the state $|1\rangle$ is the initial ground state required for the Rydberg excitation scheme. We show then how the Raman system provides a useful way to characterize and optimize the optical pumping stage providing the initialization of the atomic state into the desired state $|1\rangle$, which is a crucial prerequisite to achieve highly contrasted coherent Rabi oscillations towards Rydberg excited states.

3.1 Zeeman effect: an overview

In a static external magnetic field \vec{B} , the total magnetic dipole moment of a ^{87}Rb atom $\hat{\mu}$ interacts with the magnetic field and the degeneracy of the magnetic sub-levels is broken. The interaction hamiltonian reads:

$$\begin{aligned} \hat{H}_B = -\hat{\mu} \cdot \vec{B} &= \frac{\mu_B}{\hbar} (g_S \hat{S} + g_L \hat{L} + g_I \hat{I}) \cdot \vec{B} \\ &\simeq \frac{\mu_B}{\hbar} (2\hat{S}_z + \hat{L}_z) \cdot B_z, \end{aligned} \quad (3.1)$$

by taking the magnetic field to be along the z -direction which defines the quantization axis. In this expression, $\mu_B = e\hbar/2m_e$ is the Bohr magneton and the numbers g_S , g_L and g_I are respectively the electron spin, electron orbital, and nuclear Landé g -factors, which we approximated to $g_S = 2$, $g_L = 1$ and $g_I = 0$.

In all the experiments presented in this thesis, the energy shifts due to magnetic fields are typically below 10 MHz which is very small compared to the hyperfine splittings of the ground state $5S_{1/2}$ ($\nu_{\text{hfs}} \simeq 6.83$ GHz) and the first excited states $5P_{1/2}$ and $5P_{3/2}$ (on the order of 100 MHz). For these states, the hamiltonian \hat{H}_B can be treated as a time-independent weak perturbation of the unperturbed hyperfine structure hamiltonian \hat{H}_{HFS} . To lowest order, this perturbation does not mix the unperturbed eigenstates $|J, I, F, m_F\rangle$ such that F is still a good quantum number and the interaction hamiltonian becomes:

$$\hat{H}_B^{(1)} = \frac{\mu_B}{\hbar} g_F \hat{F}_z B_z, \quad (3.2)$$

where g_F is the hyperfine Landé g -factor. Approximate g_F factors of all hyperfine states involved in the D1 and the D2 transitions are shown in Fig. A.1 (more details about their calculation can be found in Steck (2008)). To lowest order, the energy shift of each Zeeman sub-level is the expectation value of the perturbation hamiltonian $\hat{H}_B^{(1)}$:

$$\Delta E(F, m_F) = \langle F, m_F | \hat{H}_B^{(1)} | F, m_F \rangle = \mu_B g_F m_F B_z. \quad (3.3)$$

Thus for weak magnetic fields, the degenerate magnetic Zeeman sub-levels split linearly with the static magnetic field amplitude B_z , as it is illustrated in Fig. 3.2(a) for the hyperfine

level $F=1$ and $F=2$ of the ground state $5S_{1/2}$. The splitting in this regime is commonly called the *normal Zeeman effect*.

We can notice from the previous expression that the transition between the hyperfine ground states $|F=1, m_F=0\rangle$ and $|F=2, m_F=0\rangle$ is not shifted by first order Zeeman effect¹. The frequency ν_{hfs} of this transition called the *clock transition* of ^{87}Rb is 6.834682610 GHz and it is used as an atomic reference frequency standard (Bize *et al.*, 1999). Then, by measuring the frequency of the transition between another pair of Zeeman sub-levels (e.g. $|F=1, m_F=0\rangle$ and $|F=2, m_F=1\rangle$) and by comparing it to the clock frequency reference, one can access to the static magnetic field amplitude B seen by the trapped atoms, and compensate the residual components transverse to the quantization axis with external coils, as we will see in Sec. 3.2.

3.2 Cancellation of residual magnetic fields with microwave spectroscopy

In this section, we describe the setup that we implemented to apply microwaves inside the vacuum chamber, and thus allow to perform the spectroscopy of the ground states in order to compensate for static magnetic fields.

3.2.1 Magnetic dipole transitions between hyperfine ground states

Spectroscopy of the internal ground states of ^{87}Rb atoms can be performed by driving transitions between the hyperfine levels $F=1$ and $F=2$. These two states are spherically symmetric S states such that direct electric dipole coupling is zero. However, coherent transitions can be driven by magnetic dipole interactions in the microwave regime using time-dependent magnetic fields of the form:

$$\vec{B}(t) = B \cos(\omega t) \vec{\epsilon}, \quad (3.4)$$

where B is the magnetic field amplitude, $\omega/2\pi$ is the driving microwave frequency, and $\vec{\epsilon}$ is the polarization of the magnetic field. Such transitions are commonly used in atomic physics experiments to manipulate the state of qubits encoded onto two Zeeman sub-levels of an atom hyperfine ground states. The orbital momentum L is zero for ground states, so the interaction hamiltonian \hat{H}_B from Eq. 3.1 simplifies to:

$$\hat{H}_B(t) = \frac{\mu_B B}{\hbar} \cos(\omega t) (2\hat{S}) \cdot \vec{\epsilon}, \quad (3.5)$$

Microwave π -transitions are obtained when the polarization of the magnetic field $\vec{\epsilon}$ is linear and aligned along the quantization axis z . The interaction hamiltonian is proportional to \hat{S}_z , and the matrix elements of $\hat{H}_B(t)$ can be calculated between two Zeeman sub-levels expressed in the basis $\{m_I, m_J\}$. The calculation of the coupling between the two clock states gives:

$$H_B^{0 \rightarrow 0}(t) = \langle F=1, m_F=0 | \hat{H}_B(t) | F=2, m_F=0 \rangle \simeq \mu_B B_0 \cos(\omega t). \quad (3.6)$$

¹Indeed, this clock transition frequency depends on the magnetic field amplitude only to second order as 575.15 Hz/G^2 . Before cancellation, the ambient magnetic field is on the order of 1 G such that the frequency shift of the clock transition is below 1 kHz.

The Rabi frequency of the clock transition $\Omega = \mu_B B_0 / \hbar$ is thus proportional to the magnetic field amplitude B_0 at the atoms position.

Similar calculations can be conducted to compute the coupling strengths of the other two π transitions $|F=1, m_F=-1\rangle \rightarrow |F=2, m_F=-1\rangle$ and $|F=1, m_F=+1\rangle \rightarrow |F=2, m_F=+1\rangle$, leading to similar expressions with prefactors $\sqrt{3}/2$. Coupling strengths of σ -transitions can also be calculated in a similar way. The polarization $\vec{\epsilon}$ of the magnetic field is then chosen to be σ^+ or σ^- in Eq. 3.5. In the end, the coupling strengths and the corresponding Rabi frequencies are also proportional to the magnetic field amplitude B_+ and B_- respectively associated to σ^+ and σ^- polarizations, such as in Eq. 3.6, with prefactors on the order of unity.

However in practice in our vacuum chamber, the magnetic field structure at the position of the atoms is strongly modified by the metallic support of the lens holders (see Sec. 1.2.2). The theoretical expressions of the coupling strengths such as the ones shown in Eq. 3.6 can be used to find relevant orders of magnitude for the expected Rabi frequencies of each microwave transition, although the amplitudes B_0 , B_+ and B_- seen by the atoms could not be estimated much better than within a factor two or three as we will show in Sec. 3.2.4.

3.2.2 Hyperfine ground states detection scheme

The manipulation of the atoms internal state require to implement state-dependent detection schemes allowing to discriminate between the several possible states the atom can occupy. Ideally, one would want to be able to distinguish all possible Zeeman sub-levels by performing non-destructive measurements of each internal state. In practice, this can be achieved only for certain well chosen states. In a similar experimental configuration of a single atom in a microscopic optical dipole trap in vacuum, Fuhrmanek *et al.* (2011) demonstrated such a scheme for the Zeeman state $|5S_{1/2}, F=2, m_F=2\rangle$ by using an optical non destructive fluorescence measurement with a probe resonant on the cycling transition $|5S_{1/2}, F=2, m_F=2\rangle \rightarrow |5P_{3/2}, F=3, m_F=3\rangle$. Enough scattered photons can then be detected before the atom is heated up out of the trap. Similar schemes were also implemented in cavity QED experiments where the strong coupling between atoms and photons increases the efficiency of the scattered photons collection (Bochmann *et al.*, 2010).

However, a destructive but simpler detection scheme can be easily implemented to discriminate between the two hyperfine ground states $F=1$ and $F=2$ using a push-out technique (Kuhr *et al.*, 2003). It is based on the hyperfine state-selective loss of the atom when it is illuminated by a laser with σ^+ polarization and resonant on the cycling transition $|5S_{1/2}, F=2, m_F=2\rangle \rightarrow |5P_{3/2}, F=3, m_F=3\rangle$. For this, we use in our experiment the same vertical 780 nm probe beam as described in Sec. 2.3.4, with a high saturation parameter $I/I_{\text{sat}} \simeq 3$. If the atom is initially prepared in any Zeeman sub-levels of the ground state $|5S_{1/2}, F=1\rangle$ when the push-out beam is sent, then the beam detuning is about 1000Γ off-resonance such that the atom scatter almost no photon ($\Gamma_{\text{sc}} \simeq 1.5 \text{ s}^{-1}$) and stays at the bottom of the trap. However if the atom is in any Zeeman sub-level of $|5S_{1/2}, F=2\rangle$, the push-out beam quickly pumps the atom into the cycling transition where it scatters many photons and is heated up out of the trap². We calibrated the detection efficiency by measuring the recapture rate after initializing the hyperfine state either into $F=1$ or $F=2$ and sending the push-out beam. The experimental sequence is similar to the one illustrated in

²Each scattered photon increases the mean thermal energy of the atom by $2E_{\text{rec}}$, which corresponds in temperature unit to about 700 nK. In a trap of typical depth $U_0/k_B = 1 \text{ mK}$, the atom needs to scatter about $1000/0.7 \simeq 1500$ photons to be ejected from the trap.

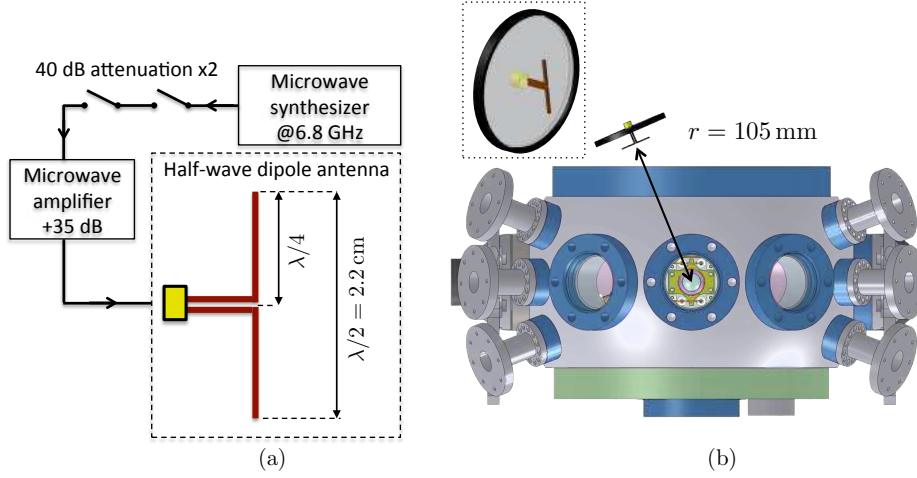


Figure 3.1: Microwave generation setup. (a) Schematic of the microwave circuits which includes the layout of the antenna. (b) Positioning of the antenna.

the next paragraph in Fig. 3.2, without the microwave pulse. After the detection of a single atom, the initialization in $F = 1$ (resp. $F = 2$) is performed by keeping only the molasses cooling beams (resp. the repumper beams) for about 10 ms. After applying the push-out pulse for 2.5 ms, we found the typical following recapture rate averaged over 200 sequences:

$$\begin{aligned} \text{Initial preparation in } F = 1: & \quad P_{\text{recap}} = 96\% \\ \text{Initial preparation in } F = 2: & \quad P_{\text{recap}} = 2\%. \end{aligned} \quad (3.7)$$

3.2.3 Setup for the microwave generation

The circuit that we used for the microwave signals generation is shown in Fig. 3.1(a). The microwave frequency at about 6.835 GHz is delivered by a Rhode & Schwartz synthesizer that can be controlled via GPIB from the computer program. The microwave signal goes then to a 35 dB amplifier (from RFPFA) and then to a half-wave dipole antenna. Two fast microwave switches (2 ns, 40 dB attenuation) placed in series at the output of the synthesizer allow to switch on and off the microwave pulses efficiently.

The half-wave dipole antenna is shown in Fig. 3.1(a). It is formed by two quarter-wavelength conductors with length $d = \lambda/4 = c/4\nu = 1.1$ cm placed back to back for a total length of $L = 2d = \lambda/2 = 2.2$ cm. The conductors are mounted onto a 2 inches metallic back plate to redirect a fraction of the power emitted in the opposite direction by the antenna towards the vacuum chamber. Though the geometry of the antenna would only support a linear polarization, it turned out that the rather complex metallic environment inside the vacuum chamber created a mix of all possible polarization components at the position of the atoms.

The antenna was placed outside the vacuum chamber at a distance of about $r = 10.5$ cm as depicted in Fig. 3.1(b). In the far field and in the direction orthogonal to the antenna, the magnetic field can be estimated by:

$$B = \frac{Z_0 I_0}{2\pi c r} \simeq 6.7 \text{ mGauss}, \quad (3.8)$$

where $Z_0 = c \cdot \mu_0 \simeq 376.73$ Ohm is the impedance of free space, $r \simeq 105$ mm is the radial distance from the antenna, and I_0 is the maximum of the current distribution along the dipole

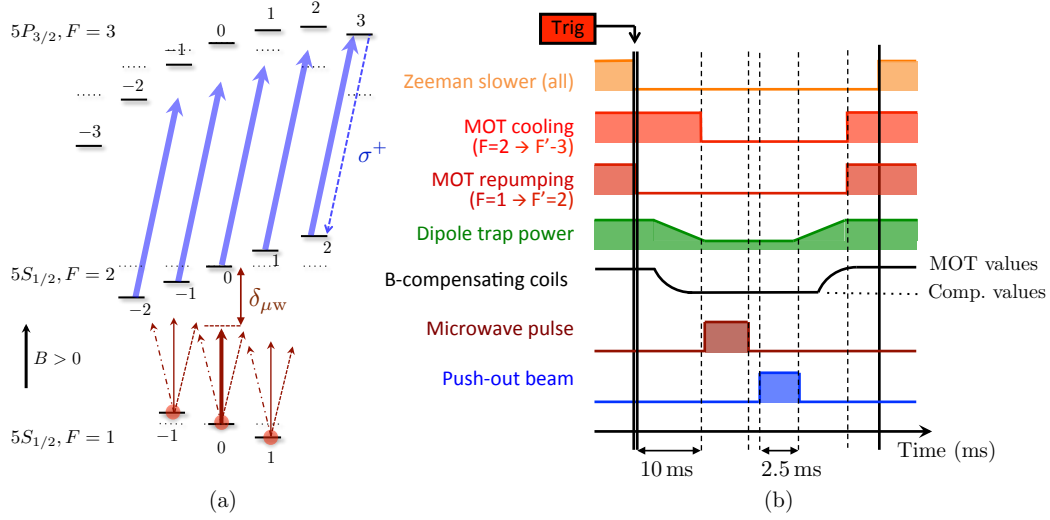


Figure 3.2: Ground state hyperfine level spectroscopy using microwaves. (a) Internal structure of the ^{87}Rb states $5S_{1/2}$ and $5P_{3/2}$. The closed transition $|5S_{1/2}, F=2, m_F=2\rangle \rightarrow |5P_{3/2}, F=3, m_F=3\rangle$ used for the push-out detection scheme is also represented. Dashed lines represent the energy levels in the presence of the dipole trap. Solid lines show the Zeeman energy shifts in the presence of an external magnetic field with amplitude $B > 0$ along the quantization axis. (b) Experimental sequence. The thick vertical black bar at $t=0$ ms symbolizes the initial atom presence checking procedure (step 1 in Fig. 2.2). The repumping beams are switched off first to provide an initial optical pumping into hyperfine ground state $F=1$, in which all Zeeman sub-levels are equally populated on average. The dipole trap power is lowered by a factor three to improve the push-out efficiency. In the middle of the sequence, a microwave pulse is optimized to transfer the population from $F=1$ to $F=2$ depending on the value of the external magnetic field provided by the compensation coils and on the microwave frequency $\omega/2\pi$.

length. The microwave power was about 35 dBm, corresponding to a current $I_0 \simeq \sqrt{2P/R} \simeq 350$ mA for an optimal impedance of $R=50 \Omega$.

As we already mentioned, the polarization of the magnetic field at the position of the atoms is a mixture of the three components π , σ^+ and σ^- due to the metallic complex environment. Assuming that a third of the total amplitude B contributes to each polarization component, we could use Eq. 3.6 to estimate the Rabi frequency expected for the clock transition:

$$\Omega^{0 \rightarrow 0} \simeq \frac{1}{3} \frac{\mu_B B}{\hbar} \simeq 2\pi \times 3 \text{ kHz}. \quad (3.9)$$

3.2.4 Zeeman shifts measurements

Experimental sequence

The experimental sequence is shown in Fig. 3.2. After the detection of a single atom, the magnetic field gradients and the repumper beams of the MOT are switched off while the cooling beams are kept on, which optically pumps the atom into the ground state hyperfine level $F=1$. At the same time, the compensation coils are commuted from the MOT optimizing values to the values required for the Zeeman spectroscopy. Then, a microwave pulse of frequency $\omega_{\mu w}/2\pi$ and duration t is sent onto the trapped atom. As the atom is initially prepared into the Zeeman sub-level $|F=1, m_F\rangle$, a coherent oscillation can be

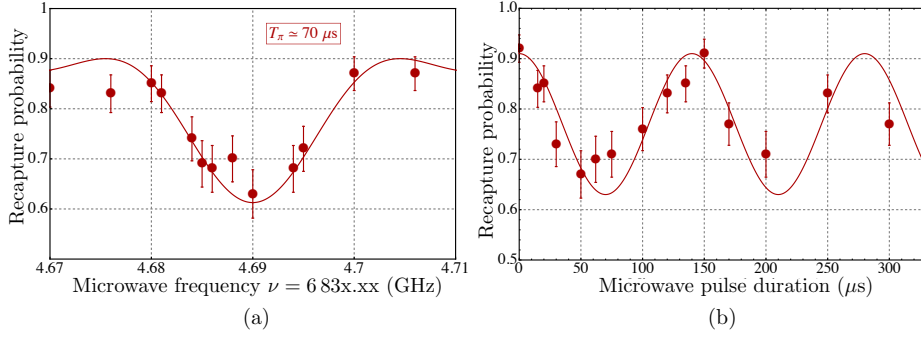


Figure 3.3: Clock transition spectroscopy. (a) Microwave frequency scan with a pulse duration of $70 \mu\text{s}$. (b) Coherent Rabi oscillations with a microwave center frequency $\nu_0 \simeq 6.834690 \text{ GHz}$. Each data point is an average result over 100 sequences. The solid lines are fits of the form $y_0 + A \cdot P_{|F=2, m_{F'}\rangle}(t)$.

driven towards another Zeeman sub-level $|F=2, m_{F'}\rangle$ separated by the energy $\hbar\omega_0$. The probability $P_{|F=2, m_{F'}\rangle}(t)$ to find the atom into the state $|F=2, m_{F'}\rangle$ after the microwave pulse of duration t is described by the Rabi formula:

$$P_{|F=2, m_{F'}\rangle}(t) = \frac{\Omega^2}{\Omega^2 + \delta_{\mu\text{w}}^2} \sin\left(\sqrt{\Omega^2 + \delta_{\mu\text{w}}^2} \frac{t}{2}\right)^2, \quad (3.10)$$

where Ω is the Rabi frequency corresponding to the microwave transition and $\delta_{\mu\text{w}} = \omega_{\mu\text{w}} - \omega_0$ is the pulse detuning from the resonance ω_0 .

After the microwave pulse, a push-out beam is sent during 2.5 ms on the atom to discriminate between the occupation of the hyperfine level, as it is described in Sec. 3.2.2. The discrimination is more efficient with lower power in the dipole trap, which is thus ramped down during all the sequence to about a third of the initial value. The last step is to check if the atom is present or not at the end of the sequence by performing a fluorescence measurement with initial MOT parameters.

Clock transition spectroscopy $|F=1, m_F=0\rangle \rightarrow |F=2, m_F=0\rangle$

We started with initial low values of current in the compensation coils $I_x = I_y = 0 \text{ A}$, and $I_z = 1 \text{ A}$, and looked for the almost unperturbed clock transition by scanning the microwave frequency near $\nu_{\text{HFS}} = 6.834682 \text{ GHz}$. Surprisingly, this transition was found for a microwave synthesizer frequency $\nu_0 \simeq 6.834690 \text{ GHz}$ which corresponds to a positive shift of 8 kHz from the theoretical clock transition frequency (this shift was probably due to a bias in the microwave synthesizer calibration). Furthermore, the experimental Rabi frequency $\Omega \simeq 2\pi \times 7 \text{ kHz}$ was twice as big as the value expected from Eq. 3.9.

Fig. 3.3(a) shows the recapture probability as a function of the microwave pulse frequency for an optimized pulse duration of $60 \mu\text{s}$. We checked that we could drive coherently the transition by performing a Rabi oscillation measurement at the microwave frequency ν_0 as shown in Fig. 3.3(b). The oscillation drops only from 95 % to about 65 % because the atom internal initial state is equally spread over the three Zeeman sub-levels $m_F = -1$, $m_F = 0$ and $m_F = +1$ before the microwave pulse. Out of 100 sequences realizations, only a third of the atoms participated effectively to the oscillation.

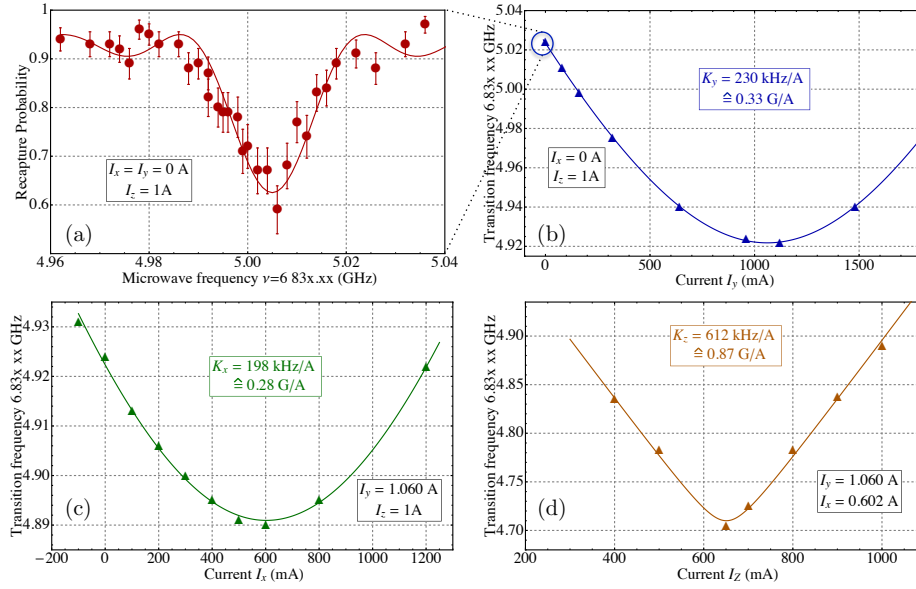


Figure 3.4: Zeeman shifts measurements using microwave spectroscopy. (a) Microwave frequency scan with a pulse duration of $50\ \mu\text{s}$. The solid line is a fit of the form $y_0 + A \cdot P_{|F=2, m_{F'}\rangle}(|F=1, m_F=0\rangle, t)$. (b) (c) and (d) show the frequency of the transition $|F=1, m_F=0\rangle \rightarrow |F=2, m_{F'}=1\rangle$ as a function of the current in the pair of compensation coils x , y and z . The solid lines are hyperbolic fits of the form $\nu_{\text{HFS}} + \sqrt{\Delta\nu(B_{\text{res}})^2 + K_i^2(I_i - I_{i0})^2}$ for $i = x, y, z$.

Spectroscopy of the transitions $|F=1, m_F=0\rangle \rightarrow |F=2, m_F=1\rangle$ and $|F=1, m_F=1\rangle \rightarrow |F=2, m_F=0\rangle$

Next, we kept the same microwave pulse duration $T = 70\ \mu\text{s}$ and we scanned the microwave frequency to look for the other microwave transitions. We found the first one around $\nu_0 + \delta\nu$ with $\delta\nu \simeq 320$ kHz (scan shown in Fig. 3.4(a)), and other transitions at $\nu_0 + 2\delta\nu$ and $\nu_0 + 3\delta\nu$ proving that the microwave pulse contained all polarizations. The transition at $\nu_0 + \delta\nu$ corresponded then to the two possible transitions $|F=1, m_F=0\rangle \rightarrow |F=2, m_F=1\rangle$ or $|F=1, m_F=1\rangle \rightarrow |F=2, m_F=0\rangle$ (see the Zeeman shifts structure in Fig. 3.2(a)) which are both sensitive to first order Zeeman effect by 700 kHz/Gauss. Then, we tuned the values of the currents in the compensation coils, and follow the peak frequency of these two transitions³. The results are shown in Fig. 3.4(b), (c) and (d) respectively for the pairs of compensating coils centered on the axes x , y and z of the experiment. The position of the line depends on the absolute value $B = |\vec{B}| = (B_x^2 + B_y^2 + B_z^2)^{1/2}$ of the external static magnetic field seen by the atoms. The evolution of the line position as a function of one of the B-field components is then an hyperbola. The slope K_i of their asymptote gives a calibration of the shift induced by the compensating coils in kHz/A which can then be converted into Gauss/A as the transition is known to shift by 700 kHz/Gauss. The slope coefficients K_i and the values of current I_i^0 to cancel the residual fields were:

$$\begin{aligned}
 K_y &= 230 \text{ kHz/A} \hat{=} 0.33 \text{ G/A} & \text{and} & & I_y^0 &= 1.06 \text{ A} \\
 K_x &= 198 \text{ kHz/A} \hat{=} 0.28 \text{ G/A} & \text{and} & & I_x^0 &= 0.60 \text{ A} \\
 K_z &= 612 \text{ kHz/A} \hat{=} 0.87 \text{ G/A} & \text{and} & & I_z^0 &= 0.65 \text{ A},
 \end{aligned} \tag{3.11}$$

³Starting from the value of the current for which the derivative was zero, we followed in fact the symmetric transitions $|F=1, m_F=0\rangle \rightarrow |F=2, m_F=-1\rangle$ or $|F=1, m_F=-1\rangle \rightarrow |F=2, m_F=0\rangle$.

where the experimental values of the slopes K_i are compatible with ab initio calculations based on Biot-Savart law within 5 %.

With the values of current I_x^0 , I_y^0 and I_z^0 , one can see in Fig. 3.4(d) that we could decrease the residual relative frequency shift from the measured clock frequency ν_0 down to about 10 kHz, which corresponds to a residual magnetic field of 14 mGauss. This residual shift could possibly be due to dynamic rotating magnetic fields at 50 Hz caused by the electronic devices around the vacuum chamber. Afterwards, we implemented the possibility to synchronize the experiments with the mains at 50 Hz. Unfortunately, we have not repeated the microwave spectroscopy measurements with this synchronization. However, we tried to observe signs of improvements with the Raman spectroscopy setup developed later on during the thesis and described in the next section.

3.3 Stimulated Raman transitions

In this section, we describe the Raman laser system at 795 nm inspired by A. Gaëtan's thesis work on the former experimental apparatus which we also implemented on the new Rydberg experiment. This laser system allows to coherently manipulate the internal state of the qubit:

$$|0\rangle = |5S_{1/2}, F=1, m_F=1\rangle \quad \text{and} \quad |1\rangle = |5S_{1/2}, F=2, m_F=2\rangle. \quad (3.12)$$

3.3.1 Choice of the qubit

The two-level quantum system presented above has good properties to be chosen as a qubit:

- First of all, the two states of a qubit should be very long lived states. In the case of alkali atoms such as rubidium, the internal ground state is always composed of two very long-lived hyperfine levels separated by several gigahertz which are typically in the reach of microwave or two-photon optical Raman transitions.
- The two qubit states can be chosen either from the same hyperfine ground state, or from the two different alkali hyperfine states. In the first case, common detection schemes relying on state-dependent scattering of photons are not suited because the two states have almost the same energy and the scattered photons are hard to discriminate in the frequency domain. More elaborated techniques based on polarization detection (Volz *et al.*, 2006) can be implemented. We preferred to work in the more simple configuration of two qubit states from the two distinct hyperfine levels.
- The most natural choice would be to work with the two clock states $|F=1, m_F=0\rangle$ and $|F=2, m_F=0\rangle$ which are insensitive to magnetic field fluctuations to first order, as described in Sec. 3.1, and thus have longer coherence time. This solution was investigated by J. Beugnon during his thesis. However, among the other possible qubit states combination, we chose two for which the initialization can be performed by using optical pumping, as it is the case for the states of Eq. 3.12, and for which the state $|\uparrow\rangle = |1\rangle = |5S_{1/2}, F=2, m_F=2\rangle$ can be coupled to the Rydberg states $|nD, F=3, m_F=3\rangle$ with large angular coefficients.

On our setup, the state of this qubit can be manipulated by using either microwave or two-photon Raman transitions. The real advantage of the second technique is that the Rabi

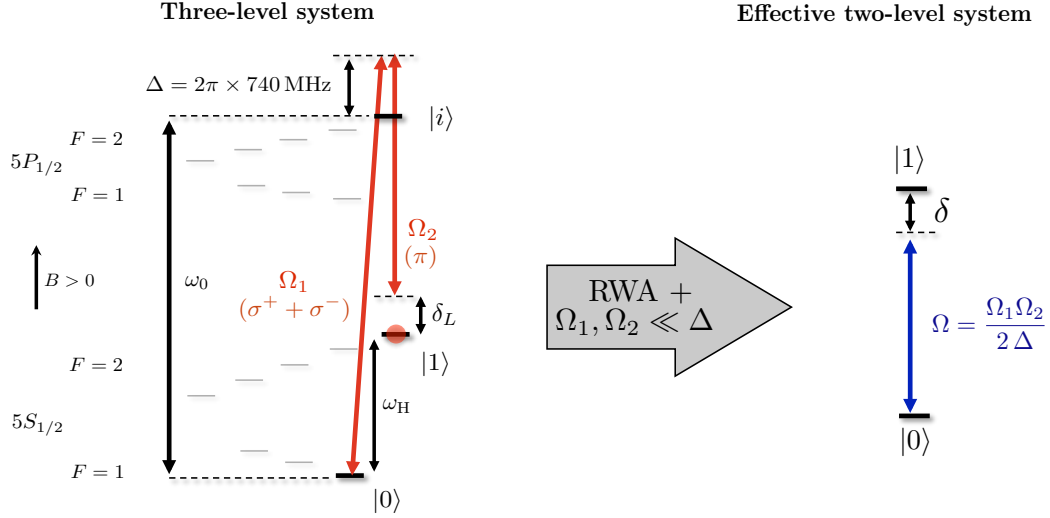


Figure 3.5: Two-photon Raman transitions.

frequencies that can be reached (above 10 MHz in [Yavuz *et al.* \(2006\)](#); [Jones *et al.* \(2007\)](#)) are much higher than the ones typically achieved by microwave radiations (10 kHz in our experiment, up to few hundreds of kHz in [Moehring *et al.* \(2007\)](#)). Such fast manipulation (less than 1 μs) allows to overcome the qubit decoherence time (on the order of 1 ms).

3.3.2 Two-photon electric-dipole transitions

Manipulation of the internal ground state of ^{87}Rb atoms can be performed by driving coherent two-photon electric-dipole transitions. Two main examples of such transitions implemented in this thesis are the Rydberg excitations and the Raman transitions between two Zeeman sub-levels of the hyperfine ground states, as described below. We will only sum up the main properties for these transitions and we will refer to [Bonin and McIlrath \(1984\)](#) for a more detailed description.

Let us consider the three-level system in the lambda configuration shown in Fig. 3.5. The states $|0\rangle = |5S_{1/2}, F=1, m_F=1\rangle$ and $|1\rangle = |5S_{1/2}, F=2, m_F=2\rangle$ are separated by the energy $\hbar\omega_H$, and the intermediate excited state $|i\rangle = |5P_{1/2}, F=2, m_F=2\rangle$ has an energy $\hbar\omega_0$ and a finite decay rate Γ . This system interacts with two 795 nm laser fields $\vec{\mathcal{E}}_1$ and $\vec{\mathcal{E}}_2$ with frequencies ω_1 and ω_2 , coupling respectively the states $|0\rangle$ and $|1\rangle$ to the intermediate state $|i\rangle$ with the Rabi frequencies Ω_1 and Ω_2 (defined as real numbers). We define the detunings $\Delta = \omega_1 - \omega_0$ and $\delta_L = \omega_1 - \omega_2 - \omega_H$.

Though direct electric dipole coupling is zero between the two hyperfine ground states $F=1$ and $F=2$, the two qubit states $|0\rangle$ and $|1\rangle$ can be coupled by the electric dipole hamiltonian at second order. In our case for which the rotating wave approximation is valid ($|\Delta| = 2\pi \times 740 \text{ MHz} \ll \omega_{1,2} \simeq 2\pi \times 10^{14} \text{ Hz}$) and for large detunings $\Delta \gg \Omega_{1,2}, \Gamma$, the three-level system can be reduced to an equivalent two-level system with the states $|0\rangle$ and $|1\rangle$. The effective Rabi frequency Ω and the effective detuning δ are:

$$\Omega = \frac{\Omega_1 \Omega_2}{2 \Delta} \quad \text{and} \quad \delta = \delta_L - \left(\frac{\Omega_1^2}{4 \Delta} - \frac{\Omega_2^2}{4 \Delta} \right), \quad (3.13)$$

where the terms $\Omega_1^2/(4\Delta)$ and $\Omega_2^2/(4\Delta)$ correspond to the light shifts of the states $|0\rangle$ and $|1\rangle$ induced by the laser fields $\vec{\mathcal{E}}_1$ and $\vec{\mathcal{E}}_2$ respectively. During the transition, the relative phase

of the two Raman beams has to remain stable (a phase lock setup is described in Sec. 3.3.3). Then, assuming that the system is initially prepared into the state $|1\rangle$, the probability $P_{|0\rangle}(t)$ to find it in state $|0\rangle$ after applying the two-photon excitation for a duration t is described by the Rabi formula:

$$P_{|0\rangle}(\delta, t) = \frac{\Omega^2}{\Omega^2 + \delta^2} \sin\left(\sqrt{\Omega^2 + \delta^2} \frac{t}{2}\right)^2. \quad (3.14)$$

A more accurate model based on the optical Bloch equations formalism would allow to take into account the spontaneous scattering rate Γ_{sc} due to the state $5P_{1/2}$, which reads in this case:

$$\Gamma_{\text{sc}} = \Gamma \left(\frac{\Omega_1^2}{4\Delta^2} + \frac{\Omega_2^2}{4\Delta^2} \right). \quad (3.15)$$

This scattering rate is responsible for decoherence in the effective two-level system and it leads to a damping of the Rabi oscillations. However, for the typical laser power at 795 nm that we used in the various Raman experiments presented below, the Rabi frequencies Ω_1 and Ω_2 were smaller than $2\pi \times 50$ MHz with a detuning $\Delta = 2\pi \times 740$ MHz. The ratio between the induced scattering rate Γ_{sc} and the effective Rabi frequency Ω was then smaller than 3% and most of the data are very well fitted without including a damping term.

3.3.3 Laser system at 795 nm

Laser diodes

The layout of the Raman laser system is shown in Fig. 3.6(a). The two laser beams at 795 nm used to perform the Raman transitions are produced by two distinct grating-stabilized external cavity diode lasers (module DL100, from Toptica[®]), labeled respectively $F=1$ and $F=2$. Each laser diode has a typical output power of 100 mw. A built-in 35 dB optical isolator allows to suppress possible back reflections towards the diode. The output mode is good enough to get about 40% coupling efficiency into PM single mode fibers without using mode-matching telescopes.

Phase lock

The frequency of laser diode $F=2$ is stabilized using an external Fabry-Perot cavity and a standard saturated absorption spectroscopy setup, as it is described in Sec. 4.2.3. This allows to maintain the residual fluctuations of the detuning Δ below about 100 kHz for several hours.

Then, the relative frequency and phase of the two Raman lasers are stabilized using a beatnote lock. As shown in Fig. 3.6(a), a beam with frequency ν_1 coming from the diode $F=1$ is combined with a beam with frequency ν_2 coming from the diode $F=2$ using a PBS cube. The two beams are projected onto the same polarization with a half-wave plate and a second PBS cube used as a polarizer before they are sent onto a fast photodiode. The layout of the feedback loop electronics is shown in Fig. 3.6(b). The beatnote signal from the photodiode of frequency $\delta/2\pi = \nu_1 - \nu_2 \simeq 6.834$ GHz is sent to a first microwave mixer together with a very stable microwave reference delivered by a microwave synthesizer (from Rohde & Schwarz). The frequency of the microwave reference signal has to be shifted by 10 MHz from the targeted frequency lock point $\nu_{\text{ref}} \simeq 6.834 + 0.01$ GHz.

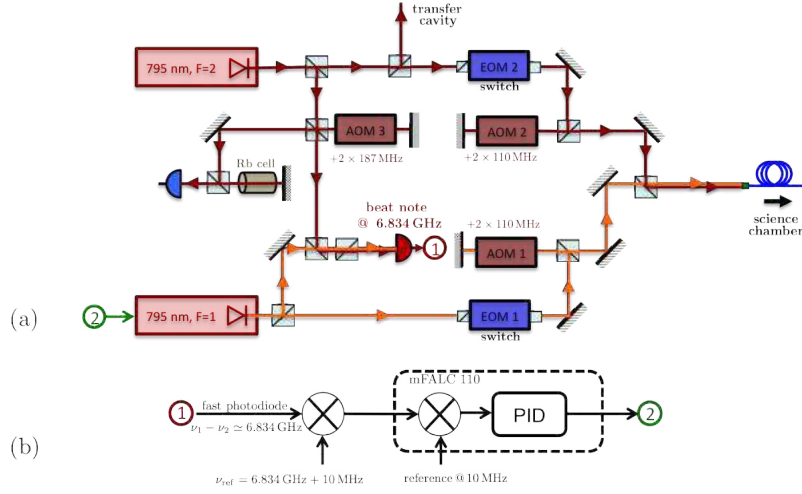


Figure 3.6: Layout of the Raman optical setup. (a) Schematics of the Raman optical table. (b) Microwave circuits used for the beatnote lock.

The output signal of the first mixer thus beats at about $\nu_{\text{beat}} \simeq 10 \text{ MHz}$. Then we used a commercial locking module (the Fast Analog Linewidth Control module – mFALC 110 – from Toptica[®]) designed for fast phase locking of two lasers to an external microwave reference. Inside the module, a second microwave mixer combines the output of the first mixer with the stable 10 MHz output from the synthesizer reference oscillator (at the rear of the device), and delivers a sinusoidal error signal at the frequency difference $\nu_{\text{beat}} - 10 \text{ MHz}$. After passing through several PID controllers, the error signal is sent back to the Bias Tee current input of the laser diode $F = 1$, enforcing the frequency ν_1 to fulfill the condition $\nu_{\text{beat}} - 10 \text{ MHz} = 0$, e.g. $\nu_1 - \nu_2 = \nu_{\text{ref}} \pm 10 \text{ MHz}$. The bandwidth of the phase-locked loop module is about 10 MHz, which is bigger than the typical linewidth of the two diode lasers (about 100 kHz) and makes the lock possible. Once locked, the 3-dB linewidth of the beatnote signal was measured below 100 Hz (limited by the resolution bandwidth of the spectrum analyser⁴).

Finally, the relative frequency between the two Raman beams is adjusted by tuning the microwave frequency of the synthesizer, controlled by the computer via a GPIB port.

Raman pulse shaping

Each Raman beam goes through a fast electro-optical modulator⁵ (EOM 1 and 2) and a double pass acousto-optic modulator (AOM 1 and 2) before being combined on a PBS cube and coupled into a PM fiber. The EOM module consists in a birefringent crystal through which the laser beam polarization is rotated proportionally to an external DC voltage ($\simeq 250 \text{ V}$). The EOM crystals are placed between two crossed polarizers (Glan-Thompson) and the orientations of their axes are optimized in order to switch on and off the laser beams with typical switching times of 5-10 ns and with an attenuation⁶ of about 50 dBm. The double pass AOMs (order +1) are used also as switches to reach an almost perfect extinction ($> 70 \text{ dB}$). The AOMs 1 and 2 are driven by the same RF synthesizer at 110 MHz.

⁴Anritsu MS2602A.

⁵Linos LM202.

⁶The attenuation was measured at the output of the fiber.

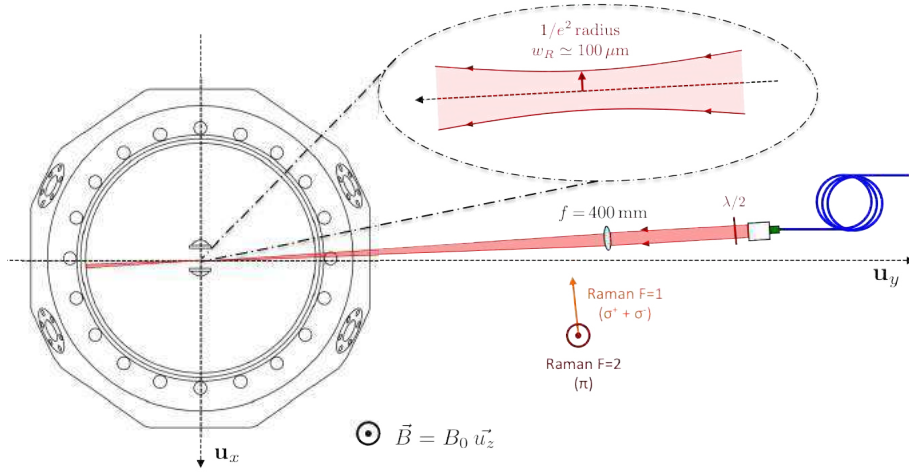


Figure 3.7: Alignment of the Raman beams inside the chamber.

After a double pass in AOM 3 driven at 187 MHz by a fourth RF synthesizer⁷, the Raman laser $F = 2$ is locked onto the saturated absorption peak $|5S_{1/2}, F = 3\rangle \rightarrow |5P_{1/2}, F = 2 \text{ co } 3\rangle$ of the isotope ^{85}Rb . This peak is blue-shifted from the resonance $|5S_{1/2}, F = 2, m_F = 2\rangle \rightarrow |5P_{1/2}, F = 2, m_F = 2\rangle$ in ^{87}Rb by about 884 MHz. So, the resulting one-photon detuning is $\Delta = 884 - 2 \times 187 + 2 \times 110 = 740$ MHz.

Finally, the two Raman beams are brought to the science chamber via the PM fiber as shown in Fig. 3.7. A half-wave plate is used to align the polarization of the Raman diode $F = 2$ along the vertical axis. As the two beams have orthogonal polarizations, the second one is linearly polarized in the horizontal xy plane, which corresponds to a polarization of the form $\sigma^+ + \sigma^-$ and not only σ^+ . However, in the three-level lambda configuration described in Fig. 3.5, one can see that in the presence of B , no state from $5P_{1/2}$ can contribute to a σ^- transition once the initial state of the atom is prepared into $|1\rangle$. This is true as long as the magnetic field amplitude is large enough such that the effective two-photon detuning $\delta' = 2\pi \times 1.4$ MHz/G from the transition $|5S_{1/2}, F = 1, m_F = 1\rangle \rightarrow |5S_{1/2}, F = 2, m_F = 0\rangle$ is large compared to the effective two-photon Rabi frequency Ω' coupling these two states. The coupling Ω' is four times smaller (smaller angular matrix elements) than the coupling Ω corresponding to $|5S_{1/2}, F = 1, m_F = 1\rangle \rightarrow |5S_{1/2}, F = 2, m_F = 2\rangle$. Thus, to operate with $\Omega/2\pi$ up to 1 MHz, e.g. $\Omega'/2\pi$ up to 250 kHz, one needs to apply a magnetic field of 1 G, ensuring $\Omega' \leq \delta'/10$.

Half of the power of the beam $F = 1$ with the polarization σ^+ is useful in this configuration, the other half only contributes very slightly to heating the atom. After the half-wave plate, the two Raman beams are focused by a plano-convex lens with focal length $f = 400$ mm. At the atom position, they have a waist of about $100 \mu\text{m}$.

3.3.4 Raman spectra of the transition $|F = 2, m_F = 2\rangle \rightarrow |F = 1, m_F = 1\rangle$

Experimental sequence

The experimental sequence realized to perform the Raman transitions was very similar to the one used for the microwave spectroscopy of the ground state structure in Sec. 3.2.4, except that the state of the atom was initially optically pumped into the state $|1\rangle$. The

⁷This fourth RF frequency synthesizer is also phase-locked to the master synthesizer.

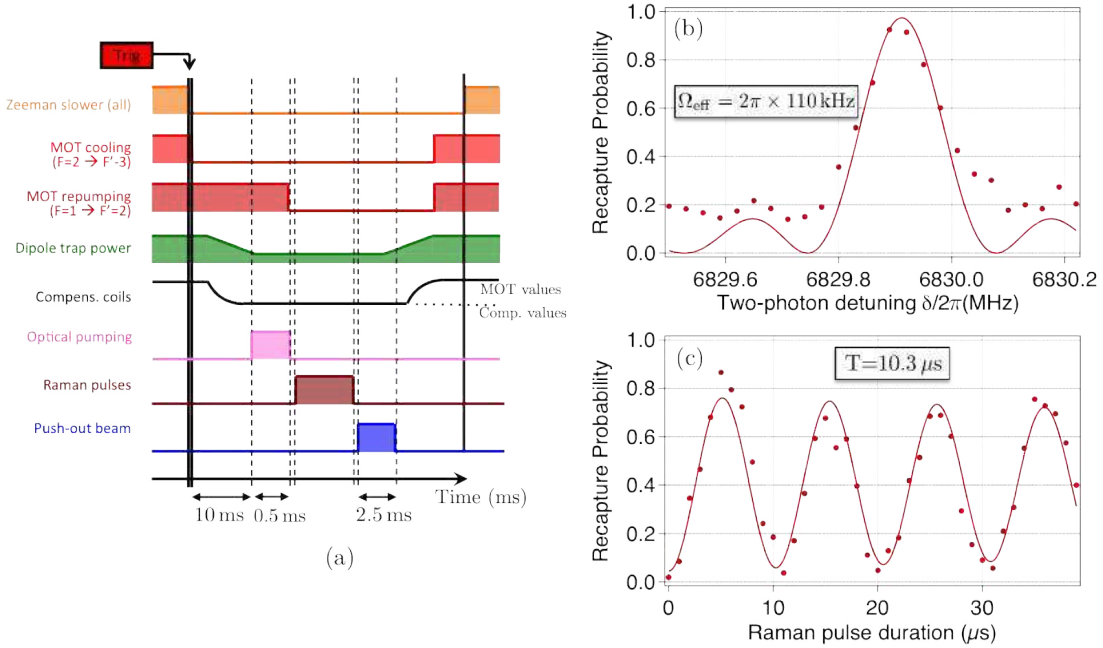


Figure 3.8: Raman spectroscopy measurements. (a) Experimental sequence. (b) Spectrum of the transition $|F=2, m_F=2\rangle \rightarrow |F=1, m_F=1\rangle$. The duration of the pulse was $5 \mu\text{s}$. (c) Rabi oscillation at the peak frequency 6829.9 MHz. Each data point of (b) and (c) is an average result over 100 experiments. The solid lines are fits of the form $y_0 + A \cdot P_{|0\rangle}(\delta, t)$, see Eq. 3.14.

sequence is shown in Fig. 3.8(a). We used the values of current obtained in the last section to optimize the cancellation of the residual transverse magnetic field. The vertical magnetic field was about -2.2 G .

The optical pumping beam is derived from the main laser system at 780 nm. It goes through a single-pass AOM (order -1) to be near-resonant with the transition $5S_{1/2}, F=2 \rightarrow 5P_{3/2}, F=2$. Then it is combined with the probe beam using a PBS cube and thus coupled into the same PM fiber that goes to the vacuum chamber table. There, both beams are projected onto the same polarization axis using a half-wave plate at 45° and a PBS cube used as a polarizer. Finally, they are combined with one vertical cooling beam of the MOT on a PBS cube and they all go through the same quarter-wave plate after which the probe and the optical pumping beams become σ^+ -polarized. At the atoms position, the optical pumping beam has a $1/e^2$ radius of 1 mm. We used typically $5 \mu\text{W}$ during about $500 \mu\text{s}$ to pump initially the atom into the dark state $|5S_{1/2}, F=2, m_F=2\rangle$.

After the optical pumping step, the Raman pulse of two-photon detuning δ and duration t was sent to the trapped atom. Finally, the same detection scheme as described in Sec. 3.2.2 allowed to discriminate in which hyperfine level the atom was after the Raman pulse.

The first experimental spectrum of the transition $|F=2, m_F=2\rangle \rightarrow |F=1, m_F=1\rangle$ that we realized is shown in Fig. 3.8(b). The laser powers into the beams $F=1$ and $F=2$ were respectively $6 \mu\text{W}$ and $12 \mu\text{W}$ (only half of it is useful) focused on a waist $w = 100 \mu\text{m}$ which corresponds to Rabi frequencies $\Omega_1 \simeq \Omega_2$ on the order of $2\pi \times 20 \text{ MHz}$. Using Eq. 3.13, the expected effective Rabi frequency Ω was estimated at about $2\pi \times 120 \text{ kHz}$, close to the measured value. During this measurement, the push out beam at 780 nm had not enough power, which explains why the recapture probability does not decrease below 0.2 even far away from the resonance. We quickly fixed the problem for the Rabi oscillation measurements taken at

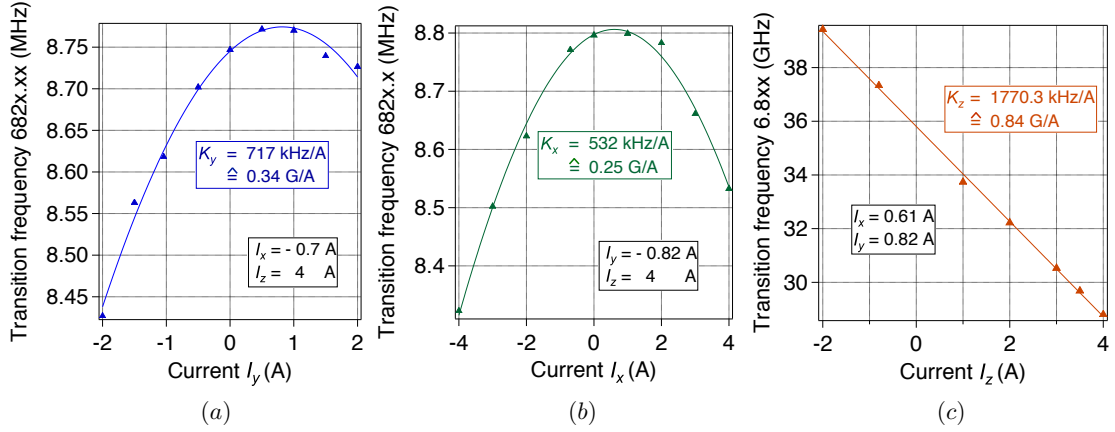


Figure 3.9: Zeeman shifts measurements using Raman spectroscopy. (a) (b) and (c) show respectively the frequency of the Raman transition $|F=2, m_F=2\rangle \rightarrow |F=1, m_F=1\rangle$ as a function of the current in the compensation coils x , y and z . The solid lines in (a) and (b) are hyperbolic fits of the form $\nu_{\text{HFS}} + \sqrt{\Delta\nu(B_{\text{res}})^2 + K_i^2(I_i - I_{i_0})^2}$ for $i = x, y, z$. The solid line in (c) is a linear fit.

the peak frequency of the spectrum as shown in Fig. 3.8(c). The contrast was not yet close to unity. It was improved later by finely tuning the polarization of the optical pumping beam (see Sec.3.3.5).

Zeeman shifts measurements

The Raman spectroscopy could be used as a second method to measure the residual transverse magnetic fields. The transition $|F=2, m_F=2\rangle \rightarrow |F=1, m_F=1\rangle$ shifts linearly with the magnetic field with a slope of 2.1 MHz/Gauss (see Sec. 3.1). We measured the frequency of the Raman transition as a function of the values of current in the coils. The results are shown in Fig. 3.9. In Tab. 3.1, we compare the results found with this method to the ones obtained with the microwaves. As expected, the values of the slopes K_i agree rather well, within 5-10%. However, the values of currents to cancel properly the transverse magnetic fields (mainly I_y^0) seemed to have been slightly modified, which could be due to new positioning of electrical devices around the chamber in the time between the two sets of measurements.

Axis	Microwave spectroscopy	Raman spectroscopy
x	$K_x = 198 \text{ kHz/A}$ (0.28 G/A) $I_x^0 = 0.6 \text{ A}$	$K_x = 532 \text{ kHz/A}$ (0.25 G/A) $I_x^0 = 0.61 \text{ A}$
y	$K_y = 230 \text{ kHz/A}$ (0.33 G/A) $I_y^0 = 1.06 \text{ A}$	$K_y = 717 \text{ kHz/A}$ (0.34 G/A) $I_y^0 = 0.82 \text{ A}$
z	$K_z = 612 \text{ kHz/A}$ (0.87 G/A) $I_z^0 = 0.65 \text{ A}$	$K_z = 1770 \text{ kHz/A}$ (0.84 G/A) $I_z^0 = 0.6 \text{ A}$

Table 3.1: Comparison between microwaves and Raman calibrations.

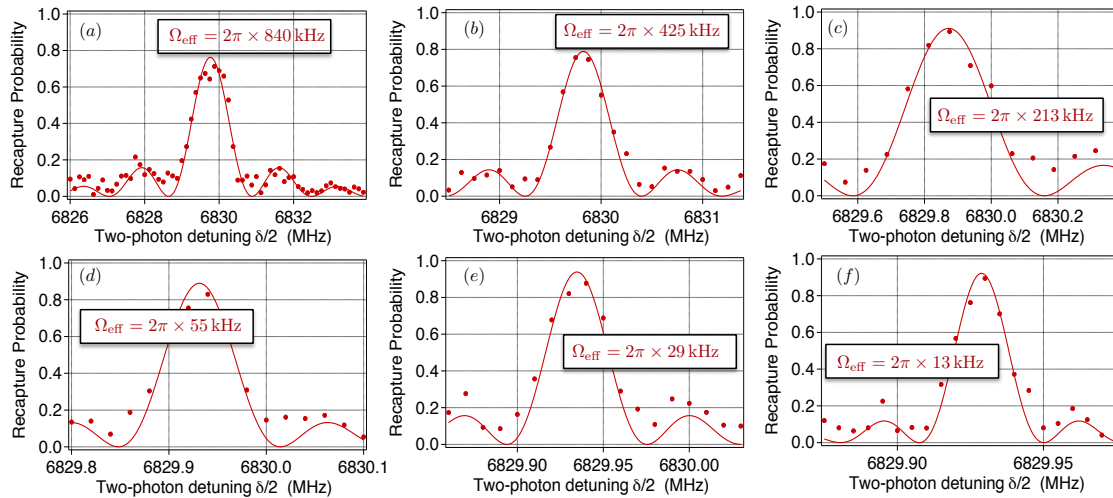


Figure 3.10: Spectra of the transition $|F=2, m_F=2\rangle \rightarrow |F=1, m_F=1\rangle$. From (a) to (b), the Rabi frequency $\Omega/2\pi$ is reduced from 840 kHz to 13 kHz. The solid lines are fits of the form $y_0 + A \cdot P_{|0\rangle}(\delta, t)$, see Eq. 3.14.

	Pulse duration	Expected linewidth	Measured linewidth
(a)	0.7 μs	715 kHz	835 kHz
(b)	1.4 μs	357 kHz	426 kHz
(c)	2.8 μs	178 kHz	213 kHz
(d)	10 μs	50 kHz	55 kHz
(e)	20 μs	25 kHz	29 kHz
(f)	40 μs	12.5 kHz	13 kHz

Table 3.2: Comparison between experimental and theoretical spectra linewidths.

Residual magnetic field fluctuations

The transition $|F=2, m_F=2\rangle \rightarrow |F=1, m_F=1\rangle$ shifts linearly with the magnetic field with a slope of 2.1 MHz/Gauss. Before optimizing the optical pumping, we tried to estimate the amplitude of residual magnetic field fluctuations present at the atoms position. For this, we reduced step by step the power in each Raman beam to reduce the effective Rabi frequency until the transition spectrum gets broadened by the field fluctuations. In Fig. 3.10, we show Fourier limited spectra of the transition for π -pulse duration up to 40 μs , which correspond to a Rabi frequency Ω of about $2\pi \times 13$ kHz. Table 3.2 sums up the results. For effective Rabi frequencies lower than 6 kHz, the contrast of the spectrum dropped below 0.7 and the fits gave linewidths always bigger than 9 kHz. With the sensitivity of the transition of 2.1 MHz/Gauss, we concluded that the residual magnetic field fluctuations were then on the order of $0.010/2.1 = 5$ mGauss.

These fluctuations were already rather small as compared to the Rabi frequency of the Raman transitions. However, by looking for the possible noise sources, we realized that all the measurements presented above were performed while eddy currents, due to the commutation of the compensation coils, were still running inside the science chamber. While these currents exponentially decay, the associated magnetic field contributes to the total Zeeman shift, which is not constant in time anymore. Thus, it could be worth to repeat the

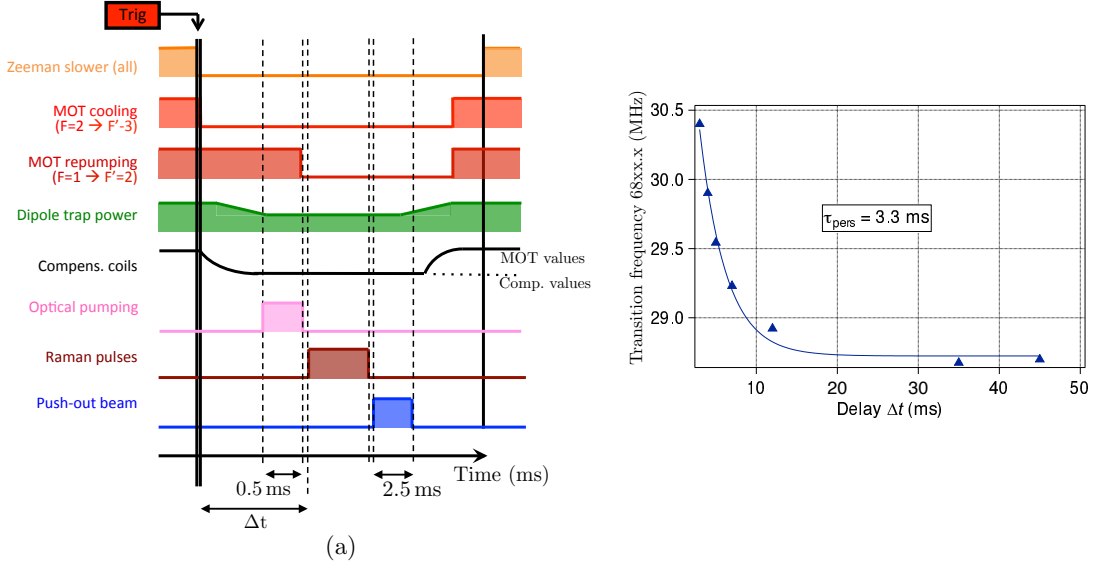


Figure 3.11: Persistent currents spectroscopy. (a) Experimental sequence. (b) Frequency of the transition as a function of the delay Δt between the commutation of the coils and Raman pulse. The solid line is a fit of the form $y_0 + A \exp(-t/\tau_{\text{pers}})$, with $A = 1.7$ MHz and $\tau_{\text{pers}} \simeq 3.3$ ms.

measurements presented above after a certain delay to ensure that these parasitic currents are negligible. Then, we anticipate residual magnetic field fluctuations to be even smaller than 5 mGauss.

Eddy currents

The commutation of the compensation coils in the middle of the sequence induces transient currents inside the science chamber (probably in the CF copper gaskets) which are not so short-lived. When we realized this, we actually used the Raman spectroscopy tool to measure the amplitude of the induced magnetic field B_{ind} which typically decays exponentially as a function of the delay Δt after the commutation. As shown in Fig. 3.11(a), the experimental sequence realized was almost identical as before. The values of the current $I_x = 0.61$ A, $I_y = 0.82$ A and $I_z = 4$ A were kept constant while we varied the delay Δt between the trigger of the coils commutation and the Raman pulse. The results are shown in Fig. 3.11(b).

The shift of the transition due to the eddy currents decays exponentially with a typical time $\tau_{\text{pers}} \simeq 3.3$ ms. The Raman experiments presented above were all performed at $\Delta t \simeq 10$ ms. At this time, the transition was still shifting by 25 kHz/ms. For the Raman spectrum with effective Rabi frequencies $\Omega/2\pi$ on the order of 5 kHz corresponding to a π -pulse of duration 100 μ s, the frequency of the transition was shifting during the measurement by 2.5 kHz = $\Omega/(2 \times 2\pi)$, which explains why the spectra we took were broadened and had a lower contrast.

In the following, we always used a delay on the order of 40 ms to avoid slow drifts of residual induced magnetic fields.

3.3.5 Optical pumping optimization

Finally, we optimized the contrast of the Rabi oscillations of the Raman transition, as shown in Fig. 3.12. After solving the issue related to the transient currents, we finely optimized

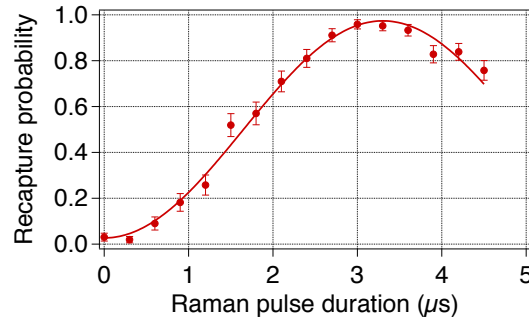


Figure 3.12: Optimized optical pumping efficiency. Rabi oscillation on the transition $|F=2, m_F=2\rangle \rightarrow |F=1, m_F=1\rangle$ realized after optimizing the optical pumping beam polarization. Each data point is an average result over 100 experiments. The solid line is a fit of the form $y_0 + A \cdot P_{|0\rangle}(\delta, t)$, see Eq. 3.14. The contrast of the oscillation is about 96 %.

the polarization of the optical pumping beam with a quarter-wave plate placed just after a PBS cube. The contrast of the Raman oscillation observed is about 96 %. Based on the typical readout efficiency of our hyperfine level detection scheme (see Sec. 3.2.2), this result is compatible with an optical pumping efficiency close to unity.

3.3.6 Conclusion

In this chapter, we showed how we could manipulate the internal ground state of the single atoms with either microwave radiations or two-photon Raman transitions. In particular, the efficiency of the optical pumping preparation in state $|5S_{1/2}, F=2, m_F=2\rangle$ was measured to be on the order of 96 %. These results were very promising to the implementation of coherent Rydberg excitations.

Chapter 4

Coherent excitation of a single atom towards Rydberg states

Contents

4.1	Rydberg states $nD_{3/2}, m_j = 3/2\rangle$	86
4.2	Excitation scheme	87
4.2.1	Two-photon transition	87
4.2.2	Laser systems	90
4.2.3	Transfer cavity lock	91
4.2.4	Rydberg pulse parameters	93
4.3	Experimental realization	95
4.3.1	Alignment of the beam at 795 nm	95
4.3.2	Alignment of the beam at 474 nm	96
4.3.3	Rydberg state detection	99
4.3.4	Spectra of Rydberg excitations	99
4.4	Cancellation of residual electric fields	101
4.4.1	Preliminary results without the ITO coating	101
4.4.2	Stark spectroscopy with single atoms	103
4.4.3	Coherent Rabi oscillations in compensated electric field	106
4.4.4	Conclusion	110

So far we have described how to trap and to detect a single atom of ^{87}Rb in a microscopic optical dipole trap (Chapter 1), how we implemented the computer control allowing to perform various experimental sequences with this atom (Chapter 2), and more specifically we showed that we were able to manipulate coherently the state of the qubit encoded onto the atom internal states $|5S_{1/2}, F = 1, m_F = 1\rangle = |0\rangle$ and $|5S_{1/2}, F = 2, m_F = 2\rangle = |1\rangle$ (Chapter 3). After optimization of the optical pumping as shown in Fig. 3.12, the typical contrast of the coherent Raman transition is higher than 96% and is compatible with a preparation efficiency in state $|1\rangle$ close to 100%. Towards the implementation of fast quantum gates as proposed in Jaksch *et al.* (2000); Möller, Madsen, and Mølmer (2008) and Müller *et al.* (2009), the next step was to demonstrate an accurate experimental control of coherent Rydberg excitations with our new apparatus.

In this Chapter, we start by describing briefly the Rydberg excitation scheme and the laser system that we implemented following the works of A. Gaëtan and C. Evellin on the former apparatus of the group. Then, we will present the typical spectroscopic measurements of $nD_{3/2}$ Rydberg excited states as well as the realization of coherent transitions towards these states. In particular, we will show that the conductive ITO coating deposited on the surfaces of the lenses facing the atoms turned out to be necessary to achieve a stable electric environment required for Rydberg states manipulation. Finally, we will show how we compensated for residual DC electric fields by performing Stark spectroscopy with the set of electrodes operating under vacuum. The possibility to cancel such parasitic fields proved to be a great tool to prevent Rydberg states mixing and thus improve the Rydberg blockade efficiency, as we will see in Sec. 5.2.5.

4.1 Rydberg states $|nD_{3/2}, m_j = 3/2\rangle$

All the Rydberg experiments presented in this thesis were performed using Rydberg states of the form¹ $|nD_{3/2}, m_j = 3/2\rangle$, with n ranging from 37 to 100. Such states can be used to implement quantum gates protocols based on the Rydberg blockade. Fig. 4.1 illustrates again the principle of the blockade, as presented in the introduction. Assuming that a laser source is used to drive the transition $|g\rangle \rightarrow |r\rangle$ with a Rabi coupling Ω , the first condition required to operate in the Rydberg blockade regime reads:

$$\Omega \ll \Delta E(R)/\hbar. \quad (4.1)$$

Then, in order to achieve coherent excitation with good efficiency, a second condition is to keep the effective lasers detuning from the resonance δ small compared to the Rabi coupling Ω :

$$\delta \ll \Omega. \quad (4.2)$$

For our experiments, the effective detuning can be fairly reduced by performing the Rydberg excitation in free space (dipole trap off). Indeed, if we did not, the single atoms would experience position dependent lightshifts that can vary from one experiment to another by a tenth of the trap depth, e.g. 1 or 2 MHz. Then, another limitation is set by the residual temperature of the atoms before switching off the trap, on the order of 30-40 μK and which leads to a mean Doppler effect of about 150 kHz. As we did not cool the atoms further, we aimed at operating in a regime where:

$$2\pi \times 150 \text{ kHz} \ll \Omega \ll \Delta E(R)/\hbar. \quad (4.3)$$

Thus, this imposes to use Rydberg states $|r\rangle$ to which we can couple to with Rabi frequencies $\Omega \geq 2\pi \times 1 \text{ MHz}$, and for which the energy shift $\Delta E(R)/h$ of the doubly excited state $|rr\rangle$ due to the interactions is larger than 10 MHz. The interaction energy shift $\Delta E(R)$ can also be increased by reducing the interatomic distance R , with a lower bound fixed by the optical resolution of the imaging system used to focus the traps, to about 3 μm . Finally, the lifetime τ of the chosen Rydberg state has to be large compared to the excitation time Ω^{-1} .

¹We can note that the two-photon excitation scheme that we implemented can also be used to address the S states $|nS_{1/2}, m_j = -1/2\rangle$.

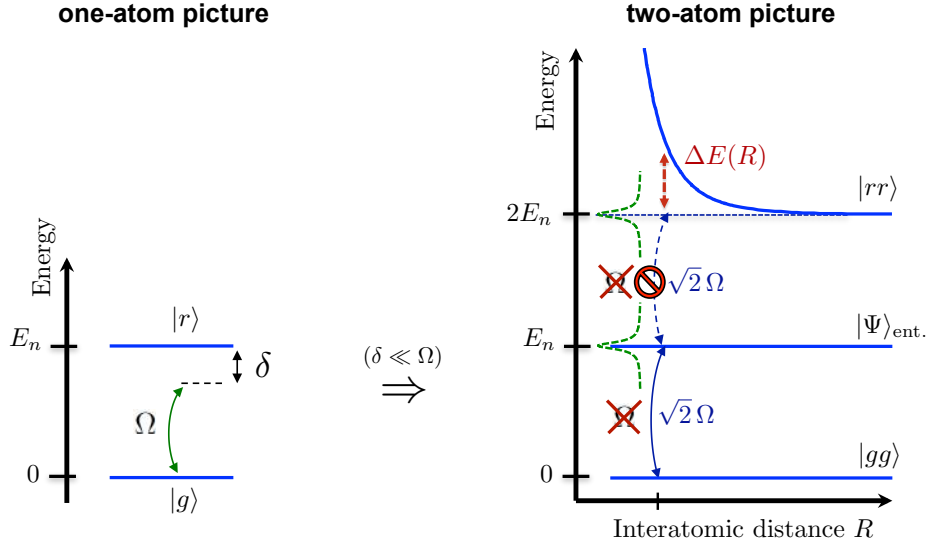


Figure 4.1: Principle of the Rydberg blockade.

The Rydberg states of the form $|nD_{3/2}, m_j = 3/2\rangle$, with $n \gtrsim 60$ fulfill all these requirements:

- The energy shifts ΔE are larger than 10 MHz for $R \simeq 5 \mu\text{m}$.
- Their lifetime τ are on the order of 100 μs (see Sec. B.1.5).
- They can be excited from the qubit state $|1\rangle = |5S_{1/2}, F = 2, m_F = 2\rangle$ with a two-photon transition via the intermediate state $5P$. Selection rules even allow to excite the stretched state $|nD_{3/2}, F = 3, m_F = 3\rangle$ which have high coupling strengths Ω_B to the state $5P_{1/2}$. As we will see in Sec. 4.4.3, the effective couplings Ω towards these Rydberg states can be tuned up to about $2\pi \times 5$ MHz without introducing too much dissipation via $5P_{1/2}$.

Furthermore, the energy shifts ΔE depend also on the external electric field \mathbf{F} and can be enhanced by tuning this field to reach *Förster resonances*. Such resonances have been studied in Walker and Saffman (2008) and are described in Sec. B.2. The Rydberg states $|nD_{3/2}, m_j = 3/2\rangle$ with $n \geq 59$ are good candidates to study these resonances.

4.2 Excitation scheme

4.2.1 Two-photon transition

The ^{87}Rb Rydberg states that we want to excite are separated from the ground state $5S_{1/2}$ by an energy $E \simeq hc/\lambda$, where λ is about 297 nm. Powerful laser sources with a wavelength so far in the UV domain are rather expensive. It is much more convenient to implement a two-photon excitation scheme, as it was done in previous experiments with either frozen Rydberg gas (Singer *et al.*, 2004; Afrousheh *et al.*, 2004; Liebisch *et al.*, 2005; van Ditzhuijzen *et al.*, 2006) or with single atoms in microscopic tweezers (Johnson *et al.*, 2008; Miroschnyenko *et al.*, 2010).

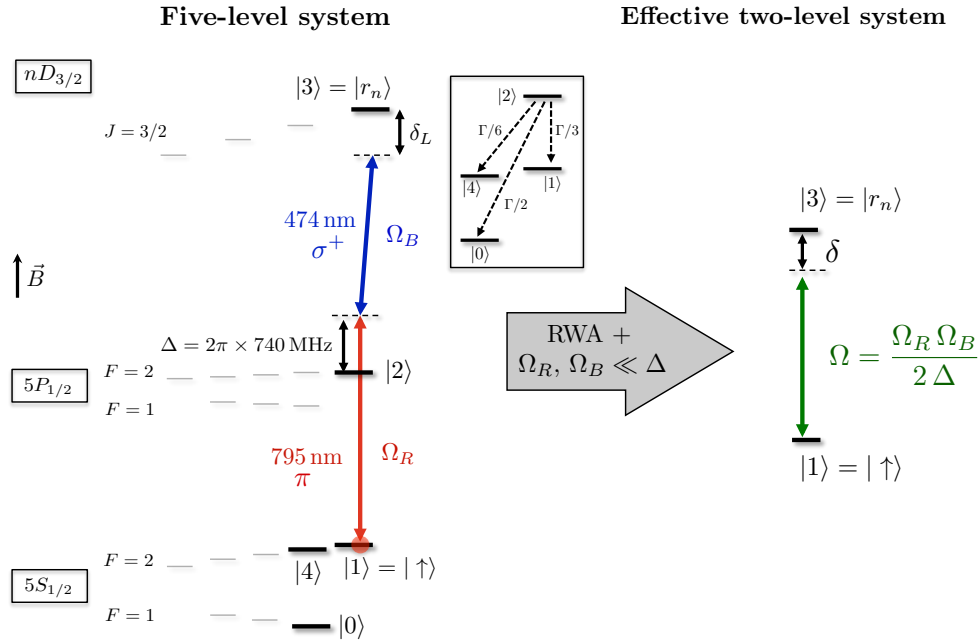


Figure 4.2: Rydberg excitation scheme.

In our experiment, we reproduced the two-photon excitation scheme implemented on the former apparatus of the group during A. Gaëtan's thesis, as shown in Fig. 4.2. First, we consider only the three-level system composed of the states $|1\rangle = |5S_{1/2}, F=2, m_F=2\rangle$, $|2\rangle = |5P_{1/2}, F=2, m_F=2\rangle$ and $|3\rangle$, respectively of energy E_1 , E_2 and E_3 , where $|3\rangle$ is a chosen Rydberg state of the form $|nD_{3/2}, F=3, m_F=3\rangle$. The states $|2\rangle$ and $|3\rangle$ have a finite decay lifetime, respectively Γ_P and Γ_R . A first π -polarized laser field at 795 nm of frequency ω_R allows to couple the initial state $|1\rangle$ to the intermediate excited state $|2\rangle$, with a Rabi frequency Ω_R . A second σ^+ -polarized laser field at 474 nm of frequency ω_B is used to couple the state $|2\rangle$ to the chosen Rydberg state $|3\rangle$. As the hyperfine structure splitting² is smaller than the linewidth of the laser excitation, it is more relevant to work with the fine structure basis $|3\rangle = |nD_{3/2}, F=3, m_F=3\rangle = |nD_{3/2}, m_j=3/2\rangle$. We define the detunings $\Delta = \omega_R - (E_2 - E_1)/\hbar$ and $\delta_L = (\omega_R + \omega_B) - (E_3 - E_1)/\hbar$. Such an excitation scheme is very similar to the two-photon transition scheme implemented for the Raman transitions that we described in Sec. 3.3.2. The rotating wave approximation $|\Delta| = 2\pi \times 740 \text{ MHz} \ll \omega_{R,B} \sim 2\pi \times 10^{14} \text{ Hz}$ is also well verified.

Effective two-level system without dissipation

In the large detunings limit $\Delta \gg \{\Omega_{R,B}, \Gamma\}$ as for the Raman scheme, the three-level system described above can be reduced to an equivalent two-level system, where the ground state $|1\rangle$ couples to the Rydberg state $|3\rangle$ with an effective Rabi frequency Ω and an effective detuning δ reading:

$$\Omega = \frac{\Omega_R \Omega_B^*}{2 \Delta} \quad \text{and} \quad \delta = \delta_L - \left(\frac{|\Omega_R|^2}{4 \Delta} - \frac{|\Omega_B|^2}{4 \Delta} \right), \quad (4.4)$$

²The hyperfine splitting is smaller than 300 kHz for $n \geq 50$, see details in Sec. B.1.2.

where the terms $|\Omega_R|^2/(4\Delta)$ and $|\Omega_B|^2/(4\Delta)$ correspond to the light shifts of the states $|1\rangle$ and $|3\rangle$ induced by the laser fields at 795 nm and 474 nm respectively. Then, assuming that the atom is initially prepared in $|1\rangle$, the probability $P_{|3\rangle}(\delta, t)$ to find the atom in state $|3\rangle$ after applying the two-photon excitation for a duration t is given by the Rabi formula:

$$P_{|3\rangle}(\Omega, \delta, t) = \frac{\Omega^2}{\Omega^2 + \delta^2} \sin\left(\sqrt{\Omega^2 + \delta^2} \frac{t}{2}\right)^2. \quad (4.5)$$

Five-level system with spontaneous emission

However, in some of our Rydberg experiments, the validity of the large detunings approximation $\Delta \gg \{\Omega_{R,B}, \Gamma_P, \Gamma_R\}$ could be questioned. Indeed, although the conditions $\Delta \gg \{\Omega_B, \Gamma_P, \Gamma_R\}$ were well verified with our typical experimental parameters (see Sec. 4.2.4), several Rydberg excitations experiments were carried out with the parameter Ω_R almost on the order of Δ , to achieve effective Ω as large as possible. In such cases, the spontaneous emission *via* the intermediate state $|2\rangle$ is not negligible on the excitation timescale and leads to a damping of the Rabi oscillations between $|1\rangle$ and $|3\rangle$ that we observed experimentally. The spontaneous scattering rate Γ_{sc} , due to the state $5P_{1/2}$ of decay rate $\Gamma = 2\pi \times 5.75$ MHz, can be obtained perturbatively from the average population in $|2\rangle$, and reads:

$$\Gamma_{sc} = \Gamma \left(\frac{\Omega_R^2}{4\Delta^2} + \frac{\Omega_B^2}{4\Delta^2} \right). \quad (4.6)$$

A more accurate model needs to take into account the fact that $|2\rangle$ can spontaneously decay to the states $|1\rangle$, $|4\rangle$ and $|0\rangle$, as defined in Fig. 4.2, with rates $\Gamma_P/3$, $\Gamma_P/6$ and $\Gamma_P/2$ respectively. Numerical simulations which solve the optical Bloch equations for the five-level system $\{|0\rangle, |1\rangle, |2\rangle, |3\rangle, |4\rangle\}$ allow to fit more accurately the data exhibiting damping, as we will see in more details in Sec. 4.4.3 (Miroshnychenko *et al.*, 2010). In particular, this method reproduces very well the asymmetrical shape of the damping observed for large values of Ω_R using our Rydberg detection scheme (see Fig. 4.15).

However for the sake of simplicity, we used this model for comparison with our experimental data only for one-atom experiment. Indeed, for N -atom experiments the size of the density matrix increases as $5^N \times 5^N$ and the computational time required to solve the Bloch equations increases exponentially. We preferred to include the dissipation with an alternative phenomenological approach, as described below.

Effective two-level system with spontaneous emission

An alternative approach consisted in solving the optical Bloch equations for the reduced density matrix ρ associated to the sub-system $\{|g\rangle, |r\rangle\}$. The hamiltonian and dissipator of the system read:

$$H = \hbar \begin{pmatrix} 0 & \Omega^*/2 \\ \Omega/2 & -\delta \end{pmatrix} \quad \text{and} \quad \mathcal{L} = \gamma \begin{pmatrix} \rho_{rr} & -\rho_{gr} \\ -\rho_{rg}/2 & -\rho_{rr} \end{pmatrix}, \quad (4.7)$$

where Ω and γ are respectively the phenomenological coupling between $|g\rangle$ and $|r\rangle$ and the damping rate. When the excitation is on resonance, and assuming that the system is initially prepared in state $|g\rangle$, the probability $P_{|g\rangle}(t)$ to find the atom in $|g\rangle$ after applying the two-photon excitation for a duration t can be expressed explicitly (Loudon, 2000) as:

4.2.3 Transfer cavity lock

To realize the two-photon excitation scheme, the frequency $\omega_R + \omega_B$ needs to be stabilized in order to fulfill the resonance condition $\delta \simeq 0$ (see Eq. 4.4). In practice, it means that the residual fluctuations of the effective detuning δ must remain small compared to the effective Rabi frequency Ω during the time required to perform a Rydberg excitation experiment (about 30 minutes for a full Rabi curve). Typically, we used $500 \text{ kHz} \leq \Omega/2\pi \leq 5 \text{ MHz}$, so we aimed at keeping the fluctuations of $\delta/2\pi$ below about 100 kHz.

A common technique to achieve the required stability is to use an external *transfer cavity* (TC), as shown in Fig. 4.3 (a). During this thesis, we used a confocal Fabry-Perot cavity 216-C⁺ from Coherent. This cavity had a free spectral range (FSR) of 300 MHz and its length L could be adjusted with a PZT placed on the rear mirror. We measured a finesse of about 280 at 795 nm and 200 at 950 nm. The principle of the locking scheme that we implemented is the following.

Locking scheme

The first step consists in locking the frequency of the first laser at 795 nm to the frequency of a transmission peak through the transfer cavity using a Pound-Drever-Hall (PDH) method (Black, 2001). The resonances of the cavity are used to feed back a fast correction signal to the laser which stabilizes the laser frequency, and narrows the laser linewidth below about 100 kHz.

In a second step, the frequency of this laser is scanned by tuning the length L of the transfer cavity with its piezoelectric transducer. A beam derived from the same laser is sent at the same time through a standard saturated absorption setup which allows to monitor the laser frequency. By acting back on the piezoelectric of the cavity, the length L is actively stabilized such that the laser stays at resonance with a chosen atomic transition. Compared to the PDH method, this is a slow correction that compensates the long-term drifts of the laser frequency.

Finally, once both the transfer cavity and the first laser at 795 nm are locked, the frequency of the second laser is locked to a transmission peak of the cavity again using a Pound-Drever-Hall method.

Lock of the 795 nm laser onto the transfer cavity

The setup that we implemented is shown in Fig. 4.3 (a). First, a beam derived from the 795 nm laser $F = 2$ with a PBS cube went through an electro-optical modulator (EOM 3) used as a phase modulator. This EOM was driven by a PDD 110 module from Toptica at 20 MHz and produced the sidebands required to implement the PDH method. After passing through a dichroic mirror, the beam was coupled into the transfer cavity. The reflection from the cavity was collected on the fast photodiode³ PD 2. Finally, the signal from PD 2 was sent to the PDD 110 module which produced the error signal fed to the FET input current modulation of the DL Pro $F = 2$.

³Amplified photodiode PDA10A-EC from Thorlabs, Inc.

Lock of the cavity length

Another beam derived from the 795 nm laser $F=2$ with a PBS cube went through a double-pass acousto-optic modulator⁴ (AOM 3) before entering the saturated absorption setup. This AOM was driven at the central frequency 187.3 MHz modulated at 50 kHz with a modulation depth of about 500 kHz.⁵ The modulation allowed to implement a standard lock scheme on the saturated absorption peak $|5S_{1/2}, F=3\rangle \rightarrow$ cross-over $2'-3'$ of the isotope ^{85}Rb . This peak is blue-shifted from the resonance $|5S_{1/2}, F=2, m_F=2\rangle \rightarrow |5P_{1/2}, F=2, m_F=2\rangle$ of ^{87}Rb by about 884 MHz. Finally, the error signal was fed to the high voltage driver of the TC piezoelectric. We will see in Sec. 4.2.4 that for those settings, $\Delta/2\pi \simeq 740$ MHz.

Lock of the 948 nm laser onto the transfer cavity

The last step is to lock the blue laser at 474 nm to the transfer cavity. In practice, we stabilized the master diode frequency at 948 nm onto the TC which also ensured the frequency stability at 474 nm. Indeed, the TA SHG pro system allowed to extract a fraction of the laser beam at 948 nm before it enters the tapered amplifier. This extracted beam was split into two with a PBS cube. One output was coupled into a fiber and sent to an accurate wavemeter⁶ to measure the absolute frequency of the master diode. The other output was coupled into a fiberized electro-optic modulator⁷ (EOM 4). At the output, the beams at 948 nm and at 795 nm were combined using a dichroic mirror, and coupled into the transfer cavity. Again, we collected the reflection from the cavity using a quarter-wave plate combined with PBS cube, and sent it on the second fast photodiode⁸ PD 3.

In this case, there was no need to add a frequency modulation to the 948 nm beam, as it was done for the 795 nm beam with EOM 3, to implement a PDH lock onto the transfer cavity. Indeed, the current of the master diode is already modulated at 20 MHz by a PDD 110/dual module of the TA SHG Pro system, to achieve the internal PDH lock onto the cavity of the frequency doubling stage. The error signal of this internal PDH lock is fed to the piezoelectric transducer of the SHG cavity. This frequency modulation was thus used to implement our own PDH lock of the master diode frequency.

However at this step, the length L of the transfer cavity was fixed. Thus the frequency of the 948 nm laser diode could not be scanned if it were directly locked onto a transmission peak for which the frequency is of the form $\nu_p = p \times c/4L = p \times 300$ MHz. Thus, fiberized EOM 4 was used to produce sidebands, shifted from the diode central frequency by multiple of the EOM driving frequency ν_{EOM} . As the current of the master diode was modulated at 20 MHz, the frequency of each of the sidebands created by EOM 4 was also modulated at 20 MHz, and all of them produced a PDH error signal that could be fed to the current modulation input of the 948 nm master diode.

⁴AOM MT200 from AA Opto-Electronic.

⁵The central frequency was chosen to minimize residual laser power modulation after the AOM which can convert into fluctuations of the error signal offset and thus degrade the stability of the frequency lock. Without optimizing the central frequency, we could observe the offset of the error signal drifting by more than its peak to peak amplitude over several minutes. It correspond to frequency shifts of the 795 nm laser larger than about 10 MHz. We estimated it by scanning the offset of the lock over the full range by hand while we measured the relative frequency shift on the High Finesse wavemeter.

⁶The wavemeter was the Angstrom WS-U 10 from HighFinesse with a short term relative stability <2 MHz.

⁷Fiberized EOM from EOSpace, with 10 GHz bandwidth and low V_π ($\simeq 3$ V).

⁸Fast photodiode PDA10CF from Thorlabs, Inc.

Finally, once a chosen sideband⁹ was locked to the transfer cavity using the PDH method, the frequency of the 948 nm could be varied by tuning the driving frequency ν_{EOM} of EOM 4 in the range 100-500 MHz which covered the free spectral range $\text{FSR} \simeq 300$ MHz of the transfer cavity. The RF synthesizer providing the driving frequency ν_{EOM} was controlled by the computer program via GPIB port.

Performances

With all feedback loops closed, the linewidth of each Rydberg laser was estimated at about 150 kHz from the amplitude of the error signal calibrated in frequency. This estimation is in good agreement with the results of Sec. 4.4.3 directly obtained with atoms. More accurate characterization of the linewidths were performed on the former apparatus using delayed self-heterodyne measurements (Okoshi, Kikuchi, and Nakayama, 1980). We will reproduce such measurements in the future.

4.2.4 Rydberg pulse parameters

Beam at 795 nm

As we already described in Sec. 3.3.3, the main laser beam at 795 nm was first sent through a fast electro-optical modulator¹⁰ (EOM 2) used to switch on and off the laser light with typical switching times of 5-10 ns and with an attenuation of about 50 dB¹¹. Then, the beam went through a double-pass acousto-optical modulator driven at 110 MHz (AOM 2, order +1) also used as a switch to reach an almost perfect extinction. The resulting one-photon detuning was thus $\Delta = 884 - 2 \times 187 + 2 \times 110 = 740$ MHz. Finally the beam was coupled into a PM fiber and brought to the vacuum chamber table. The output was almost a TEM_{00} mode with an output power up to about 15 mW.

A sketch of the experimental configuration implemented for the Rydberg excitation on the vacuum chamber table is shown in Fig. 4.4. A half-wave plate at the output of the fiber allowed to adjust π -polarization of the beam (linear and \parallel to the vertical z axis). Then, we used a plano-convex lens of focal length $f = 400$ mm to focus the beam down to a $1/e^2$ radius $w_R \simeq 100 \mu\text{m}$ at the position of the trapped atoms, as we measured beforehand with a beam profiler.

The maximum Rabi frequency expected is $\Omega_R^{\text{max}} = |d_R| \mathcal{E}_R^{\text{max}} / \hbar$. Using the Wigner-Eckart theorem, the dipole matrix element d_R can be decomposed (Steck, 2008) into a product of a reduced matrix elements $\langle j = 1/2 || er || j' = 1/2 \rangle$, and a Clebsch-Gordan (CG) coefficient $\langle 1/2, 1/2; 1, 0 | 1/2, 1/2 \rangle$. Both initial and final states are stretched states, such that the CG-coefficient corresponds to the transition $|5S, j = 1/2, m_j = 1/2 \rangle \rightarrow |5P, j' = 1/2, m'_j = 1/2 \rangle$. Using the numerical value of $\langle j = 1/2 || er || j' = 1/2 \rangle$ from Steck (2008), we found:

$$\begin{aligned} d_R &= \langle j = 1/2 || er || j' = 1/2 \rangle \times \langle 1/2, 1/2; 1, 0 | 1/2, 1/2 \rangle \\ &= -2.99 |e| a_0 \times \sqrt{1/3} \\ &\simeq -1.46 \cdot 10^{-29} \text{ C.m,} \end{aligned} \tag{4.9}$$

⁹We used mostly the orders ± 1 which exhibit the error signals with the steepest slopes.

¹⁰EOM LM0202 P5W IR from Linos.

¹¹The attenuation was measured at the output of the fiber bringing the beam to the vacuum chamber table. Fine tuning of polarization and EOM drivers voltages were needed to reach 50 dB of extinction

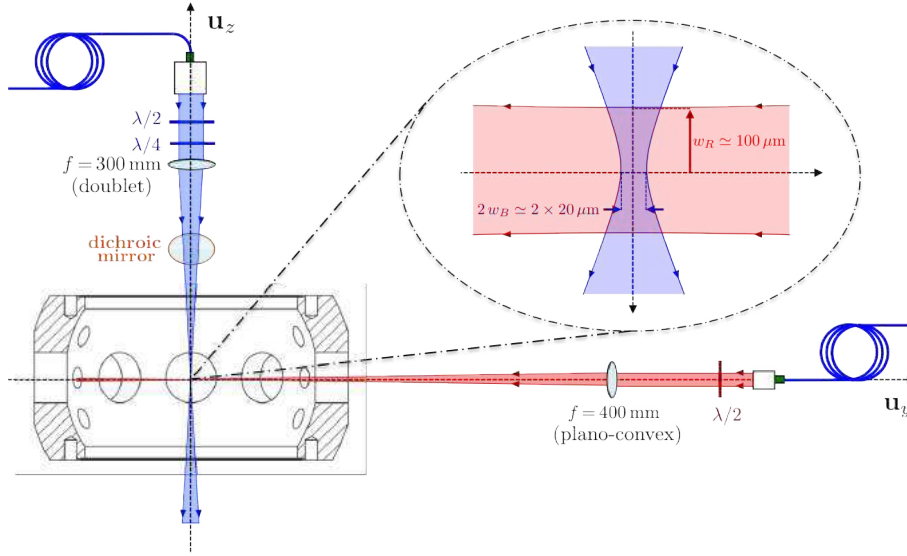


Figure 4.4: Laser beam configuration for the Rydberg excitation.

Focusing the beam down to about $100\ \mu\text{m}$, the Rabi frequency $\Omega_R/2\pi$ that we could expect was then:

$$\frac{\Omega_R}{2\pi} [\text{MHz}] = \frac{|d_R| \mathcal{E}_R}{h} = \frac{|d_R|}{h} \sqrt{\frac{4P_R}{\pi \epsilon_0 c w_R^2}} = 152.8 \sqrt{\frac{P_R}{1\ \text{mW}}}. \quad (4.10)$$

In our experiments, it was tuned in the typical range 10-600 MHz by adjusting the power P_R between $5\ \mu\text{W}$ and 15 mW.

Beam at 474 nm

The laser beam at 474 nm was also sent through an electro-optical modulator¹² (EOM 5) used as a switch before being coupled into a PM fiber ($\simeq 50\%$ efficiency) and brought to the vacuum chamber table. The power available at the exit of the fiber was up to about¹³ 90-100 mW. The blue beam was then combined with the vertical beam of the MOT on a dichroic mirror and sent inside the chamber. The viewports on the vertical axis had been deposited with an AR-coating and have a good transmission at 474 nm of about 98%. On a day to day basis over several weeks of measurements, the blue power seen by the trapped atoms was always kept around 90 mW.

However, the dipole elements $d_B(n)$ for the transitions $|5P, j=1/2, m_j=2\rangle \rightarrow |nD, j'=3/2, m'_j=3/2\rangle$ are much smaller than for the first transition at 795 nm. During the thesis of A. Gaëtan, the group of P. Pillet calculated for our group all the numerical values of the radial matrix elements $\langle n', l', j' | e r | n, l, j \rangle$ for n ranging from 30 to 82, in good agreement with our more recent calculations (see Sec. B.1.4). Using the Wigner-Eckart decomposition described in Eq. 5.30, each dipole element $d_B(n)$ can be written as a product of such a reduced radial matrix element by an angular term with Wigner-3j and 6j symbols. For $n=58$, the radial integral is about $-0.01936 |e| a_0$, and the angular term is $1/\sqrt{3}$.

¹²EOM 0202 P5W Vis from Linos.

¹³The power available at the output of the doubling cavity was slightly dependent of the chosen blue frequency needed for each Rydberg state n ; it varied from 80 to 100 mW, for n ranging from about 50 to 80.

In practice, for the typical power available at 474 nm, we had to focus much more the blue beam as compared to the red beam in order to achieve Rabi frequencies $\Omega_B(n)/2\pi = |d_B(n)|\mathcal{E}_B/h$ on the same orders of magnitude. But, we did not want to focus the blue beam too much either, in order to keep the blue power as homogenous as possible over the array of trapped atoms. A reasonable tradeoff was to focus the beam down to about $20\ \mu\text{m}$ ($1/e^2$ radius) with a doublet of focal length $f = 300\ \text{mm}$, as we measured beforehand with a beam profiler. After the lens, a half-wave plate and a quarter-wave plate allowed to adjust the σ^+ -polarization of the beam with respect to the magnetic field axis. In the end, with about 90 mW blue power focused down to about $20\ \mu\text{m}$, the maximum Rabi frequency at 474 nm for $n = 58$ that we could achieve was:

$$\Omega_B^{\text{max}}(n = 58) = \frac{|d_B(n = 58)|\mathcal{E}_B^{\text{max}}}{\hbar} = \frac{|d_B(n = 58)|}{\hbar} \sqrt{\frac{4P_B^{\text{max}}}{\pi \epsilon_0 c w_B^2}} \simeq 2\pi \times 45\ \text{MHz}. \quad (4.11)$$

Finally, the Rabi frequencies Ω_B scale as $(n^*)^{-3/2}$ (see Sec. B.1.4), so one can compute easily their orders of magnitude for the other Rydberg states $nD_{3/2}$.

4.3 Experimental realization

This section presents our first experimental observations of Rydberg excitations on the new apparatus. We start by describing the alignment procedure of the laser beams onto the trapped atoms, which is similar for both 795 nm and 474 nm beams. Then we detail our Rydberg detection scheme. Finally, we show our first observations of coherent Rydberg excitations.

4.3.1 Alignment of the beam at 795 nm

Our procedure to align the 795 nm beam consisted in maximizing the loss rate induced when this beam was shone at the single atoms while they were in the trap. The more laser intensity they saw, the quickest they got ejected from the trap, although we do not know what are the exact loss mechanisms (combination of heating and force), and if the loss rate is exactly proportional to the intensity at 795 nm, or not. As mentioned above, a lens with a focal length $f = 400\ \text{mm}$ is used to focus the beam down to about $100\ \mu\text{m}$ ($1/e^2$ radius). This corresponds to a Rayleigh range of about 4 cm so the longitudinal alignment can be done with a simple ruler in this case.

The experimental sequence we used to align the beam in the transverse direction is shown in Fig. 4.5 (a). After the detection of a single atom in the trap, the 795 nm laser is switched on for 40 ms while the MOT beams are still on. At the same time, we monitored the fluorescence signal detected on the photon counting module, with a time resolution of $1\ \mu\text{s}$. We started counting the fluorescence 10 ms before sending the 795 nm beam, the counting duration was thus 50 ms in total. Then, we accumulated fluorescence signals over 100 sequences. With this method, the decay of the fluorescence rate was very well fitted by an exponential decay with lifetime τ . A typical result is shown in Fig. 4.5 (b) with time bins of $100\ \mu\text{s}$. We used typically a power $P_R \simeq 1\ \text{mW}$ with a detuning $\Delta/2\pi \simeq 740\ \text{MHz}$. The saturation parameter $s = (I/I_{\text{sat}})/(1 + 4\Delta^2/\Gamma^2)$ was then about 0.01. Thus, with a good alignment, the atom scattered about $\Gamma \cdot s \simeq 400\ 000\ \text{photons/s}^{-1}$. For each scattering event, its mean thermal energy increases by $2E_{\text{rec}} = 2k_B T_{\text{rec}}$. Thus, in a trap depth $U/k_B \simeq 1\ \text{mK}$, it took about $U/(2k_B T_{\text{rec}})(\Gamma s)^{-1} \simeq 3\ \text{ms}$ to eject the atom from the trap.

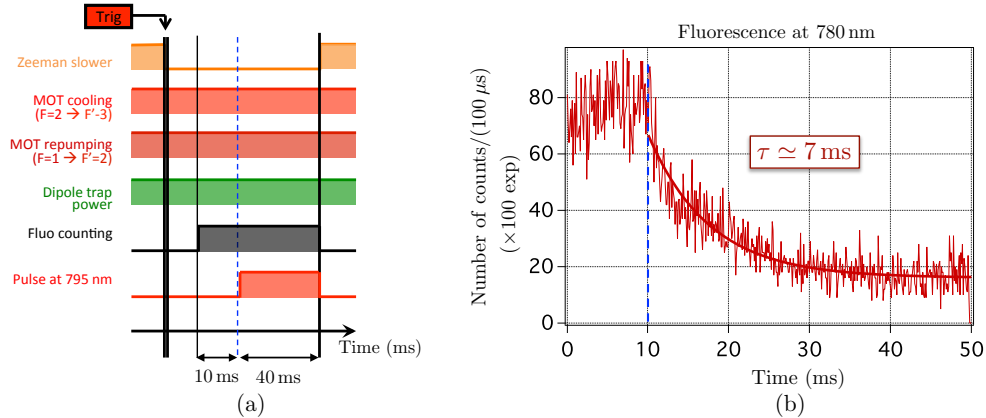


Figure 4.5: Alignment procedure of the beam at 795 nm. (a) Experimental sequence. The thick vertical black bar at $t = 0$ ms symbolizes the initial atom presence checking procedure (step 1 in Fig. 2.2). (b) Evolution of the fluorescence rate detected on the counter during a time window of 50 ms. The beam at 795 nm is switched on at $t = 10$ ms. Typically, we used $P_R = 1$ mW and a single-photon detuning $\Delta/2\pi = 740$ MHz.

On the vacuum chamber table, the output fiber coupler of the 795 nm laser beam was mounted into a 1" Fine Adjustment mirror mount, with 170 TPI screws. The orientation of each screw was calibrated using an angular scale behind the mount. After a pre-alignment of the laser onto the MOT cloud, we varied the orientation of the beam, with an accuracy of about $\pm 2.5^\circ$. Combining the mechanical parameters of the mirror mount¹⁴ with the focal length $f = 400$ mm of the lens used to focus the beam at 795 nm, we estimated that the beam was shifted by about $4.75 \mu\text{m}/^\circ$ in the focal plane of the lens. Thus, we measured the evolution of the decay rate $1/\tau$ as a function of the beam position. The results are shown respectively in Fig. 4.6 (a) and (b). Even if it is not easy to identify a clear relationship between the light intensity at 795 nm seen by the atoms and the decay rate $1/\tau$, the data could be rather well fitted by gaussian curves, with the following $1/e^2$ radii ΔL_H and ΔL_V respectively along the horizontal and the vertical directions:

$$\Delta L_H \simeq 106 \pm 19 \mu\text{m} \quad \text{and} \quad \Delta L_V \simeq 80 \pm 12 \mu\text{m}. \quad (4.12)$$

The value of ΔL_H is in good agreement with the size of the beam expected with our focusing setup at 795 nm. These results point out small residual aberrations in the horizontal direction. This was not really an issue: once the alignment was done, the atoms only explored the center of the beam where the intensity was then almost constant.

4.3.2 Alignment of the beam at 474 nm

The alignment procedure of the beam at 474 nm was the same as the one described in the thesis of A. Gaëtan. It is very similar to the previous method implemented for the beam at 795 nm. It consisted in maximizing the loss rate induced by the blue beam shone at the single atoms while they are in the trap together with the MOT beams switched on.

We typically used a power $P_B \simeq 5$ mW. A doublet with a focal distance $f = 300$ mm focused the beam down to about $20 \mu\text{m}$ ($1/e^2$ radius), which corresponds to a Rayleigh range of about 2.6 mm. Then, the experimental sequence we used is shown in Fig. 4.7 (a). After

¹⁴We used a mirror mount from Fine Adjustment with a pitch of 0.15 mm and a lever arm of 35 mm.

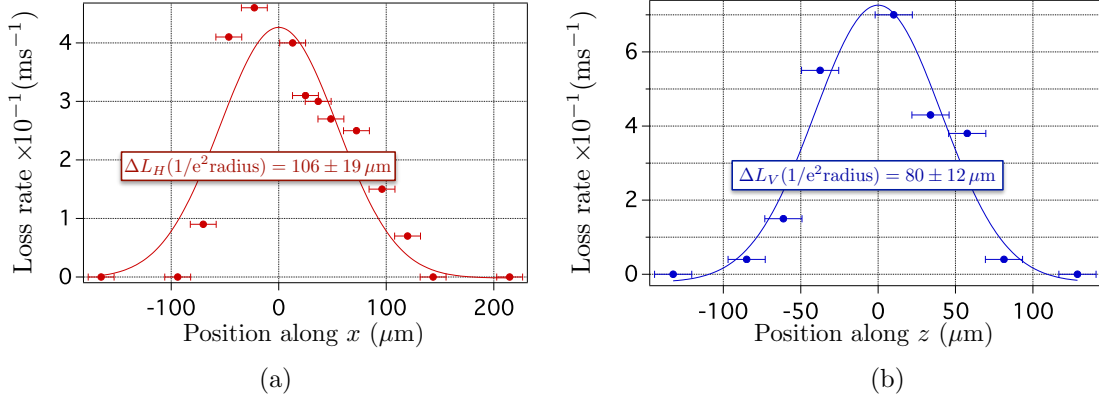


Figure 4.6: Fine alignment of the beam at 795 nm. Evolution of the atom loss rate with the beam position along the horizontal axis x (a) and vertical axis z (b) of the experiment. The error bars $\pm 12 \mu\text{m}$ correspond to a reading accuracy of the orientation of each screw onto the angular reference of $\pm 2.5^\circ$.

the detection of a single atom in the trap, the 474 nm laser is switched on for 40 ms while the MOT beams are still on. The two-photon transition (780 nm + 474 nm) ionizes the atom. Such a photoionization process results in the loss of the atom (other loss mechanisms are negligible on the time scale of this experiment). When the blue beam is switched on, the lifetime of the atom in the trap follows an exponential decay, with a decay constant τ inversely proportional to the intensity I_B and the photoionization cross section σ (Gabbanini, Gozzini, and Lucchesini, 1997):

$$\frac{1}{\tau} = f \frac{I_B \sigma}{h\nu_B}, \quad (4.13)$$

where f is the probability that the atom is in state $5P_{3/2}$ in stationary regime, and ν_B is the frequency of the blue laser. Aligning the beam consists in maximizing I_B , e.g. minimizing τ . To measure the decay time τ , we performed fluorescence measurements as described in the previous section. We started counting the fluorescence of the trapped atom 10 ms before switching on the beam at 474 nm. The counting duration was also 50 ms in total, and we summed the signals obtained after 100 sequences. A typical result is shown in Fig. 4.7 (b) with time bins of 100 μs .

On the vacuum chamber table, the output fiber coupler of the 474 nm laser beam was mounted into a linear XYZ translation stage with an accuracy of $\pm 5 \mu\text{m}$ in the transverse directions, and $\pm 50 \mu\text{m}$ along the longitudinal axis z . We could directly measure the evolution of the decay rate $1/\tau$ as a function of the position of the fine translation screws along the transverse directions x and y , and repeat this procedure at different positions along the z -axis. The results are shown in Fig. 4.8, and reveal the astigmatism of the imaging system, possibly due to the dichroic plate at 45° . Once the position along the z -axis was optimized, the typical transverse dimensions w_x and w_y measured (at $1/e^2$ radius) were:

$$\begin{aligned} w_x &\simeq 17 \pm 2 \mu\text{m} \\ w_y &\simeq 22 \pm 3 \mu\text{m} \end{aligned} \quad \text{and} \quad \bar{w} = \sqrt{w_x w_y} \simeq 21 \mu\text{m}. \quad (4.14)$$

Once the two laser beams used for the Rydberg excitation were aligned on the trapped atoms, we were ready to perform the spectroscopy of Rydberg states. We will now describe the Rydberg detection scheme we used in our experiments.

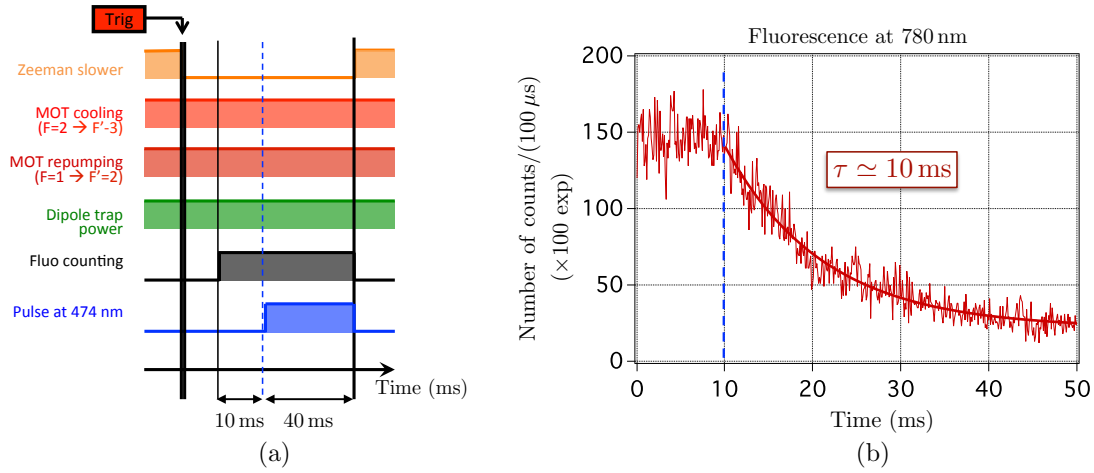


Figure 4.7: Alignment procedure of the beam at 474 nm. (a) Experimental sequence. The thick vertical black bar at $t=0$ ms symbolizes the initial atom presence checking procedure (step 1 in Fig. 2.2). (b) Evolution of the fluorescence rate detected on the counter during a time window of 50 ms. The blue beam is switched on at $t=10$ ms.

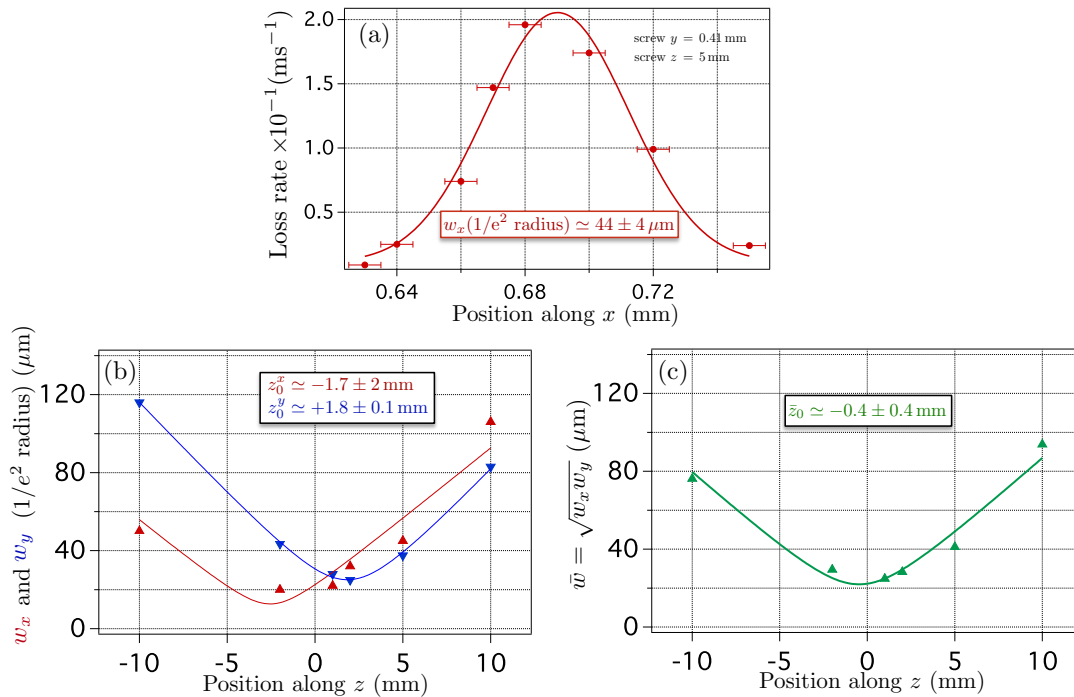


Figure 4.8: Fine alignment of the beam at 474 nm. (a) Evolution of the atom loss rate $1/\tau$ with the position of the fine adjusting screw of the XY-translation stage along axis x . The error bars $\pm 5 \mu\text{m}$ represent half a screw graduation. (b) $1/e^2$ radii w_x and w_y as a function of the position along the z axis. (c) mean $1/e^2$ radius $\bar{w} = \sqrt{w_x w_y}$ as a function of the position along z .

4.3.3 Rydberg state detection

Our new experimental apparatus comprises a charge detector operating under vacuum for positive detection of Rydberg states (see Sec. 1.2.3). However for the sake of simplicity, we preferred to begin our Rydberg experiments by reproducing the previous detection scheme implemented on the former apparatus. Then, as it worked out well enough for the investigations of the dipole-dipole interactions conducted almost until the end of this thesis, the charge detection setup has not been implemented for the moment.

The Rydberg detection scheme used for all the experiments presented in this manuscript consisted in a negative detection scheme, based on the loss of the atom when it was successfully excited towards a Rydberg state. Indeed, our 850 nm dipole trap of angular frequency ω induces positive light shifts for all Rydberg states with $n \geq 50$. The polarizability $\alpha(\omega)$ can be obtained by treating classically the valence electron as a free electron:

$$\alpha(\omega) = -\frac{e^2}{m_e \epsilon_0 \omega^2} \simeq -650 \text{ \AA}^3. \quad (4.15)$$

The mean interaction energy between the classical electron of polarizability $\alpha(\omega)$ and the trapping light field \mathcal{E} is then $-\alpha(\omega)\epsilon_0\mathcal{E}^2/2$ which is positive. With a typical power of about 3 mW at which we operate our 850 nm trapping laser, the lightshift is estimated at about +1 MHz; a Rydberg state is thus slightly anti-trapped. One can use this property to detect when a trapped atom has been successfully excited towards a Rydberg state if the typical lifetime τ_{Rydberg} is longer than the time τ_{escape} that it takes for the atom to leave the trap:

$$\tau_{\text{Rydberg}} \gg \tau_{\text{escape}}. \quad (4.16)$$

The typical time τ_{escape} is mainly determined by the residual temperature T of the atoms in the trap. This was characterized in Sec. 2.3.2 with a release and recapture method. The probability to recapture an atom after 50 μs was already below 10%. The positive light shifts also contributes to eject the Rydberg atoms slightly faster. A shift of 1 MHz on a gaussian spot with a $1/e^2$ radius of 1 μm leads to a force that shifts the position of the atom by about 3 μm after 50 μs .

The Rydberg lifetime τ_{Rydberg} results from a competition between several mechanisms:

- a spontaneous decay rate toward lower states (see Sec. B.1.5), with a typical time $\tau_{\text{rad}} = \tau_s \cdot (n^*)^\beta$. For $n \geq 50$, $\tau_{\text{rad}} \geq 150 \mu\text{s}$,
- a depopulation process induced by the black body radiation emitted by the environment at $T \simeq 300 \text{ K}$, with a typical time $\tau_{\text{BBR}} \simeq 165 \mu\text{s}$,
- a photoionization process induced by the trapping laser at 850 nm with a typical time $\tau_{\text{trap}} \simeq 1.4 \text{ ms}$.

At the end, it is hard to estimate accurately the efficiency η_{Rydberg} of such a detection method. We will see in Sec. 4.4.3 that the experimental data obtained for coherent Rabi oscillations were consistent with a detection efficiency $\eta_{\text{Rydberg}} \geq 90 \%$.

4.3.4 Spectra of Rydberg excitations

Finally, the experimental sequence we implemented to perform the spectroscopy of the Rydberg states $nD_{3/2}$ is shown in Fig. 4.9 (a). The preliminary steps of optical pumping

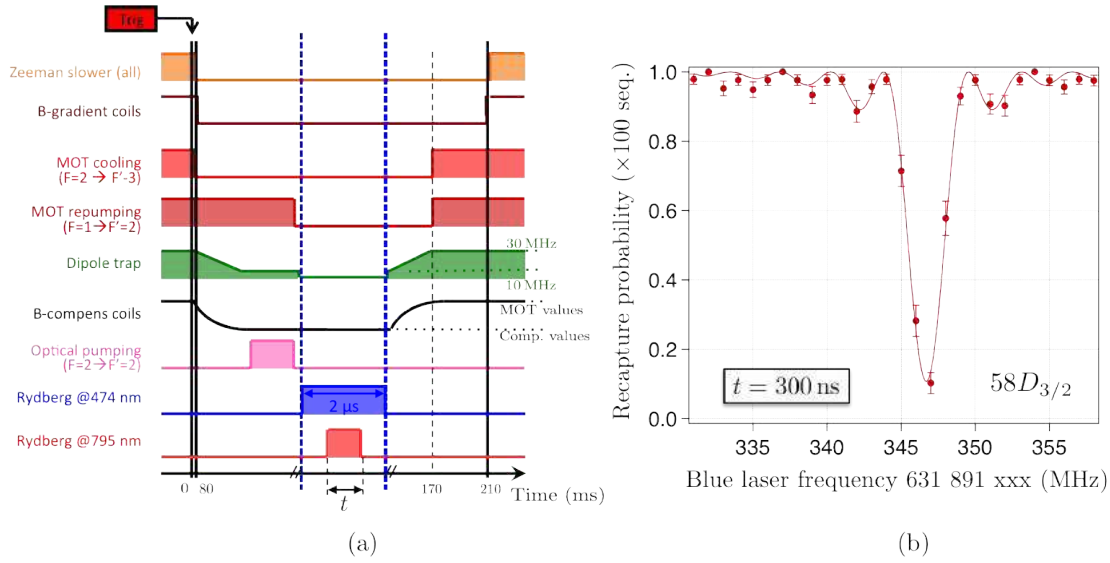


Figure 4.9: Rydberg excitation spectroscopy. (a) Experimental sequence. The thick vertical black bar at $t = 0$ ms symbolizes the initial atom presence checking procedure (step 1 in Fig. 2.2). (b) Spectrum of the excitation towards the Rydberg state $58D_{3/2}$ based on the loss detection scheme. Each data point is an average result over 100 sequences. The solid line is a fit of the form $y_0 + A \cdot P_3(\Omega, \omega_B - \omega_{B_0}, t = 300 \text{ ns})$, see Eq. 4.5. The fit gives $y_0 \simeq 0.98 \pm 0.005$, $\Omega \simeq 2\pi \times (1.7 \pm 0.08)$ MHz, $A = -0.87 \pm 0.02$ and $\omega_{B_0}/2\pi \simeq 631\,891\,346.7 \pm 0.02$ MHz.

have already been described in Sec. 3.3.4:

- First, the MOT cooling beams were switched off while the repumper beams were kept on during approximately 10 ms to prepare the atom in hyperfine state $F = 2$. At some point during this process, the compensation coils are commuted to the set of values chosen to apply a magnetic field in the vertical direction while cancelling the magnetic fields in the transverse direction. The power of the optical dipole trap was ramped down adiabatically by a factor of three to lower the amplitudes of effective magnetic fields induced by the strongly focused trapping beam. Finally, about $500 \mu\text{s}$ of optical pumping with a power of $5 \mu\text{W}$ allowed to prepare the atom into the initial state $|1\rangle = |5S_{1/2}, F = 2, m_F = 2\rangle$.
- Then, the dipole trap was switched off for typically $2 \mu\text{s}$ to perform the Rydberg excitations in free space. This way, the effective two-photon detuning δ did not vary at each realization of the sequence because of the light shifts induced by the trap that would depend on the position of the atom. At the same time, the blue beam at 474 nm and of tunable frequency $\omega_B/2\pi$ was switched on and sent to the atoms.
- Centered at half the duration of the blue pulse, we sent the laser pulse at 795 nm of tunable duration t .
- After that, the Rydberg lasers were switched off while the trapping beam was turned back on and ramped up to its original power. Finally, a fluorescence measurement was performed at the end of the sequence to check if the atom was recaptured or not.

The result of each sequence was thus binary, and we had to repeat it about a hundred times in order to reconstruct the probability P_{recap} to recapture the atom for a given set

of parameters $\{t, \omega_B\}$. Then, by varying the frequency $\omega_B/2\pi$ of the blue laser, we could measure the spectra of several chosen Rydberg excitations. The results presented below could only be obtained after having compensated for the residual DC electric fields (see Sec. 4.4).

The first Rydberg state that we tried to excite was the state $|58D_{3/2}, F=3, m_F=3\rangle$ because it exhibits a strong quasi-Förster resonance in the absence of electric fields and thus had been studied extensively during the theses of A. Gaëtan and C. Evellin. In Fig. 4.9 (b), we show the excitation spectrum of this state obtained with the powers $P_B \simeq 90$ mW ($\Omega_B \simeq 2\pi \times 40$ MHz) and $P_R \simeq 0.16$ mW ($\Omega_R \simeq 2\pi \times 65$ MHz). The experimental data can be rather well fitted by functions of the form $y_0 + A \cdot P_{|3\rangle}(\Omega, \omega_B - \omega_{B_0}, t = 300$ ns), in which $P_{|3\rangle}$ is the function described in Eq. 4.5. Far from the resonance, the recapture probability is not really 100%. In most of our experimental spectra, it always saturates at $y_0 \simeq 0.97$. Indeed, after a sequence of about 210 ms, the trapped atoms can be lost due to collisions with residual gas in the vacuum chamber. The value 0.97 is compatible with a lifetime $\tau \approx 8$ s of the atoms in the trap, as we measured in Sec. 2.3.1. The fitted value of the effective Rabi frequency $\Omega \simeq 2\pi \times 1.7$ MHz is in good agreement with Eq. 4.4. Finally, the value of $|A|$ is on the order of 87%. Taking into account that the damping is not zero as we will discuss more in Sec. 4.4.3, this implies a detection efficiency $\eta_{\text{Rydberg}} \geq 90\%$.

4.4 Cancellation of residual electric fields

The Rydberg states have very large polarizabilities. They are thus very sensitive to DC electric fields that can induce mixing with other neighbouring states. For this reason, the aspheric lenses operating close to the atoms have been coated with an ITO conductive layer (see Sec. 1.1.2) to guarantee a passively stable electrostatic environment. Furthermore, the apparatus has been equipped with electrodes to apply controlled electric fields. In this section, we will show that both proved indeed to be crucial for the success of the Rydberg experiments.

First, we present a few set of data obtained without the ITO layer on the lenses. Then, with ITO, we describe how we could cancel stray fields with Stark spectroscopy. Finally, we present the typical experimental data of coherent Rydberg excitations obtained after field compensation and which proved to be well contrasted.

4.4.1 Preliminary results without the ITO coating

Here, we present preliminary results obtained without the ITO coating on the surfaces of the lenses facing the atoms.

Rydberg state $58D_{3/2}$

We started first by performing the spectroscopy of the Rydberg state $58D_{3/2}$. It turned out that we had trouble finding the Rydberg lines. Yet, the quantum defect theory allows to predict the absolute frequency of a chosen Rydberg transition within 1 MHz. After checking all the parameters of our experimental sequence, electric fields were suspected. Some evidences of excitations were found approximately 60 MHz at the red of the theoretical transition. As the contrast was weak, we piled up several Rydberg pulses one after the other as in the sequence shown in Fig. 4.9 (a) in order to increase the signal. After piling up five Rydberg pulses with optimized durations, we saw more clearly weird excitation

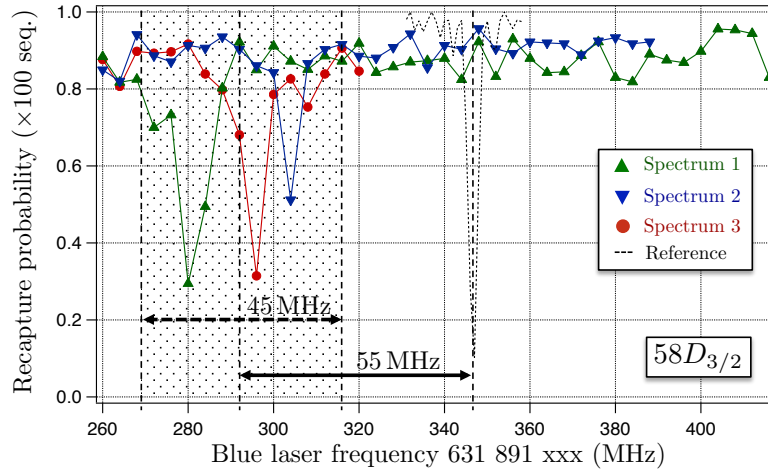


Figure 4.10: Spectroscopy of the Rydberg state $58D_{3/2}$ realized with and without the ITO coating.

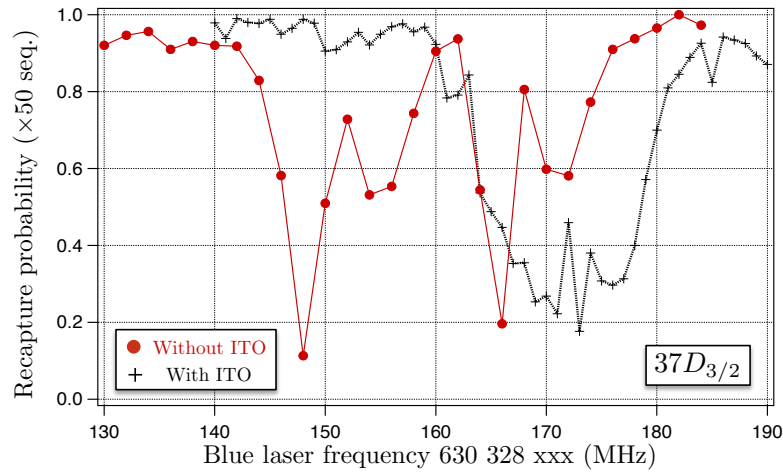


Figure 4.11: Spectroscopy of the Rydberg state $37D_{3/2}$ realized with and without the ITO coating.

spectra. Three of them are shown in Fig. 4.10 (a) in blue (down triangles), red (circles) and green (up triangles) respectively. The three were obtained with the exact same set of laser pulses parameters. For comparison, the reference spectrum of the same Rydberg state from Fig. 4.9 (b), which we obtained with ITO, and after having compensated for DC stray fields, is represented by the black dashed line.

The conclusion was twofold. First, the DC stray fields were not negligible and could be estimated using the polarizability $\alpha(58D_{3/2}) \simeq 600 \text{ MHz}/(\text{V}/\text{cm})^2$ and the average shift observed $\Delta E \simeq 55 \text{ MHz}$ to about $|F| = [2\Delta E/\alpha(58D_{3/2})]^{1/2} \simeq 0.45 \pm 0.15 \text{ V}/\text{cm}$. Second, they fluctuated between two spectrum acquisitions. Each data point is an average result over 100 sequences and the repetition rate of the experiment was slightly higher than 1 Hz, so one spectrum typically took 30-40 minutes. Thus, the amplitude of the electric field seen by the atoms was drifting on long time scales, but slow enough that we could still resolve some excitations features. To confirm this, we tried to aim at a lower excited Rydberg state, with a lower polarizability.

Rydberg state $37D_{3/2}$ (without ITO)

We studied next the state $37D_{3/2}$ of polarizability¹⁵ $\alpha(37D_{3/2}) \simeq 24 \text{ MHz}/(\text{V}/\text{cm})^2$. Thus, we checked that with a residual field estimated on the order of $0.45 \pm 0.15 \text{ V}/\text{cm}$, we could find the transition at the expected frequency within 2.5 MHz. The result obtained also after piling up five Rydberg pulses with optimized duration is shown in red (circles) in Fig. 4.11. For comparison, we also show in black (crosses) the reference spectrum of the same state obtained afterwards when the apparatus was working fine. The red spectrum exhibited four peaks. The two peaks on the right were identified as the branches $|m_j| = 1/2$ (right) and $|m_j| = 3/2$ (left), the latter being shifted three times more in external electric fields.

These results clearly indicated that without ITO coating, parasitic electric fields prevented us performing coherent Rydberg excitations.

4.4.2 Stark spectroscopy with single atoms

Once we had reopened the system, installed other lenses coated with ITO, and reached UHV conditions again¹⁶, the Rydberg transitions were found much closer to the expected two-photon frequencies. Furthermore, they were not shifted anymore from one spectrum measurement to another.

Excitation spectra in external electric fields

The next step was then to test the electrodes installed inside the vacuum chamber by performing the spectroscopy of a chosen Rydberg state in the presence of an external controlled electric field.

With the octopole geometry of electrodes described in Sec. 1.2.3, we saw that a field $\mathbf{F} = F_i \mathbf{u}_i$ with $i = x, y, z$ could be obtained in principle by applying the electric potentials V_i^+ on the four electrodes on one side of plane P_i , and V_i^- on the four electrodes on the other side of plane P_i . In practice, one of the eight electrodes was grounded, and only three parameters ΔV_x , ΔV_y and ΔV_z allowed to compute the electric potential required on each electrode so to achieve a field $\mathbf{F} = F_x \mathbf{u}_x + F_y \mathbf{u}_y + F_z \mathbf{u}_z$. The field amplitudes F_i are of the form $F_i = \Delta V_i / l_i$, where the coefficients l_i are effective lengths that we needed to calibrate using the Rydberg atoms as references.

The Stark spectroscopy measurements were performed with the state $58D_{3/2}$. We started by varying ΔV_x with $\Delta V_y = \Delta V_z = 0 \text{ V}$ to tune the amplitude F_x of the electric field along the axis x , transverse to the quantizations axis z . The sequence we used was the same as the one shown in Fig. 4.9 (a) and it was repeated 50 times for each value of the field. The amplitude of the quantization magnetic field was -3 G .

The results are shown in Fig. 4.12. When $|\Delta V_x|$ was larger than about 5 V, two peaks are identified. The one shifted the most is indicated by a black arrow with a solid line, and can be attributed to the branch $|m_j| = 3/2$ of the state $58D_{3/2}$. The other one that remains almost unshifted with the variation of ΔV_x is indicated by a black dashed arrow, and can

¹⁵The polarizability $\alpha(nD_{3/2})$ scales as n^{*7} , where n^* is the effective quantum defect (see Sec. B.1.1). For $nD_{3/2}$, the quantum defect is 1.35, so the polarizability of the state $37D_{3/2}$ was estimated to $\alpha(37D_{3/2}) = \alpha(58D_{3/2}) \cdot (35.65/56.65)^7 \simeq 24 \text{ MHz}/(\text{V}/\text{cm})^2$

¹⁶We could also take advantage of this second bake-out procedure to improve slightly the vacuum performances, mostly by activating more properly the NEG pump, as described in Sec. 1.3.3. The improvements could be estimated by measuring a lifetime $\tau \simeq 8 \text{ s}$ of the atoms in the trap (to be compared to $\tau \simeq 3 \text{ s}$ before, as described in Sec. 2.3.1).

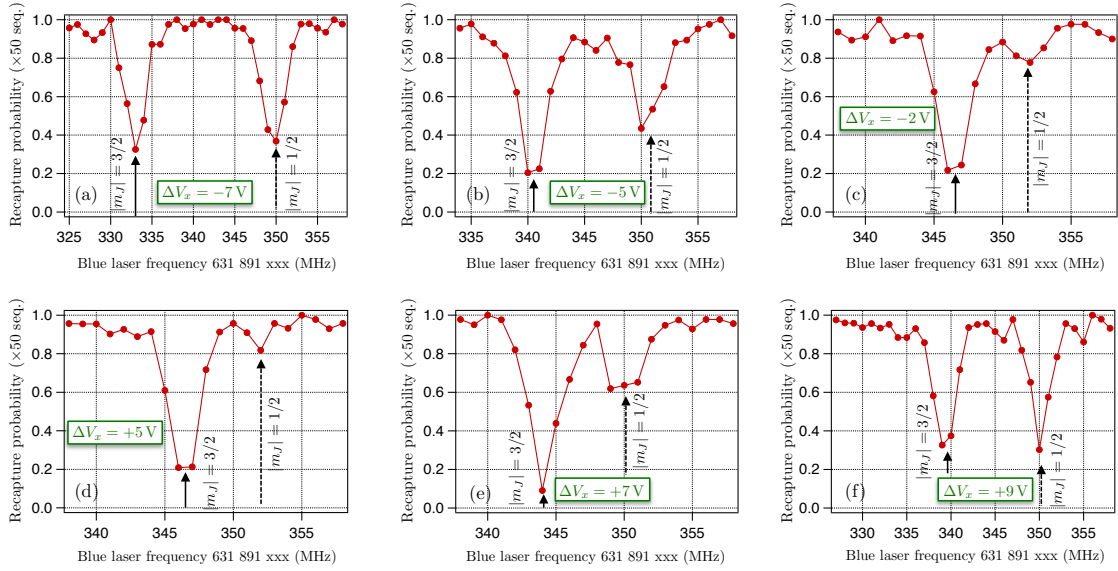


Figure 4.12: Excitation spectra of Rydberg state $|58D_{3/2}, m_j = 3/2\rangle$ in external electric field along the transverse x direction.

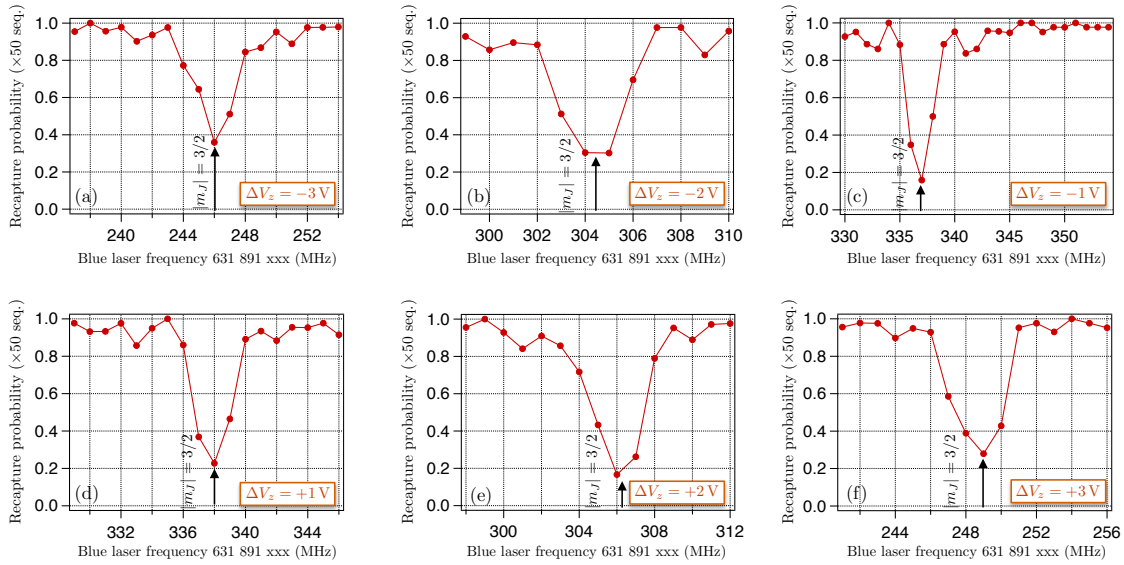


Figure 4.13: Excitation spectra of Rydberg state $|58D_{3/2}, m_j = 3/2\rangle$ in external electric field along the transverse z direction.

be attributed to the branch $|m_j| = 1/2$. Indeed, in the presence of transverse electric fields, the eigenstates of the total hamiltonian are mixed states: the eigenstates corresponding to the branch $|m_j| = 1/2$ contain a fraction of the original state $|58D_{3/2}, m_j = 3/2\rangle$ which we could couple to. However, the mixing decreases as the amplitude of the transverse electric field seen by the atom decreases, and so the coupling strength to the second peak decreases as well. The second peak almost disappeared when $-2\text{ V} \leq \Delta V_x \leq +2\text{ V}$.

Then we repeated the same procedure for the other two axes y and z . The spectra obtained for the y -axis were very similar to the ones for axis x . However, the spectra obtained for the z -axis are slightly different, as shown in Fig. 4.13. As we expected, we did not see any second peak appear for large values of ΔV_z . Indeed, in this case, the electric

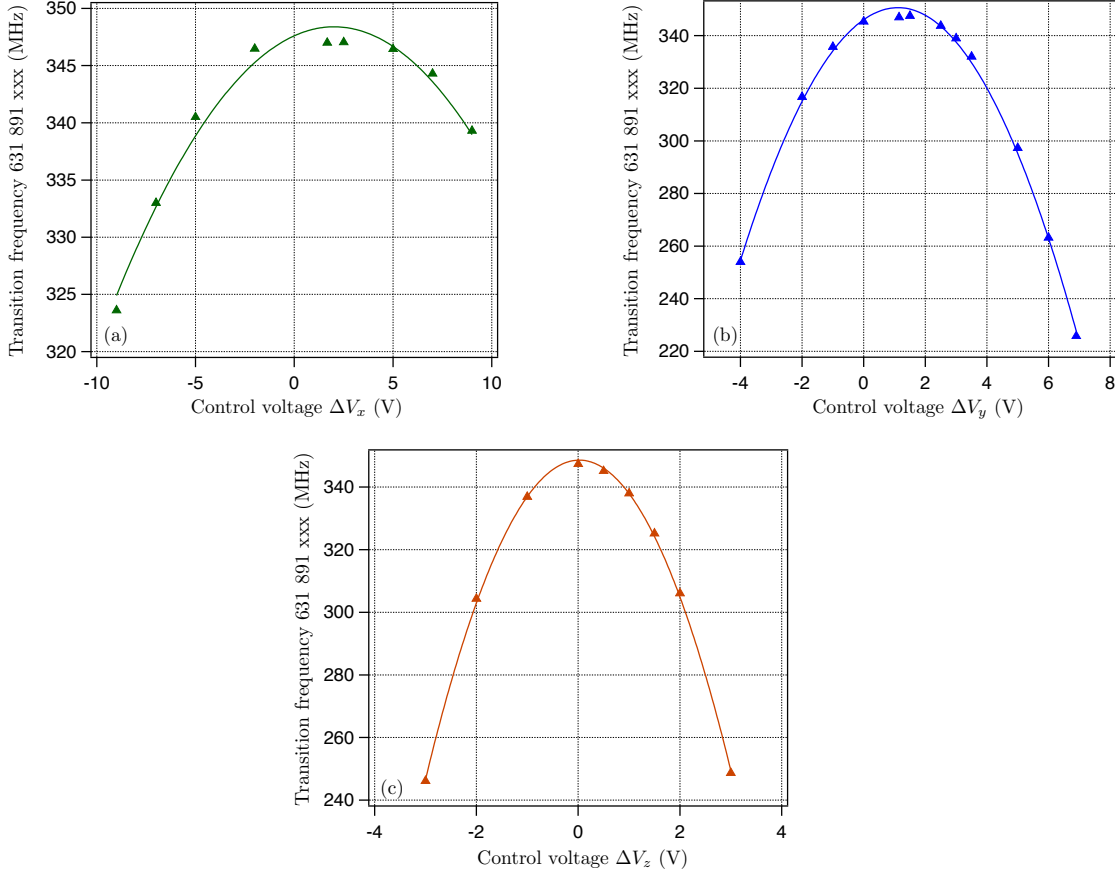


Figure 4.14: Stark spectroscopy of the branch $|m_j| = 3/2$ of state $58D_{3/2, j=3/2}$. (a), (b) and (c) show respectively the frequency of the Rydberg laser at 474 nm on resonance with the transition as a function of ΔV_x , ΔV_y and ΔV_z . The solid lines are fits of the form $\nu_{B_0} + C_i(\Delta V_i - \Delta V_{i_0})^2$.

field can not mix two states belonging to branches with different values of $|m_j|$. As long as the Stark effect is quadratic, the state $|58D_{3/2}, m_j = 3/2\rangle$ remains an eigenstate of the total hamiltonian.

Experimental Stark maps

In Fig. 4.14, we plotted the evolution of the transition frequency attributed to the branch $|m_j| = 3/2$ as a function of the voltages ΔV_x , ΔV_y and ΔV_z respectively in (a), (b) and (c). The curves have nice symmetrical shape and this procedure allowed us to measure the voltages ΔV_{i_0} to apply in order to compensate for stray electric fields. Furthermore, a calibration of the electric field applied on the atoms can be obtained by comparing the data with calculated Stark shifts. For D states, these shifts are quadratic in weak electric fields (see Sec. B.1.6). However, for the data points obtained at large field along y and z , the energy shifts were up to about 100 MHz, which is larger than the fine structure splitting of the state $58D$ (on the order of 50 MHz). We probably explored the regime where the shift was not quadratic anymore.

Accurate calculations of Stark maps are currently underway. However, the polarizability of the state $|58D_{3/2}, m_j = 3/2\rangle$ had already been calculated in the group. In a preliminary approach, we fitted our experimental data by quadratic functions of the form $\nu_{B_0} - C_i(\Delta V_i -$

Axis	Coefficient C_i	Effective length l_i^{cal}	Effective length l_i^{simu}
x	$C_x = 0.19 \text{ MHz/V}^2$	$l_x^{\text{cal}} \simeq 40 \text{ cm}$	$l_x^{\text{simu}} \simeq 19.2 \text{ cm}$
y	$C_y = 3.7 \text{ MHz/V}^2$	$l_y^{\text{cal}} \simeq 9 \text{ cm}$	$l_y^{\text{simu}} \simeq 4.4 \text{ cm}$
z	$C_z = 11.2 \text{ MHz/V}^2$	$l_z^{\text{cal}} \simeq 5.2 \text{ cm}$	$l_z^{\text{simu}} \simeq 3.7 \text{ cm}$

Table 4.1: Calibration of the electrodes.

$\Delta V_{i_0})^2$, where the C_i coefficients are expressed in MHz/V^2 . Then, by combining C_i with the value of the polarizability $\alpha \simeq 550 \text{ MHz}/(\text{V}/\text{cm})^2$ of the state $|58D_{3/2}, m_j = 3/2\rangle$, we could obtain a rough calibration of the effective length $l_i^{\text{cal}} = [\alpha/(2C_i)]^{1/2}$ allowing to estimate the field $F_i = \Delta V_i/l_i^{\text{cal}}$ seen by the atoms, as listed in Tab. 4.1.

With this procedure, we obtained large deviations between the values l_i^{simu} predicted by 3D simulations (see Sec. 1.2.3) and the calibrated values l_i^{cal} , even along the x axis for which the shifts were not so large compared to the fine structure splitting, and thus for which we probably explored the quadratic regime.

To understand better these deviations, we consider first comparing the data with more accurate Stark maps. Second, another explanation could be that the 3D simulations did not include the presence of the dielectric ceramic spacers used for isolating the electrodes from the central steel piece. The relative permittivity ϵ_r of these ceramics is on the order of 5. Adding these boundary conditions into the 3D model may alter the structure of the electric field at the position of the atoms, and would be consistent with the lower field amplitudes that we observed.

4.4.3 Coherent Rabi oscillations in compensated electric field

Finally, we performed coherent transitions between the initial ground state $|5S_{1/2}, F = 2, m_F = 2\rangle = |1\rangle$ and a chosen Rydberg state $|nD_{3/2}, m_j = 3/2\rangle$. The experimental sequences implemented were the same as the ones shown in Fig. 4.9 (a), except that the frequency ν_B of the laser at 474 nm was fixed, and we varied the duration t of the pulse at 795 nm. A spectrum measurement as described before was always performed just before starting the acquisition of Rabi oscillation measurements, to determine the frequency ν_{B_0} of the two-photon Rydberg resonance.

Four typical results obtained with the Rydberg state $|62D_{3/2}, m_j = 3/2\rangle$ are presented in Fig. 4.15. These four cases provide an overview of the data we obtained with one-atom experiments over the full range of values of Ω that we could achieve. In each case, we compare the experimental data with two models:

- In the figures (a), (c), (e) and (g), the solid line (green) is the solution of the optical Bloch equations solved for the 5-level system $\{|0\rangle, |1\rangle, |2\rangle, |3\rangle, |4\rangle\}$, as described in Sec. 4.2.1, which includes an input parameter η_{Rydberg} that takes into account an effective Rydberg detection efficiency, as it is described below. The decay rates in the dissipations are the intrinsic lifetimes of each state. The parameters $\Omega_B/2\pi$ and $\Delta/2\pi$ of the hamiltonian were fixed at about 40 MHz and 740 MHz. Then, we adjusted the last parameter $\Omega_R/2\pi$ and δ to fit the data. Finally, as our Rydberg detection scheme allows to detect atoms that would be recaptured at the end of a sequence, what we reconstruct experimentally is the probability not to be in the Rydberg state, which reads in this model $1 - \rho_{33}(t)$, where $\rho_{33}(t)$ is the normalized population into

the Rydberg state $|3\rangle$. The solid line shown in the figures (a) are fits of the form $1 - \eta_{\text{Rydberg}} \cdot \rho_{33}(t)$, with $\eta_{\text{Rydberg}} = 0.95$.

- In the figures (b), (d), (f) and (h), the solid line (blue) is a fit of the experimental data by the function $P_{|g\rangle}(\Omega, \gamma, t)$ from Eq. 4.8 with Ω and γ as free parameters.

In all cases, the power of the laser at 474 nm was about 90 mW. Only the power of the laser at 795 nm was varied to adjust the two-photon effective Rabi frequency Ω .

Case: $8 \text{ MHz} \leq \Omega/2\pi$

One example is shown in Fig. 4.15 (a)-(b) and was obtained with a power of 8 mW at 795 nm. In this case, the oscillations were damped significantly even between the first and the second arch. As $\Omega_R \simeq \Delta$, the dissipation due to the spontaneous scattering at 795 nm induced by the intermediate state $5P_{1/2}$ is not negligible. When such a process occur, the atom can decay into the states $|0\rangle$ or $|4\rangle$ (see Fig. 4.2) which do not participate anymore to the excitation dynamics. However, an atom that would have decayed to one of these two states is trapped again by the optical tweezer, and it is recaptured at the end of a sequence. That is why the recapture probability that we reconstruct is damped asymmetrically. This is very well reproduced by the first model in green.

The effective two-level model can not reproduce this pattern and thus becomes really inaccurate after the fourth arch. It is however good enough to reproduce the data up to about the second arch. We will see in the next chapter that the generalization of this effective model applied to a two-atom system could thus be used in this limit to fit the data of two-atom experiments.

Case: $1 \text{ MHz} \leq \Omega/2\pi \leq 4.3 \text{ MHz}$

Two results are shown in Figs. 4.15 (c)-(d) and (e)-(f), that were obtained respectively with a power of 2.1 mW and 200 μW at 795 nm. In this case, the damping of the oscillation is small. Therefore, the two models are almost equally good to describe the experimental data.

Case: $\Omega/2\pi \leq 0.6 \text{ MHz}$

Finally, we discuss a last example for which the effective Rabi frequency was tuned below 1 MHz. The result is shown in Fig. 4.15 (g)-(h) and was obtained with a power of 31 μW at 795 nm. Here, although we accessed only to one and a half arch of the Rabi oscillations, the shape of the damping observed experimentally seems to be more symmetric.

Here, other effects come into play. First, the Doppler effect due to the non-zero temperature of our distribution of single atoms in the trap has to be averaged out over the 100 sequences realized for each data point. The typical width of the velocity distribution at $T = 50 \mu\text{K}$ is $\sigma_v = (k_B T/m)^{1/2} \simeq 0.06 \text{ m/s}$. The order of magnitude of this effect can thus be estimated to about $\sigma_\delta^{\text{Doppler}} = |\vec{k}_R + \vec{k}_B| \cdot \sigma_v \simeq 2\pi \times 150 \text{ kHz}$. This was studied in details in Ryabtsev *et al.* (2011) and it can be seen that the related damping could exhibit a much more symmetric shape. Second, the linewidths of the Rydberg lasers, estimated on the order of 200 kHz each, and residual fluctuations of the transfer cavity lock also induce fluctuations of the effective two-photon detuning δ .

An effective approach to take these effects into account is to use a distribution of effective detunings $P(\delta)$ that would be centered on zero. Then, the experimental data result in the

convolution of this distribution with the model chosen to describe the Rabi oscillations. The dashed line represented on Figs. 4.15 (g)-(h) is the result of the convolution of the function $P_{|g\rangle}(\Omega, \gamma=0, t)$ used in our second model by a gaussian distribution of detunings with $1/e^2$ width $\sigma = 2\pi \times 250$ kHz.

Summary of the results

The results obtained for these four typical set of parameters are summed up below in Tab. 4.2. All the data were obtained with $\Delta = 2\pi \times 740$ MHz. We compare the values of the effective Rabi frequency Ω^{th} computed using Eq. 4.4 with the values Ω^{fit} obtained from the fits. The ratio is systematically on the order of 1.5 which could be due to an error in estimating the size of the red or the blue beams at the position of the atoms. Also, we can notice that the effective Rabi frequency Ω^{th} tend to be overestimated at large values of Ω_R by using Eq. 4.4. This is expected as the condition $\Omega_R \ll \Delta$ is not verified anymore.

We also compare the values of the scattering rate Γ_{sc} computed using Eq. 4.6 with the value γ^{fit} obtained from the fits using the effective two-level approach. The two decay rates seems to match rather well in the middle of the range of Ω . However, when Ω_R is not negligible compared to Δ , Eq. 4.6 is not valid at all anymore. On the contrary, when Ω_R is very small compared to Δ , we discussed above various other sources of damping that explain why the effective damping γ^{fit} extracted from the fits do not agree with the prediction of Eq. 4.6.

Case	$\Omega_R/2\pi$	$\Omega^{\text{th}}/2\pi$	$\Omega^{\text{fit}}/2\pi$	$\Omega^{\text{th}}/\Omega^{\text{fit}}$	$\Gamma_{\text{sc}}/2\pi$	$\gamma^{\text{fit}}/2\pi$	$\Gamma_{\text{sc}}/\gamma^{\text{fit}}$
1	435 MHz	13 MHz	8 MHz	1.62	0.5 MHz	0.15 MHz	3.5
2	220 MHz	6.5 MHz	4.3 MHz	1.54	0.13 MHz	0.11 MHz	1.2
3	68 MHz	2 MHz	1.4 MHz	1.44	0.017 MHz	0.021 MHz	0.82
4	27 MHz	0.8 MHz	0.6 MHz	1.34	0.007 MHz	0.035 MHz	0.20

Table 4.2: Summary of the coherent Rydberg excitation parameters. $\Omega_B/2\pi = 40$ MHz for all the experiments.

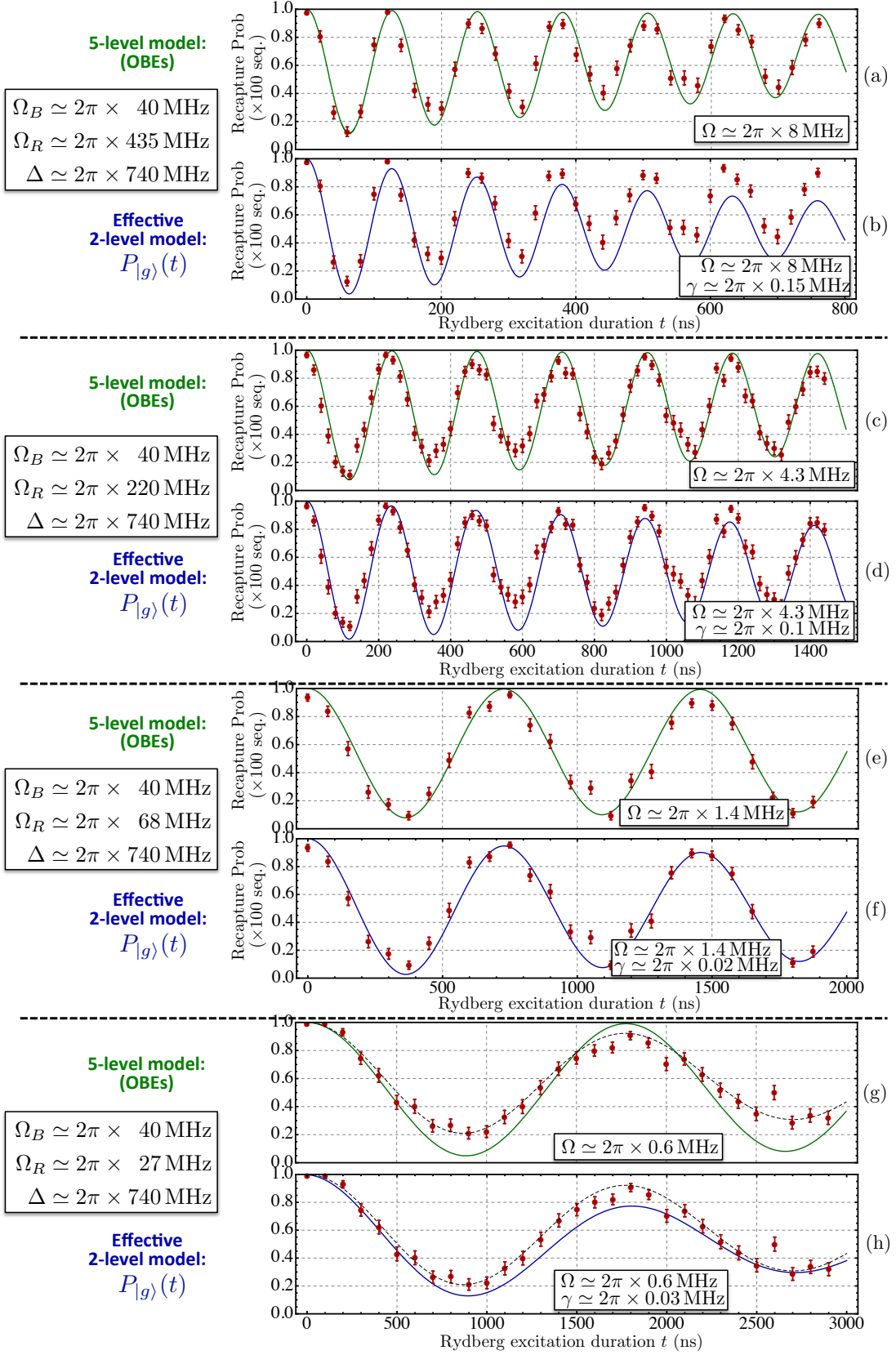


Figure 4.15: Rabi oscillations on the transition $|1\rangle \rightarrow |3\rangle = |62D_{3/2}, m_j = 3/2\rangle$. (a) and (b): $\Omega/2\pi \simeq 8$ MHz. (c) and (d): $\Omega/2\pi \simeq 4.3$ MHz. (e) and (f): $\Omega/2\pi \simeq 1.4$ MHz. (g) and (h): $\Omega/2\pi \simeq 0.6$ MHz.

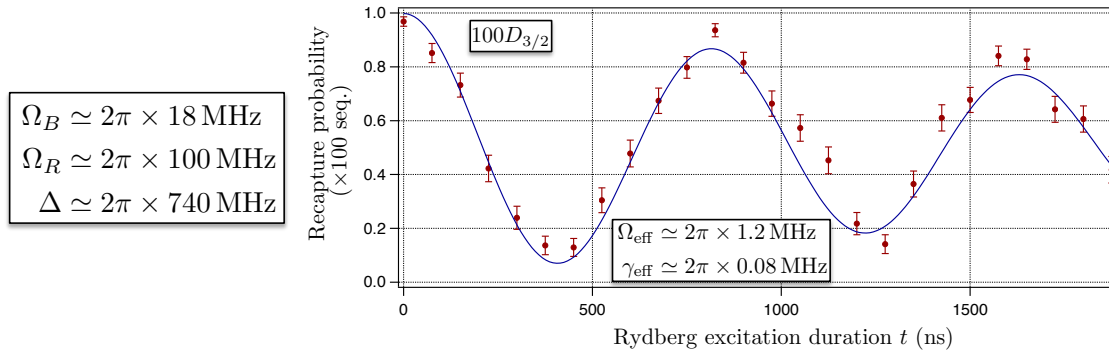


Figure 4.16: Rabi oscillation on the transition $|1\rangle \rightarrow |3\rangle = |100D_{3/2}, m_j = 3/2\rangle$.

4.4.4 Conclusion

The Rydberg setup that we implemented was good enough to achieve highly contrasted Rabi oscillations towards the Rydberg state $|62D_{3/2}, m_j = 3/2\rangle$, proving a good stability of the two-photon transition detuning δ , with residual fluctuations below 200 kHz. However, a second version of the laser lock using an ultra-stable cavity from Boulder Precision E-O has recently replaced the transfer cavity from Coherent and should allow to reduce even more the residual fluctuations of the effective detuning δ . Then, by cooling further initially the atoms (adiabatic ramp, sideband cooling), this could allow to observe much lower damping for small excitation Ω .

Also, the implementation of the electrodes that cancel the residual stray field amplitude allowed to prevent the targeted Rydberg states from mixing with other neighbouring Rydberg states. We will see in Sec. 5.2.5 that this improved the quality of the blockade experiments.

Finally, in Fig. 4.16, we show the results that we obtained with $n=100$, in order to test the stability of the electric field seen by the atoms. The damping fitted from the data of about $2\pi \times 0.08$ MHz might not be due only to the spontaneous scattering described by Eq. 4.6 (on the order of $2\pi \times 0.03$ MHz) and could show the influence of residual electric field fluctuations due to electronic noise on our electrodes. Fortunately, it is not necessary to reach such highly excited states in order to implement the Rydberg blockade mechanism within arrays of up to 5×5 atoms with a site separation of 4-5 μm .

Chapter 5

Direct measurement of the van der Waals interaction between two Rydberg atoms

Contents

5.1	Van der Waals interactions between Rydberg atoms: an overview	112
5.2	Experimental investigation of the blockade	114
5.2.1	Two-trap setup and calibration of R	115
5.2.2	Experimental sequences and typical data	117
5.2.3	Fully independent regime: $n = 62$ and $R = 15.5 \mu\text{m}$	119
5.2.4	Blockade regime: $n = 62$ and $R = 4 \mu\text{m}$	120
5.2.5	Cancellation of electric field matters!	122
5.2.6	Partial blockade regime	123
5.3	Modeling of partial blockade	127
5.3.1	Schrödinger equations in the effective 3-level system	127
5.3.2	Bloch equations in the 4-level system	128
5.3.3	Extraction of $ \Delta E /h$ and error bars analysis	129
5.3.4	Measurements of the van der Waals interaction	132
5.4	Theoretical calculations of the interaction ΔE	134
5.4.1	Construction of the basis	135
5.4.2	Calculation of dipole matrix elements $\langle n', l', j', m'_j \hat{d}_q n, l, j, m_j \rangle$	136
5.4.3	C_6 calculations from second-order perturbation theory	137
5.4.4	Diagonalization of the interaction hamiltonian	139
5.4.5	Conclusion	141

In this chapter, we report the direct measurement of the van der Waals interaction between two Rydberg atoms separated by a tunable distance R of a few micrometers. It represents the first physics experiment done with the new experimental apparatus. Fine control of the interaction is demonstrated, which allows us to observe the blockade with enhanced performances with respect to the experiences of 2008-2009 (Gaetan, 2009). This

control represents the main result of the thesis, and opens exciting perspectives for the future implementation of multi-particle entanglement.

The van der Waals-Loudon interaction $\Delta E(R) = C_6/R^6$ between two neutral, polarizable particles separated by a distance R is more common than one would think in everyday life. It underlies a wide range of physical effects, from the condensation of non-polar gases, to the ability of geckos or spiders to climb on sheer surfaces (Israelachvili, 2010), or the rearrangement of proteins inside the human body.

However, it is a very weak interaction that only becomes relevant when the inter-particle separation becomes very small, which makes it rather hard to probe. For a macroscopic system, van der Waals interaction between the constituent atoms or molecules can be inferred by measuring thermodynamics quantities (Hiemenz and Rajagopalan, 1997). At the level of individual particles, spectroscopy of the vibrational levels close to the dissociation limit of a diatomic molecule, analyzed semiclassically, allows one to extract the long-range interaction between atoms (LeRoy and Bernstein, 1970). Progress in atomic physics allowed to measure it between atoms and a surface with a variety of techniques (Aspect and Dalibard, 2002). However, a direct measurement of the interaction between two individual atoms in their ground state would be extremely challenging as it is very small (\leq mHz in frequency units). In contrast, the interaction between Rydberg atoms is much stronger, and scales rapidly with the principal quantum number as n^{11} . Using this property, interaction between Rydberg atoms and a surface has been measured at relatively large distances (Anderson *et al.*, 1988; Sandoghdar *et al.*, 1992).

Here, we report on the measurement of the C_6/R^6 interaction between two isolated Rydberg atoms prepared in a well defined quantum state. We will start by introducing the main properties of the van der Waals interaction between two atoms excited to Rydberg states. Then, we will present our experimental observations of the blockade. Fine control of the interaction allowed us to investigate the partial blockade regime for which the single-atom Rabi frequency Ω for excitation to a chosen Rydberg state $|r\rangle$ is on the same order of magnitude than the energy shift $\Delta E(R) = C_6/R^6$ of the doubly excited state $|rr\rangle$. The two-atom system was initially prepared in the ground state and submitted to a Rydberg excitation. In this regime, the time-evolutions of each two-atom state populations exhibit coherent oscillations with several characteristic frequencies that depend strongly on the ratio $\Delta E(R)/\hbar\Omega$. We will show that a rather simple model based on the optical Bloch equations is in good agreement with the experimental data, and allowed us to extract the van der Waals energy for various interatomic distances and for several Rydberg states. We could thus observe the C_6/R^6 dependence of this interaction, and check the dramatic variations of the C_6 coefficients with n between the states $n = 53, 62$ and 82 , as we reported in Béguin *et al.* (2013) (we reproduced the paper in App. E). Finally, we will describe ab-initio calculations of the C_6 coefficients, which agree well with the experimental values that we measured.

5.1 Van der Waals interactions between Rydberg atoms: an overview

We consider our experimental configuration of two alkali ^{87}Rb atoms A and B separated by a distance $R > 3\ \mu\text{m}$, assuming the absence of external electric or magnetic fields. In their ground state, the two atoms interact mostly via the magnetic dipole-dipole interaction which scales as $1/R^3$ but which remains weaker than 1 Hz in frequency units (Saffman and Molmer, 2010). On the other hand, if the two atoms are brought to excited Rydberg states

which exhibit large electric dipole moments, the electrostatic interaction is enhanced by several orders of magnitude and becomes the dominant interaction that shifts the energy of the doubly excited state $|rr\rangle$. When the typical size of each atomic wavefunction is much smaller than the separation R between the atoms¹, one can restrict the multipole expansion of the electrostatic hamiltonian to the dominant dipole-dipole term between the dipole $\hat{\mathbf{d}}_A$ and $\hat{\mathbf{d}}_B$:

$$\hat{H}_{dd} = \frac{1}{4\pi\epsilon_0} \frac{\hat{\mathbf{d}}_A \cdot \hat{\mathbf{d}}_B - 3(\hat{\mathbf{d}}_A \cdot \mathbf{u})(\hat{\mathbf{d}}_B \cdot \mathbf{u})}{R^3}, \quad (5.1)$$

where $\mathbf{u} = \mathbf{R}/|\mathbf{R}|$ is a unit vector pointing from atom A towards atom B . We consider this hamiltonian as a weak perturbation to the unperturbed hamiltonian \hat{H}_0 describing the two-atom system. To first order, the energy shift $\Delta E^{(1)}$ of a given two-atom state $|rr\rangle$ due to the perturbation is zero:

$$\Delta E^{(1)} = \langle \hat{H}_{dd} \rangle = \frac{1}{4\pi\epsilon_0} \frac{\langle r | \hat{\mathbf{d}}_A | r \rangle \langle r | \hat{\mathbf{d}}_B | r \rangle - 3 \langle r | \hat{\mathbf{d}}_A \cdot \mathbf{u} | r \rangle \langle r | \hat{\mathbf{d}}_B \cdot \mathbf{u} | r \rangle}{R^3} = 0, \quad (5.2)$$

because the atom states $|r\rangle$ are of definite parities, and the dipole operators $\hat{\mathbf{d}}_{A,B}$ are odd operators. Thus, one needs to lead the perturbative calculation to second order. The energy shift $\Delta E^{(2)} = \Delta E$ of the two-atom state $|rr\rangle$ takes the form:

$$\Delta E = \frac{C_6}{R^6}. \quad (5.3)$$

This resulting interaction is the van der Waals-London interaction that decays rather quickly with the interatomic distance as $1/R^6$. The C_6 coefficient can be computed by the expression:

$$C_6 = \sum_{|\phi, \phi'\rangle} \frac{|\langle \phi | \hat{\mathbf{d}}_A | r \rangle \langle \phi' | \hat{\mathbf{d}}_B | r \rangle - 3 \langle \phi | \hat{\mathbf{d}}_A \cdot \mathbf{u} | r \rangle \langle \phi' | \hat{\mathbf{d}}_B \cdot \mathbf{u} | r \rangle|^2}{(4\pi\epsilon_0)^2 (2E_r - (E_\phi + E_{\phi'}))}, \quad (5.4)$$

where the summation involves all the possible states $|\phi, \phi'\rangle = |n, l, j, m_j\rangle_A \otimes |n', l', j', m'_j\rangle_B$ different from the state $|rr\rangle$. A detailed procedure to compute these coefficients will be presented at the end of the chapter. However, we can already get a quick estimate of these coefficients using the characteristic scaling laws that apply to alkali Rydberg states. Indeed, let us consider the terms that appear in the sum in Eq. 5.4:

- The numerators are composed of the sum of products of two dipole matrix elements, which are then squared. For Rydberg states, the size of the wave functions scales roughly as $a_0 n^2$, so the dipole element increases as $ea_0 n^2$. Thus, the numerators in Eq. 5.4 scale as $e^4 a_0^4 n^8$.
- The denominators can be written as the sum of the two terms that involve the difference between two-atom states energies $(E_r - E_\phi) + (E_r - E_{\phi'})$. The energy of a Rydberg state scale approximately as R_y/n^2 , where R_y is the Rydberg unit of energy. If we forget about possible resonances² for which the two terms could almost

¹In our case, the size of the Rydberg wavefunctions scales as $a_0(n^*)^2$ (see Sec. B.1.4). For Rydberg states $n \leq 100$, the size of the wavefunctions are smaller than 500 nm which fulfill the condition above for the range of interatomic distances $R > 3 \mu\text{m}$ to which we have access experimentally.

²Such resonances are called quasi-Förster resonances, see Sec. B.2.1.

cancel out, the energy difference between two neighbouring Rydberg states scale then as R_y/n^{-3} .

In the end, the C_6 coefficients scale as n^{11} and can be expressed with typical atomic quantities by:

$$C_6 \approx \frac{e^4 a_0^4 n^{11}}{R_y}. \quad (5.5)$$

With this naive scaling, the van der Waals interaction should lead to an energy shift of about 20 MHz for doubly excited states $|n_A, n_B\rangle$ with $n = 62$ and separated by $3 \mu\text{m}$. Such a shift would be an order of magnitude larger than the width of the Rydberg excitation $\hbar\Omega$ that we can achieve to excite a single atom towards such a Rydberg state, as we showed in Sec. 4.4.3, and should thus allow us to observe the blockade regime described in Sec. 4.1.

In reality, a few resonant terms in the expression of a C_6 coefficient for which the denominators are very small can strongly affect the resulting value (Reinhard *et al.*, 2007). For some Rydberg states, one or a few terms with the same sign exhibit strong resonances which tend to increase the expected value. On the contrary, it can also happen for other Rydberg states that a few terms with opposite signs perfectly cancel out, reducing dramatically the amplitude of the coefficient, as we will see in more details in Sec. 5.4.3.

5.2 Experimental investigation of the blockade

In this section, we will present the observation of the blockade mechanism for several two-atom states $|rr\rangle$, where $|r\rangle = |nD_{3/2}, m_J = 3/2\rangle$ is coupled to the atom ground state $|g\rangle = |5S_{1/2}, F = 2, m_F = 2\rangle$ by the effective Rabi frequency Ω . The van der Waals interaction shifts the eigenenergy of $|rr\rangle$ by the quantity $\Delta E_n(R)$. The principle of the experiments is the following. Initially, the two-atom system is prepared in the ground state $|gg\rangle$ when the Rydberg excitation pulse is sent. By varying the interatomic distance and thus the relative strength of $\Delta E_n(R)$ and $\hbar\Omega$, two limiting regimes can be identified, as shown in Fig. 5.1:

- if $\Delta E_n(R) \ll \hbar\Omega$, then the two atoms behave independently, and the doubly excited state $|rr\rangle$ can be coherently populated,
- if $\Delta E_n(R) \gg \hbar\Omega$, then the excitation of $|rr\rangle$ is off-resonant. This is the mechanism called the Rydberg (or dipole) blockade.

In the second case, the ground state $|gg\rangle$ couples in fact to the entangled state:

$$|\Psi\rangle_{\text{ent.}} = \frac{1}{\sqrt{2}} \left(e^{i\mathbf{k} \cdot \mathbf{R}_A} |rg\rangle + e^{i\mathbf{k} \cdot \mathbf{R}_B} |gr\rangle \right), \quad (5.6)$$

where the phase factors $e^{i\mathbf{k} \cdot \mathbf{R}_A}$ and $e^{i\mathbf{k} \cdot \mathbf{R}_B}$ depend on the position of each atom A and B in their corresponding dipole traps, at the time of the excitation³. A clear experimental signature that the ground state couples to an entangled state is the enhancement of the effective coupling to the single excitation branch by a factor $\sqrt{2}$, that can be directly measured experimentally as we are going to show below.

³Previous experiments on the former apparatus showed that this rather short-lived state $|\Psi\rangle_{\text{ent.}}$ with random phase factors could be mapped with a second Rydberg pulse onto the more useful entangled state $(|g'g\rangle + |gg'\rangle)/\sqrt{2}$, where $|g'\rangle = |5S_{1/2}, F = 1, m_F = 1\rangle$. This cancels out the random phase factors (Wilk *et al.*, 2010).

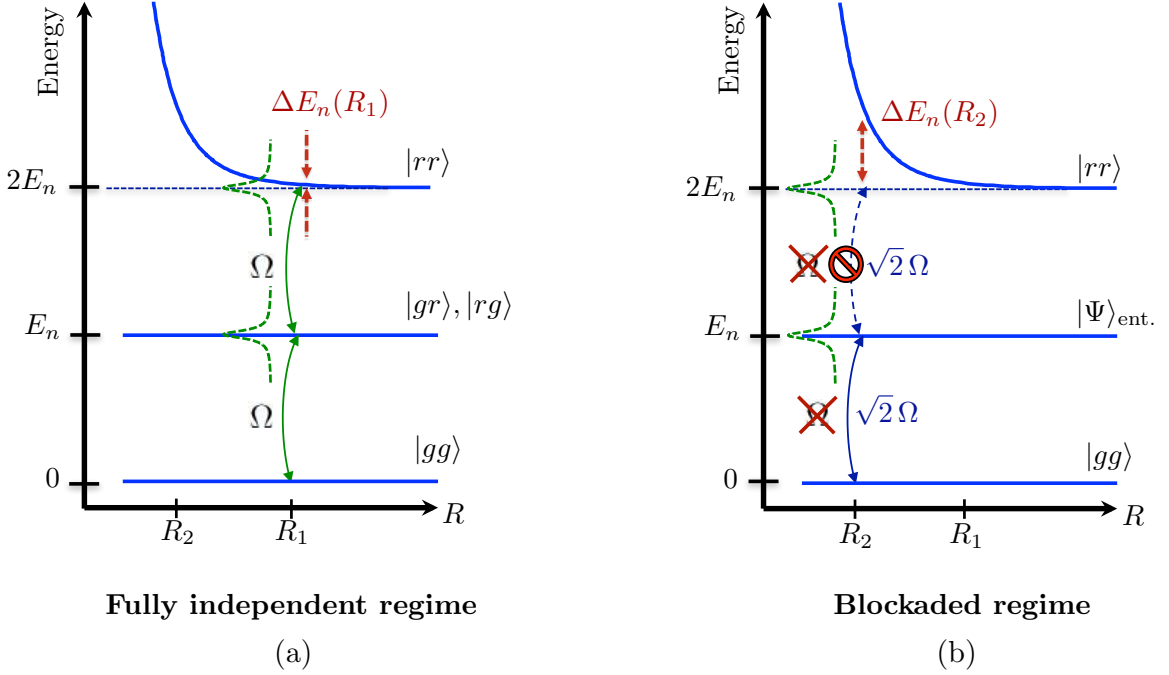


Figure 5.1: Excitation of the two-atom system in two limiting regimes. (a) Fully independent regime. The interatomic distance $R = R_1$ is so large that $\Delta E_n(R_1) \ll \hbar\Omega$ and the two atoms behave completely independently. (b) Blockaded regime. On the contrary in this case the interatomic distance $R = R_2$ is so small that $\Delta E_n(R_2) \gg \hbar\Omega$ and the doubly excited state $|rr\rangle$ is completely off-resonant with the Rydberg excitation. In this case, the ground state $|gg\rangle$ couples to an entangled state $|\Psi\rangle_{\text{ent.}}$ with a collective coupling enhanced by a factor $\sqrt{2}$ as compared to the single-atom case.

First, we will present the experimental results corresponding to these two limiting regimes independent of $\Delta E_n(R)$. Then, we will show results obtained in the transition region in which $\Delta E_n(R)$ and $\hbar\Omega$ are on the same order of magnitude, which we will refer to as the *partial blockade regime*. In this regime, the dynamics will thus exhibit two characteristic frequencies that are combination of $\Delta E_n(R)/\hbar$ and $\Omega/2\pi$.

5.2.1 Two-trap setup and calibration of R

A first description of the setup implemented to trap two single atoms was given in Sec. 1.4.2. It is shown again in Fig. 5.2(a). A trapping laser beam was brought to a breadboard facing the vacuum chamber via a PM fiber. There, a first PBS cube allowed to separate it in two beams shown in green and red that correspond respectively to the two distinct dipole traps A and B. These two beams were combined onto a second PBS cube with a small angle θ , they were both projected onto the same vertical linear polarization and were finally focused by the aspheric lens of focal length $f = 10$ mm. In the focal plane, they were thus separated by the distance $R = f\theta$. In order to investigate the blockade mechanism as a function of the interatomic distance R , the first step was to be able to measure rather accurately the separation between the two dipole traps. Indeed the interaction scaling as $1/R^6$, only 10% uncertainty on the trap separation would already yield a bias of about a factor 2 on the interaction energy.

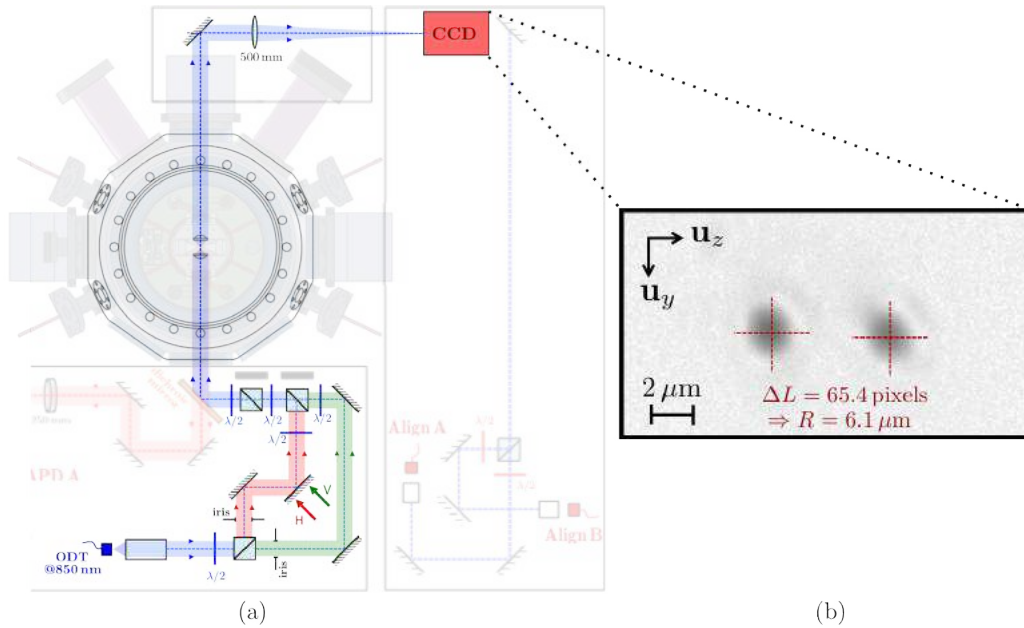


Figure 5.2: Setup used for two-atom experiments. (a) Overview of the breadboard used for sending the two dipole traps at a controlled interatomic distance R . The vertical (V) and horizontal (H) screws of the mirror mount that we adjusted to vary the distance R are indicated with two arrows. (b) Typical picture taken with the CCD shown in (a). The two spots were fitted by 2D gaussians to determine the positions of the centers (y_1, z_1) and (y_2, z_2) . The distance between the two traps (measured in pixels) was then determined by $\Delta L = \sqrt{(z_2 - z_1)^2 + (y_2 - y_1)^2}$, assuming that the traps are focused in the same plane.

For this, we used a cheap CCD camera⁴ with a pixel size of $4.65 \mu\text{m}$ to image the two trapping beams after they have been transmitted through the chamber. The imaging system was composed of the second aspheric lens under vacuum, of focal length $f = 10 \text{ mm}$, and a plano-convex lens of focal length $f = 500 \text{ mm}$ placed behind the chamber, as shown in Fig. 5.2(a). Thus, the yz plane of the trapped atoms was conjugated onto the CCD sensor with a magnification of about 50. The dipole traps of $2 \mu\text{m}$ diameter in real space are thus imaged onto about 20 pixels, as shown in Fig. 5.2(b).

We calibrated our imaging system by measuring the displacement of the image of one trap onto the camera after turning the vertical screw (V) of the Fine Adjustment mirror mount depicted in Fig. 5.2(a) by half a turn, e.g. 180° , yielding a displacement of 354 ± 1 pixels. Beforehand, we had measured with the same mirror in the same position the variation of the incident angle of this trapping beam for half a turn of the screw. We had found $\theta = 3.3 \text{ mrad}$ with a relative uncertainty below 3%. Finally, by trusting the focal length specification of the first aspheric lens $f = 10 \pm 0.1 \text{ mm}$, we can measure that the displacement of one trap in the atoms plane for half a turn is about $f\theta = 33 \mu\text{m}$ with a relative uncertainty below 4%. The resulting relative uncertainty on the value of R was below 5%. In the end, we computed the distance between the two dipole traps in real space R by measuring the distance (in pixels) between their images ΔL that we multiplied by the calibration factor K , which read:

$$R = K \cdot \Delta L \quad \text{with} \quad K = \frac{33}{354} = 93 \text{ nm/pixel}. \quad (5.7)$$

⁴CCD camera DMK 41BU02 from Imaging Source[®].

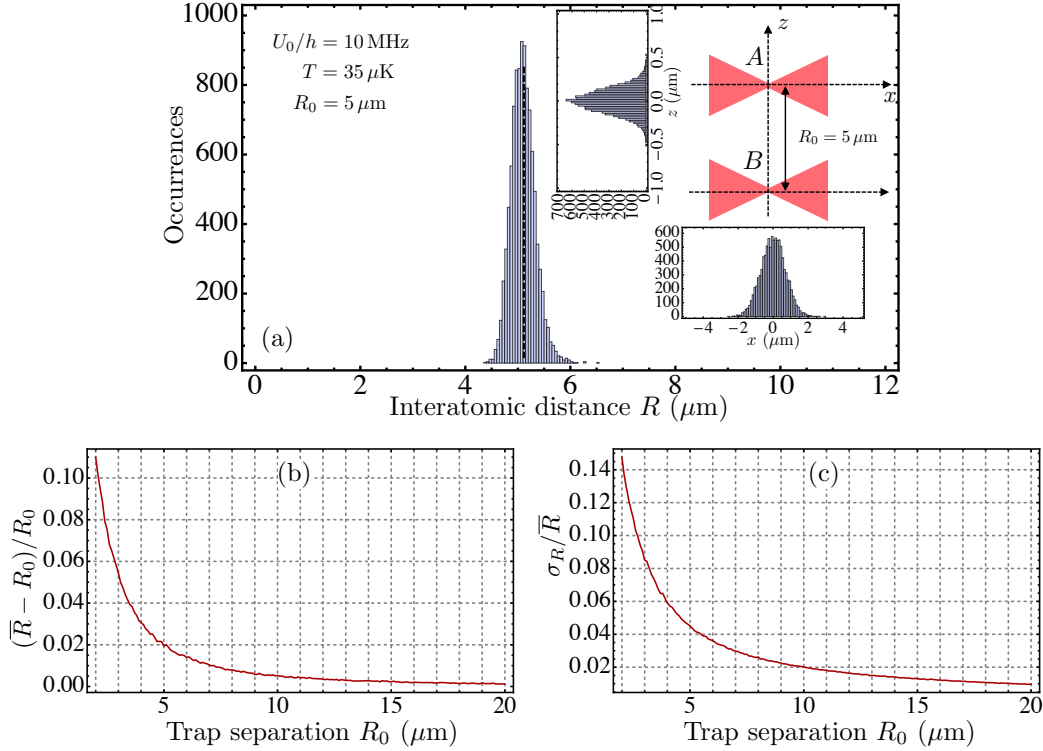


Figure 5.3: Dispersion in R . (a) Histogram of the distances R , when the two traps are separated by $R_0 = 5 \mu\text{m}$, obtained for $U_0/h = 10 \text{ MHz}$ and $T = 35 \mu\text{K}$. The inset shows the typical width of the transverse and longitudinal positions of an atom in one tweezer. (b) represents $(\bar{R} - R_0)/R_0$. (c) represents the relative width of the distribution σ_R/\bar{R} .

Dispersion in R due to the atoms temperature

As we already described in Sec. 2.3.2, the energy distribution of our trapped atoms just before sending the Rydberg excitation pulse can be described by a thermal Boltzmann distribution of temperature $T \simeq 35 \mu\text{K}$. The position of a trapped atom is thus normally distributed, with the standard deviations $\sigma_{\perp} = \sqrt{k_B T / (m\omega_{\perp}^2)} \simeq 130 \text{ nm}$ in the transverse directions y and z of the trap, and $\sigma_{\parallel} = \sqrt{k_B T / (m\omega_{\parallel}^2)} \simeq 700 \text{ nm}$ along x , with our experimental parameters $U_{\text{trap}}/h \simeq 10 \text{ MHz}$ and $w_{\text{trap}} (@1/e^2) \simeq 1 \mu\text{m}$. It means that when the two atoms are held in two dipole traps separated by the distance R_0 , their interatomic distance R at the time of the Rydberg excitation varies from one experiment to another. Fig. 5.3 (a) shows the histogram of R obtained for 10000 samples with $R_0 = 5 \mu\text{m}$.

The mean \bar{R} of the distribution is slightly larger than the distance measured between the two traps R_0 (see Fig. 5.3 (b)). The difference is below 2% for $R > 5 \mu\text{m}$, such that we decided to assume $\bar{R} \approx R_0$. Also, Fig. 5.3 (c) shows that the standard deviation of the distribution σ_R is less than 5% of the mean \bar{R} for $R_0 > 5 \mu\text{m}$. Thus, we did not take into account the dispersion in the interatomic distances into our data analysis.

5.2.2 Experimental sequences and typical data

The experimental configuration implemented to study the blockade mechanism is sketched in Fig. 5.4(a). The interatomic axis was aligned with the quantization axis along the ver-

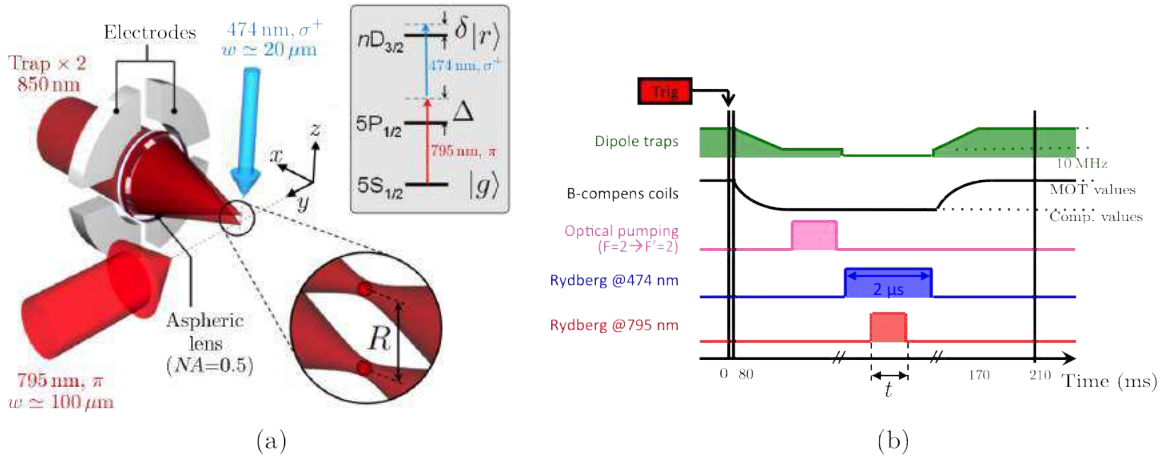


Figure 5.4: Experimental configuration to investigate the blockade. (a) Sketch of the experimental setup. Two atoms are trapped in microscopic optical tweezers separated by R . The inset shows the two photon excitation scheme. The intermediate detuning was always $\Delta \simeq 2\pi \times 740$ MHz. (b) Main features of the experimental sequence. The thick vertical black bar at $t = 0$ ms symbolizes the initial atom presence checking procedure (step 1 in Fig. 2.2).

tical z . The experimental sequences realized with two atoms were the same as the ones used for observing the coherent Rydberg excitation of a single atom, described in Sec. 4.4.3. The depths of the two traps were decreased to about 10 MHz (in frequency units) and we performed an initial stage of optical pumping that prepared the system into the ground state $|gg\rangle$, as shown in Fig. 5.4(b). At this point, the dipole traps were switched off to perform the Rydberg excitation in free space for a variable duration t . The two traps were then switched back on and their power were ramped up to their original value. Finally, a last fluorescence measurement was performed to check independently if the atoms A and B were recaptured at the end of the sequence.

The complete procedure we used for the blockade measurements was the following. Once the distance R was adjusted to the desired value, we always performed experiments with only one atom, by blocking the trapping beam A or B . With only one trap, an initial scan (as described in Sec. 4.3.4) allowed us to tune the frequency of the blue laser ν_B on resonance with the targeted Rydberg state $|nD\rangle$, e.g. $\delta \simeq 0$ (see the inset in Fig. 5.4(a)). Then, this frequency was fixed and we only varied the duration of the Rydberg excitation t . Such coherent excitation measurements with atom A alone, and then atom B alone, allowed to measure individually the experimental Rabi frequencies Ω_A and Ω_B of each atom. The sequence was repeated a hundred times for each excitation duration t_i and for each atom. Typically, we could check that the Rabi frequencies Ω_A and Ω_B experienced by the two atoms were the same within less than 5%. Finally, the two traps were sent together in the chamber and similar Rabi oscillation measurements were performed using the same sequence, but triggered on the simultaneous presence of the two atoms.

With one-atom experiments (repeating the sequence about 100 times for each duration t_i), we can thus reconstruct:

- P_{g_A} , the probability to recapture atom A . We will then assume that the probability P_{r_A} to have excited the atom A in the Rydberg state $|r\rangle$ reads $P_{r_A} = 1 - P_{g_A}$,
- P_{g_B} , the probability to recapture atom B . We will assume that the probability P_{r_B} to have excited the atom B in the Rydberg state reads $P_{r_B} = 1 - P_{g_B}$.

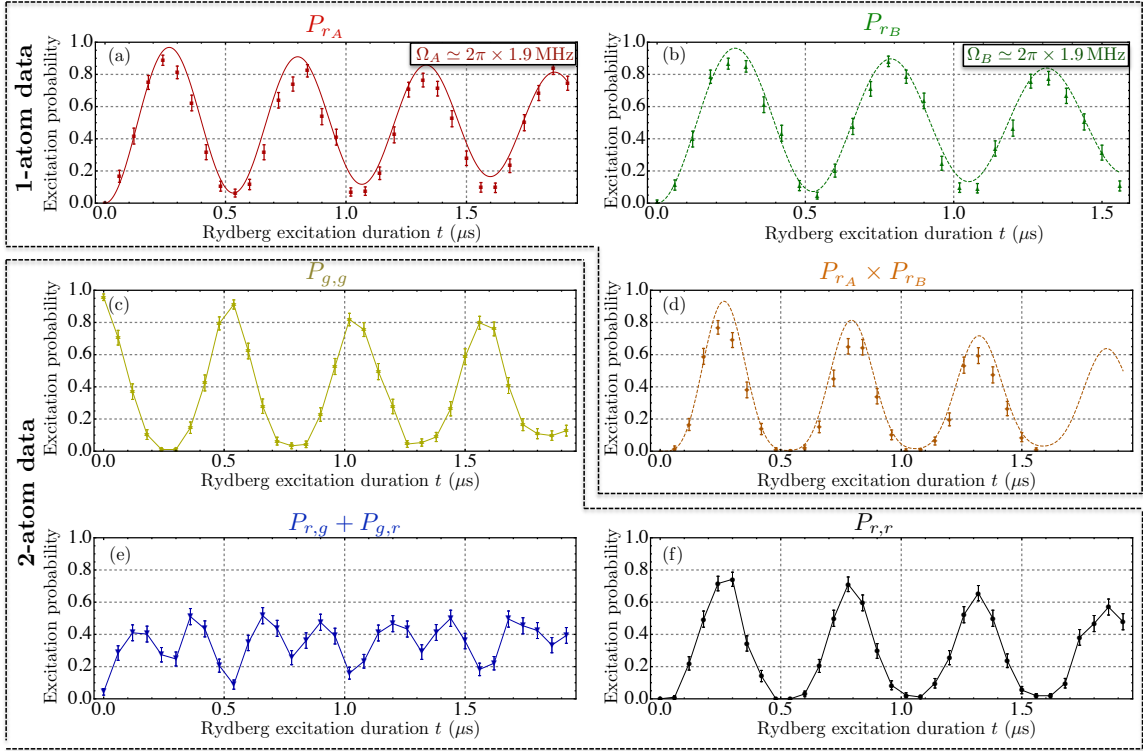


Figure 5.5: Independent regime. The block containing (a), (b) and (d) shows results obtained with one-atom experiment. The block containing (c), (e) and (f) shows results obtained with two-atom experiments. (a) and (b) show respectively the coherent excitation of atom A (red squares) alone and atom B (green up triangles) alone towards the state $|62D_{3/2}, m_J = 3/2\rangle$. All the data points are averaged over 100 sequences. (d) shows the product $P_{r_A} \cdot P_{r_B}$ obtained from the experimental data (orange diamonds). The error bars show the statistical uncertainties. The solid lines are the fits using the function $P_{|g\rangle}(\Omega, \gamma, t)$ from Eq. 4.8. Then, (c), (e) and (f) show respectively the data of the two-atom populations P_{gg} (yellow stars), $P_{r,g} + P_{g,r}$ (blue down triangles) and P_{rr} (black disks). The data points are joined to guide the eye.

With two-atom experiments (repeating the sequence 100 times for each duration t_i with the two atoms initially present), we can thus reconstruct:

- P_{gg} , the probability to excite neither atom A or B ,
- P_{rg} , the probability to excite atom A but not atom B ,
- P_{gr} , the probability to excite atom B but not atom A ,
- P_{rr} , the probability to excite both atoms A and B .

For one or two-atom experiments, the duty cycle is about 1 Hz. Taking a set of data with 20 duration t_i takes about 30 min for atom A alone, 30 min for atom B , and then 30 min for the two-atom experiment.

5.2.3 Fully independent regime: $n = 62$ and $R = 15.5 \mu\text{m}$

We will start by showing the typical results obtained in the case where the two atoms are far enough from each other to behave independently. The state was $|62D_{3/2}\rangle$ and the two atoms were separated by $R = 15.5 \mu\text{m}$. First, we show in Fig. 5.5 the results of the one-atom experiments performed with atom A alone (a), then atom B alone (b), from

which we extracted the effective Rabi frequencies Ω_A and Ω_B , that were measured to be at about $\simeq 2\pi \times 1.9$ MHz within 5%. As discussed in Sec. 4.4.3, the data exhibits a small damping mainly due to the spontaneous emission via the intermediate state $5P_{1/2}$. We then performed the same experiment with the two atoms at the same time. In the ideal case where the van der Waals interaction would be perfectly zero, the two atoms should behave completely independently. Assuming that the Rydberg excitations had no dissipation, the evolution of the populations P_{r_A} and P_{r_B} for one-atom experiments would read:

$$P_{r_A}(t) = P_{r_B}(t) = \sin^2(\Omega t/2) \quad \text{and} \quad P_{g_A}(t) = P_{g_B}(t) = \cos^2(\Omega t/2). \quad (5.8)$$

Thus, the populations of the two-atom states would evolve as:

$$P_{rr}(t) = P_{r_A}(t) \cdot P_{r_B}(t) = \sin^4(\Omega t/2) \quad (5.9)$$

$$P_{gg}(t) = P_{g_A}(t) \cdot P_{g_B}(t) = \cos^4(\Omega t/2), \quad (5.10)$$

and,

$$\begin{aligned} P_{rg}(t) + P_{gr}(t) &= P_{r_A}(t) \cdot [1 - P_{r_B}(t)] + [1 - P_{r_A}(t)] \cdot P_{r_B}(t) \\ &= 2 \sin^2(\Omega t/2) \cos^2(\Omega t/2) \\ &= \frac{1}{2} \sin^2(\Omega t). \end{aligned} \quad (5.11)$$

Indeed, the data we obtained for the population P_{gg} (resp. P_{rr}) shown in (c) (resp. (f)) is shaped as a \cos^4 (resp. \sin^4) function. The oscillations are damped and the contrast is not exactly one, but this is expected as the Rabi oscillations obtained for one-atom excitation are not 100% contrasted. A more accurate comparison can be done between (d) showing the product $P_{r_A} \cdot P_{r_B}$ computed with the experimental data for each atom A and B obtained independently, and (f) showing the evolution of P_{rr} . The two sets of data match very well. Finally, we also notice that the data corresponding to $P_{rg} + P_{gr}$ shown in (c) exhibit a coherent evolution with a frequency at twice the one-atom frequencies $\Omega_{A,B}$ and with an amplitude varying between 0 and 0.5, as expected from Eq. 5.11. Let us number the minima assuming that the first one is the first point at $t=0$. One can see that even minima are not as low as the odd ones. These even minima of $P_{rg} + P_{gr}$ occur when P_{rr} is maximum, and experimentally limited to about 0.75. Indeed, the excitations of the atoms A or B alone do not exceed about 90% efficiency (see Fig. 5.5 (a) and (b)), thus the doubly excited state population cannot exceed about 0.8, while P_{gg} is expected to be about 0.01. Thus, as $P_{rr} + (P_{rg} + P_{gr}) + P_{gg} = 1$, the even minima can not be lower than about 0.2.

5.2.4 Blockade regime: $n = 62$ and $R = 4 \mu\text{m}$

We now show in Fig. 5.6 the results obtained with the same parameters but with the atoms closer to each other, at a distance of $R = 4 \mu\text{m}$. In (c), (e) and (f), one can see the evolution of the various two-atoms states. In this case, the comparison between (d) and (f) shows clearly that $P_{rr} \neq P_{r_A} \cdot P_{r_B}$. The doubly excited state is almost never populated: $P_{rr} \leq 0.06$ up to $t = 2 \mu\text{s}$. Taking into account the imperfections of single atom excitations, the quality of the blockade is almost compatible with 100%. We show below in Sec. 5.2.5 that this was achieved thanks to the cancellation of stray electric fields. This demonstrates that the new apparatus allows to reach a new level of control over the dipole-dipole interaction, and thus fulfill its main requirement. These results are very promising for the future investigations of entanglement schemes based on the blockade!

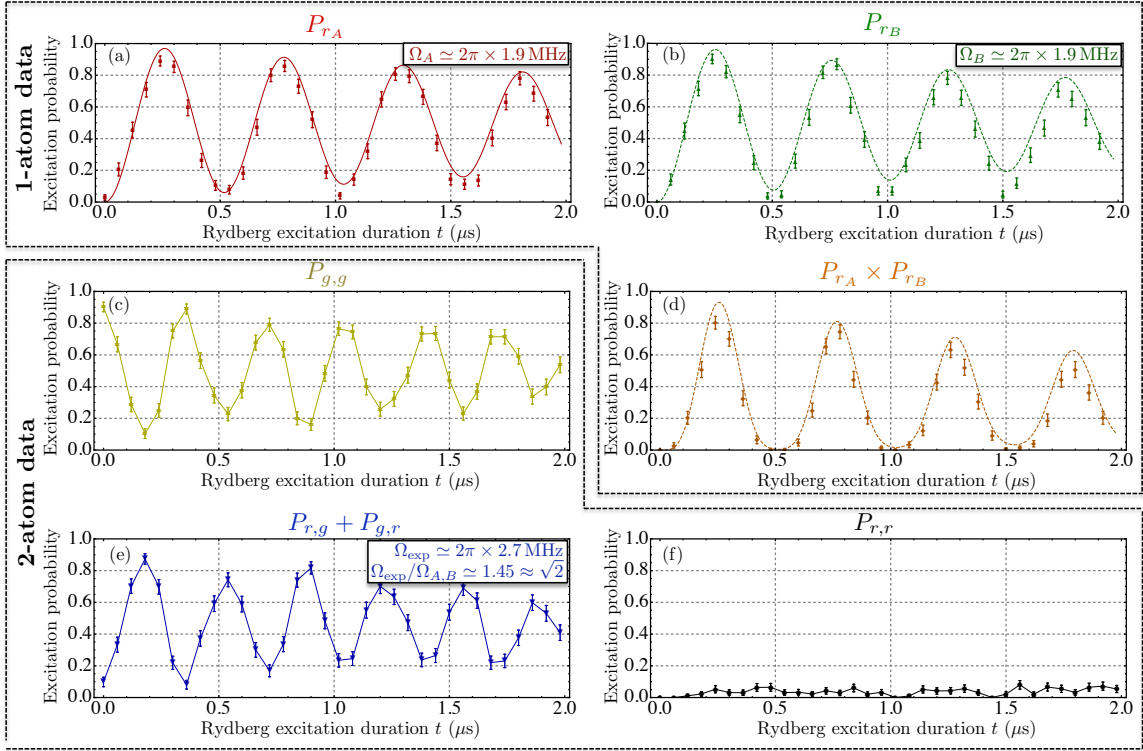


Figure 5.6: Blockaded regime. Same as Fig. 5.5, but with $R = 4 \mu\text{m}$ instead of $15.5 \mu\text{m}$.

Indeed, in Fig. 5.6, we notice that the sum $P_{rg} + P_{gr}$ evolves as a sine function at a frequency enhanced by a factor $1.45 \approx \sqrt{2}$ compared to the one-atom references $\Omega_{A,B}$. This can be understood rather simply by introducing the two-atom Dicke states:

$$\begin{cases} |\Psi_{\text{Dicke}}^+\rangle = \frac{1}{\sqrt{\Omega_A^2 + \Omega_B^2}} \left(\Omega_A e^{i\mathbf{k} \cdot \mathbf{R}_A} |rg\rangle + \Omega_B e^{i\mathbf{k} \cdot \mathbf{R}_B} |gr\rangle \right) \\ |\Psi_{\text{Dicke}}^-\rangle = \frac{1}{\sqrt{\Omega_A^2 + \Omega_B^2}} \left(\Omega_B e^{i\mathbf{k} \cdot \mathbf{R}_A} |rg\rangle - \Omega_A e^{i\mathbf{k} \cdot \mathbf{R}_B} |gr\rangle \right), \end{cases} \quad (5.12)$$

and using the basis $\{|gg\rangle, |\Psi_{\text{Dicke}}^+\rangle, |\Psi_{\text{Dicke}}^-\rangle, |rr\rangle\}$ to describe our two-atom system. For each atom A and B , the ground state $|g\rangle$ is coupled to the excited state $|r\rangle$ by the electric dipole hamiltonian, with an effective coupling $\hbar\Omega_{A,B}e^{-i\mathbf{k} \cdot \mathbf{R}_{A,B}}$. The two-atom states $|gg\rangle$ and the Dicke state $|\Psi_{\text{Dicke}}^+\rangle$ are thus coupled by the operator \hat{V} expressed by:

$$\hat{V} = \hbar\Omega_A e^{i\mathbf{k} \cdot \mathbf{R}_A} |r\rangle \langle g|_A \otimes \mathbb{1}_B + \hbar\Omega_B e^{i\mathbf{k} \cdot \mathbf{R}_B} \mathbb{1}_A \otimes |r\rangle \langle g|_B + h.c. \quad (5.13)$$

Then, the coupling Ω_C between the two-atom states $|gg\rangle$ and $|\Psi_{\text{Dicke}}^+\rangle$ is:

$$\begin{aligned} \hbar\Omega_C &= \langle \Psi_{\text{Dicke}}^+ | \hat{V} |gg\rangle \\ &= \langle \Psi_{\text{Dicke}}^+ | \left(\hbar\Omega_A e^{i\mathbf{k} \cdot \mathbf{R}_A} |rg\rangle + \hbar\Omega_B e^{i\mathbf{k} \cdot \mathbf{R}_B} |gr\rangle \right) \\ &= \hbar\sqrt{\Omega_A^2 + \Omega_B^2}. \end{aligned} \quad (5.14)$$

If we assume further that $\Omega_A = \Omega_B = \Omega$, then we finally have $\Omega_C = \sqrt{2}\Omega$. The collec-

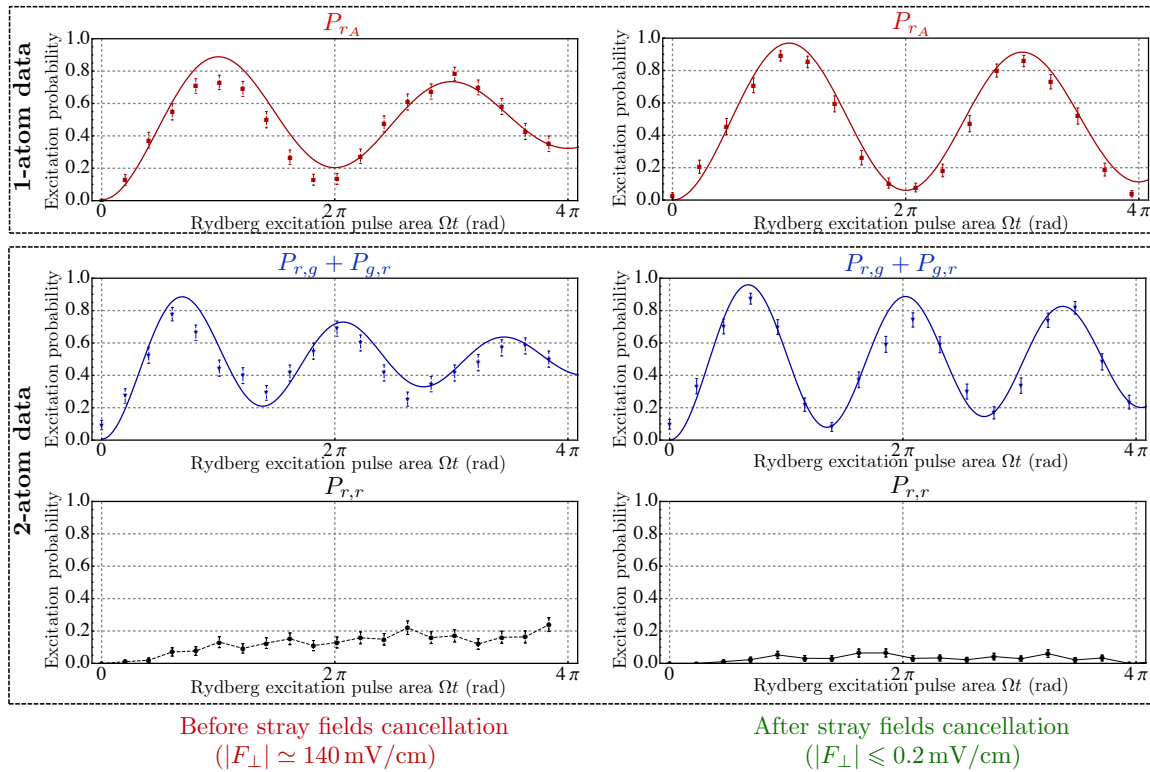


Figure 5.7: Comparison of blockade data before and after the cancellation of stray electric fields. *Left:* One-atom and two-atom excitation data with transverse fields of amplitude estimated to $|F_{\perp}| \simeq 140$ mV/cm. *Right:* typical data with $|F_{\perp}| \leq 0.2$ mV/cm.

tive coupling to the two atom state $|\Psi_{\text{Dicke}}^+\rangle$ is $\sqrt{2}$ times as large as the coupling for an atom alone. In a similar way, one can check that the coupling between $|gg\rangle$ and $|\Psi_{\text{Dicke}}^-\rangle$ is zero. So, during the excitation, the two-atom state can be written as the sum $|\Psi\rangle = c_{gg}|gg\rangle + c_{\text{ent}}|\Psi_{\text{Dicke}}^+\rangle + c_{rr}|rr\rangle$. In our experiment, $|\Psi\rangle$ is projected onto the natural basis $\{|gg\rangle, |rg\rangle, |gr\rangle, |rr\rangle\}$, and thus we measure the populations $P_{gg} = |c_{gg}|^2$, $P_{rr} = |c_{rr}|^2$ and the two populations P_{rg} and P_{gr} . Finally, the sum $P_{rg} + P_{gr} = 1 - (P_{gg} + P_{rr})$ corresponds precisely to a measurement of the initial population $|c_{\text{ent}}|^2 = 1 - (|c_{gg}|^2 + |c_{rr}|^2)$ of the state $|\Psi_{\text{Dicke}}^+\rangle$ before the projection.

5.2.5 Cancellation of electric field matters!

We mentioned in Chap. 4 that residual transverse electric fields can induce non negligible mixing between the chosen Rydberg state $|r\rangle$ and other neighbouring Rydberg states not coupled to $|g\rangle$ via the laser excitation, or exhibiting Förster zeros (Walker and Saffman, 2008). In practice, we compared the data obtained before and after having compensated the residual electric fields with the electrodes for the same set of parameters. Results are shown in Fig. 5.7 for $n = 62$, $R = 4 \mu\text{m}$, and $\Omega \simeq 2\pi \times 2$ MHz.

For one-atom experiment, the damping of the oscillations towards the state $|62D_{3/2}, m_j = 3/2\rangle$ was larger with stray fields. This could be due to coupling with other neighbouring states $|r_i\rangle$ close in energy, most probably from the branch $|m_j| = 1/2$, which mix partially with

the targeted state $m_j = 3/2$. As we used typically a magnetic field of about 3 G, such states were shifted in energy by a few MHz via the Zeeman effect and the couplings might thus have been slightly off-resonant. Beatnotes between the different excitation channels might result in an apparent damping of the oscillations on the timescale of the excitation. For two-atom experiments, the damping of the oscillations towards the entangled state was also much larger with stray fields, and the doubly excited state got partially populated over time: $P_{rr} \simeq 0.20$ at $t = 2 \mu\text{s}$.

The cancellation of these fields was thus a crucial milestone in the experiment that improved at once the quality of the blockade, and opened promising perspectives for the study of multi-particle entanglement.

5.2.6 Partial blockade regime

After having investigated the two limiting regimes of blockade, we now turn to the intermediate regime where the van der Waals energy ΔE_n is on the same order as the width of the Rydberg excitation $\hbar\Omega$. We repeated the same measurements for various interatomic distances. In this regime, the behaviour of the collective system is governed by the two frequencies Ω and ΔE . Therefore, as Ω can be measured independently using one-atom experiment, a careful analysis of the two-atom data should yield ΔE .

The results obtained in the case $n = 62$ for a Rabi frequency $\Omega = 2\pi \times 4.3 \text{ MHz}$ and R equals to 6.8, 7.8 and 8.8 μm and are shown in Fig. 5.8. It was convenient to show the results as a function of the Rydberg pulse area in order to compare them to the ones obtained for the extreme regimes presented above. On the left in (a), P_{r_A} shows the coherent Rabi oscillation between $|g\rangle$ and $|r\rangle$ obtained with only trap A while the trap B was switched off. On the right, we show the product $P_{r_A} \times P_{r_B}$ computed with the experimental data P_{r_A} and P_{r_B} obtained with single-atom experiments performed successively with each trap. Then from (b) to (f), we show the coherent evolution of the populations $P_{rg} + P_{gr}$ and P_{rr} , respectively in the left and the right columns. (b) and (f) show the data corresponding to the limiting cases already presented above. For intermediate distances, we observe *partial blockade* for which the doubly excited state $|rr\rangle$ can be partially populated. In this regime, the evolution of the populations $P_{rg} + P_{gr}$ and P_{rr} exhibit several frequencies. The resulting time-dependent features are related to the ratio between the van der Waals energy ΔE_n and the width of the Rydberg excitation $\hbar\Omega$. As we will see in the following section 5.3, these can be very well understood by simply solving the Schrödinger equations in the three-level system with the states $|gg\rangle$, $|\Psi_{\text{Dicke}}\rangle$ and $|rr\rangle$.

After having studied the case $n = 62$, we applied the same method to the cases $n = 53$ and $n = 82$. A selection of the results for each case are shown in Fig. 5.9 and Fig. 5.10. The data shown for the case $n = 53$ were obtained with a single-atom Rabi frequency $\Omega = 2\pi \times 0.9 \text{ MHz}$. One can notice that the damping of the oscillations is slightly larger than in the case $n = 62$, which could be explained by residual fluctuations of the excitation detuning (see Sec. 4.4.3). The data shown in the case $n = 82$ were obtained with a single-atom Rabi frequency $\Omega = 2\pi \times 4.3 \text{ MHz}$, and show also a larger damping than the ones obtained in the case $n = 62$. There, the dissipation is essentially due to spontaneous emission via the $5P_{1/2}$ intermediate state, as we had to use large power at 795 nm to achieve $\Omega = 2\pi \times 4.3 \text{ MHz}$.

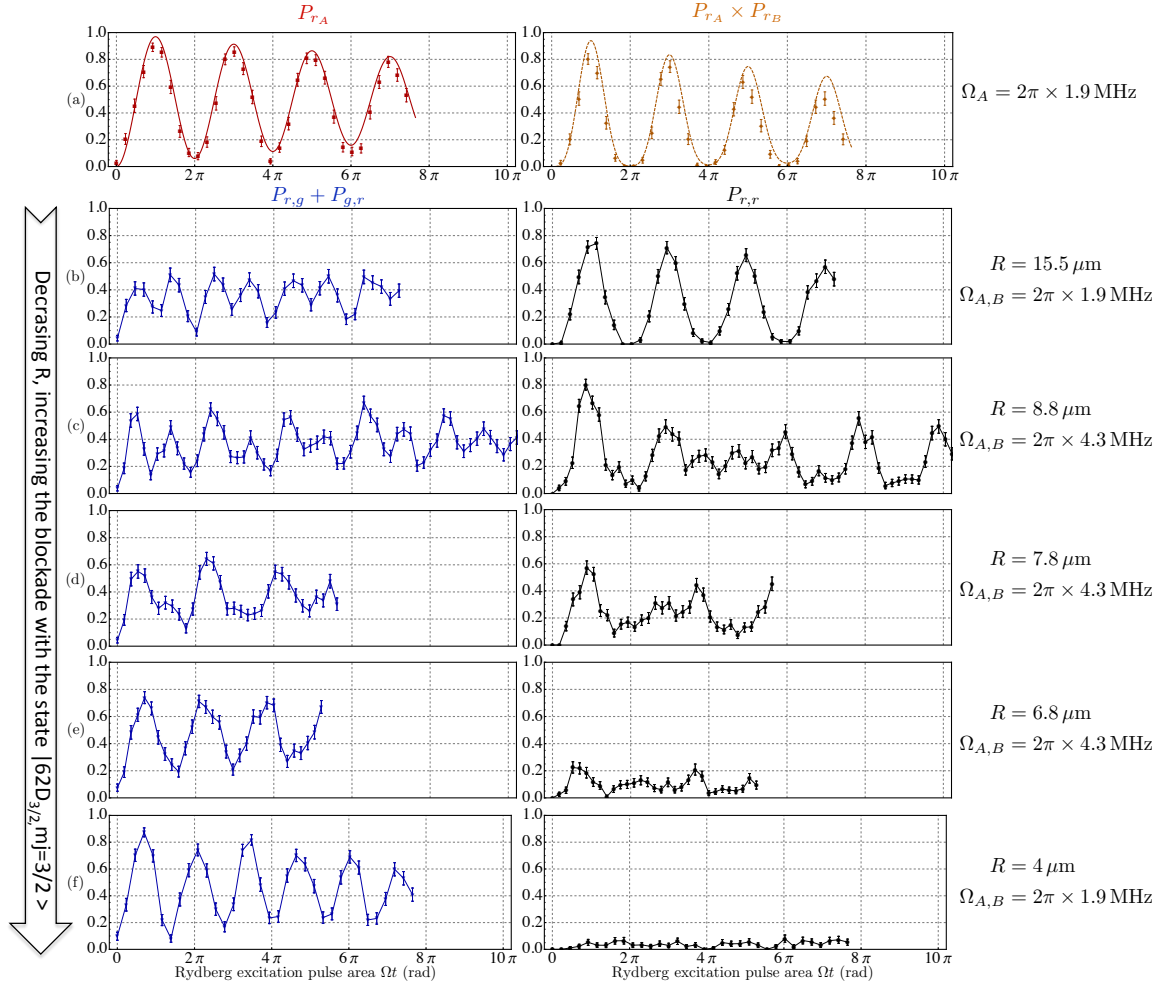


Figure 5.8: From independent to blocked regime, via partial blockade, with the Rydberg state $|62D_{3/2}, m_J=3/2\rangle$. (a) single-atom Rabi oscillations P_{r_A} between $|g\rangle$ and $|r\rangle$ (red squares) and product of the excitation probabilities P_{r_A} and P_{r_B} obtained with trap A alone and trap B alone, with the other trap off (orange diamonds). The error bars correspond to statistical uncertainties. The solid lines are the fits using the function $P_{|g\rangle}(\Omega, \gamma, t)$ from Eq. 4.8. (b)-(f) Probability $P_{r_g} + P_{g_r}$ to excite one and only one atom to the Rydberg state (blue triangles), and doubly Rydberg excitation probability P_{r_r} , versus excitation pulse area Ωt . From (c) to (e), Ω is kept constant while R decreases, yielding increasing blockade. The data points to guide the eye. Error bars are statistical.

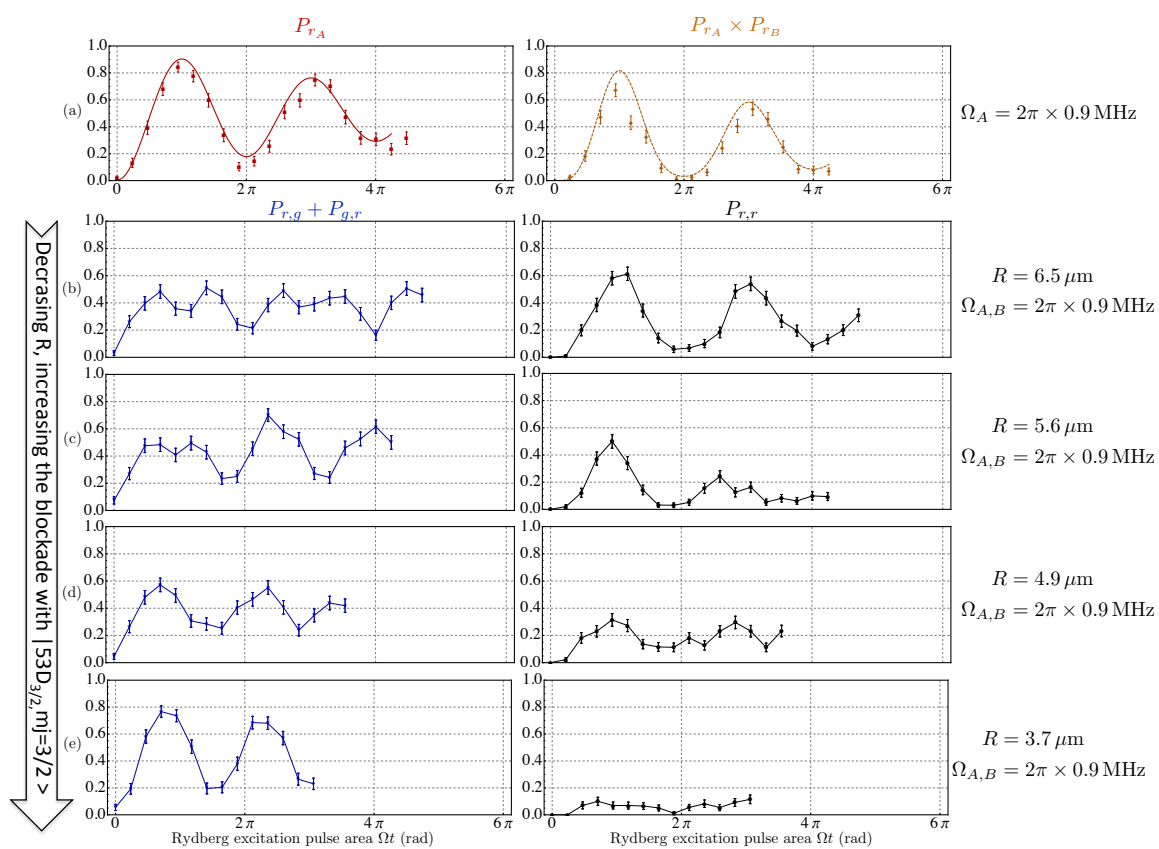


Figure 5.9: From independent to blockaded regime, via partial blockade, with the Rydberg state $|53D_{3/2}, m_J=3/2\rangle$. Same as Fig. 5.8 but with $n=53$.

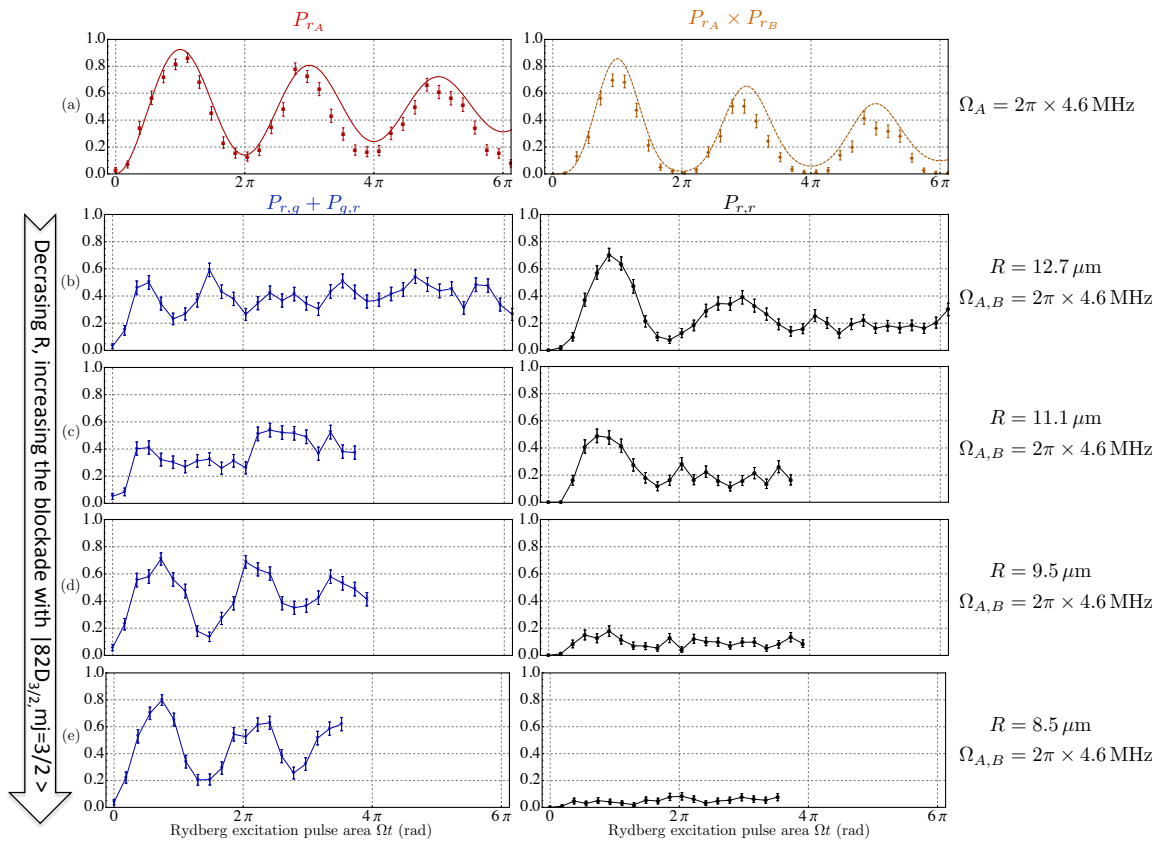


Figure 5.10: From independent to blocked regime, via partial blockade, with the Rydberg state $|82D_{3/2}, m_J=3/2\rangle$. Same as Fig. 5.8 but with $n=82$.

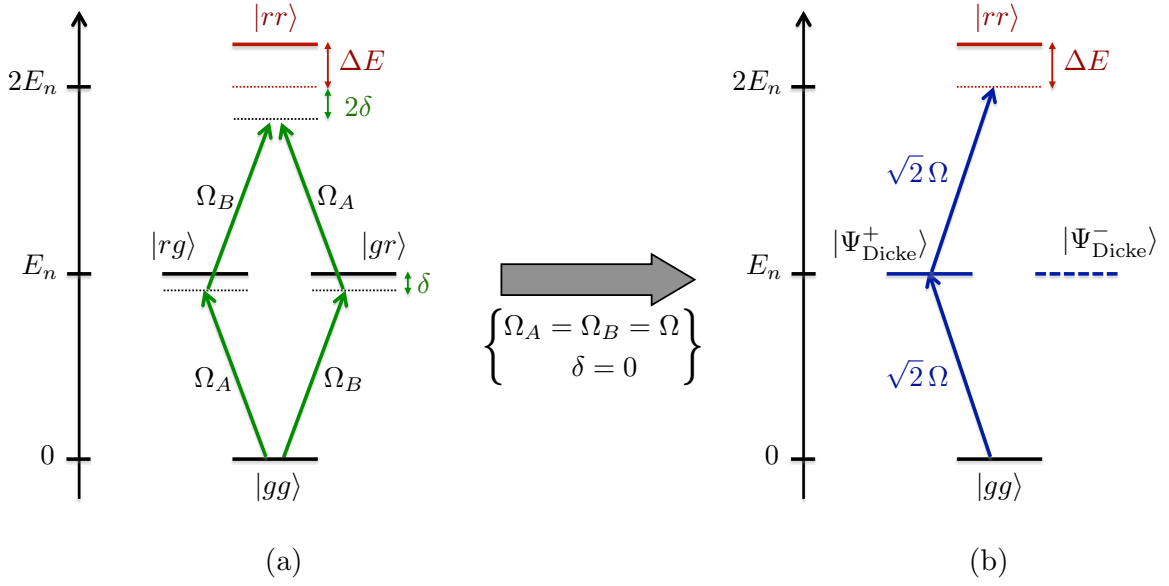


Figure 5.11: Modeling the two-atom system. (a) Four-level system. (b) Three-level system in the limit $\Omega_A = \Omega_B = \Omega$ and $\delta = 0$ involving the Dicke state $|\Psi_{\text{Dicke}}^+\rangle$.

5.3 Modeling of partial blockade

We will now show that the coherent evolution of our two-atom system can be modeled rather simply. For each value of the interatomic distance R and each value of the single-atom Rabi couplings $\Omega_{A,B}$, let us consider the four level system of states $\{|gg\rangle, |rg\rangle, |gr\rangle, |rr\rangle\}$ already presented and shown in Fig. 5.11 (a). First, we will not include the dissipation, and study the dynamics of the system with the Schrödinger equation. Then, we will refine the model to include the dissipation using the optical Bloch equations.

5.3.1 Schrödinger equations in the effective 3-level system

In the limit where the two atoms are shone with the same laser power used for the Rydberg excitations ($\Omega_A = \Omega_B = \Omega$), the system reduces to the three-level system shown in Fig. 5.11(b). At each time, the state of the system is thus of the form $|\Psi(t)\rangle = c_{gg}(t)|gg\rangle + c_{\text{ent}}(t)|\Psi_{\text{Dicke}}^+\rangle + c_{rr}(t)|rr\rangle$, where the coefficients $c_i(t)$ are complex probability amplitudes. We calculated that the coupling between $|gg\rangle$ and the symmetric Dicke state $|\Psi_{\text{Dicke}}^+\rangle$ was enhanced by a factor of $\sqrt{2}$. In the same way, one can show that the coupling between the symmetric Dicke state $|\Psi_{\text{Dicke}}^+\rangle$ and the doubly excited state $|rr\rangle$ is also enhanced by a factor $\sqrt{2}$. Using the rotating wave approximation, the evolution of such a system can be obtained by solving the Schrödinger equations which read (assuming that Ω is real, and $\delta = 0$):

$$\begin{cases} 2i \dot{c}_{gg} = \sqrt{2}\Omega c_{\text{ent}} \\ 2i \dot{c}_{\text{ent}} = \sqrt{2}\Omega c_{gg} + \sqrt{2}\Omega c_{rr} \\ 2i \dot{c}_{rr} = \sqrt{2}\Omega c_{\text{ent}} + 2\Delta E c_{rr}, \end{cases} \quad \text{with} \quad \begin{cases} c_{gg}(0) = 1 \\ c_{\text{ent}}(0) = 0 \\ c_{rr}(0) = 0, \end{cases} \quad (5.15)$$

where we have omitted the interaction terms between ground-state atoms or between a ground-state and a Rydberg atom⁵. The time evolution of the system depends only on the parameter $\Delta E/\hbar\Omega$. The numerical solutions obtained with this ratio ranging from 0.1 up to 10 are shown in Fig. 5.12. We can clearly identify features comparable to experimental data, especially in the case $n = 62$ shown in Fig. 5.8, where the damping was small. A quantitative comparison allows to measure the ratio $\Delta E/\hbar\Omega$, obtaining the highest accuracy when the ratio is on the order of unity. As we measure Ω with single-atom experiments, we can then extract the van der Waals energy ΔE . The physics of our two-atom experiments can thus be described and understood with a rather elementary quantum mechanical approach.

However, the Schrödinger model does not allow to take into account the dissipation that can be observed in the experimental data. Therefore, we refined our model by using the optical Bloch equations approach.

5.3.2 Bloch equations in the 4-level system

Let us go back to the four-level system presented in Fig. 5.11 (a). In the two-atom basis $\{|gg\rangle, |rg\rangle, |gr\rangle, |rr\rangle\}$, and using the rotating wave approximation again and choosing the effective Rabi frequencies to be real, the hamiltonian is:

$$\hat{H} = \hbar \begin{pmatrix} 0 & \Omega_A/2 & \Omega_B/2 & 0 \\ \Omega_A/2 & -\delta & 0 & \Omega_B/2 \\ \Omega_B/2 & 0 & -\delta & \Omega_A/2 \\ 0 & \Omega_B/2 & \Omega_A/2 & \Delta E/\hbar - 2\delta \end{pmatrix}, \quad (5.16)$$

To be more accurate now, we also allowed for the detuning δ of the single-atom Rydberg excitation not to be zero, in order to take into account possible drifts of the transfer cavity lock. The dissipation observed experimentally can be taken into account by solving the optical Bloch equations (OBEs) for the two-atom density matrix $\dot{\hat{\rho}} = -i[\hat{H}, \hat{\rho}]/\hbar + \mathcal{L}$. The dissipative term \mathcal{L} can be written as:

$$\mathcal{L} = \mathcal{L}_A \otimes \rho_B + \rho_A \otimes \mathcal{L}_B, \quad \text{where} \quad \mathcal{L}_i = \gamma_i \begin{pmatrix} \rho_{rr} & -\rho_{gr}/2 \\ -\rho_{rg}/2 & -\rho_{rr} \end{pmatrix}_{i=\{A,B\}} \quad (5.17)$$

is the dissipator for atom $i = \{A, B\}$ expressed in the basis $\{|g\rangle, |r\rangle\}$ and where ρ_i is the reduced density matrix of atom $i = \{A, B\}$. The dissipator can be written in this way assuming that cooperative effects such as super-radiance remain negligible. This is legitimate as the inter-atomic distance R is much larger than the wavelength $\lambda \simeq 795$ nm of the D1 transition which dominates the dissipation *via* spontaneous emission.

In practice, we always had $\Omega_A \simeq \Omega_B$ and $\gamma_A \simeq \gamma_B$ within less than 5%. Such a model is the generalization of the effective two-level approach to describe the single-atom excitation introduced in Sec. 4.2.1 to the case of a two-atom system. For the single-atom case, we showed that the model was good as long as we restricted the analysis to the first two or three Rabi oscillations. For longer excitation durations, the five-level model which includes the states $\{|0\rangle, |1\rangle, |2\rangle, |3\rangle, |4\rangle\}$ accounting for all possible decay channels would reproduce more accurately the data.

⁵For $R > 1 \mu\text{m}$, the van der Waals interaction between ground-state atoms is in the 10^{-8} Hz range, the magnetic dipole-dipole interaction is in the mHz range. Between a ground-state and a Rydberg atom, the van der Waals interaction is in the Hz range.

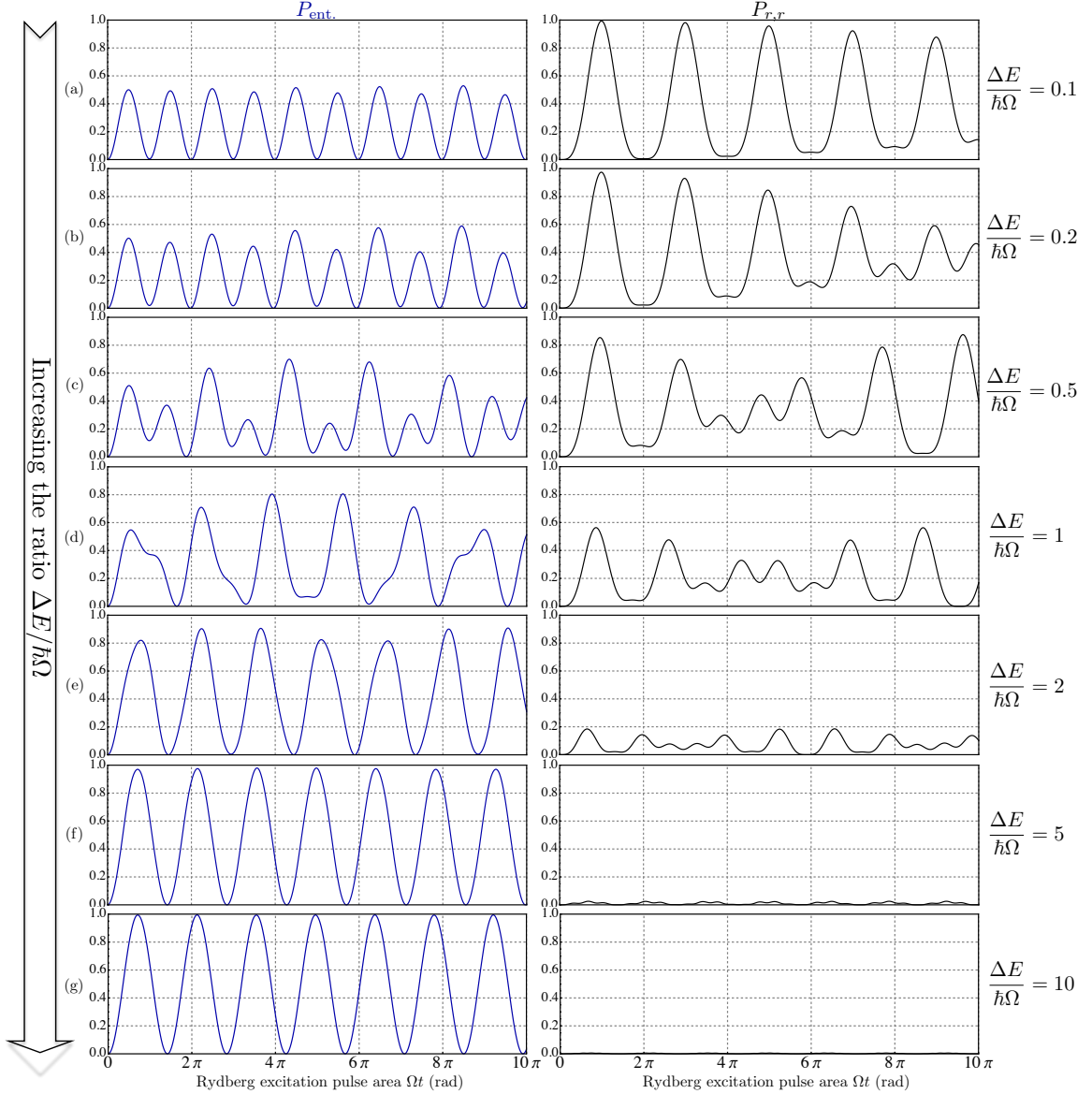


Figure 5.12: Numerical solutions of the Schrödinger equations in the three-level system.

5.3.3 Extraction of $|\Delta E|/h$ and error bars analysis

For each partial blockade experiment that we realized with the two-atom placed at a given interatomic distance R , we measured the van der Waals interaction ΔE between the two atoms by proceeding as follows.

Concerning the model, the parameters $\Omega_A \simeq \Omega_B$ and $\gamma_A \simeq \gamma_B$ were obtained by fitting the single-atom data with the function $P_{|g\rangle}(\Omega, \gamma, t)$ introduced in Sec. 4.2.1. Then, the only remaining parameters left were:

- ΔE : the van der Waals energy shift,
- δ : the single-atom detuning.

These two parameters were varied in a range of discrete values to fit the experimental data corresponding to $P_{gg}(t_i)$, $(P_{rg} + P_{gr})(t_i)$ and $P_{rr}(t_i)$ that we obtained for a set of

discrete excitation durations $\{t_i\}_{i=1,\dots,N}$ with the numerical solution of the OBEs. We chose the discrete values $\Delta E_j/\hbar > 0$ to cover the typical range $[\Omega/5, 5\Omega]$ by steps of 0.1 MHz in frequency units. We did not test the solutions of the model with negative values of ΔE_j . Indeed, when the single-atom excitation detuning δ is close to zero, the evolution of the populations of all the two-atom states are not affected by the sign of ΔE . Now, for all our experiments, a preliminary scan performed with only one trap allowed to fix approximately $\delta \simeq 0$. Thus, we do not expect the χ^2 minimization procedure described here to yield a final value of δ far different from zero. That is also why the discrete values $\delta_k/2\pi$ were only varied in the range $[-2 \text{ MHz}, +2 \text{ MHz}]$ by steps of 0.1 MHz. We thus emphasize that our method could only give access to the absolute value of the van der Waals interaction energy $|\Delta E|$.

Regarding now the experimental data, we could choose three sets of independent data for each two-atom experiment:

- **Set 1:** $P_{gg}(t_i)$ and $(P_{rg} + P_{gr})(t_i)$,
- **Set 2:** $P_{gg}(t_i)$ and $P_{rr}(t_i)$,
- **Set 3:** $(P_{rg} + P_{gr})(t_i)$ and $P_{rr}(t_i)$,

as the three populations are related by $P_{gg}(t_i) + (P_{rg} + P_{gr})(t_i) + P_{rr}(t_i) = 1$ and thus are not independent. For example, set 1 was composed of $2N$ independent data points of the form $\{(t_i, P_{gg}(t_i)); (t_i, (P_{rg} + P_{gr})(t_i))\}$ where $i = \{1, \dots, N\}$. For the sake of convenience, the data points of each of the three sets can be relabeled in a more adapted way as $\{(x_i, y_i)\}_{1,2,3}$ where $i = \{1, \dots, 2N\}$.

For each value of the free parameters $\{\Delta E_j, \delta_k\}$, we computed the reduced χ^2 coefficient corresponding to each of the three data sets as:

$$\chi_{1,2,3}^2(\Delta E_j, \delta_k) = \frac{1}{2N - d} \sum_{i=1}^{2N} \left(\frac{y_i - m(x_i, \Delta E_j, \delta_k)}{\sigma} \right)^2, \quad (5.18)$$

where $d=2$ is the number of adjustable parameters in our model and $m(x_i, \Delta E_j, \delta_k)$ is the value predicted by the model for the data point of abscissa x_i with the free parameters ΔE_j and δ_k . We weighted each data point by the same quantity σ .

If our measurements of y_i were limited only by the quantum projection noise, the statistical errors resulting from the repetition of 100 sequences to get one data point would have been $\sigma_i = \sqrt{y_i(1 - y_i)/100}$ (binomial distribution). Then, data points y_i close to 0 or 1 would be associated to small errors bars σ_i that would contribute to increase significantly the resulting value of χ^2 , and so of the error bars that we would infer (see below). We are however limited by the fluctuations of the apparatus. By repeating the same measurement many time, we measured the statistical error to be almost uniform and about $\sigma = 0.08$.

We obtained thus three distinct functions $\chi_{1,2,3}^2$ of two discrete parameters ΔE_j and δ_k . A contour plot of such 2D functions obtained in the case $n = 62$, $R = 8.8 \mu\text{m}$ corresponding to the data (c) in Fig. 5.8 are shown in Fig. 5.13 (a), (b) and (c). From the minimization of the three independent functions $\chi_{1,2,3}^2$, we found three values of the van der Waals energy $\Delta E_{1,2,3}/h$ and three values of the single-atom excitation detuning $\delta_{1,2,3}$. The final values extracted were computed by taking the following mean values:

$$\frac{|\overline{\Delta E}|}{h} = \frac{\Delta E_1 + \Delta E_2 + \Delta E_3}{3h} \quad \text{and} \quad \frac{\bar{\delta}}{2\pi} = \frac{\delta_1 + \delta_2 + \delta_3}{3 \times 2\pi}. \quad (5.19)$$

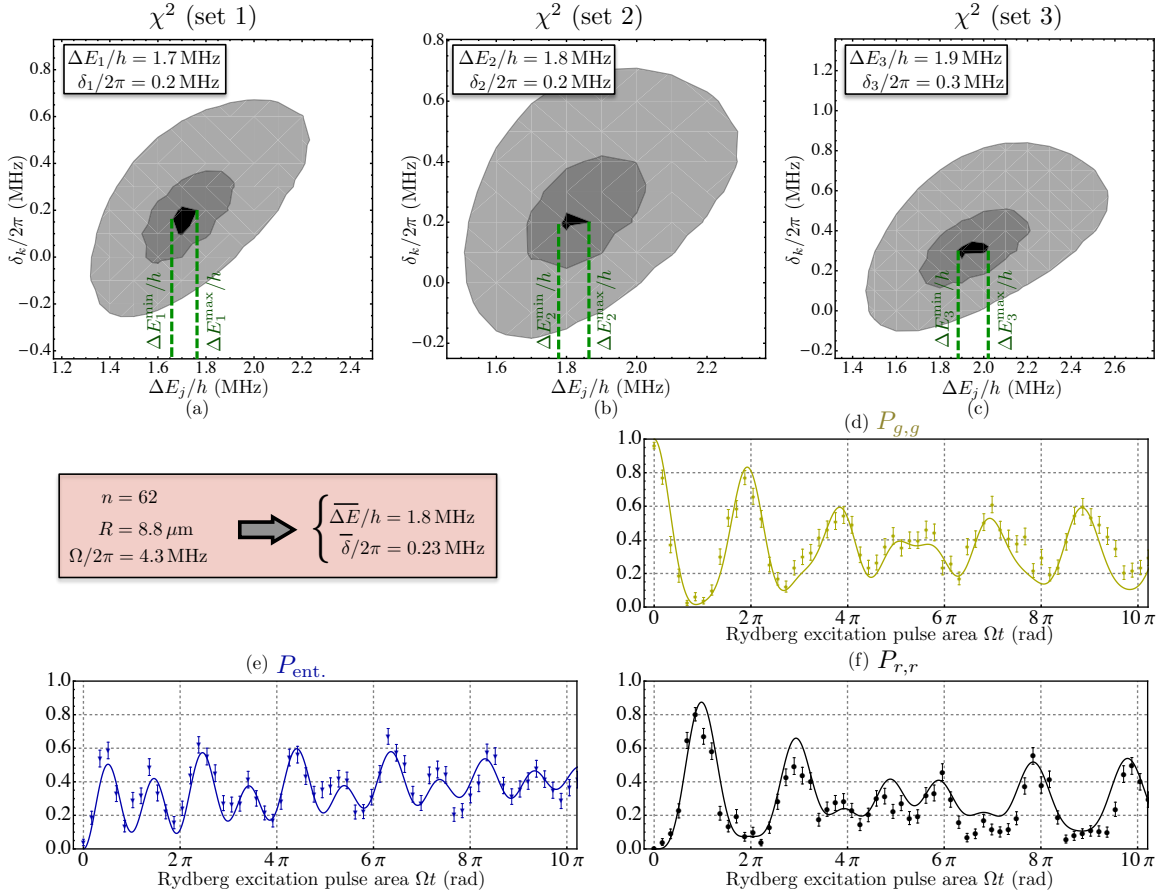


Figure 5.13: Extraction of ΔE in the case $n = 62$ and $R = 8.8 \mu\text{m}$. (a), (b) and (c) show respectively a contour plot of the 2D functions χ^2 as a function of the two parameters $\Delta E/h$ and $\delta/2\pi$ obtained for the set 1, 2 and 3. On each plot, we indicated the values of $\Delta E/h$ and δ which minimized the function χ^2 to the value χ_{\min}^2 . The first, second, and third contours represent respectively the zone for which $\chi^2 \in [\chi_{\min}^2, \chi_{\min}^2 + 1/(2N - 2)]$, $\chi^2 \in [\chi_{\min}^2 + 1/(2N - 2), \chi_{\min}^2 + 10/(2N - 2)]$ and $\chi^2 \in [\chi_{\min}^2 + 10/(2N - 2), \chi_{\min}^2 + 50/(2N - 2)]$. (d), (e) and (f) show respectively the experimental data of the populations P_{gg} , $P_{rg} + P_{gr}$ and P_{rr} as a function of the Rydberg pulse area Ωt . The solid lines show the solutions of the model based on the Bloch equations using the final values $\overline{\Delta E}$ and $\overline{\delta}$.

Figure 5.13 (d), (e) and (f) show the experimental data of the populations P_{gg} , $P_{rg} + P_{gr}$ and P_{rr} as a function of the Rydberg pulse area Ωt in the case $n = 62$, and $R = 8.8 \mu\text{m}$. The solid lines show the solutions of the model based on the Bloch equations using the parameters $|\overline{\Delta E}|$ and $\overline{\delta}$.

Error bars on the value obtained for $|\overline{\Delta E}|$ were determined using the 2D plots of the χ^2 functions. A central contour was drawn on each of these plots that represents the area in the 2D space spanned by $\Delta E_j/h$ and $\delta_k/2\pi$ for which an interpolation of the discrete function χ^2 has values in the range $[\chi_{\min}^2, \chi_{\min}^2 + 1/(2N - 2)]$. We determined the minimum and the maximum values $\Delta E_{1,2,3}^{\min}$ and $\Delta E_{1,2,3}^{\max}$ in this domain, as shown in Fig. 5.13 (a), (b) and (c). Then, we kept the extreme values obtained from the three independent plots to define the error bars:

$$\begin{cases} \Delta E^{\min} &= \min(\Delta E_1^{\min}, \Delta E_2^{\min}, \Delta E_3^{\min}) \\ \Delta E^{\max} &= \max(\Delta E_1^{\max}, \Delta E_2^{\max}, \Delta E_3^{\max}) \end{cases} \quad (5.20)$$

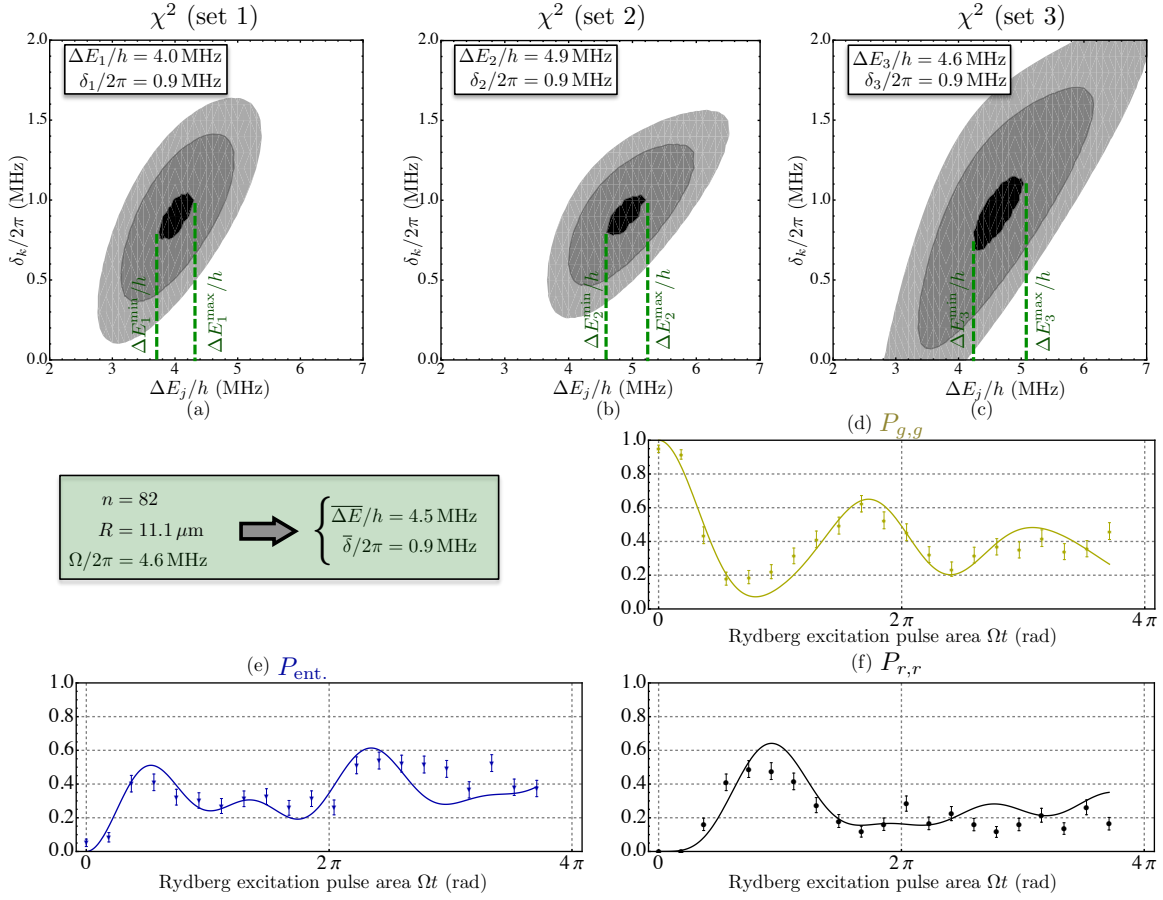


Figure 5.14: Extraction of ΔE in the case $n = 82$ and $R = 11.1 \mu\text{m}$. (Same method as Fig. 5.13 but for $n = 82$ and $R = 11.1 \mu\text{m}$).

Finally, the final measurement of the absolute value of the van der Waals energy belongs to the confidence interval:

$$|\overline{\Delta E}(R)| \in [\Delta E^{\min}(R), \Delta E^{\max}(R)] \quad (5.21)$$

We show another set of data in Fig. 5.14, obtained in the case $n = 82$, and $R = 11.1 \mu\text{m}$. The error bars obtained were indeed smaller when the chosen Rabi frequency was on the same order of magnitude as the interaction energy. We checked that forcing on purpose $\delta = 0$ and $\gamma = 0$ in the fitting procedure (thus reducing the model used for fitting to the three-level model based on the Schrödinger equations explained in Sec. 5.3.1), yields comparable values of $|\Delta E|/h$ within 20 %.

5.3.4 Measurements of the van der Waals interaction

The procedure described above was thus repeated systematically for various interatomic distances R and by exciting the atoms successively towards the three distinct Rydberg states $|53D_{3/2}, m_J = 3/2\rangle$, $|62D_{3/2}, m_J = 3/2\rangle$ and $|82D_{3/2}, m_J = 3/2\rangle$. We chose large Rabi frequencies at small interatomic distances in order to optimize the χ^2 minimization, and vice-versa. In some cases, we also checked that the interaction energy obtained did not depend on the chosen Ω by doubling or halving it, while keeping R constant. The measurements

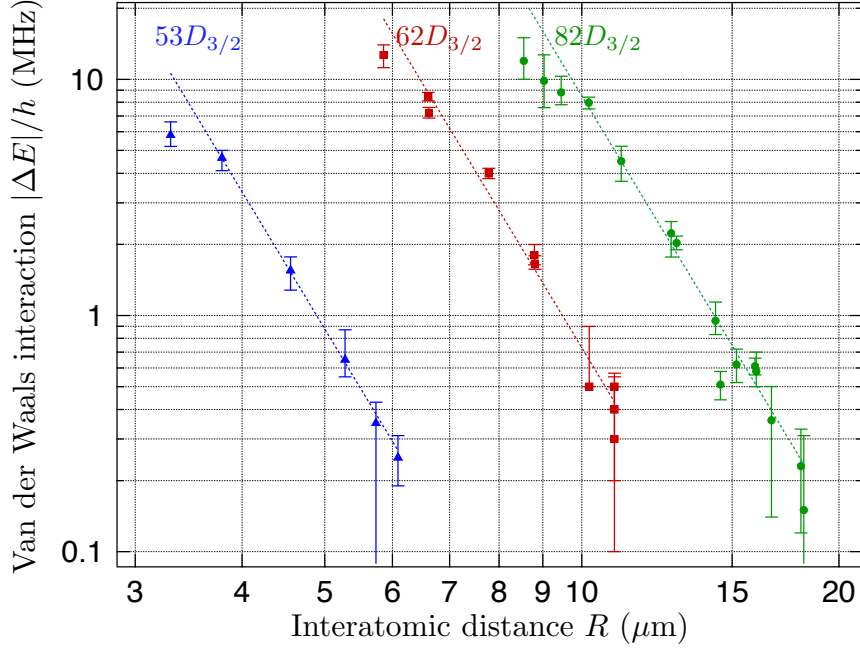


Figure 5.15: Magnitude $|\Delta E|/h$ of the interaction energy between atoms in $|nD_{3/2}, m_J = 3/2\rangle$ versus the interatomic distance R for $n = 53$ (blue), $n = 62$ (red) and $n = 82$ (green). Error bars are obtained as explained in the main text. The dashed lines are fits of the experimental data of the form $|C_6|_{\text{exp}}/R^6$.

of the van der Waals interaction energy we measured in each case with the corresponding error bars are shown in Fig. 5.15.

n	Assuming $ \Delta E = C_p _{\text{exp}}/R^p$
	p
53	6.1 ± 0.5
62	5.1 ± 0.2
82	5.8 ± 0.2

(a) Fitted value of the power law exponent p for $n = 53, 62$ and 82 .

n	Assuming $ \Delta E = C_6 _{\text{exp}}/R^6$
	$ C_6 _{\text{exp}}$ (GHz $\cdot \mu\text{m}^6$)
53	13.7 ± 1.2
62	730 ± 20
82	8500 ± 300

(b) Experimental $|C_6|$ coefficients for $n = 53, 62$ and 82 .

Table 5.1: Fitting the data with two approaches.

We fitted the experimental data corresponding to each Rydberg states using two approaches. The first one assumes a power law $|\Delta E| = |C_p|_{\text{exp}}/R^p$, where $|C_p|_{\text{exp}}$ and p are adjustable parameters. In this case, the coefficient $|C_p|_{\text{exp}}$ is expressed in $\text{Hz} \cdot \mu\text{m}^p$ and it is not straightforward to compare it with a theory. In Tab. 5.1(a), we only show the results obtained for p . As we only have data for ΔE covering a decade and a half (with error bars), the uncertainty in determining p are rather large, even though compatible with $p = 6$.

The second approach assumes $|\Delta E| = |C_6|_{\text{exp}}/R^6$, with $|C_6|_{\text{exp}}$ as an adjustable parameter. The experimental values of the C_6 coefficients obtained are listed in Table 5.1 (b). In the next section, we will show that *ab-initio* calculations of the interaction energy were performed, yielding theoretical values $|C_6|_{\text{th}}$ that agree well with our data.

5.4 Theoretical calculations of the interaction ΔE

The effects of the dipole blockade in the laser Rydberg excitation offers attractive possibilities for quantum information processing with single atoms (Jaksch *et al.*, 2000) or dense atomic ensembles (Lukin *et al.*, 2001). Thus, the dipole-dipole interaction has been studied theoretically in several groups in the past ten years, providing a rich literature on the subject (Singer *et al.*, 2005; Reinhard *et al.*, 2007).

However, it was convenient for our group to implement a code to compute the strength of the dipole-dipole interaction for our specific parameters. A first version was developed in Mathematica during A. Gaëtan's thesis in 2010. It turned out to be rather slow, probably due to the fact that Mathematica is an interpreted language. With the great help of R. Chicireanu, we converted the code into Matlab, which improved a lot the computation speed.

The principle of the numerical calculations is the following. Let us consider again the expression of the interaction hamiltonian considering only the first dipole-dipole term \hat{H}_{dd} shown in Eq. 5.1. In our experiment, the two atoms were aligned along the vertical quantization axis z , so the hamiltonian reads in this case:

$$\hat{H}_{\text{dd}} = \frac{1}{4\pi\epsilon_0} \frac{\hat{d}_{A,x} \cdot \hat{d}_{B,x} + \hat{d}_{A,y} \cdot \hat{d}_{B,y} - 2\hat{d}_{A,z} \cdot \hat{d}_{B,z}}{R^3}. \quad (5.22)$$

Now, by introducing for each atom the spherical dipole operators \hat{d}_1 , \hat{d}_0 and \hat{d}_{-1} defined by:

$$\begin{cases} \hat{d}_{+1} = -\frac{1}{\sqrt{2}} (\hat{d}_x + i\hat{d}_y) \\ \hat{d}_0 = \hat{d}_z \\ \hat{d}_{-1} = \frac{1}{\sqrt{2}} (\hat{d}_x - i\hat{d}_y), \end{cases} \quad (5.23)$$

the hamiltonian can be written:

$$\hat{H}_{\text{dd}} = \frac{1}{4\pi\epsilon_0} \frac{-\hat{d}_{A,+1} \cdot \hat{d}_{B,-1} - \hat{d}_{A,-1} \cdot \hat{d}_{B,+1} - 2\hat{d}_{A,0} \cdot \hat{d}_{B,0}}{R^3}. \quad (5.24)$$

If we neglect the effects of the residual electric or magnetic fields⁶, the total hamiltonian of the system is reduced to the sum of the unperturbed hamiltonian \hat{H}_0 with the interaction hamiltonian \hat{H}_{dd} :

$$\hat{H}_{\text{tot}} = \hat{H}_0 + \hat{H}_{\text{dd}}. \quad (5.25)$$

For the typical Rydberg states around $n \approx 50-80$ that we used, the fine structure splitting is larger than 20 MHz and thus can be resolved with laser excitations. However, the hyperfine splitting is below 200 kHz and can be neglected. Thus, we treated the hamiltonian in the fine basis composed of two-atom states of the form $|n, l, j, m_j\rangle_A \otimes |n', l', j', m'_j\rangle_B$. Our goal was then to compute the energy shifts ΔE_n of the unperturbed two-atom states $|nD_{3/2}, m_J = 3/2\rangle_A \otimes |nD_{3/2}, m_J = 3/2\rangle_B$ of \hat{H}_0 , induced by the dipole-dipole perturbation

⁶The two-atom experiments presented previously were performed after having compensated the electric fields, so the effect of residual electric field should be negligible. However, we used a magnetic field of about 3 G along the quantization axis. The Zeeman shifts were thus on the order of 5-6 MHz, which has to be compared with the fine structure splittings. For $n \leq 62$, the splittings are larger than 50 MHz, so mixing between states of different J should remain negligible. For $n = 82$, the fine structure splitting is about 20 MHz and we may consider including the effect of the magnetic field in this case.

hamiltonian. For this, one can adopt two approaches:

- At large interatomic distances R , we saw in Sec. 5.1 that the interaction hamiltonian \hat{H}_{dd} can be treated as a weak perturbation of \hat{H}_0 . The energy shifts ΔE_n can be obtained from second-order perturbation theory and take the form $C_6(n)/R^6$. The general expression of the C_6 coefficients was given in Eq. 5.4.
- At shorter distances however, the dipole-dipole hamiltonian causes mixing between unperturbed states which are not eigenstates of the total hamiltonian anymore. The general approach is thus to diagonalize \hat{H}_{tot} for various distances R and identify the branch that corresponds to a chosen unperturbed state $|nD_{3/2}, m_J = 3/2\rangle_A \otimes |nD_{3/2}, m_J = 3/2\rangle_B$ in the limit $R \rightarrow \infty$.

Both approaches requires to compute dipole matrix elements (for each atom A and B) of the form $\langle n', l', j', m'_j | \hat{d}_q | n, l, j, m_j \rangle$, with $q \in \{-1, 0, 1\}$. First, we will describe how to restrict the hamiltonian to a finite set of two-atom states in order to perform numerical calculations. Then, we will detail the calculations of the dipole matrix elements. Finally, we will present the results of the two approaches.

5.4.1 Construction of the basis

In order to compute the shift ΔE_n of the states $|nD_{3/2}, m_J = 3/2\rangle_A \otimes |nD_{3/2}, m_J = 3/2\rangle_B$, the computational bases were constructed with all the other two-atom states $|n_A, l_A, j_A, m_{j_A}\rangle \otimes |n_B, l_B, j_B, m_{j_B}\rangle$ according to the following conditions:

- $|n - n_{A,B}| \leq 4$ and $|2E_n - (E_{n_A} + E_{n_B})| \leq h \times 5 \text{ GHz}$, where the Rydberg states energies were computed according to the quantum defect theory presented in Sec. B.1.1. We checked that including states beyond these two conditions did not modify the resulting value of the C_6 coefficients, nor the value of the energy shift $\Delta E(R)$ obtained after diagonalizing the total hamiltonian for $R > 3 \mu\text{m}$, by more than 1%. Indeed, for this range of distances, the terms of the interaction hamiltonian can not exceed 100 MHz, while the differences in energy with these states are larger than several GHz, and thus their contribution is negligible.
- $0 \leq l_{A,B} \leq 4$. Indeed, direct coupling with our states of interest $|nD_{3/2}, m_J = 3/2\rangle_A \otimes |nD_{3/2}, m_J = 3/2\rangle_B$ can only occur for states with $l_{A,B} = 1$ or 3 because of the selection rules related to dipole couplings. However, states with $l = 3$ (resp. $l = 1$) can be coupled to some other states with $l = 4$ (resp. $l = 0$). This induces an indirect coupling between the states of interest and these states with angular momenta $l = 0, 4$, but already as a second-order correction. Therefore states with $l > 4$, that couple even more indirectly to the targeted states $|nD_{3/2}, m_J = 3/2\rangle_A \otimes |nD_{3/2}, m_J = 3/2\rangle_B$, can be omitted.
- $m_{j_A} + m_{j_B} = 3$. Indeed, the one-atom operators $\hat{d}_{-1,0,1}$ couple only states with the conditions $m'_j = m_j - 1$, $m'_j = m_j$ and $m'_j = m_j + 1$ respectively. Thus, one can notice that in our experimental configuration, the interaction hamiltonian of Eq. 5.24 couples only two-atom states of same total angular momentum $m'_{j_A} + m'_{j_B} = m_{j_A} + m_{j_B} = m_{\text{tot}}$. The two-atom states that will be coupled to $|nD_{3/2}, m_J = 3/2\rangle_A \otimes |nD_{3/2}, m_J = 3/2\rangle_B$ must therefore fulfill $m_{\text{tot}} = 3/2 + 3/2 = 3$.

Typically for the cases $n = 53, 62$ and 82 , the two-atom basis we considered were composed of 278, 436 and 1268 states respectively.

5.4.2 Calculation of dipole matrix elements $\langle n', l', j', m'_j | \hat{d}_q | n, l, j, m_j \rangle$

Once the two-atom basis is chosen, some algebra is required to compute the dipole matrix elements of the form $\langle n', l', j', m'_j | \hat{d}_q | n, l, j, m_j \rangle$ in the fine basis, with $q = \{-1, 0, 1\}$. The operators \hat{d}_q are related to the spherical harmonics by $\hat{d}_q = e\hat{r}\sqrt{4\pi/3}Y_1^q(\theta, \phi)$ which form a set of irreducible tensors of rank one. Here, we follow the derivation from [Weissbluth \(1978\)](#). The Wigner-Eckart theorem can be applied to separate these dipole matrix elements into a product of an angular integral, and a reduced matrix element $\langle n', l', j' | \hat{d} | n, l, j \rangle$ which does not depend on m_j nor q :

$$\langle n', l', j', m'_j | \hat{d}_q | n, l, j, m_j \rangle = (-1)^{j'-m'_j} \begin{pmatrix} j' & 1 & j \\ -m'_j & q & m_j \end{pmatrix} \langle n', l', j' | \hat{d} | n, l, j \rangle, \quad (5.26)$$

where the brackets denote the Wigner-3j symbol. The reduced matrix elements $\langle n', l', j' | \hat{d} | n, l, j \rangle$ is related to the reduced matrix elements $\langle n', l' | \hat{d} | n, l \rangle$ in the decoupled basis $|n, s, l, m_l\rangle$ by:

$$\langle n', l', j' | \hat{d} | n, l, j \rangle = (-1)^{l'+s'+j+1} \delta_{s,s'} \sqrt{(2j'+1)(2j+1)} \left\{ \begin{matrix} j' & 1 & j \\ l & s' & l' \end{matrix} \right\} \langle n', l' | \hat{d} | n, l \rangle. \quad (5.27)$$

where the braces denote a Wigner-6j symbol. The reduced matrix elements $\langle n', l' | \hat{d} | n, l \rangle$ is defined by:

$$\langle n', l' | \hat{d} | n, l \rangle = (-1)^{l'} \sqrt{(2l'+1)(2l+1)} \begin{pmatrix} l' & 1 & l \\ 0 & 0 & 0 \end{pmatrix} \langle n', l', j' | e\hat{r} | n, l, j \rangle, \quad (5.28)$$

where $\langle n', l', j' | e\hat{r} | n, l, j \rangle$ is a radial matrix element that corresponds to the overlap between the radial wavefunctions and the dipole operator:

$$\langle n', l', j' | e\hat{r} | n, l, j \rangle = \int_0^\infty R_{n',l',j'}^*(r) (er) R_{n,l,j}(r) r^2 dr. \quad (5.29)$$

The radial wavefunction of a given Rydberg state $|n, l, j\rangle$ can be computed by numerically integrating an effective Schödinger equation in which the eigenenergy $E(n, l, j)$ of the Rydberg state is calculated using the quantum defects theory. For this, we implemented a numerical method based on the Numerov algorithm described in [Zimmerman *et al.* \(1979\)](#) (for more details, refer to Sec. [B.1.4](#)). This method allowed us to tabulate the numerical values of the radial matrix elements $\langle n', l', j' | e\hat{r} | n, l, j \rangle$, for $10 \leq n', n \leq 100$, $0 \leq l', l \leq 4$ and for each j' (resp. j) in the range $[|l' - 1/2|, |l' + 1/2|]$ (resp. $[|l - 1/2|, |l + 1/2|]$).

The final expression of the dipole matrix element $\langle n', l', j', m'_j | \hat{d}_q | n, l, j, m_j \rangle$ is obtained by combining Eq. [5.26](#), [5.27](#), and [5.28](#), and could be computed using the tabulated numerical values of $\langle n', l', j' | e\hat{r} | n, l, j \rangle$:

$$\begin{aligned} \langle n', l', j', m'_j | \hat{d}_q | n, l, j, m_j \rangle &= (-1)^{j'-m'_j+j-1/2} \sqrt{(2l'+1)(2l+1)(2j'+1)(2j+1)} \\ &\times \left\{ \begin{matrix} j' & 1 & j \\ l & s' & l' \end{matrix} \right\} \begin{pmatrix} j' & 1 & j \\ -m'_j & q & m_j \end{pmatrix} \begin{pmatrix} l' & 1 & l \\ 0 & 0 & 0 \end{pmatrix} \langle n', l', j' | e\hat{r} | n, l, j \rangle. \end{aligned} \quad (5.30)$$

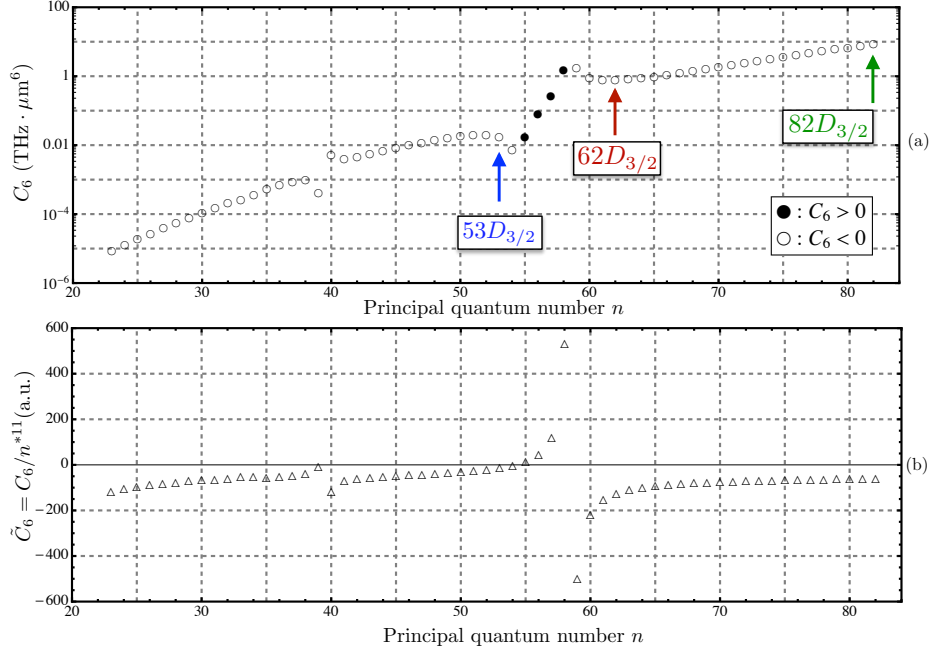


Figure 5.16: Numerical calculations of C_6 coefficients versus principal quantum number n , for the $|nD_{3/2}, m_j = 3/2\rangle$ series. (a) Numerical values of C_6 in $\text{THz} \cdot \mu\text{m}^6$. (b) Scaled values $\tilde{C}_6(n) = C_6/n^{*11}$ in atomic units.

5.4.3 C_6 calculations from second-order perturbation theory

Using the expression of the interaction hamiltonian of Eq. 5.24 corresponding to our experimental configuration with the two atoms aligned vertically, the coefficients C_6 of the states $|nD_{3/2}, m_J = 3/2\rangle_A \otimes |nD_{3/2}, m_J = 3/2\rangle_B = |rr\rangle$ could be computed numerically by:

$$C_6 = \frac{1}{(4\pi\epsilon_0)^2} \sum_{|\phi\phi'\rangle} \frac{|\langle\phi\phi'| - \hat{d}_{A,+1} \cdot \hat{d}_{B,-1} - \hat{d}_{A,-1} \cdot \hat{d}_{B,+1} - 2\hat{d}_{A,0} \cdot \hat{d}_{B,0} |rr\rangle|^2}{2E_r - (E_\phi + E_{\phi'})}, \quad (5.31)$$

where the summation involves all the states $|\phi\phi'\rangle$ of the finite basis constructed previously. The numerical values obtained are shown in Fig. 5.16(a) and are in very good agreement with the ones obtained in the group of G. Raithel (Fig.4(a) in Reinhard *et al.* (2007)).

The expected dramatic increase of the C_6 coefficients with the principal quantum number n can be observed. We also show in (b) the scaled values $\tilde{C}_6 \propto C_6/n^{*11}$, where $n^* = n - \delta(n, l, j)$ is the effective quantum number, relevant for Rydberg states (see Sec. B.1.1). The rough scaling of the C_6 coefficients as the power 11th of n was qualitatively discussed in Sec. 5.1. Here, we can check that the scaling approach captures only the average behaviour of the C_6 coefficients with n . Deviations occur due to accidental quasi-Förster resonances (see Sec. B.2.1) for $n = 40$ and $n = 58$, for which two terms (a certain $|\phi_A\rangle \otimes |\phi'_B\rangle$ and its symmetric by exchanging A and B) in the sum of Eq. 5.31 have very low denominators, yielding increased values of C_6 . On the contrary, the cases $n = 39$ and $n = 54$ show partial cancellation of the C_6 due to the accidental summation of two pairs of main contributing terms with almost equal amplitudes but opposite signs.

In Fig. 5.17, we sorted in descending order the terms that contribute to more than 99% to the final value of the C_6 coefficient in the cases $n = 53, 62, 82$ that we investigated experimentally. In Tab. 5.2, the theoretical absolute values $|C_6|_{\text{th}}$ in these three cases are

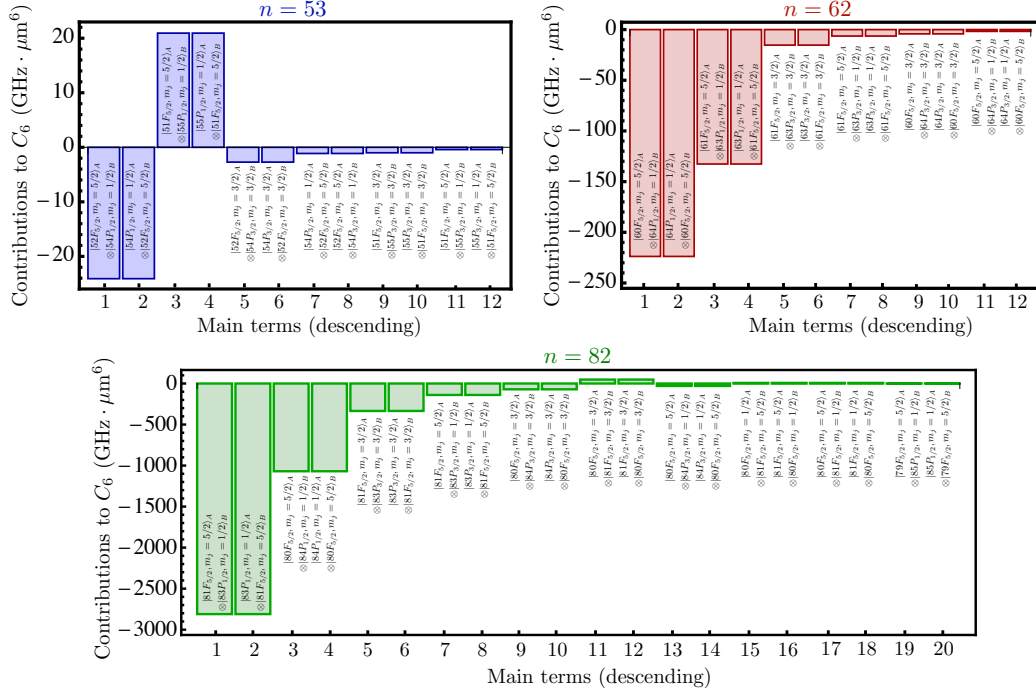


Figure 5.17: Sorting the terms that contribute to more than 99 % to the C_6 in the cases $n = 53, 62, 82$. The contributions to the C_6 from the sum in Eq. 5.31 are sorted in descending order of their absolute value. The case $n = 53$ (close to $n = 54$, discussed in the text) illustrates how the value of the coefficient can be reduced due to the summation of two leading terms with similar amplitudes but opposite signs.

listed together with the experimental values obtained in the previous section.

Determining the uncertainties for the numerical values of $|C_6|_{\text{th}}$ is not straightforward. In addition to the fact that the sum in Eq. 5.31 is truncated, other errors result from the computation of the radial wavefunctions. One way to estimate these errors was to add random, uniformly-distributed relative errors of $\pm 0.5\%$ to the radial matrix elements $\langle n', l', j' | e\hat{r} | n, l, j \rangle$ appearing in the calculations. By doing so, we found error bars for $|C_6|_{\text{th}}$ of about 2% in the cases $n = 62$ and $n = 82$. On the other hand for $n = 53$, the error bar was 10%. Indeed, in this case, one can see in Fig. 5.17 that the calculation of the C_6 coefficient involves the summation of two pairs of large contributing terms, which partially cancel each other. Thus, introducing small errors in the values of the radial matrix elements leads to a larger error bar on the C_6 coefficient.

Finally, taking into account error bars, the agreement between our measurements and the calculated C_6 is good within about 5%.

n	$ C_6 _{\text{exp}}$ (GHz · μm^6)	$ C_6 _{\text{th}}$ (GHz · μm^6)
53	13.7 ± 1.2	16.9 ± 1.7
62	730 ± 20	768 ± 15
82	8500 ± 300	8780 ± 150

Table 5.2: Experimental and theoretical $|C_6|$ coefficients for $n = 53, 62$ and 82 .

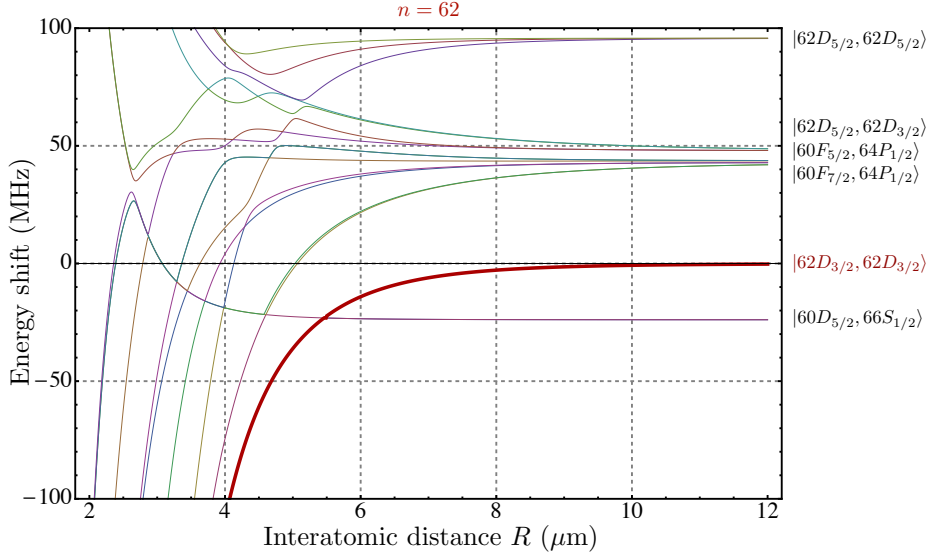


Figure 5.18: Numerical calculation of the dipole-dipole interaction between two atoms in state $|62D_{3/2}, m_j = 3/2\rangle$. The basis used for the calculation contained 436 two-atom states. We only represented states close in energy up to 100 MHz from the target. The van der Waals regime is observed until $R \simeq 6 \mu\text{m}$.

5.4.4 Diagonalization of the interaction hamiltonian

However, as mentioned in Sec. 5.4, the perturbative calculations are not valid anymore at short distance. Thus, we also checked that the range of distances that we investigated experimentally in the three cases $n = 53, 62$ and 82 corresponded indeed to the van der Waals regime of the dipole-dipole interaction.

For this, we diagonalized the total hamiltonian \hat{H}_{tot} , expressed within the same basis as described in Sec. 5.4.1, for various interatomic distances R ranging from 2 to $20 \mu\text{m}$. The matrix \hat{H}_{tot} is a $n \times n$ hermitian matrix, such that only $n(n+1)/2$ terms need to be computed. We saw in Sec. 5.4.1 that the size of the basis n could range from about 300 to 1300 depending on which Rydberg state is studied. The number of terms to compute vary thus from about 50 000 to 850 000, but with a lot of terms equal to zero, according to the selection rules. Then, non-zero terms are products of an angular coefficient and a radial integral as shown in Eq. 5.30. The angular coefficient is calculated using the definition of Wigner-3j and 6j symbols which involves rather long computation time (to calculate many products of factorials). The radial integral is obtained by searching the right value into the file where all the matrix elements are tabulated.

An easy trick can be used to optimize the speed of the calculations. It consists in computing the matrix elements only once for all values of R . The hamiltonian of Eq. 5.25 can be written as:

$$\hat{H}_{\text{tot}} = \hat{H}_0 + \hat{H}_{\text{dd}} = \hat{H}_0 + \frac{1}{4\pi\epsilon_0} \frac{\hat{V}}{R^3}. \quad (5.32)$$

The matrix \hat{H}_0 is diagonal in the basis $|\phi\phi'\rangle$. Choosing the energy of the state $|nD_{3/2}, m_J = 3/2\rangle_A \otimes |nD_{3/2}, m_J = 3/2\rangle_B = |rr\rangle$ of interest as the origin, the matrix elements on the diagonal are $E_\phi + E'_\phi - 2E_r$. They are quickly computed using the quantum defects (see Sec. B.1.1). Then, the matrix elements of \hat{V} are calculated using Eq. 5.30. The calculations of \hat{H}_0 and

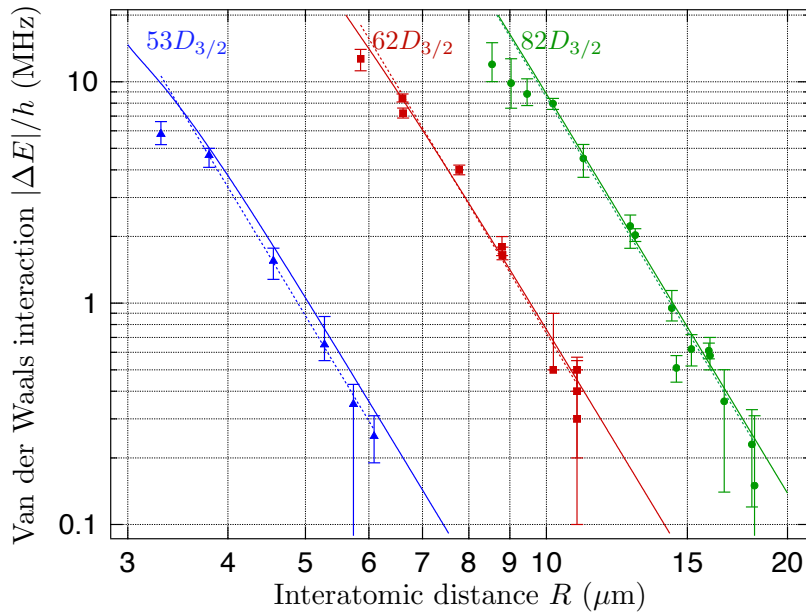


Figure 5.19: Magnitude $|\Delta E|/h$ of the interaction energy between atoms in $|nD_{3/2}, m_J = 3/2\rangle$ versus the interatomic distance R for $n = 53$ (blue), $n = 62$ (red) and $n = 82$ (green). Same as Fig. 5.15. The solid lines show the results of ab-initio numerical calculations of the van der Waals interaction based on the diagonalization of \hat{H}_{tot} .

\hat{V} takes about 500s on a MacBook Pro equipped with Intel Core i5 processor and 8 Go of RAM. Then, the calculation and the diagonalization of \hat{H}_{tot} for 1000 values of R take only about 30s. We show the results of the calculation in the case $n = 62$ in Fig. 5.18 for R ranging from 2 to 12 μm and for states of energy departing at most by 100 MHz from the origin.

The same procedure was repeated in the cases $n = 53$ and $n = 82$. This method allowed us to calculate in each case the absolute value of the dipole-dipole interaction $|\Delta E_n|/h$ for the branch corresponding to the state $|nD_{3/2}, m_J = 3/2\rangle_A \otimes |nD_{3/2}, m_J = 3/2\rangle_B$ in the independent atoms limit. Thus, we could finally compare directly the results of our measurements described in Sec. 5.3.3 with the ab-initio calculations of the dipole-dipole interaction (solid lines) in the log-log plot of Fig. 5.19. Although a tiny change of slopes can be seen at $R = 3.5 \mu\text{m}$ for $n = 53$, the van der Waals approximation is valid at the chosen interatomic distances for the three Rydberg states. Furthermore, the agreement between the measurements and the calculated energy shifts is very good.

However, it appears that for the largest values of $|\Delta E|/h$, the experimental data are systematically lower than the theoretical expected values. At the moment, the reason why the experimental method seems to fail in these cases is not clear. Recently, Li *et al.* have studied the influence of the mechanical effects induced by the interactions that can strongly affect the dynamics of the two-atom states populations (Li, Ates, and Lesanovsky, 2013). In particular, they showed that this could cause decoherence in the excitation dynamics thus reducing the efficiency of the blockade. In the future, we might consider including these effects in our model to check whether or not this could explain the deviations observed between the predictions of the present model and the experimental data at large interaction energies.

5.4.5 Conclusion

The Rydberg blockade between a pair of atoms excited towards a Rydberg state is now well controlled on the experiment. We demonstrated it in the simplest geometry where the two atoms were aligned along the quantization axis. However, the van der Waals interaction is not isotropic for the Rydberg states $|nD_{3/2}, m_j = 3/2\rangle$ that we studied. It will be especially relevant for the implementation of the blockade in arrays of trapped atoms with various angles θ between the quantization axis and the axis defined by each pair of sites. In the van der Waals regime, the C_6 coefficients can be computed as a function of θ using the method that we implemented and described in Sec. 5.4.3. For a pair of atoms in $nD_{3/2}$ states, the interaction is significantly anisotropic, and can be reduced by more than 50% at $\theta = \pi/2$ from the maximum value obtained at $\theta = 0$ (Reinhard *et al.*, 2007). For a pair of atoms in $nS_{1/2}$ states however, the interaction is almost isotropic. We have started to investigate this θ -dependence theoretically and experimentally for both cases.

Conclusion and outlook

In this thesis, we presented the design, the construction and the characterization of a new experimental apparatus that aims at implementing quantum information protocols in arrays of trapped single atoms, by taking advantage of the strong dipole-dipole interactions between Rydberg states. This experimental project was motivated by the successful experiments realized on the previous Rydberg apparatus by A. Gaëtan and C. Evellin, who demonstrated the possibility to entangle two individual atoms trapped in microscopic optical tweezers using the Rydberg blockade (Gaëtan *et al.*, 2009; Wilk *et al.*, 2010).

We first described the features of our apparatus built to overcome the main limitations identified by our predecessors (ITO coating on the lenses, electrodes, compact setup). In chapter two, we presented a set of experiments developed during previous theses (Schlosser, 2001; Reymond, 2002; Darquié, 2005) that allowed to characterize the microscopic dipole traps (size, depth, oscillation frequencies, ...) and the external state of single atoms inside such traps (lifetime, temperature). Then, we described in chapter three how we could manipulate the internal ground states of our trapped atoms using either microwaves or Raman transitions. Microwave spectroscopy proved to be an ideal tool to compensate residual magnetic fields, improving the initialization of our chosen atomic qubit. We also checked that Raman transitions could be used to perform qubit rotations and read out, with an overall efficiency larger than 95%. In chapter four, we presented the excitations of the atoms towards various Rydberg states $|nD_{3/2}, m_j = 3/2\rangle$ up to $n = 100$, with an efficiency compatible with 95%. Using Stark spectroscopy, we confirmed our ability to control the external electric field seen by the atoms, and we checked that these fields were stable on long timescales. Finally in chapter five, we presented Rydberg blockade experiments with two atoms separated by a tunable distance R , which we varied to observe either the fully independent regime (large R) or the completely blockaded regime (small R). We showed that compensating for residual electric fields allowed to improve the control over the dipole-dipole interaction, yielding a blockade of much higher quality than observed before. This fine control allowed us to investigate partial blockade configurations in the van der Waals regime. The van der Waals interaction energy $\Delta E_n(R) = C_6/R^6$ could be directly measured between two single atoms at controlled distances.

The level of control demonstrated in these preliminary experiments with two atoms opens exciting perspectives for the implementation of the blockade in multi-atoms systems. To pursue further our experimental investigations in this direction, new experimental tools have already been implemented on the apparatus.

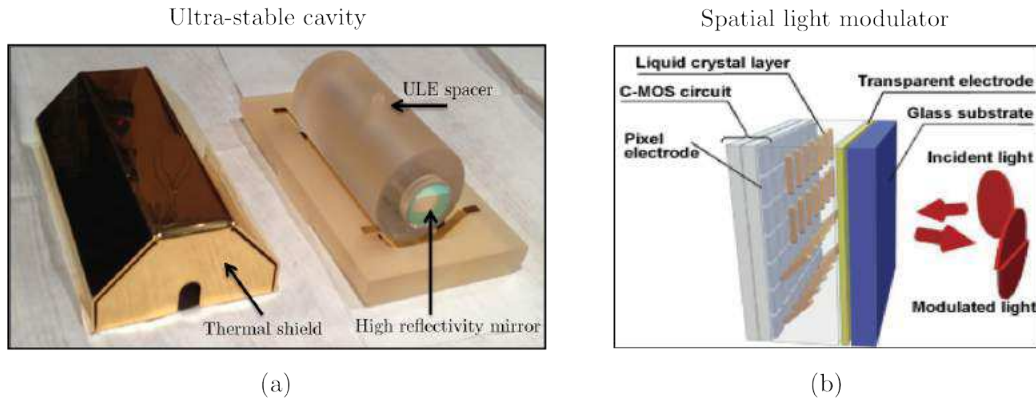


Figure 5.20: Upgrades of the experimental apparatus. (a) Picture of our ultra-stable FP reference cavity. The Fabry-Perot mirrors were mounted onto a ultra low expansion (ULE) spacer, regulated in temperature. The assembly is placed in a thermally insulated vacuum housing, and is operated at about 10^{-6} mbar. (b) Operating principle of the LCOS-SLM (taken from Hamamatsu website). The device consists in a matrix of pixels containing nematic liquid crystals. The orientation of the crystals in each pixel can be tuned by applying appropriate voltages on the pixel electrode. When a laser beam at 850 nm is reflected on the SLM screen, the phase imprinted locally by one pixel can be tuned from 0 to 2π .

Recent improvements

According to the initial plan described in Sec. 1.1.1, the setup has already been upgraded to explore multi-atom configurations, and now includes:

- an ultra-stable reference cavity from Stable Lasers Systems[®], shown in Fig. 5.20(a), to replace the one we used from Coherent. Passively stable with a FSR of 1.5 GHz and a finesse of about 20 000, this cavity should allow to narrow the linewidths of the Rydberg lasers below the kHz level and significantly reduce the fluctuations of the Rydberg excitation detuning on long time scales.
- a spatial light modulator (LCOS-SLM from Hamamatsu), sketched in Fig. 5.20(b), allowing to generate arbitrary 2D patterns of microscopic optical dipole traps.
- an EMCCD camera (Andor iXon Ultra 897), with highly sensitive pixels and low read out noise, that should allow to replace the single photon counting modules for imaging the single atoms in the 2D patterns of traps.

The cavity and the SLM have been characterized and are now fully operational. Single-atom imaging with the EMCCD camera will be investigated in a near future.

Work in progress

Using the upgraded version of the apparatus, the project has been moving forward quickly. Before increasing the number of atoms, further investigations on our control of the dipole-dipole interactions between two atoms have been pursued to study geometry-dependent effects due to the anisotropy of the dipolar interaction, and the tunability of the interaction with external electric fields. In parallel, optimization of the 2D intensity patterns generated by the SLM has been investigated using a Shack-Hartmann wavefront sensor and show promising results.

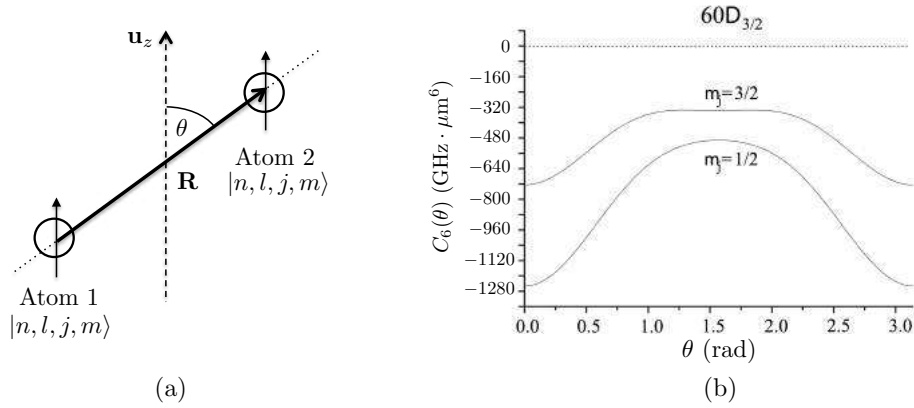


Figure 5.21: Angular dependence of the C_6 coefficient. (a) Two interacting Rydberg atoms separated by a vector \mathbf{R} which defines an angle θ with the quantization axis z . (b) Angular dependence of the C_6 coefficient of the state $|60D_{3/2}\rangle \otimes |60D_{3/2}\rangle$, for different m_j (graph taken from Reinhard *et al.* (2007)).

Anisotropy effects

In 2D patterns of traps, the internuclear axes of some pairs of atoms are not aligned with the quantization axis z . As the dipole-dipole interaction is not isotropic (see Eq. 5.1), the strength of the interaction varies with the angle θ between z and the axis defined by the pair, shown in Fig. 5.21(a). This angular dependence has already been studied in 1D dense sample of Rydberg atoms (Carroll *et al.*, 2004) in the dipole-dipole regime (C_3/R^3 interaction) where an external electric field was applied to control the orientation of the dipoles. In our two-atom experiments, the angle θ can be easily varied while keeping the interatomic distance R constant. Then, the same method described in Sec. 5.3.3 can be applied to measure the variations of the van der Waals interaction with the angle θ and compare them with theoretical expectations (see Fig. 5.21 (b)). Current investigations are showing promising results and a publication is in preparation.

Tuning the interaction with the electric field

The dipole-dipole interaction can be tuned by applying external electric fields. In particular, the interaction energy shifts ΔE_n of certain two-atom states $|rr\rangle$ where $|r\rangle = |nD_{3/2}, m_j = 3/2\rangle$ can be enhanced by reaching pure Förster resonances (see Sec. B.2.2), which would allow us to increase the range of the blockade in our 2D patterns.

In a set of preliminary experiments, we studied the case $n = 62$ with the two atoms and the electric field \mathbf{F} aligned along the quantization axis z . In a first treatment of the two-atom system in the presence of F , we considered only the five states shown in Fig. 5.22(a), where the Rydberg state $|r'\rangle$ and $|r''\rangle$ are respectively the states $|60F_{5/2}, m_j = 5/2\rangle$ and $|64P_{1/2}, m_j = 1/2\rangle$. In the absence of external field, the two-atom state $|r'_{A,B}, r''_{B,A}\rangle$ is separated from the target state $|rr\rangle$ by the energy difference Δ . From Eq. B.25, one can see that this energy difference is related to the shift in energy ΔE of the state $|rr\rangle$ and the coupling term of the form C_3/R^3 . Then for several values of the field F , we performed two-atom experiments in the partial blockade regime, similar to the ones described in chapter five. Coherent evolution of the two-atom states populations were compared to the solutions of OBEs applied to the five-level system of Fig. 5.22(a) and allowed to measure the energy difference $|\Delta|$.

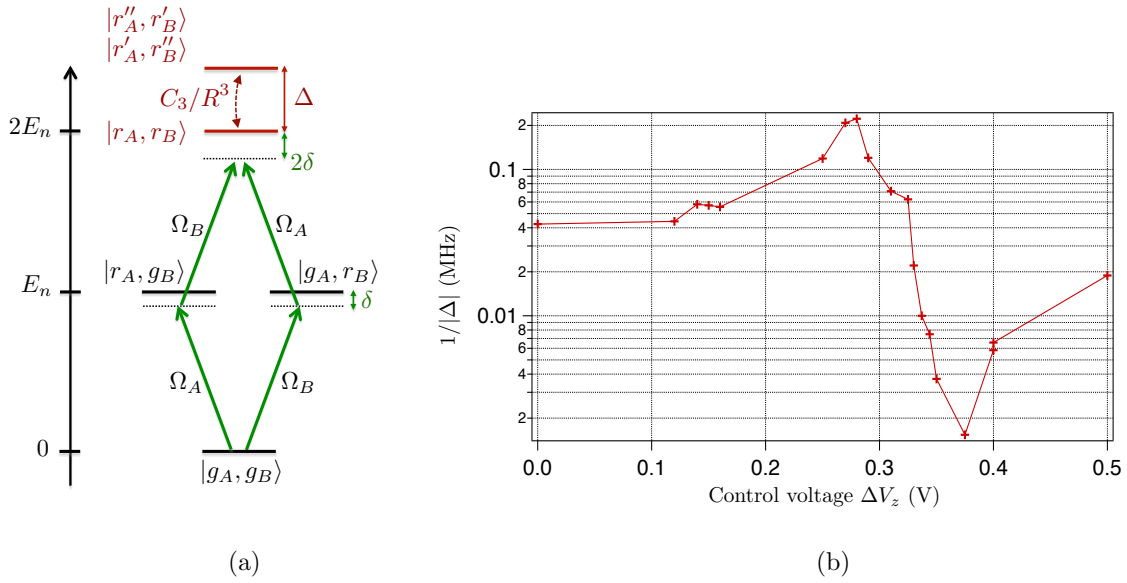


Figure 5.22: Preliminary studies of Förster resonances. (a) Five-level model (b) Estimates of $|\Delta|$ versus the voltage V_z .

Preliminary results concerning the variations of $1/|\Delta|$ with the external voltage applied on our electrodes are shown in Fig. 5.22 (b). A decrease of $|\Delta|$ translates in an enhancement of the interaction. At $\Delta V_z = 0.27$ V ($F \simeq 50$ mV/cm), this enhancement was estimated to a factor of about 5. The interaction can also be decreased by increasing $|\Delta|$. Going from $\Delta V_z = 0.27$ V to 0.37 V, the interaction is decreased by two orders of magnitude! This ability could also be useful for switching off the interactions between two different traps, while still blocking atoms inside the same trap (see the deterministic loading scheme below).

Further analysis of the experimental data including more two-atom states in the hamiltonian are currently underway.

Generation of 2D patterns of traps

The SLM has been fully characterized and is now part of the setup shown in Fig. 5.23 (a). High quality patterns of microscopic traps were generated and optimized, showing a low level of parasitic diffracted light; as an example, a pattern with up to 24 traps is shown in Fig. 5.23 (b). These patterns can be operated in the single atom loading regime. Oscillation frequencies and trap depths were characterized with atoms and look very promising to investigate multi-atom systems. A paper describing the results related to this new trap generation setup is in preparation.

Future investigations

Deterministic loading

All the experiments presented in this thesis were performed by loading single atoms from a MOT cloud into microscopic optical tweezers by operating in the single atom regime described in Sec. 1.1.1, in which a trap is filled on average half of the time. With a reasonable loading rate of about 20 s $^{-1}$, the average time one has to wait before N traps are filled is

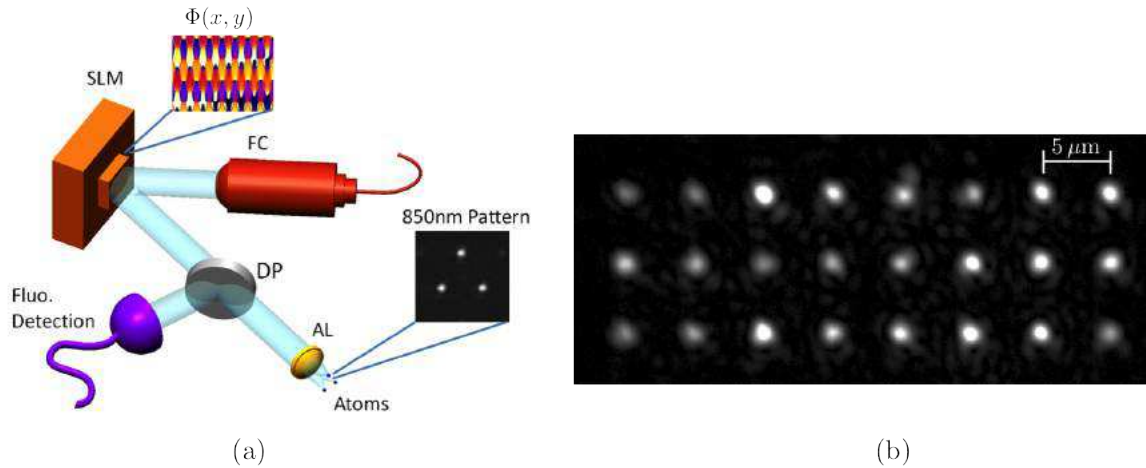


Figure 5.23: Towards multi-atom systems. (a) Setup with the SLM (FC = Fiber Collimator, SLM = Spatial Light Modulator, DP = Dichroic Plate, AL = Aspheric Lens). (b) 3×8 array of dipole traps.

$2^N/50$ ms. Such a probabilistic loading scheme thus becomes rather inefficient already for $N \gtrsim 5$.

Therefore, deterministic loading schemes will have to be investigated soon. Recently, a loading efficiency of 82.7% was demonstrated by using inelastic blue-detuned light-assisted collisions favoring one-atom losses over two-atom losses, as reported in Grünzweig *et al.* (2010). Another interesting possibility would be to investigate a scheme using the Rydberg blockade inside each microscopic trap operating in multi-atom regime, as proposed by Beterov *et al.* (2011). A first step in this direction has been demonstrated recently in Ebert *et al.* (2013). The principle of this scheme is illustrated in Fig. 5.24. Each trap i of a chosen pattern would be initially filled with N_i atoms, on the order of ten, prepared in a Zeeman sub-level of $F = 2$ (step 1). By operating in the regime $b < R_{\text{blockade}} < a$, the Rydberg lasers would drive one excitation in each trap, which could be mapped onto a Zeeman sub-level of $F = 1$ (step 2). Finally, a laser resonant either with the D1 or the D2 lines could be tuned on resonance with the ground state $F = 2$ and used to blow out all the atoms except one (step 3). The scheme raises the challenge of achieving efficient Rydberg excitation and mapping in a rather dense atomic sample.

Multi-particle entanglement

With the ability to generate and load various 2D patterns of traps with single atoms, our new experimental apparatus will offer an ideal platform to investigate various classes of multi-particle entanglement (Vedral, 2008), where the number of entangled particles would be tunable. In particular, the successful demonstration of contrasted coherent excitation ($\geq 90\%$) towards Rydberg states with large principal quantum number n up to 82 opens the possibility to reach efficient blockade regime between two atoms as far as $12 \mu\text{m}$. This prerequisite is promising for entangling arrays of many atoms. Multi-particle entangled states are of particular interest for the implementation of quantum computation protocols. Two main classes of entanglement could be investigated further on our apparatus.

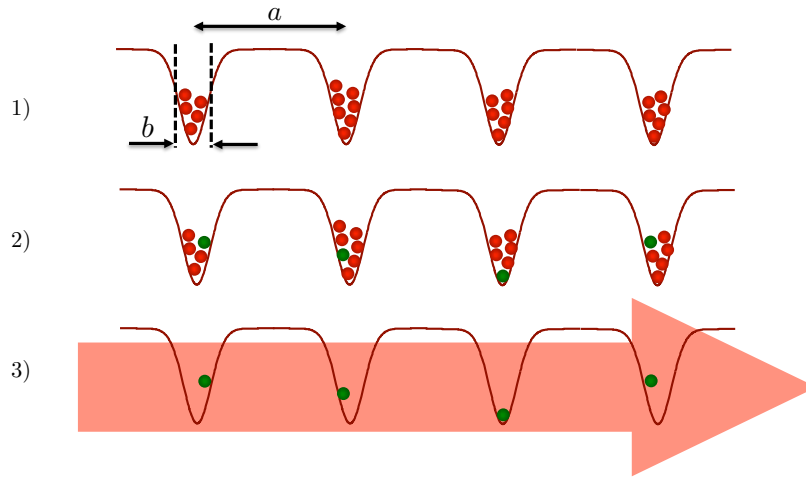


Figure 5.24: Deterministic loading scheme using the blockade.

$|W\rangle$ states

First, the entanglement scheme between two atoms implemented in [Wilk *et al.* \(2010\)](#) can easily be applied to the case of N trapped atoms; assuming that each pair of atoms in the system is blockaded, the same sequence will then couple the ground state $|g, g, \dots, g\rangle$ to the $|W\rangle$ state:

$$|W\rangle = \frac{1}{\sqrt{N}} (|g', g, \dots, g\rangle + |g, g', \dots, g\rangle + \dots + |g, g, \dots, g'\rangle), \quad (5.33)$$

where $|g\rangle$ and $|g'\rangle$ are respectively Zeeman sub-levels of the hyperfine states $F=2$ and $F=1$. First experiments with 3 atoms aligned with the quantization axis z led recently to the successful observations of the enhancement of the coupling from the ground state $|g, g, g\rangle$ to the state $|\tilde{W}\rangle = [|r, g, g\rangle + |g, r, g\rangle + |g, g, r\rangle]/\sqrt{3}$ by a factor 1.67, close to the expected value of $\sqrt{3}$.

$|GHZ\rangle$ states

Theoretical protocols for implementing generalized C-NOT gates and thus prepare in a single step $|GHZ\rangle$ states:

$$|GHZ\rangle = \frac{1}{\sqrt{2}} (|g, g, \dots, g\rangle + |g', g', \dots, g'\rangle), \quad (5.34)$$

with N atoms have been proposed in [Möller, Madsen, and Mølmer \(2008\)](#); [Müller *et al.* \(2009\)](#). These protocols also make use of the Rydberg blockade, and our experimental system would be ideal to implement them experimentally. In the long run, spins systems with long-range dipole-dipole interactions could also be simulated ([Lesanovsky, 2011](#)).

Appendix A

Fundamental constants and main properties of ^{87}Rb

This appendix includes the definitions of the physical constants used in this thesis together with the main properties of ^{87}Rb . More information can be found in the detailed reference [Steck \(2008\)](#).

A.1 Fundamental constants

ϵ_0	$8.854\,18 \cdot 10^{-12}$ As/Vm	vacuum permittivity
μ_0	$4\pi \cdot 10^{-7}$ H/m	vacuum permeability
c	299 792 458 m/s	speed of light in the vacuum
e	$1.602\,189\,2 \cdot 10^{-19}$ C	electron charge
h	$6.626\,068\,96 \cdot 10^{-34}$ Js	Planck's constant
k_B	$1.380\,6504 \cdot 10^{-23}$ J/K	Boltzmann's constant
μ_B	$h \cdot 1.399\,624\,604$ MHz/Gauss	Bohr magneton

Table A.1: Selected fundamental constants ([Steck, 2008](#)).

A.2 Properties of ^{87}Rb

General properties:

Atomic mass	m_a	1.443×10^{-25} kg
Ionization energy	E_I	1 010 024 918.3(6) MHz
Nuclear spin	I	3/2

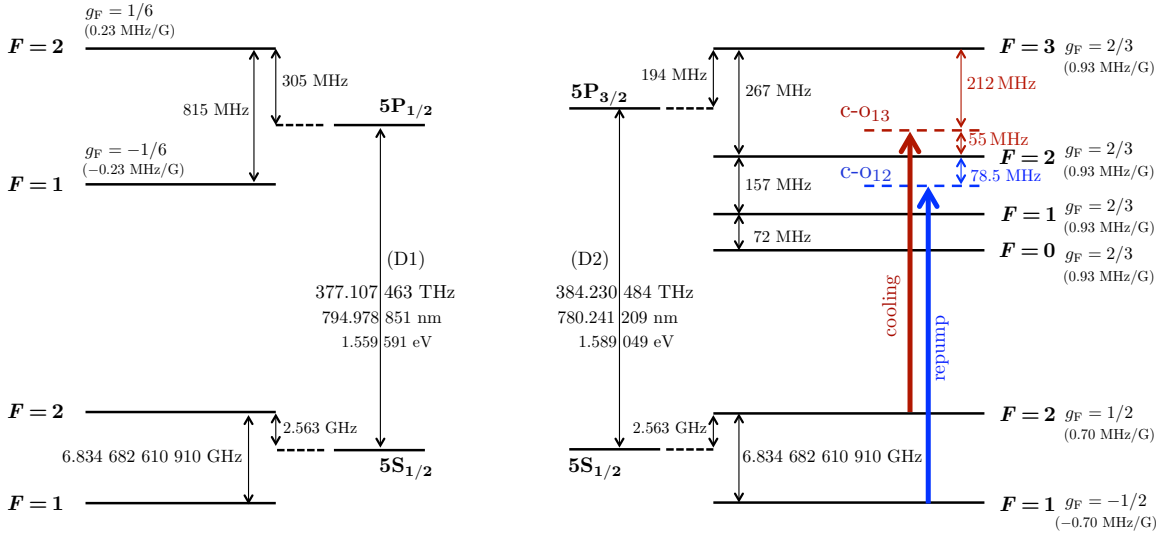


Figure A.1: Hyperfine structure of ^{87}Rb . Lock positions on standard saturated absorption setup are shown for the molasses laser and the repump laser at 780 nm.

D1 transition ($5^2S_{1/2} \leftrightarrow 5^2P_{1/2}$):

Decay rate	Γ	$2\pi \times 5.75 \text{ MHz}$
Recoil frequency	ω_r	$2\pi \times 3.633 \text{ MHz}$
Dipolar matrix element	$(j' = 1/2 er j = 1/2)$	$2.993 a_0$

D2 transition ($5^2S_{1/2} \leftrightarrow 5^2P_{3/2}$):

Decay rate	Γ	$2\pi \times 6.07 \text{ MHz}$
Recoil frequency	ω_r	$2\pi \times 3.771 \text{ MHz}$
Dipolar matrix element	$(j' = 3/2 er j = 1/2)$	$4.227 a_0$

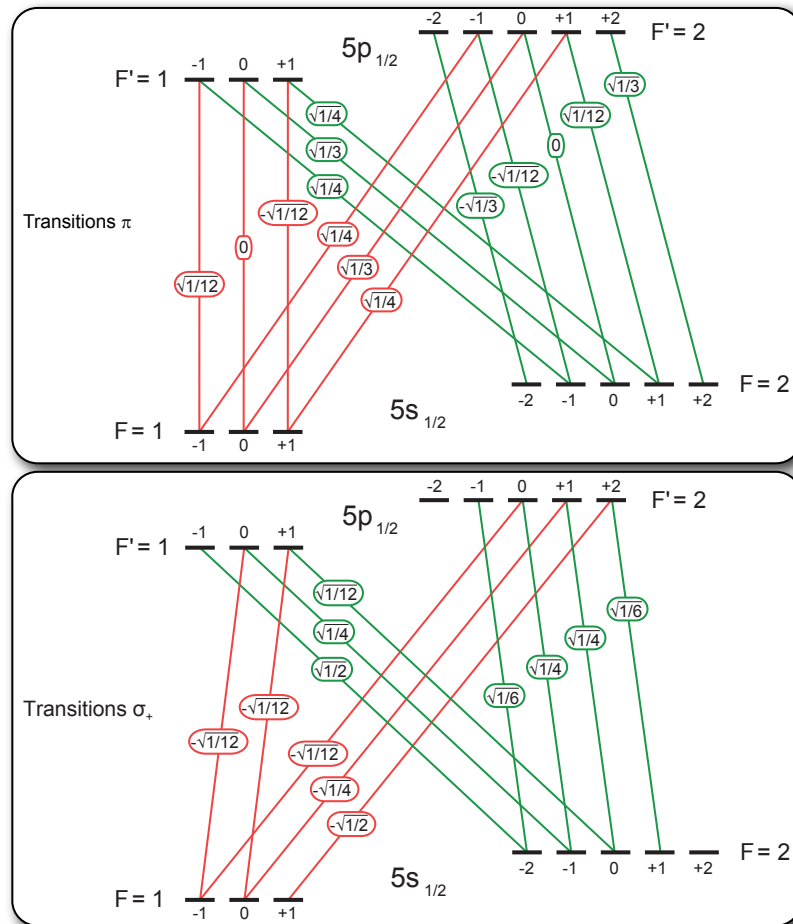


Figure A.2: Clebsch-Gordan coefficients for σ_+ and π transitions of the D1 line, in the hyperfine structure.

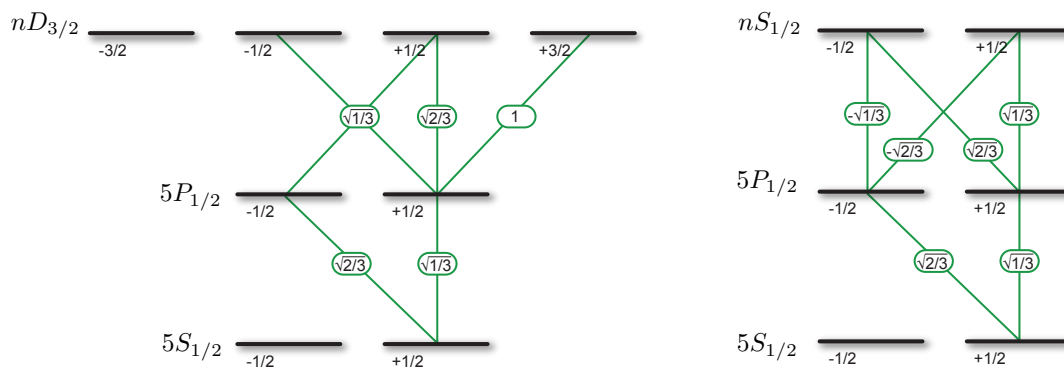


Figure A.3: Clebsch-Gordan coefficients for the transition toward Rydberg states $|nD_{3/2}\rangle$ and $|nS_{1/2}\rangle$.

Appendix B

Properties of Rydberg states in alkali atoms

Contents

B.1 Effective approach: quantum defect theory	154
B.1.1 Quantum defects	154
B.1.2 Fine and hyperfine structure splittings	155
B.1.3 State-selective ionization	156
B.1.4 Numerical calculations of Rydberg radial wavefunctions	157
B.1.5 Rydberg states lifetime	159
B.1.6 Stark effect	160
B.2 Förster resonances	161
B.2.1 Quasi-Förster resonances	163
B.2.2 Tuning pure Förster resonances with external electric fields	163

The alkali metals such as rubidium are elements of the first column of the periodic table. The main property shared by all alkali atoms in their ground states is to have their electron shells completely filled by electrons, except the outer one where a single electron, commonly called the *valence* electron, is in an *s*-orbital. In an alkali atom containing Z protons, the valence electron feels essentially a net elementary charge of one unit, as the Z positive charges in the nucleus are effectively shielded by $Z - 1$ negative charges of the inner electrons. Thus, spectroscopic properties of alkali are somehow similar to the ones of the hydrogen atom.

In such hydrogenic systems, the valence electron can be excited towards states with large principal quantum number n , commonly referred to as *Rydberg states*. These states exhibit peculiar properties including large dipole moments, exaggerated responses to electric fields, and long lifetimes that may allow to implement efficient quantum gates between neutral atom qubits in the framework of quantum information processing.

The goal of this appendix is twofold. First, we introduce qualitatively the basic properties of Rydberg states. Secondly, we use it to group information (theoretical expressions or numerical tabulated values) more specifically related to the case of ^{87}Rb atoms and to which we often refer to in the main text.

Property	n^* -scaling	Case $n = 62$
Binding energy $E_{n,l,j}$	$1/n^{*2}$	-0.9 THz
Energy difference of neighbouring n states	$1/n^{*3}$	30 GHz
Ionization electric field	$1/n^{*4}$	23 V/cm
Typical orbital radius $r_{n,l,j}$	n^{*2}	$3500 a_0$
Dipole moment between adjacent n states	n^{*2}	$3500 e a_0$
Radiative lifetime τ	n^{*3}	$220 \mu\text{s}$
Scalar polarizabilities α	n^{*7}	$900 \text{ MHz}/(\text{V}/\text{cm})^2$

Table B.1: Scaling laws for main properties of Alkali Rydberg states.

B.1 Effective approach: quantum defect theory

A very accurate quantitative description of Rydberg states in hydrogenoid systems can be derived from the quantum defect theory. A complete introduction to the subject is given in the book written by T. F. Gallagher [Gallagher \(1994\)](#).

This description allows to derive the main important scaling laws concerning alkali Rydberg states properties in terms of an effective principal quantum number n^* , that we will describe in the next section. These properties are summed up in Tab. [B.1](#).

B.1.1 Quantum defects

In an alkali atom of atomic number Z , the outermost valence electron moves in an almost hydrogenic Coulomb potential resulting from a compact ion core with Z protons in the nucleus, and the lower electron shells filled with $Z - 1$ electrons. As for hydrogen, we describe the states of the system in the fine basis by wavefunctions $\psi_{n,l,j,m_j}(r, \theta, \phi)$, where n is the principal quantum number, l is the quantized orbital angular momentum, j is the total angular momentum, and m_j is the projection of j onto the quantization axis. In the case of alkali metal different from hydrogen, the electrostatic interactions between electrons and protons form a N -body problem which has no analytical solution.

However, excited Rydberg states correspond to states where the valence electron orbits mainly far away from the ion core, where the nuclear charges are screened by the electrons filling the inner shells. Thus, near the core region, the Rydberg states wavefunctions have such low amplitudes that it becomes valid to approximate the potential as a sum of a pure Coulomb potential and short range corrections. In practice, corrections in the model are needed to agree with experimental observations only for low orbital angular momentum states, typically with $l \leq 3$, for which the valence electron orbit is so extremely elliptic that it penetrates enough the compact ion core to expose the electron to the unscreen nuclear charge. The inner electrons can also be polarized by the presence of the valence electron. These two interactions increase the binding energy of the Rydberg states with low l relative to the equivalent hydrogenic states. Within the framework of quantum defect theory, the eigenenergies $E_{n,l,j}$ of alkali Rydberg states can be calculated effectively using the hydrogen energies formula with small effective corrections that depend on n, l, j :

$$E_{n,l,j} = -\frac{\text{Ry} \left(1 + \frac{m_e}{m_a}\right)^{-1}}{(n_{n,l,j}^*)^2} \quad (\text{B.1})$$

State	Quantum defect	
$S_{1/2}$	δ_0	3.131 180 4(10)
(Li <i>et al.</i> , 2003)	δ_2	0.178 4(6)
$P_{1/2}$	δ_0	2.654 884 9(10)
(Li <i>et al.</i> , 2003)	δ_2	0.290 0(6)
$P_{3/2}$	δ_0	2.641 673 7(10)
(Li <i>et al.</i> , 2003)	δ_2	0.295 0(7)

(a) S, P states

State	Quantum defect	
$D_{3/2}$	δ_0	1.348 091 71(40)
(Li <i>et al.</i> , 2003)	δ_2	-0.602 86(26)
$D_{5/2}$	δ_0	1.346 465 72(30)
(Li <i>et al.</i> , 2003)	δ_2	-0.596 00(18)
$F_{5/2}$	δ_0	0.016 519 2(9)
(Han <i>et al.</i> , 2006)	δ_2	-0.085(9)
$F_{7/2}$	δ_0	0.016 543 7(7)
(Han <i>et al.</i> , 2006)	δ_2	-0.086(7)

(b) D, F states

Table B.2: Quantum defects of ^{87}Rb .

where R_y is the Rydberg unit of energy, m_e is the electron mass, m_a is the atomic mass, and n^* is an effective principal quantum number defined by $n_{n,l,j}^* = n - \delta_{n,l,j}$. The numbers $\delta_{n,l,j}$ are called quantum defects, and can be calculated with the Ritz formula:

$$\delta_{n,l,j} = \delta_0(l,j) + \frac{\delta_2(l,j)}{(n - \delta_0(l,j))^2} + \frac{\delta_4(l,j)}{(n - \delta_0(l,j))^4} + \dots \quad (\text{B.2})$$

For rubidium, the values of $\delta_0(l,j)$ and $\delta_2(l,j)$ were measured experimentally on a cloud of cold atoms by the group of T. F. Gallagher and can be found in the reference Li *et al.* (2003) for the nS , nP and nD series, and in the reference Han *et al.* (2006) for the nF series. For convenience, we have listed them in Tab. B.2. Quantum defects of states with $l > 3$ are almost zero. Thus, these states are degenerate for a given n ; they are referred to as the *hydrogenic* states.

The eigenenergies $E_{n,l,j}$ scaling as $(n^*)^{-2}$, the energy differences between two neighbouring Rydberg states scale as $(n^*)^{-3}$.

B.1.2 Fine and hyperfine structure splittings

Both the fine and hyperfine structure splittings scale as $(n^*)^{-3}$.

Fine structure splitting

The fine structure splittings $\Delta_{nP} = E(nP_{3/2}) - E(nP_{1/2})$, $\Delta_{nD} = E(nD_{5/2}) - E(nD_{3/2})$ and $\Delta_{nF} = E(nF_{7/2}) - E(nF_{5/2})$ can be calculated directly using the quantum defects listed in Tab. B.2 and Eq. B.1. Values in the range $50 \leq n \leq 100$ are listed in Tab. B.3:

Hyperfine structure splitting

As we mentioned above, the hyperfine structure splitting also scales as $(n^*)^{-3}$. This term results from the interaction between the nuclear spin and the total angular momentum of the valence electron. For Rydberg states with $n \geq 50$ for which the electron spends most of the time far away from the nucleus, the interaction is generally very weak. Furthermore, as l increases, the centrifugal barrier term of the Schrödinger equation prevents the electronic wavefunction from entering near the nucleus and the hyperfine interaction gets even weaker.

n	Δ_{nP} (MHz)	Δ_{nD} (MHz)	Δ_{nF} (MHz)
50	818.6	92.7	-1.3
55	605.8	69.2	-1.0
60	460.7	53.0	-0.7
65	358.6	41.4	-0.6
70	284.5	33.0	-0.5
75	229.5	26.8	-0.4
80	187.8	22.0	-0.3
85	155.6	18.3	-0.3
90	130.4	15.3	-0.2
95	110.4	13.0	-0.2
100	94.2	11.1	-0.2

Table B.3: Fine structure splitting for the P , D , and F manifolds in ^{87}Rb .

For the S manifold of ^{87}Rb , the following scaling law can be used to estimate the hyperfine splitting ν_{HFS} (in MHz):

$$\nu_{\text{HFS}} = \frac{33000}{n^*(S_{1/2})^3}. \quad (\text{B.3})$$

It reproduces with an accuracy of about 10% the measurements reported in [Li *et al.* \(2003\)](#) for $28 \leq n \leq 33$. It means that for $n \geq 50$, the hyperfine splitting is lower than 300 kHz and is almost negligible compared to the linewidth of our Rydberg excitation lasers. For higher l , the splitting is even more negligible.

B.1.3 State-selective ionization

A semi-classical approach can be used to estimate the static electric field $F_{\text{ioniz.}}(n, l, j)$ required to ionize the Rydberg state $|n, l, j\rangle$. When a static electric field of amplitude F is applied along the z axis, the total potential energy reads (in the Coulomb approximation):

$$V(r, z) = -\frac{q^2}{4\pi\epsilon_0 r} + qFz. \quad (\text{B.4})$$

The static field F 'tilts' the initial spherically symmetric Coulomb potential so that a saddle point appears along the z axis, as represented on [Fig B.1](#). By differentiating equation [B.4](#) restricted to the z axis, we find the value of the potential energy at the saddle point $z = z_0$:

$$\begin{aligned} \frac{dV(r=z, z)}{dz} = 0 &\Leftrightarrow z = z_0 = \sqrt{\frac{q}{4\pi\epsilon_0 F}} \\ V_{\text{max}} = V(z = z_0) &= -2q^{3/2} \sqrt{\frac{F}{4\pi\epsilon_0}}. \end{aligned} \quad (\text{B.5})$$

In a first approximation, when this classical local maximum is smaller than the Rydberg eigenenergy $E_{n,l,j}$, the valence electron can escape and the atom can thus be ionized. Combining equations [B.5](#) and [B.1](#), we can estimate the field $F_{\text{ioniz.}}(n, l, j)$ allowing to ionize a Rydberg state of energy $E_{n,l,j}$:

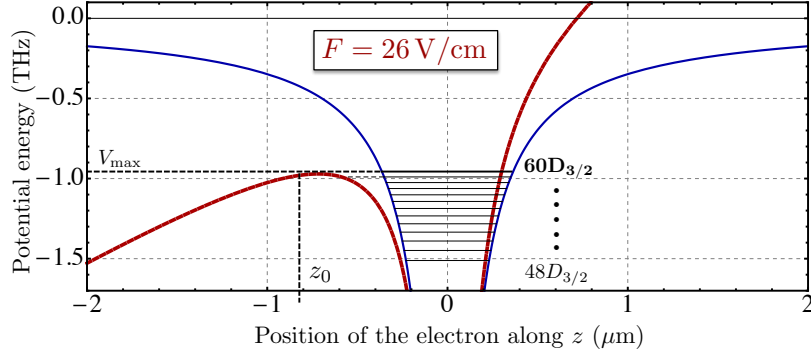


Figure B.1: Selective ionization of Rydberg states with external static electric fields. The Coulomb potential of hydrogenic systems is plotted (blue) as a function of the distance between the valence electron and the nucleus along the Z axis. Eigenenergies of the Rydberg $nD_{3/2}$ serie ranging from 48 to 60 are represented with horizontal dark solid lines. When an external static field F is applied along the z axis, the potential seen by the electron (red dashed line) is tilted and a local maximum appears. In a classical picture, the valence electron can escape for Rydberg states with eigen energies higher than this maximum. Here, for $F = 26$ V/cm, only states $nD_{3/2}$ with $n \geq 60$ are ionized.

$$V_{\max} = E_{n,l,j} \Leftrightarrow F_{\text{ioniz.}}(n, l, j) = \frac{\pi\epsilon_0}{q^3} E_{n,l,j}^2 = \frac{F_0}{16(n_{n,l,j}^*)^4}, \quad (\text{B.6})$$

where the field F_0 is the atomic unit of electric field, and is defined by:

$$F_0 \simeq \frac{16\pi\epsilon_0}{q^3} R_y^2 \simeq 5 \times 10^9 \text{ V/cm}. \quad (\text{B.7})$$

B.1.4 Numerical calculations of Rydberg radial wavefunctions

In the framework of the quantum defect theory, the wavefunctions $\psi_{n,l,j}$ for the valence electron are the solutions of the Schrödinger equation. In spherical coordinates, and using atomic units, it reads:

$$\left[-\frac{1}{2}\nabla^2 + V \right] \psi_{n,l,j}(r, \theta, \phi) = E_{n,l,j} \psi_{n,l,j}(r, \theta, \phi), \quad (\text{B.8})$$

where V is the core potential. Assuming that $V(r)$ has no angular dependence, the wavefunctions are separable as $\psi_{n,l,j}(r, \theta, \phi) = R(r)Y_l^{m_l}(\theta, \phi)$, where $Y_l^{m_l}(\theta, \phi)$ is a spherical harmonic. Inserting this into Eq. B.8 gives the equation for the radial wavefunction of the electron:

$$\left[-\frac{1}{2} \left(\frac{d^2}{dr^2} + \frac{2}{r} \frac{d}{dr} \right) + \frac{l(l+1)}{2r^2} + V(r) \right] R_{n,l,j}(r) = E_{n,l,j} R_{n,l,j}(r). \quad (\text{B.9})$$

Radial wavefunctions can then be calculated by numerically integrating the equation with a chosen central potential $V(r)$. A first approximation is to consider only the Coulomb potential, expressed by $V_{\text{Coul.}} = -1/r$ in atomic units. The potential is then refined to take into account the fine effects of core penetration and polarization by introducing an l -dependent core potential $V_C(r)$ (Marinescu, Sadeghpour, and Dalgarno, 1994). In addition to the core potential, the spin-orbit potential $V_{\text{SO}}(r)$ which causes the fine structure splitting can also be included (Theodosiou, 1984).

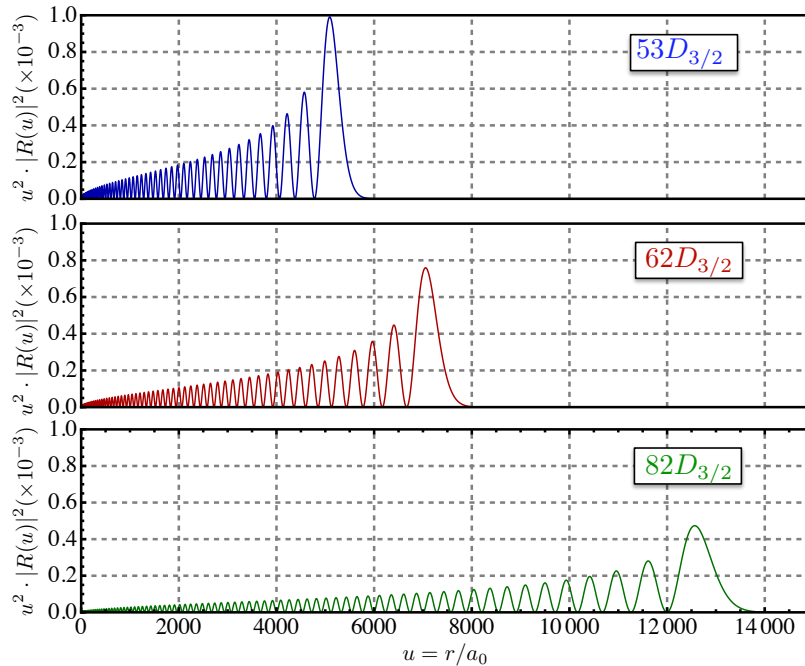


Figure B.2: Rydberg state radial probability density.

In our calculations, we followed the treatment described in [Zimmerman *et al.* \(1979\)](#), considering only the first Coulomb potential term $V_{\text{Coul.}}(r)$. To solve the differential equation of Eq. B.9 which has oscillating solutions, it is desirable for the number of grid points per oscillation to be approximately constant. In this case, the period of the Coulomb wave functions increase rapidly with r . One can thus change the variables:

$$\begin{cases} x &= \ln(r) \\ X(r) &= \sqrt{r}R_{n,l,j}(r), \end{cases} \quad (\text{B.10})$$

the radial equation of Eq. B.9 takes the standard Numerov form

$$\frac{d^2 X(x)}{dx^2} = g(x)X(x), \quad (\text{B.11})$$

where $g(x) = 2 \exp(2x)[- \exp(-x) - E_{n,l,j}] + (l + 1/2)^2$. A vector of radial positions r_j is initialized using the expression:

$$r_j = r_s e^{-jh}, \quad (\text{B.12})$$

where r_s is the starting point of the calculation, and h is the logarithmic step size of the discrete numerical integration. The procedure is executed in the inward direction, e.g. starting from very large radial distance. Indeed, the outer boundary condition is known: $X(r \rightarrow \infty) = 0$. The initial slope of the wavefunction is then chosen small, even though it can be rather random, as the integration is insensitive to the initial values. Indeed, admixtures of the incorrect solution damp out exponentially. Furthermore, proceeding in the inward direction minimizes cumulative numerical errors at large radial distances, where the contributions to the matrix elements are the most important for Rydberg states. The starting point r_s is determined by the requirement that $R_{n,l,j}(r_s) \approx 10^{-10} \times R_{n,l,j}(r_0)$, where r_0 is the outer turning point. As in [Zimmerman *et al.* \(1979\)](#), we chose $r_s = 2n(n + 15)$.

Finally, the inner final distance was fixed to $r_f = 0.01$, such that the vector of radial positions contains $j_{\max} + 2$ elements, where $j_{\max} = \lfloor \ln(r_s/r_f)/h \rfloor$. The Numerov algorithm reads:

$$\begin{cases} X(1) &= 10^{-20} \\ X(2) &= -1.05 \times 10^{-20} \\ X(i+2) &= \frac{X(i) [g(x_i) - 12/h^2] + X(i+1) [10 \cdot g(x_{i+1}) + 24/h^2]}{12/h^2 - g(x_{i+2})} \end{cases} \quad (\text{B.13})$$

At the end, we reconstruct the radial wavefunction $R(r) = X(r)/\sqrt{r}$. As an illustration, we show in Fig. B.2 the radial probability density $r^2 \cdot |R(r)|^2$ calculated numerically for the state $53D_{3/2}$, $62D_{3/2}$ and $82D_{3/2}$. The numerical values of the radial wavefunctions calculated for all the states $|n, l, j\rangle$ with $10 \leq n \leq 100$ were tabulated, and allowed us to compute dipole matrix elements in Sec. 5.4.2. One can verify that the typical radial extension scales as $a_0 (n^*)^2$, such that the radial dipole matrix elements $\langle n', l', j' | e\hat{r} | n, l, j \rangle$ scale as $ea_0 (n^*)^2$.

Strengths of the transitions $5P \rightarrow nD$

Using this method, one shows that the radial matrix elements between the levels $5P$ and nD which appear in the calculations of the Rabi couplings Ω scale as $(n^*)^{-3/2}$. Furthermore, the method surprisingly allows to compute rather accurate values of the radial wavefunction of the states $5P_{1/2}$ or $5P_{3/2}$ within 20%, even though the hydrogenoid approximation is not so well verified for $n=5$ and $l=1$.

B.1.5 Rydberg states lifetime

Once an atom has been excited towards a given Rydberg state $|n, l, j, m_j\rangle$ of energy E_{n,l,j,m_j} , the effective lifetime τ_{eff} before it decays to other states is governed in practice by two independent mechanisms:

1. Spontaneous emission towards states of lower energies, which defines a radiative lifetime $\tau_0(n, l, j, m_j)$.
2. Black-body radiation emitted by the experimental apparatus at temperature T can induce transitions to other states.

Radiative lifetime τ_0

First, the atom can spontaneously decay towards other states $|n', l', j', m'_j\rangle$ of lower energies $E_{n',l',j',m'_j} < E_{n,l,j,m_j}$, with a rate:

$$\Gamma(|n, l, j, m_j\rangle \rightarrow |n', l', j', m'_j\rangle) = \frac{4}{3} \alpha \frac{\omega^3}{c^2} |\langle n', l', j', m'_j | \hat{r} | n, l, j, m_j \rangle|^2, \quad (\text{B.14})$$

where $\alpha \simeq 1/137$ is the fine structure constant, and $\omega = (E_{n,l,j,m_j} - E_{n',l',j',m'_j})/\hbar$ is the transition frequency. The total radiative decay rate $\Gamma_0(n, l, j, m_j)$ is defined as the sum over all the spontaneous decay channels allowed by the selection rules:

$$\Gamma_0(n, l, j, m_j) = \sum_{|n', l', j', m'_j\rangle} \Gamma(|n, l, j, m_j\rangle \rightarrow |n', l', j', m'_j\rangle). \quad (\text{B.15})$$

As each term scales as ω^3 , the largest contributions correspond to states of low energies. Table B.4 below gives the radiative lifetime $\tau_0 = \Gamma_0^{-1}$ (in μs) for the series $nS_{1/2}$ and $nD_{3/2}$ from [Beterov *et al.* \(2009\)](#).

n	50	55	60	65	70	75	80	85	90	95	100
$S_{1/2}$	140	191	252	325	410	510	624	753	900	1065	1248
$D_{3/2}$	119	160	208	266	333	411	501	602	716	844	986

Table B.4: Radiative lifetime τ_0 (in μs) of the Rydberg series $nS_{1/2}$ and $nD_{3/2}$ of ^{87}Rb .

BBR-induced depopulation τ_{BBR}

Secondly, black-body radiation (BBR) from the surrounding experimental apparatus at temperature T can also induce population transfers from the initial state $|n, l, j, m_j\rangle$ towards other states, both with higher or lower energies. The total rate of BBR-induced depopulation Γ_{BBR} is expressed through the number of BBR photons per mode of frequency ω and at temperature T , given by $\bar{n}_\omega = [\exp(\hbar\omega/k_B T) - 1]^{-1}$:

$$\Gamma_{\text{BBR}} = \sum_{|n'', l'', j'', m''_j\rangle} \bar{n}_\omega \cdot \Gamma(|n, l, j, m_j\rangle \rightarrow |n'', l'', j'', m''_j\rangle), \quad (\text{B.16})$$

where $\omega = (|E_{n, l, j, m_j} - E_{n'', l'', j'', m''_j}|)/\hbar$. The sum involves all possible discrete states, and states of the continuum. However, in our experiment, the metallic piece under vacuum probably modify significantly the structure of the modes in the GHz range, which makes this calculation not simple.

Effective lifetime τ_{eff}

Finally, the effective lifetime τ_{eff} is defined by:

$$\frac{1}{\tau_{\text{eff}}} = \Gamma_0 + \Gamma_{\text{BBR}} = \frac{1}{\tau_0} + \frac{1}{\tau_{\text{BBR}}}. \quad (\text{B.17})$$

In practice, calculations of effective lifetimes is thus reduced to compute matrix elements of the form $\langle n', l', j', m'_j | \hat{r} | n, l, j, m_j \rangle$. An explicit expression of these elements was derived in Eq. 5.30 and requires to calculate rather accurately radial matrix elements of the form $\int_0^\infty \psi(r)^* r R_{n, l, j}(r) r^2 dr$, where the wavefunction $\psi(r)$ can correspond to discrete states, or states of the continuum¹. Various numerical methods were developed to compute the effective lifetimes τ_{eff} of alkali-metal atoms using Coulomb approximation ([Farley and Wing, 1981](#); [Spencer *et al.*, 1981](#)), or various core model potentials ([Theodosiou, 1984](#); [He *et al.*, 1990](#)).

B.1.6 Stark effect

In the presence of a static (weak) electric field \vec{F} , the energy levels of a bare atom are shifted: this is known as the Stark effect. Choosing the field along the z axis, the hamiltonian \hat{H}_{tot} of the system reads (in atomic units):

¹The numerical method described in Sec. B.1.4 would allow us to compute these overlap integrals, at least between two discrete Rydberg states.

$$\hat{H}_{\text{tot}} = \hat{H}_0 + \hat{H}_{\text{Stark}} = \hat{H}_0 + F \hat{z}. \quad (\text{B.18})$$

In the fine basis $|n, l, j, m_j\rangle$, the electric field term $F \hat{z}$ shows off-diagonal couplings between states with the selection rules $\Delta l = \pm 1$ and $\Delta m_j = 0$. Thus, the new energy levels and the corresponding eigenstates are found by diagonalizing \hat{H}_{tot} for various values of F . The matrix elements of the Stark interaction have the form:

$$\langle n', l', j', m'_j | \hat{H}_{\text{Stark}} | n, l, j, m_j \rangle = F \langle n', l', j' | \hat{r} | n, l, j \rangle \langle l', j', m'_j | \cos \theta | l, j, m_j \rangle \delta_{l' \pm 1, l} \delta_{m', m_j}, \quad (\text{B.19})$$

where the radial elements can be calculated following the method in Sec. B.1.4, and the angular part with angular momentum algebra.

In alkali atoms such as rubidium, the degeneracy between states $|n, l\rangle$ is broken for low orbital momenta $l \leq 3$, due to the electrostatic interactions between the ion core and the valence electron. The Rydberg states can thus be sorted in two categories: hydrogenoid states ($n, l > 3$) and non-hydrogenoid states ($n, l \leq 3$). For hydrogenoid states $|n, l, j, m_j\rangle$, the full diagonalization of \hat{H}_{tot} in a basis containing all states $3 \leq l \leq n - 1$ with $m = m_j$ is necessary to compute the desired Stark shift. In Fig. B.3, we show the result of the diagonalization obtained for the $n = 57, m_j = |3/2|$ manifold. For non-hydrogenoid states, the perturbation of the electric field acts as a second-order perturbation. The resulting Stark shift is thus quadratic in low field F . For a state $|n, l, j, m_j\rangle$, it reads:

$$\Delta E = -\frac{1}{2} \alpha F^2, \quad (\text{B.20})$$

where α is the static polarizability given by:

$$\alpha = \sum_{n', l', j', m'_j \neq n, l, j, m_j} -2 \times \frac{|\langle n', l', j', m'_j | F \hat{z} | n, l, j, m_j \rangle|^2}{E_{n, l, j} - E_{n', l', j'}}. \quad (\text{B.21})$$

We saw that the radial dipole matrix elements $\langle n', l', j' | r | n, l, j \rangle$ scale as $(n^*)^2$, so the numerators in Eq. B.21 scale as $(n^*)^4$. We also saw that the energy differences at the denominator scale as $(n^*)^{-3}$. Consequently, the static polarizability α of non-hydrogenoid states scale as $(n^*)^7$. For the states $|nD_{3/2}, m_j = 3/2\rangle$, one find $\alpha = 290, 550, 900$, and 6650 MHz/(V/cm)² respectively in the cases $n = 53, 58, 62$, and 82 .

B.2 Förster resonances

Förster resonances between two Rydberg atoms are described in [Saffman and Molmer \(2010\)](#). The term refers to similar resonance energy transfer observed between two chromophores in biology ([Förster, 1948](#)). Let us consider a pair of atoms A and B initially in a certain Rydberg state $|r\rangle$, separated by a distance R along the quantization axis z , as shown in Fig. 5.21(a) with $\theta = 0$. We saw in Sec. 5.4 that in this configuration, the dipole-dipole hamiltonian could be expressed by:

$$\hat{H}_{dd} = \frac{1}{4\pi\epsilon_0} \frac{-\hat{d}_{A,+1} \cdot \hat{d}_{B,-1} - \hat{d}_{A,-1} \cdot \hat{d}_{B,+1} - 2\hat{d}_{A,0} \cdot \hat{d}_{B,0}}{R^3}. \quad (\text{B.22})$$

The dipole-dipole interaction that shifts the energy of $|rr\rangle$ must be generally treated by diagonalizing the hamiltonian expressed in a two-atom basis including many other states, as

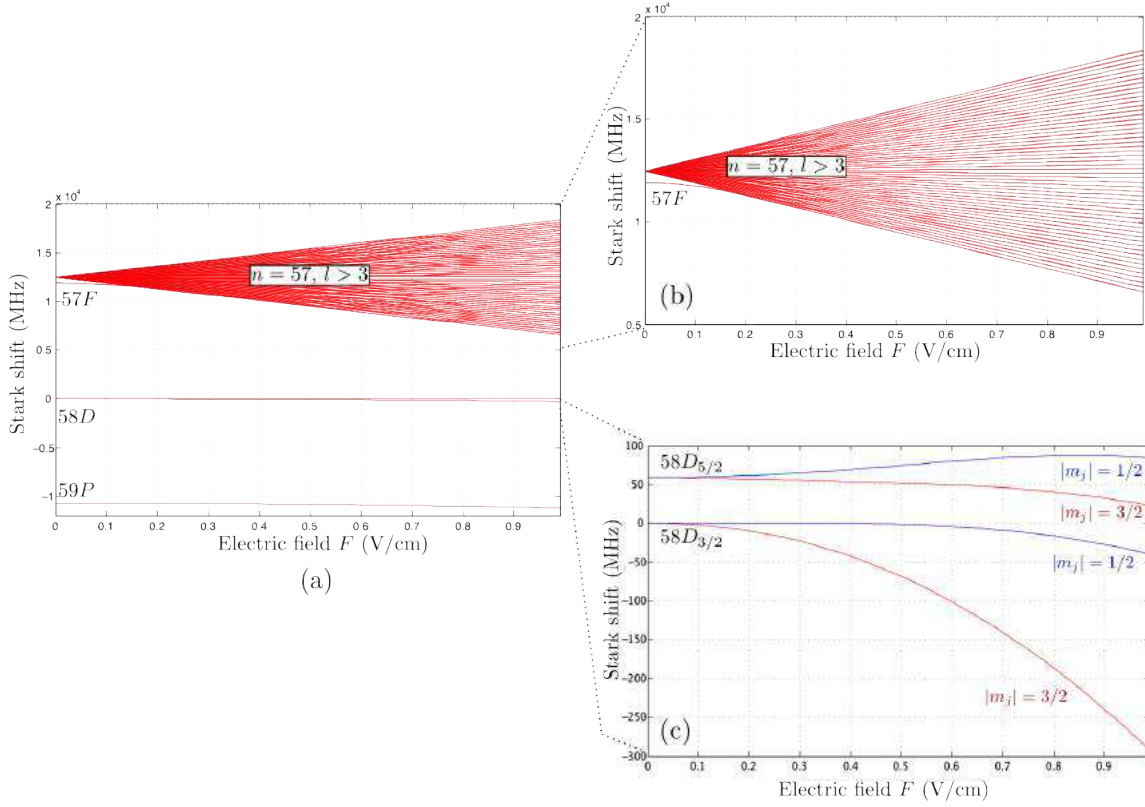


Figure B.3: (a) Stark map of $|58D_{3/2}\rangle$. (b) shows a zoom in the $n=57, m_j = |3/2|$ manifold. (c) shows the Stark shifts of the branches $m_j = |1/2|$ and $m_j = |3/2|$ of $|58D_{3/2}\rangle$.

we described in Sec. 5.4. Here, to simplify the description of the Förster resonance mechanism, we will restrict the hamiltonian to the two states that interact the most with $|rr\rangle$, and which we will label $|r'r''\rangle$ and $|r''r'\rangle$. We define the symmetric state $|S\rangle = [|r'r''\rangle + |r''r'\rangle]/\sqrt{2}$ and the anti-symmetric state $|AS\rangle = [|r'r''\rangle - |r''r'\rangle]/\sqrt{2}$. In the basis $\{|rr\rangle, |S\rangle, |AS\rangle\}$, the hamiltonian of the two-atom system \hat{H}_{tot} reads:

$$\hat{H}_{\text{tot}} = \begin{pmatrix} 0 & \sqrt{2}C_3/R^3 & 0 \\ \sqrt{2}C_3/R^3 & \Delta & 0 \\ 0 & 0 & \Delta \end{pmatrix}, \quad (\text{B.23})$$

where $\Delta = E(r') + E(r'') - 2E(r)$ represents the eigenenergies of the hamiltonian without interaction, letting the energy $2E(r)$ of the state $|rr\rangle$ be the origin. The coefficient C_3 is defined by:

$$C_3 = \frac{1}{4\pi\epsilon_0} \langle r'r'' | -\hat{d}_{A,+1} \cdot \hat{d}_{B,-1} - \hat{d}_{A,-1} \cdot \hat{d}_{B,+1} - 2\hat{d}_{A,0} \cdot \hat{d}_{B,0} | rr \rangle. \quad (\text{B.24})$$

As the anti-symmetric state $|AS\rangle$ is not coupled to the state $|rr\rangle$, the diagonalization of the hamiltonian is straightforward. The eigenenergies E_{\pm} read:

$$E_{\pm} = \frac{\Delta}{2} \pm \sqrt{\left(\frac{\Delta}{2}\right)^2 + \left(\frac{\sqrt{2}C_3}{R^3}\right)^2}, \quad (\text{B.25})$$

and the eigenstates of the system are mixed by the interaction and are expressed by:

$$\begin{cases} |\psi_+\rangle = \sin\theta \cdot |rr\rangle + \cos\theta \cdot |S\rangle \\ |\psi_-\rangle = \cos\theta \cdot |rr\rangle - \sin\theta \cdot |S\rangle \end{cases} \quad (\text{B.26})$$

where $\tan 2\theta = 2 \cdot (\sqrt{2}C_3/R^3)/\Delta$. Two limiting cases can be identified:

- **Van der Waals regime (long range):** $2\sqrt{2}C_3/R^3 \ll |\Delta|$.

This corresponds typically to the regime that we investigated experimentally. The results are presented in Sec. 5.3.4. In this case, the eigenenergies E_{\pm} can be expanded to first order:

$$E_{\pm} = \frac{\Delta}{2} \pm \frac{|\Delta|^2}{2} \left(1 + \frac{4C_3^2}{\Delta^2 R^6} \right). \quad (\text{B.27})$$

In this case, the shift in energy of the state $|\psi_-\rangle \simeq |r_A, r_B\rangle$ due to the interaction reads $\Delta E = C_6/R^6$, where the coefficient C_6 equals $-(\sqrt{2}C_3)^2/\Delta$. As the coefficient C_3 scales as the product of two dipole elements $d_A \cdot d_B \propto (n^*)^4$, and the energy difference $\Delta \propto (n^*)^{-3}$, the coefficient C_6 scales proportional to $(n^*)^{11}$.

- **Dipole-dipole regime (short range):** $2\sqrt{2}C_3/R^3 \gg |\Delta|$.

In this case, the eigenenergies E_{\pm} read:

$$E_{\pm} = \pm \frac{\sqrt{2}|C_3|}{R^3}. \quad (\text{B.28})$$

In this case, the interaction is associated to a $1/R^3$ dependence, and the eigenstates of the system are superposition states $|\psi_{\pm}\rangle = |r_A, r_D\rangle \pm |S\rangle$.

The transition between the $1/R^3$ and $1/R^6$ regimes occurs approximately when $2\sqrt{2}C_3/R^3 = |\Delta|$, so at the interatomic distance $R_{\text{critic}} = (2\sqrt{2}|C_3/\Delta|)^{1/3}$. For the three states $n = 53, 62$ and 82 , one finds respectively $R_{\text{critic}} = 3.3 \mu\text{m}$, $5.9 \mu\text{m}$, and $6.7 \mu\text{m}$.

B.2.1 Quasi-Förster resonances

More accurate calculations of the energy shifts of two-atom states $|r_A, r'_B\rangle$ require to include many more states contributing to the dipole-dipole interaction in the hamiltonian \hat{H}_{dd} . In the van der Waals regime, calculations of the C_6 coefficients based on second-order perturbation theory were described in Sec. 5.4.3. We saw in Eq. 5.31 that they involved a sum of terms of the form C_3^2/Δ . For alkali atoms such as ^{87}Rb , it happens, for two states $|rr'\rangle$ and $|r''r'''\rangle$ coupled by the dipole-dipole interaction, that the energy difference Δ at the denominator is accidentally small. Then this one term enhances by a large factor the value of the C_6 coefficients. In Fig. 5.16, one can see that it occurs twice in the series of states $|nD_{3/2}, m_j = 3/2\rangle_A \otimes |nD_{3/2}, m_j = 3/2\rangle_B$ for $n = 40$ and $n = 58$, which are almost resonant with the states $|(n-2)F_{5/2}, m_j = 5/2\rangle_A \otimes |(n+2)P_{1/2}, m_j = 1/2\rangle_B$. As the dipole-dipole interaction keeps its $1/R^3$ dependence over longer interatomic distances for these states, they are referred to as *quasi* Förster resonances.

B.2.2 Tuning pure Förster resonances with external electric fields

For certain states, the energy differences Δ can be tuned to zero using microwave fields (Afrousheh *et al.*, 2004; Bohlouli-Zanjani, Petrus, and Martin, 2007), or by applying static magnetic

fields, or electric fields (Nipper *et al.*, 2012). Such a control could allow in principle to reach pure Förster resonances for such a pair of two-atom Rydberg states. The interaction becomes thus really long-range, as it keeps its $1/R^3$ dependence over a much wider range of interatomic distances. Or, on the contrary, increasing Δ decreases the interactions. The fine control of the electric field can be a useful tool to tune the interactions in the system.

Appendix C

Custom aspheric lens: drawings, specifications and characterization

The theoretical specifications of the custom aspheric lenses operating under vacuum based on their design with CAD software called Optics Software for Layout and Optimization (OSLO) were the following:

Parameters	Custom lens
Conjugate ratio @ 850 nm	Infinite
Working distance WD	7.03 mm
Operating NA ($S \geq 0.8$ for $y \pm 25 \mu\text{m}$)	
$\lambda_{\text{trap}} = 850 \text{ nm}$:	0.50
$\lambda_{\text{im.}} = 780 \text{ nm}$:	0.54

Table C.1: Custom aspheric lens specifications.

The optical characterization of the lens was performed following one of the procedures described in [Sortais *et al.* \(2007\)](#). The Strehl ratio S of the lens was evaluated by analyzing experimental point spread functions and comparing them to the corresponding ideal case of a stigmatic system with no optical aberrations present. For the sake of simplicity, these tests were performed in air instead of vacuum. In standard conditions for temperature and pressure, the air index of refraction n_{air} is not exactly 1 but about 1.0003 so the optimal operating conjugate ratio in air had to be determined, though simulations with OSLO ensured that the lens performances should not be altered in this configuration. In order to record the point spread functions, we used the optical setup depicted on [Fig. C.1](#).

A microscope plate covered with a metallic layer filled with many sub-micron holes was illuminated from the back by a laser at the trapping (850 nm) or the imaging (780 nm) wavelength. An aberration-free objective was then used to image the microscope plate onto a 12 bits CCD camera. All the sub-micron pinholes are recognizable because their images have different intensities but equal radial widths. The microscope plate was mounted on a three-axis translation stage to allow for positioning such a sub-micron pinhole on-axis, in the focal plane of the aspheric lens. As the pinhole is small compared to $1.22\lambda/NA$, its intensity diagram is almost flat over the full lens aperture which allows to directly measure the point spread function (PSF) of the optical system onto the CCD camera. The operating numerical aperture NA is estimated by measuring the diameter of the aperture iris which

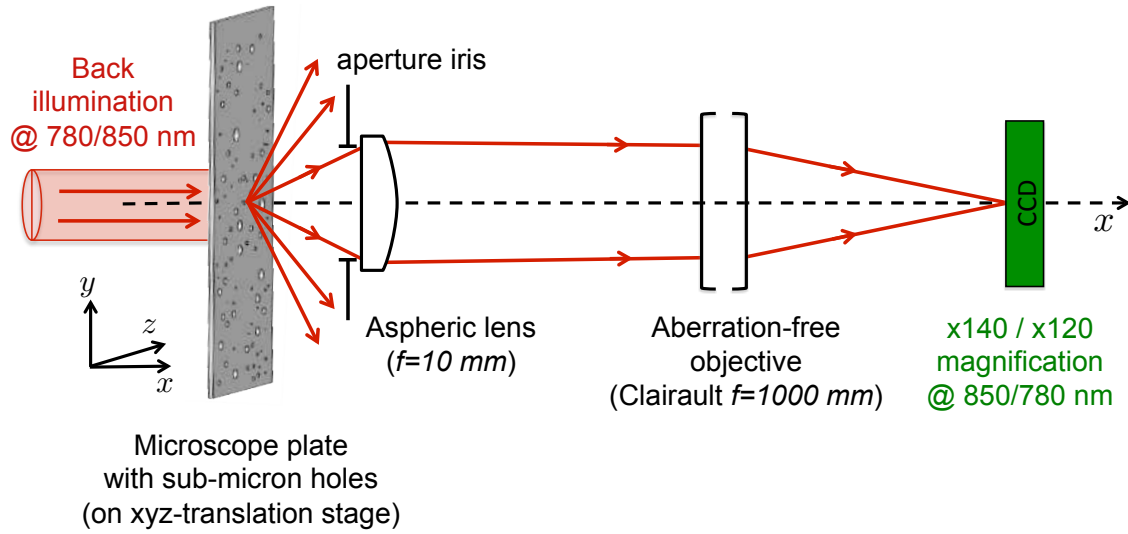


Figure C.1: PSF characterization optical set-up. Sub-micron holes on a microscope plate are illuminated by a laser at a wavelength of interest and act as point source. An aberration-free objective is used in combination with the aspheric lens being tested to image the pinholes onto a linear CCD camera. The plate is mounted in a xyz -translation stage used to align and translate the pinhole on-axis and off-axis with about $\pm 1 \mu\text{m}$ accuracy.

defines the entrance pupil of the system. The magnification is measured experimentally by moving a given pinhole with the yz -translation stages and measuring its image displacement onto the CCD camera. Incoming light flux F is computed by summing the intensity of each pixel after subtracting background. Then, the Strehl ratio is calculated by computing the theoretical PSF (2D Airy function) corresponding to an equivalent stigmatic system with same operating numerical aperture and same light flux F :

$$\text{PSF}_{\text{stig.}}(r) \propto I_{\text{stig.}} \left| \frac{2 J_1(2\pi r \frac{NA}{\lambda})}{2\pi r \frac{NA}{\lambda}} \right|^2, \quad \text{with} \quad \iint_{\text{space}} \text{PSF}_{\text{stig.}}(r) r dr d\theta = F. \quad (\text{C.1})$$

On-axis, at $\lambda_{\text{trap}} = 850$ nm, we could measure diffraction-limited performances ($S \simeq 0.85$) up to $NA \simeq 0.45$. The CCD image of the corresponding PSF corrected for the ($\times 140$) magnification of the observation objective and measured in the best focus plane is shown in Fig. C.2(a). The corresponding cross section passing through the peak intensity is plotted in (b). Then we moved the pinhole perpendicular to the optical axis with $1 \mu\text{m}$ -fine translation stages to study off-axis performances in the yz -plane. Fig. C.2(c) shows a CCD image of the PSF at $\lambda_{\text{trap}} = 850$ nm, for a field $y = 25 \mu\text{m}$. Thus, we could measure the evolution of the real peak intensity I_{peak} as a function of the transverse fields y and z and confirm the rotation symmetry of the system. The relative evolution of the peak intensity in the y -field with respect to the peak intensity on-axis is represented on Fig C.2(d). The data could be discussed as we did not make sure that the intensity of the back-illuminating laser was perfectly constant over the full field. Indeed, Strehl ratios calculated with the previous method for each field point seem to decrease more slowly with the field y . The off-axis performances of the optical system shown in Fig C.2(d) might be underestimated.

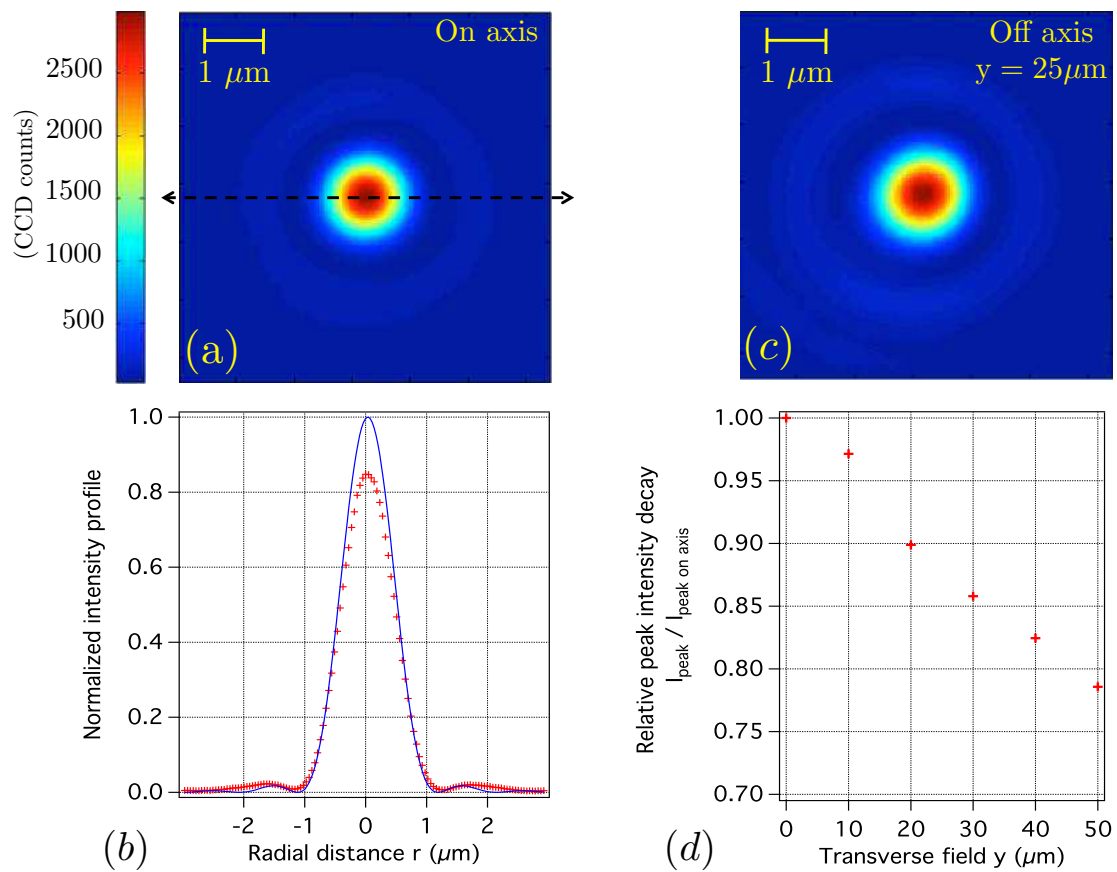


Figure C.2: PSF analysis at 850 nm. Images of the point spread function (PSF) taken with a linear CCD camera at 850 nm corrected for the ($\times 140$) magnification of the observation objective, for a sub-micron pinhole source on axis (a) and off-axis by $25 \mu\text{m}$ (c), with an operating numerical aperture $NA=0.45$. Cross-section of the point spread function on-axis shown in (a) is plotted in (b). We show the Airy function (blue solid line) for comparison. The Strehl intensity ratio is $S = 0.84$.

8		7		6		5		4		3		2		1					
RADIUS		RADIUS ERROR		IRREGULARITY		CA		CT		WD		NA		DESIGN WAVELENGTH		EFL		WAVEFRONT	
S1 ASPHERE		CX ± 0.003 mm		RMS <10 mm		RMS <10.5 mm P-V		RMS <10.5 mm P-V		RMS <10.5 mm P-V									
S2 PLANO		PL		N/A		N/A		5.379±TBD		N/A		N/A		850		10.03±1.0%		TBD	

NOTES: UNLESS OTHERWISE SPECIFIED

- [-OAI-] IS THE THEORETICAL OPTIC AXIS OF THE FIRST OPTIC SURFACE.
- [-OAZ-] IS THE THEORETICAL OPTIC AXIS OF THE SECOND OPTIC SURFACE.
- MATERIAL: D-ZLAF52LA, PREFORM PART NUMBER: TBD.
- ASPHERIC SURFACES ARE DEFINED BY:

$$Z(Y) = \dots + A_2 \cdot Y^2 + A_4 \cdot Y^4 + A_6 \cdot Y^6 + A_8 \cdot Y^8 + A_{10} \cdot Y^{10} + A_{12} \cdot Y^{12} + A_{14} \cdot Y^{14} + A_{16} \cdot Y^{16}$$

$$R \cdot (1 + \sqrt{1 - (1+K) \cdot Y^2 / R^2}) \cdot 0.5$$

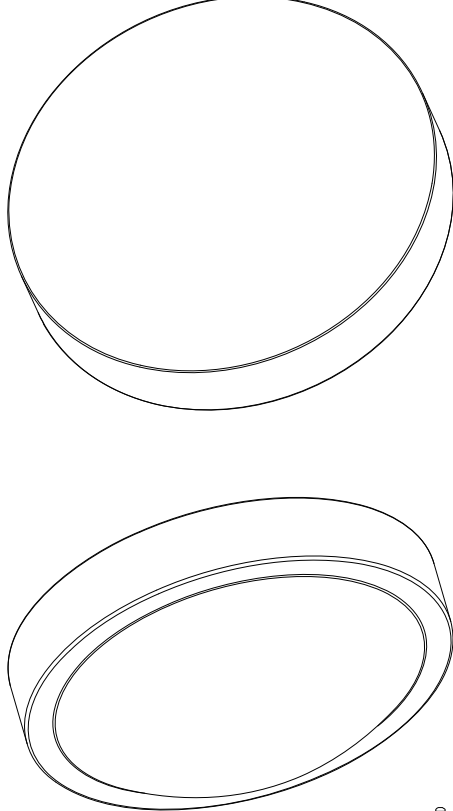
WHERE: Y= RADIAL DISTANCE FROM VERTEX IN mm

5. SURFACE DEFINITIONS:

	SURFACE 1	SURFACE 2
RADIUS	7.930072	PLANO
K	-1.025974	0.000000
A ₂	0.000000E0	0.000000E0
A ₄	1.031945E-4	0.000000E0
A ₆	-5.274804E-8	0.000000E0
A ₈	-3.258955E-9	0.000000E0
A ₁₀	2.432531E-11	0.000000E0
A ₁₂	-2.760531E-13	0.000000E0
A ₁₄	0.000000E0	0.000000E0
A ₁₆	0.000000E0	0.000000E0

- THIS ELEMENT MUST MEET THE SCRATCH/DIG REQUIREMENTS ACROSS THE FULL CLEAR APERTURES INDICATED, BOTH SIDES, PER MIL-PRF-13830B AS PROVIDED IN LIGHTPATH SPECIFICATION: TBD.
- THIS ELEMENT IS USED IN AN OBJECTIVE ASSEMBLY. TEST METHODS AND FREQUENCIES ARE DEFINED AS PROVIDED IN LIGHTPATH SPECIFICATION: TBD.

**PRELIMINARY
NOT FOR MANUFACTURE**



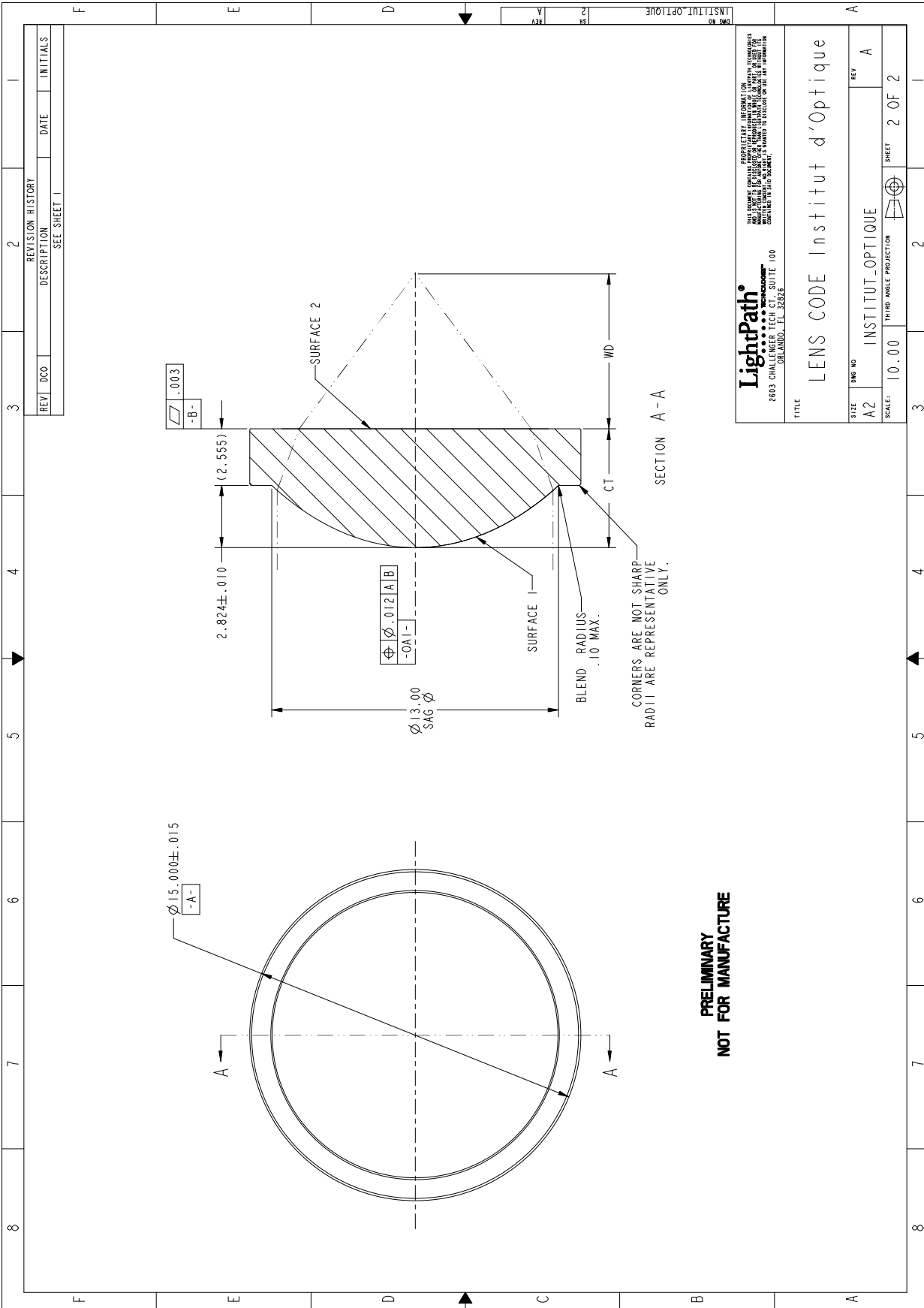
UNLESS OTHERWISE SPECIFIED
DIMENSIONS ARE IN MM.
TOLERANCES ARE:
X: ± 0.10
Y: ± 0.10
Z: ± 0.13
ANGLES: ± 0.5°

LightPath
2803 CHALLENGER TECH CT, SUITE 100
ORLANDO, FL 32836

TITLE: LENS CODE Institut d'Optique

DRAWN: RFQ/ORL	SIZE: A2	PWG NO: INSTITUT_OPTIQUE	REV: A
MATERIAL: SEE NOTES	SCALE: 10.00	THIRD ANGLE PROJECTION	SHEET 1 OF 2
SOFTWARE: Prof/ENGINEER			





**PRELIMINARY
NOT FOR MANUFACTURE**

REV	DCO	DESCRIPTION	DATE	INITIALS
SEE SHEET 1				

LightPath <small>ORLANDO, FL 32826</small>		<small>THIS DOCUMENT CONTAINS PROPRIETARY INFORMATION FOR THE MANUFACTURE OF OPTICAL COMPONENTS. IT IS THE PROPERTY OF LIGHTPATH TECHNOLOGIES AND IS NOT TO BE REPRODUCED OR TRANSMITTED IN ANY FORM OR BY ANY MEANS, ELECTRONIC OR MECHANICAL, INCLUDING PHOTOCOPYING, RECORDING, OR BY ANY INFORMATION STORAGE AND RETRIEVAL SYSTEM, WITHOUT THE WRITTEN PERMISSION OF LIGHTPATH TECHNOLOGIES.</small>	
TITLE: LENS CODE Institut d'Optique			
SIZE: A2	DWG NO: INSTITUT_OPTIQUE	REV: A	
SCALE: 10.00	THIRD ANGLE PROJECTION	SHEET: 2 OF 2	

Appendix D

Design and characterization of the Zeeman slower coils and the MOT coils

Contents

D.1 Zeeman slower coils	171
D.2 MOT coils	173

D.1 Zeeman slower coils

In our experiment, the initial MOT cloud is loaded from a standard Zeeman slower apparatus. A hot rubidium vapor with an initial temperature of about 400 K is created in an oven containing a broken rubidium ampoule and heated up with regular heating wires. An atomic beam is extracted and collimated through a small solid angle thanks to a hole drilled in a copper plate as shown in Fig. D.1. The copper plate is in contact with a nitrogen pot and allows to pump the residual rubidium vapor. A 780 nm laser resonant with ^{87}Rb closed atomic transition $|F=2, m_F=2\rangle \rightarrow |F'=3, m'_F=3\rangle$ with σ^+ polarization is shone in the direction opposite to the beam's motion and applies a radiation pressure force on the atoms. A solenoid-like coil produces a longitudinal magnetic field $B(z)$ along the atomic beam axis which varies spatially in order to compensate exactly the Doppler effect variation seen by the atoms while they are slowing down. The theoretical magnetic field profile along the propagation axis labeled y can be calculated by equating at all y the frequency of the chosen atomic transition with the frequency of the laser seen by the atom in its own motion frame:

$$\omega_{\text{laser}} = \omega_{\text{atom}}, \tag{D.1}$$
$$\omega_{\text{laser}}^0 + kv(y) = \omega_0 + (g_{F'}m_{F'} - g_F m_F) \frac{\mu_B}{\hbar} B(y),$$

where the atomic transition $|F=2, m_F=2\rangle \rightarrow |F'=3, m'_F=3\rangle$ is shifted by the linear Zeeman effect. The Landé g-factors are respectively $g_F = 1/2$ and $g_{F'} = 2/3$ (see App. A), such that $g_{F'}m_{F'} - g_F m_F = 1$. Then, assuming that the transition is saturated with a saturation

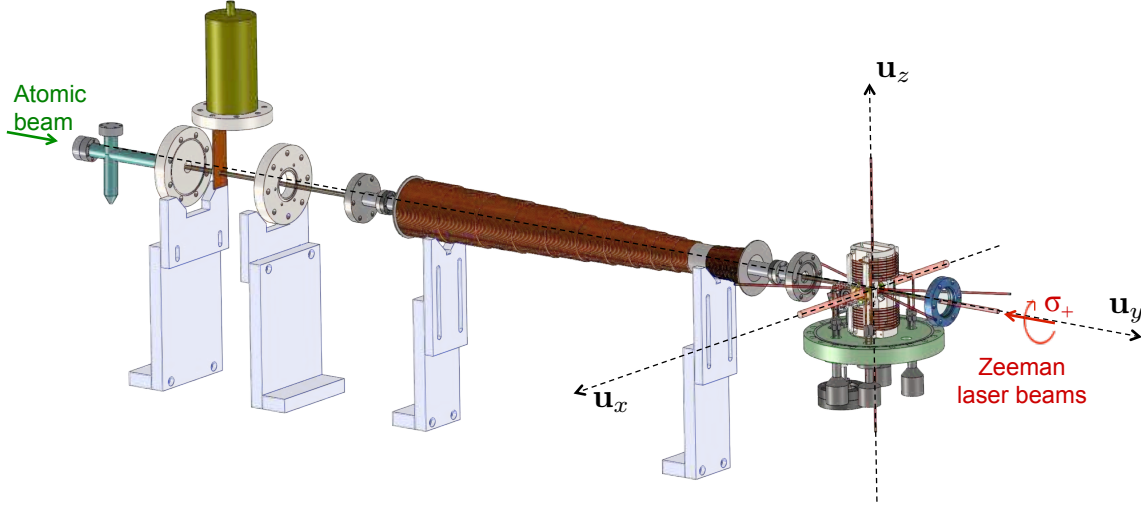


Figure D.1: Zeeman slower design.

parameter $s \simeq 3$ at all times, the atom is constantly slowed down by the negative acceleration a :

$$a \simeq \frac{\hbar k \Gamma}{2m} \frac{s}{1+s} \simeq 80\,000 \text{ m}\cdot\text{s}^{-2},$$

$$v(y) = v_0 \sqrt{1 - \frac{2ay}{v_0^2}}. \quad (\text{D.2})$$

Γ is the decay rate of the excited states $5P_{3/2}$, m is the mass of a ^{87}Rb atom, and v_0 is the initial atomic velocity along the y -axis. A nice feature of Zeeman slower is that once the profile of the longitudinal magnetic field is computed based on a certain maximum initial velocity v_0 , then all atoms with smaller velocities will meet a point along y where the resonance condition is matched and thus will be decelerated as well. In order to choose v_0 to get a decent fraction of the atoms decelerated inside the atomic beam, we can look at the velocity distribution $v = |\mathbf{v}|$ of the atoms at a temperature of about 400 K. It is not a 3D Maxwell-Boltzmann speed distribution proportional to $v^2 \exp(-mv^2/2k_B T)$ describing an ensemble of atoms in a box at temperature T . Using an effusive heated oven, the probability of an atom to emerge from the ‘box’ is proportional to its velocity (Ramsey, 1956), so the velocity distribution in the beam is then proportional to $v^3 \exp(-mv^2/2k_B T)$. Fig. D.2(a) shows such a normalized distribution with our chosen cut-off at $v_0 = 300 \text{ m/s}$ leading to a decent fraction of decelerated atoms $\eta \simeq 0.3$, and a decent Zeeman slower length $v_0^2/(2a) \simeq 50 \text{ cm}$. Now, using a laser beam detuned by $\delta = \omega_{\text{laser}}^0 - \omega_0 = -2\pi \cdot 133 \text{ MHz}$ from the unshifted atomic transition such that it does not perturb the atoms inside the MOT, the longitudinal magnetic field profile $B(y)$, shown in Fig. D.2(b), can be derived using Eq. D.1 and D.2:

$$B(y) = \frac{\hbar}{\mu_B} \left(\delta + kv_0 \sqrt{1 - \frac{2ay}{v_0^2}} \right). \quad (\text{D.3})$$

A current I_1 runs through a first long solenoid built with 10 layers of lengths l_i^1 to produce the positive part of the magnetic field amplitude. An independent current I_2 runs through

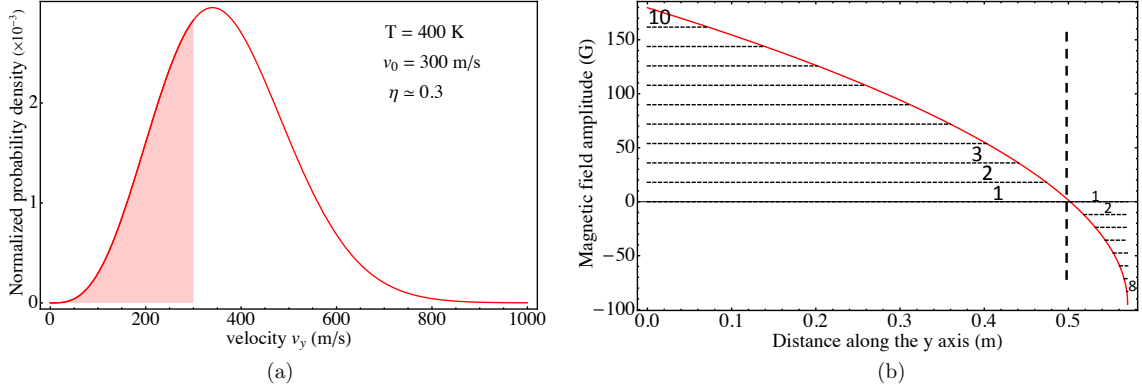


Figure D.2: Zeeman slower design parameters. (a) shows the normalized longitudinal velocity distribution computed for an effusive atomic beam at temperature $T = 400$ K. The shaded area correspond to the fraction of atoms which can be decelerated with our Zeeman slower design. (b) represents the theoretical profile of the axial magnetic field amplitude computed using Eq. D.3 for atoms with initial longitudinal velocity smaller than 300 m/s.

a second short solenoid built with 8 layers of lengths l_j^2 to produce the negative part of the magnetic field amplitude. The lengths l_i^1 and l_j^2 were computed by dividing the peak-peak amplitude of the magnetic field produced by each solenoid and divided by the chosen number of layers as depicted in Fig. D.2(b). Before operating the two Zeeman coils on the main apparatus, we tested them using a 3-axis magnetometer. Fig. D.3(a) shows experimental measurements $B_y(y_i)$ with $I_1 = -I_2 = 1$ A compared to the expected longitudinal amplitude B_y^{exp} calculated using solenoids formula. The difference is below 5%. Last, in Fig. D.3(b) we compared the on-axis profile B_y^{exp} expected for the optimized values of currents $I_1 = 3.14$ A and $I_2 = -2.07$ A to the required on-axis profile B_y^{req} computed with Eq. D.3. Along the y -axis, the error $\Delta B_y = B_y^{\text{exp}} - B_y^{\text{req}}$ is estimated to remain below 2 G between $y = 7$ cm and $y = 57$ cm. The corresponding residual shift of $2 \times 1.4 \simeq 3$ MHz is small compared to the power-broadened linewidth of the transition $\Gamma_{\text{eff}} = \Gamma \sqrt{1 + s} \simeq 12$ MHz. We checked that this should allow to capture an effective fraction of decelerated atoms $\eta_{\text{eff}} \simeq 0.27$ from the initial velocity distribution.

D.2 MOT coils

The MOT coils were designed to be placed as close to the atoms as possible with small number of loops. Thus, they have a very low inductance and could be switched from anti-Helmholtz to Helmholtz configurations in short times, on the order of $1\text{-}10 \mu\text{s}$ ¹. The coils are made in oxygen-free high thermal conductivity (OFHC) copper wires, with circular cross-section of 3 mm diameter so they can be operated up to 30 A without using any cooling system. They were mounted on the central stainless steel piece using isolating ceramic spacers in MACOR[®]. We have implemented a simple circular helical design. The two coils are separated by $L = 38$ mm, the helix pitch p is 4 mm and the helix radius R is 35 mm. With this geometry, the inductance of each MOT coil is on the order of $36 \mu\text{H}$.

The assembly shown in Fig. D.4 was tested before being operated on the experiment under vacuum using a 3-axes magnetometer to check that no magnetic inclusion was left inside the central piece during machining. Experimental data for anti-Helmholtz and Helmholtz

¹Characterization still has to be performed.

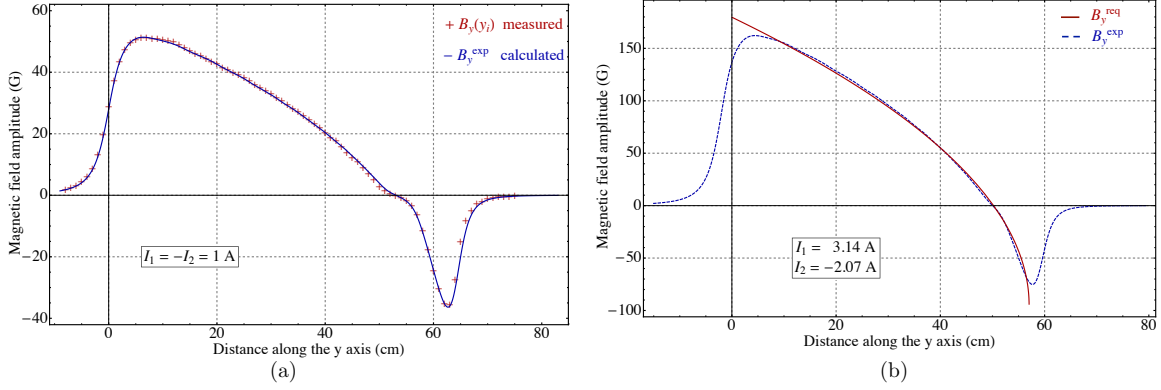


Figure D.3: Magnetic field characterization of the Zeeman coils. (a) On-axis measurements of the longitudinal magnetic field B_y , with currents $I_1 = -I_2 = 1$ A. The solid line is the expected profile calculated with solenoids formulas applied to our coils geometry. (b) Comparison between the required magnetic field profile B_y^{req} computed with Eq. D.3 and the on-axis profile B_y^{exp} expected with our Zeeman coils for the optimized values of currents $I_1 = 3.14$ A and $I_2 = -2.07$ A. The origin of the y axis is chosen at the entrance of the first Zeeman coil.

configurations are shown respectively on Fig. D.5 and Fig. D.6. They were compared to calculations applying Biot-Savart law to an helical geometry. Along the z -axis, the longitudinal magnetic field created by one helix is:

$$B_z^{\text{hel.}}(z) = \frac{\mu_0 I}{4\pi} \int_{\theta=-N\pi}^{N\pi} \frac{R^2}{(R^2 + (z - p\frac{\theta}{2\pi})^2)^{3/2}} d\theta, \quad (\text{D.4})$$

where the origin is the chosen here to be the center of the helix. Now, in the new frame where the origin is the center of the assembly and belongs to the symmetry plane of the two helical coils, the expressions of the longitudinal magnetic field for both Helmholtz and anti-Helmholtz configurations can be obtained with:

$$\begin{aligned} B_z^{\text{H}}(z) &= B_z^{\text{hel.}}(z + z_c) + B_z^{\text{hel.}}(z - z_c) \\ B_z^{\text{AH}}(z) &= B_z^{\text{hel.}}(z + z_c) - B_z^{\text{hel.}}(z - z_c), \end{aligned} \quad (\text{D.5})$$

where $\pm z_c = \pm(pN/2) + L/2$ are the positions of the centers of the two helices. Solid lines shown in Fig. D.5 and in Fig. D.6(a) are calculations obtained with the chosen helical geometry and a current of 20 A and overlap rather well to experimental measurements. By fitting the data, we obtained the following operating parameters:

Anti-Helmholtz configuration: $B'_z/I = 0.4$ G/cm/A,
 $B'_x = B'_y = -B'_z/2$,

Helmholtz configuration: $B_z/I = 1.1$ G/A,
 $B_{\perp}/I \leq 10$ mG/A

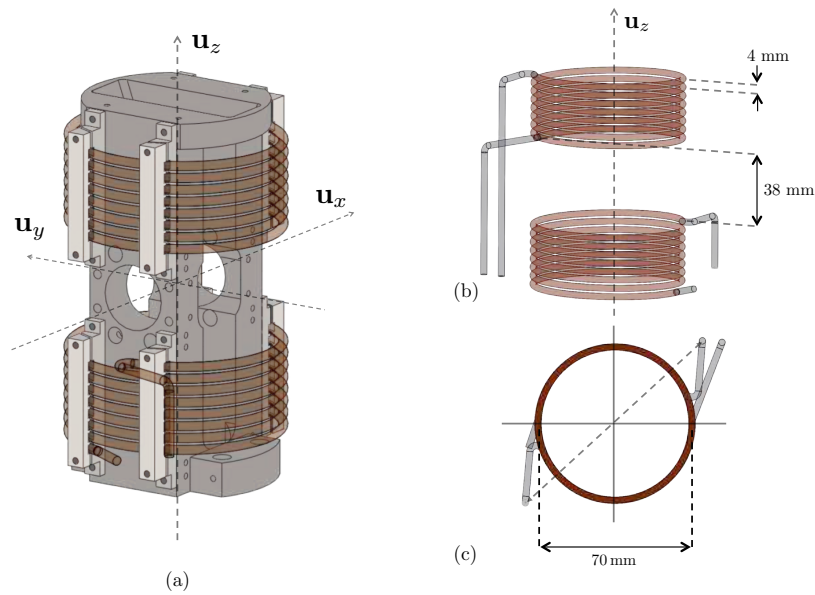
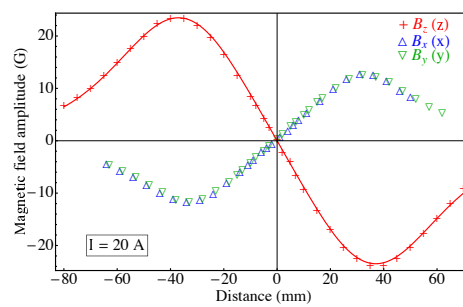
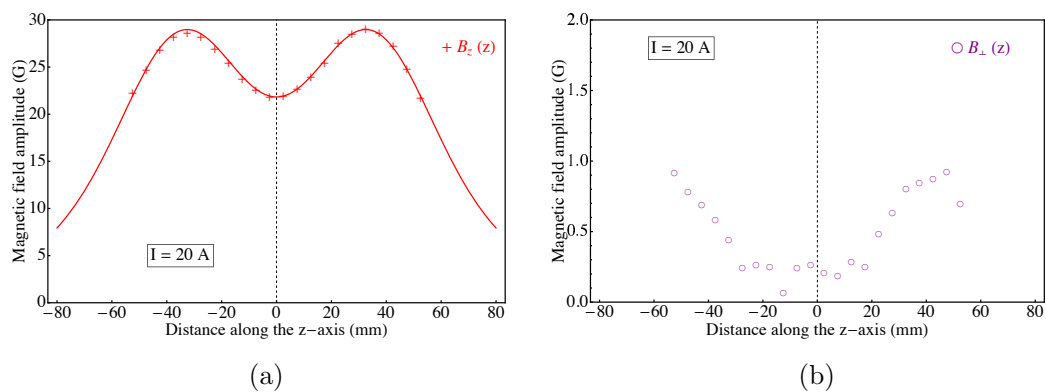


Figure D.4: MOT coils assembly.

Figure D.5: Magnetic field characterization of the MOT coils in anti-Helmholtz configuration. Measurements of the B -field longitudinal component were performed along the three main axes x , y , and z , with a current of 20 A.Figure D.6: Magnetic field characterization of the MOT coils in Helmholtz configuration. Measurements of the B -field longitudinal and transverse components were performed along the z -axis, with a current of 20 A.

Appendix E

Published article

We reproduce here the article presenting the results of chapter 5, entitled: 'Direct measurement of the van der Waals interaction between two Rydberg atoms'.



Direct Measurement of the van der Waals Interaction between Two Rydberg Atoms

L. Béguin,¹ A. Vernier,¹ R. Chicireanu,² T. Lahaye,¹ and A. Browaeys¹

¹Laboratoire Charles Fabry, Institut d'Optique, CNRS, Univ Paris Sud, 2 avenue Augustin Fresnel, 91127 Palaiseau cedex, France

²Laboratoire de Physique des Lasers, Atomes et Molécules, Université Lille 1, CNRS; 59655 Villeneuve d'Ascq cedex, France

(Received 22 March 2013; published 24 June 2013)

We report the direct measurement of the van der Waals interaction between two isolated, single Rydberg atoms separated by a controlled distance of a few micrometers. Working in a regime where the single-atom Rabi frequency for excitation to the Rydberg state is comparable to the interaction, we observe partial Rydberg blockade, whereby the time-dependent populations of the various two-atom states exhibit coherent oscillations with several frequencies. Quantitative comparison of the data with a simple model based on the optical Bloch equations allows us to extract the van der Waals energy, and observe its characteristic C_6/R^6 dependence. The measured C_6 coefficients agree well with *ab initio* calculations, and we observe their dramatic increase with the principal quantum number n of the Rydberg state.

DOI: [10.1103/PhysRevLett.110.263201](https://doi.org/10.1103/PhysRevLett.110.263201)

PACS numbers: 34.20.Cf, 03.67.Bg, 32.80.Ee

The van der Waals–London interaction $U_{\text{vdW}} = C_6/R^6$ between two neutral, polarizable particles separated by a distance R is ubiquitous in nature. It underlies many effects, from the condensation of nonpolar gases to the adhesion of gecko toes [1]. At a macroscopic scale, measuring thermodynamic quantities of a system gives indirect access to the van der Waals interaction between the constituent atoms or molecules [2]. Alternatively, one can directly measure the net force between macroscopic bodies resulting from the microscopic van der Waals forces. However, in this case, summing over the underlying C_6/R^6 interactions between individual particles results in a potential scaling as $1/L^\alpha$, where L is the separation between the bodies, and $\alpha < 6$ is a geometry-dependent exponent (e.g., $\alpha = 1$ for two spheres with a diameter $D \gg L$) [1,2].

At the level of individual particles, spectroscopy of the vibrational levels close to the dissociation limit of a diatomic molecule, analyzed semiclassically, allows one to infer the long-range interaction between atoms [3]. Progress in atomic physics has made it possible to measure van der Waals interactions between ground-state atoms and a surface (scaling as $1/L^3$, or even $1/L^4$ if retardation plays a role) with a variety of techniques [4]. However, directly measuring the van der Waals interaction between two ground-state atoms would be extremely challenging, due to their very small interaction. In contrast, Rydberg atoms (atoms with large principal quantum number n) exhibit very strong interactions that scale rapidly with n . Using this property, the interaction between Rydberg atoms and a surface has been measured at relatively large distances [5,6]. Here, we report on the measurement of the C_6/R^6 interaction between two isolated Rydberg atoms prepared in a well defined quantum state.

The principle of our experiment is the following. We irradiate the pair of atoms with lasers that couple the ground state $|g\rangle$ and the targeted Rydberg state $|r\rangle$ with

Rabi frequency Ω . Depending on the relative strength of U_{vdW} and $\hbar\Omega$, two limiting cases can be identified. If $U_{\text{vdW}} \ll \hbar\Omega$, the atoms behave independently and the doubly excited state $|rr\rangle$ can be fully populated. On the contrary, when $\hbar\Omega \ll U_{\text{vdW}}$, the excitation of $|rr\rangle$ is off resonant and thus suppressed [see Fig. 1(a)], yielding Rydberg blockade [7–9]. This leads to the appearance of “blockade spheres” inside of which only one Rydberg excitation can be created. The blockade sphere picture gives an intuitive understanding of nontrivial many-body effects in driven systems. Rydberg blockade has been observed in recent years in extended cold atom ensembles [10–14] as well as between two atoms [15,16].

In the transition region $\hbar\Omega \sim U_{\text{vdW}}$, i.e., in the partial blockade regime, the blockade sphere picture is too simplistic: the populations of the various many-atom states undergo coherent collective oscillations with several frequencies which depend on U_{vdW} . In our two-atom experiment, this allows us to extract the interaction strength. By measuring U_{vdW} for various R , we observe its characteristic $1/R^6$ dependence. The measured C_6 coefficients, which scale extremely fast with n , agree well with *ab initio* calculations. Our results prove that detailed control over the interactions between Rydberg atoms is possible; this is a prerequisite for applications to high-fidelity quantum information processing [17] and quantum simulation using long-range interatomic interactions [18].

We use two single ^{87}Rb atoms at a temperature of $50 \mu\text{K}$, loaded in 1 mK-deep microscopic optical traps from a magneto-optical trap [see Fig. 1(b)] [19]. Our new setup is designed to overcome the limitations of the apparatus used in our early studies of Rydberg blockade [16] and entanglement [20]. We use an aspheric lens under vacuum [21] with numerical aperture 0.5 (focal length 10 mm, working distance 7 mm) to focus two 850 nm trapping beams down to $1.1 \mu\text{m}$ ($1/e^2$ radius). The distance R between the traps is varied by changing the

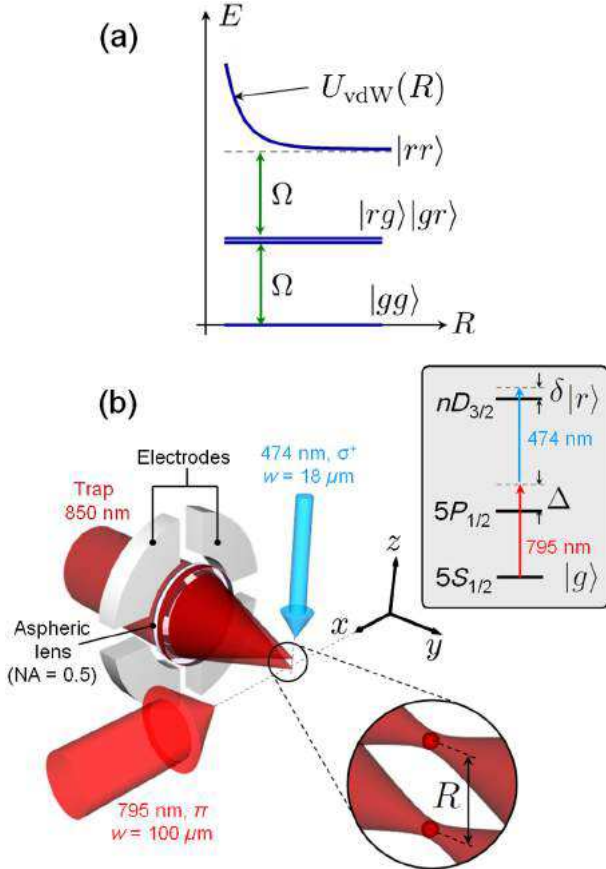


FIG. 1 (color online). (a) Principle of the Rydberg blockade. The single-atom Rabi frequency is Ω . (b) Experimental setup. Two single atoms are trapped in microscopic optical traps separated by R . Eight electrodes (four of which, facing the ones displayed here, are not shown) provide electric field control. Inset: two-photon excitation scheme (the intermediate-state detuning is $\Delta \approx 2\pi \times 740$ MHz).

incidence angle of the beams on the lens. We calibrate R by measuring the displacement of an image of the trap when changing the incidence of the trapping beams. The resulting uncertainty is below 5% [22].

The aspheric lens used to focus the trapping beams also collects the atom fluorescence from each trap on separate photon counters. The two-photon excitation from $|g\rangle = |5S_{1/2}, F=2, m_F=2\rangle$ to the Rydberg state $|r\rangle = |nD_{3/2}, m_j=3/2\rangle$ [see the inset of Fig. 1(b)], described in Ref. [23], yields coherent oscillations with single-atom Rabi frequencies $\Omega/(2\pi)$ in the range from 500 kHz to 5 MHz [see Fig. 2(a)]. The excitation pulse has a duration τ (during which the traps are off), and the laser frequencies are adjusted so that the (light-shift corrected) one-atom detuning is $\delta \approx 0$. After excitation, we infer the state of each atom by detecting its presence or absence in its respective trap (atoms in $|r\rangle$ are slightly antitrapped by the optical potential, which results in their loss). We thus reconstruct the populations P_{ij} of the two-atom states $|ij\rangle$

(i, j taking the values g, r), by repeating each sequence about 100 times [23].

Our setup was designed to minimize residual electric fields detrimental to Rydberg state manipulations: (i) the aspheric lens surface facing the atoms is coated with a conductive 200 nm-thick indium-tin-oxide layer; (ii) eight independent electrodes allow us to apply electric fields along any direction [24]. Using Stark spectroscopy on the $|62D_{3/2}, m_j=3/2\rangle$ state, we determine that with all electrodes grounded, a residual field of ~ 150 mV/cm (pointing essentially along x) was present. After applying appropriate correction voltages, the residual field is below ~ 5 mV/cm. This cancellation is critical to the success of the experiment: small (transverse) stray fields mix $|r\rangle$ with other Rydberg states not coupled to light, or exhibiting Förster zeros [25], thus degrading the blockade.

Figures 2(b)–2(e) shows the probabilities $P_{rg} + P_{gr}$ to excite only one atom, and P_{rr} to excite both, versus the area $\Omega\tau$ of the excitation pulse, for various R and Ω , in the case $n=62$. In Fig. 2(b), the atoms are far apart ($R \approx 15 \mu\text{m}$) and thus almost independent. Indeed, the probability P_{rr} of exciting both atoms is nearly equal to the product $P_{1,r}P_{2,r}$ [see Fig. 2(a)], where $P_{i,r}$ is the probability for atom i to be in $|r\rangle$, obtained in a control experiment with only trap i . In this case $P_{rg} + P_{gr}$ is expected to oscillate at frequency 2Ω between 0 and $1/2$, close to what we observe. On the contrary, in Fig. 2(e), the atoms are close ($R \approx 4.0 \mu\text{m}$) and $\Omega \approx 2\pi \times 1.9$ MHz is small enough for almost perfect blockade to occur: at all times, P_{rr} is negligible ($P_{rr} < 0.06$, with an average of 0.036), and thus differs substantially from the product of the single-atom excitation probabilities expected for independent atoms. At the same time, $P_{rg} + P_{gr}$ oscillates at $(1.49 \pm 0.07)\Omega$, close to the expected collective frequency $\sqrt{2}\Omega$ [16].

In between those regimes [see Figs. 2(c) and 2(d)], blockade is only partial: $P_{rg} + P_{gr}$ and P_{rr} show a more complex behavior, revealing nontrivial two-atom states. We model this dynamics by solving the optical Bloch equations (OBEs) [26,27]. Each atom i ($i=1, 2$) is considered as a two-level atom with ground state $|g\rangle_i$ and $nD_{3/2}$ Rydberg state $|r\rangle_i$, coupled by a near-resonant laser with Rabi frequency Ω (in practice, for our data, the atoms experience, within 5%, the same Ω). In the basis $\{|gg\rangle, |gr\rangle, |rg\rangle, |rr\rangle\}$, and using the rotating wave approximation, the Hamiltonian is

$$H = \begin{pmatrix} 0 & \hbar\Omega/2 & \hbar\Omega/2 & 0 \\ \hbar\Omega/2 & -\hbar\delta & 0 & \hbar\Omega/2 \\ \hbar\Omega/2 & 0 & -\hbar\delta & \hbar\Omega/2 \\ 0 & \hbar\Omega/2 & \hbar\Omega/2 & U_{\text{vdW}} - 2\hbar\delta \end{pmatrix}. \quad (1)$$

We omit diagonal terms corresponding to interaction between ground-state atoms (for $R = 1 \mu\text{m}$ the van der Waals interaction is in the 10^{-8} Hz range, and the

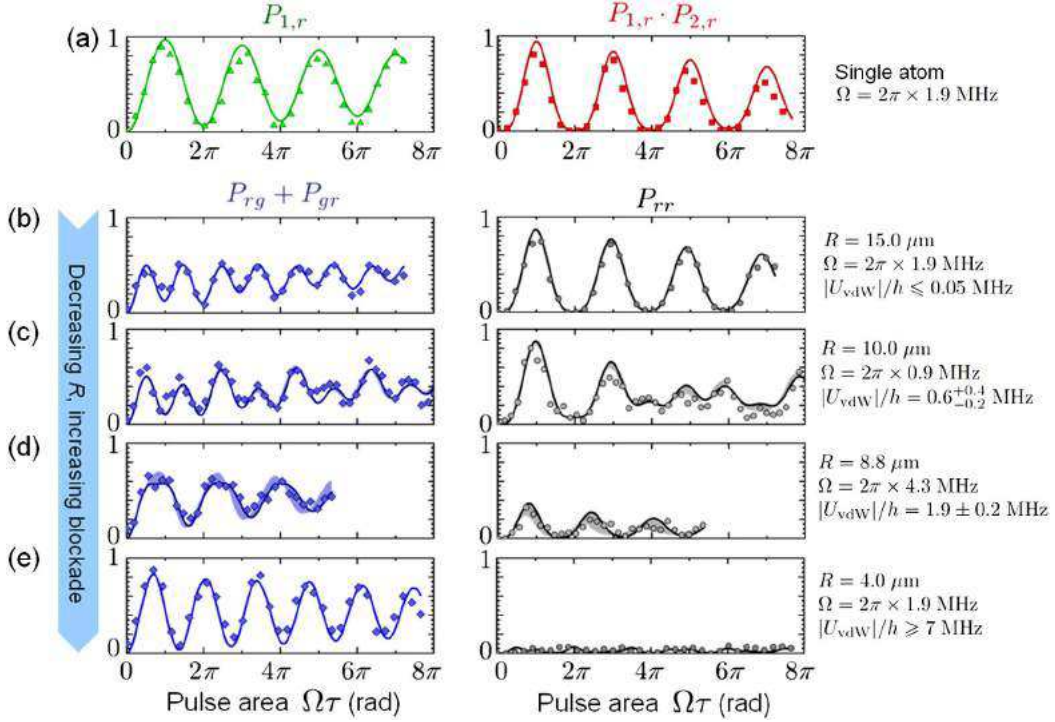


FIG. 2 (color online). From independent to blockaded atoms, via partial blockade, for $n = 62$. (a) Single-atom Rabi oscillation $P_{1,r}(\Omega\tau)$ between $|g\rangle$ and $|r\rangle$ (green triangles), and product of such excitation probabilities for single atoms in traps 1,2 with the other trap off (red squares). (b)–(e): Probability $P_{rg} + P_{gr}$ to excite one atom to the Rydberg state (blue diamonds), and double Rydberg excitation probability P_{rr} (black circles), versus excitation pulse area $\Omega\tau$. From (b) to (e), R decreases, yielding increasing blockade. Solid lines are fits of the data by the solution of the OBEs (see text). Shaded areas correspond to one standard deviation in determining $|U_{\text{vdW}}|$ (statistical error bars on Ω , at the 1% level, are not shown).

magnetic dipole-dipole interaction in the mHz range) or between a ground-state and a Rydberg atom (in the 1 Hz range at $R = 1 \mu\text{m}$), as they are negligible with respect to the relevant energy scales of the problem. Experimentally, we observe (especially for large Ω) a small damping of the oscillations, essentially due to off-resonant spontaneous emission via the $5P_{1/2}$ intermediate state. To take this into account, we solve the OBEs for the two-atom density matrix $\dot{\rho} = -i[H, \rho]/\hbar + \mathcal{L}$. We write the dissipative term as $\mathcal{L} = \mathcal{L}_1 \otimes \rho_2 + \rho_1 \otimes \mathcal{L}_2$, where

$$\mathcal{L}_i = \gamma \begin{pmatrix} \rho_{rr} & -\rho_{gr}/2 \\ -\rho_{rg}/2 & -\rho_{rr} \end{pmatrix}_i \quad (2)$$

is the dissipator for atom i (neglecting dephasing), expressed in the basis $\{|g\rangle_i, |r\rangle_i\}$, and ρ_i the reduced density matrix of atom i . This phenomenological way to include dissipation is sufficient for the present data; a more exact way would include several levels (including the $5P_{1/2}$ state) for each atom, as was done in Refs. [23,27]. We neglect cooperative effects such as super-radiance (this is legitimate as R is much larger than the wavelength $\lambda \approx 795 \text{ nm}$ of the $5S$ - $5P$ transition which dominates the dissipation via spontaneous emission) [26].

The parameters Ω and γ appearing in the model are obtained by fitting single-atom Rabi oscillation data

[see the triangles in Fig. 2(a)]. The only remaining parameters in the model are U_{vdW} and δ . We treat U_{vdW} as an adjustable parameter to fit the solution of the OBEs to $P_{rg}(t) + P_{gr}(t)$ and $P_{rr}(t)$. Examples of such fits are presented as solid lines in Figs. 2(b)–2(e) (shaded areas show the confidence interval in U_{vdW}). We also treat δ as a free parameter, to account for slow drifts of the lasers [28]. With this method, we obtain only $|U_{\text{vdW}}|$, as for $\delta \approx 0$ the sign of the interaction does not affect the dynamics. We have checked that deliberately setting $\delta = 0$ and $\gamma = 0$ in the fit (thus reducing our analysis to solving an effectively three-level Schrödinger equation), yields values of $|U_{\text{vdW}}|$ departing by at most 20% from those above. We checked that the interaction energy yielded by the fits does not depend on the chosen Ω by doubling or halving it. We emphasize that the convergence of the fit is optimal when $U_{\text{vdW}} \sim \hbar\Omega$. Combined with our range of accessible Ω , this means we can determine values of $|U_{\text{vdW}}|/h$ in the range from 0.1 to 10 MHz.

Figure 3 shows $|U_{\text{vdW}}|$ extracted from such fits versus R , for the Rydberg states $|r\rangle = |nD_{3/2}, m_j = 3/2\rangle$ with $n = 53$, $n = 62$, and $n = 82$. The data are consistent with a power law of exponent -6 . Here, the determination of the exponent is much more direct than for interacting ultracold [11] or thermal [29] ensembles, in which the

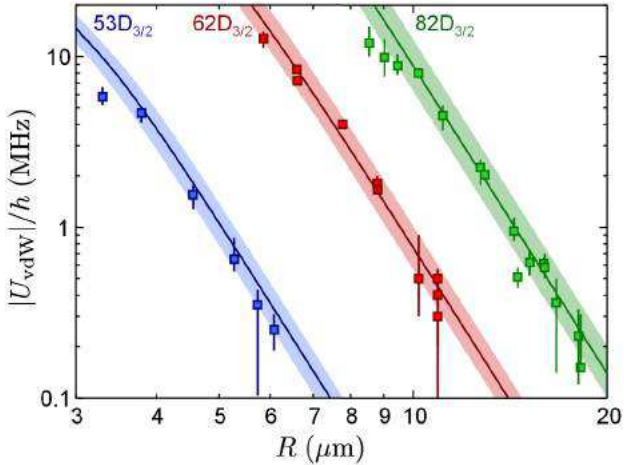


FIG. 3 (color online). Magnitude $|U_{\text{vdW}}|$ of the interaction energy between atoms in $|nD_{3/2}, m_j = 3/2\rangle$, extracted from the fits of Fig. 2, versus R , for $n = 53$ (blue), $n = 62$ (red), and $n = 82$ (green). Error bars are one standard deviation in the fitted $|U_{\text{vdW}}|$. Solid lines: *ab initio* theoretical expectations (see text) without any adjustable parameter. Shaded areas: 5% systematic uncertainty in R .

random distribution of atoms smears out the interaction R dependence. Our results illustrate the dramatic dependence of U_{vdW} with n : for instance, changing n from 53 to 62 at given R yields a fiftyfold increase in U_{vdW} . Fitting the data by $|U_{\text{vdW}}| = |C_6|_{\text{Expt.}}/R^6$ with $|C_6|_{\text{Expt.}}$ as an adjustable parameter, we obtain the values of Table I.

To compare our measurements to the theoretical expressions of $|U_{\text{vdW}}|$ (solid lines in Fig. 3), we diagonalize the interaction Hamiltonian, considering only the leading, electric dipole interaction term. From the quantum defects reported in Ref. [30], we compute radial wave functions using the Numerov algorithm [31]. We restrict the Hamiltonian to a two-atom basis $|n_1 l_1 j_1 m_{j1}, n_2 l_2 j_2 m_{j2}\rangle$ comprising only states close in energy (up to $\sim h \times 5 \text{ GHz}$) from the $|nD_{3/2}, m_j = 3/2, nD_{3/2}, m_j = 3/2\rangle$ state, and satisfying $|n - n_{1,2}| \leq 4$. This corresponds to (sparse) matrices up to $\approx 10^3 \times 10^3$ [32].

At the large distances relevant here, the dipole-dipole interaction simply shifts the two-atom levels by a quantity C_6/R^6 that can be obtained from second-order perturbation theory. At shorter distances, mixing between adjacent levels occurs [25], altering the $1/R^6$ character of the interaction (this can be seen for $n = 53$ when $R < 4 \mu\text{m}$). We obtain the $|C_6|_{\text{Th}}$ coefficients of Table I by fitting the numerically obtained interactions at distances $15 < R < 20 \mu\text{m}$. Our results are in good agreement with second-order perturbation theory calculations [33]. We get an estimate of the uncertainty in $|C_6|_{\text{Th}}$ by adding random, uniformly distributed relative errors of $\pm 0.5\%$ to radial matrix elements appearing in the Hamiltonian. The relative uncertainty is larger ($\sim 10\%$) for $n = 53$, due to cancellations of terms with opposite signs. Taking into account

TABLE I. Experimental and theoretical $|C_6|$ coefficients for $n = 53, 62$, and 82 .

n	$ C_6 _{\text{Expt.}} (\text{GHz} \cdot \mu\text{m}^6)$	$ C_6 _{\text{Th}} (\text{GHz} \cdot \mu\text{m}^6)$
53	13.7 ± 1.2	16.9 ± 1.7
62	730 ± 20	766 ± 15
82	8500 ± 300	8870 ± 150

error bars, the agreement between our measurement and the calculated C_6 is very good. It appears from Fig. 3 that for the largest values of U_{vdW} , our experimental determination systematically lies below the theory. An explanation might be that mechanical effects induced by interactions lead to a modification of the dynamics, as recently suggested [34]. Our present analysis neglects these effects and may lead to an underestimation of the actual interaction. Including these effects is left to future work.

In summary, we have directly measured the van der Waals interaction between two isolated Rydberg atoms. The level of control demonstrated here opens exciting perspectives in multiatom systems, for observing geometry-dependent effects due to the anisotropy of the dipolar interaction [35], or the nonadditivity of van der Waals interactions [36]. It is also a prerequisite for generating high-fidelity, many-atom entanglement using Rydberg blockade, as well as for quantum simulation of long-range interacting spin systems.

We thank A. Guilhaud, P. Roth, C. Beurthe, F. Moron, and F. Nogrette for technical assistance, C. Evellin for contributions at the early stage of this work, Y.R.P. Sortais for invaluable advice in the design of the setup, H. Labuhn and S. Ravets for a careful reading of the manuscript, and J. Vigué for useful discussions. L.B. is partially supported by the DGA. We acknowledge financial support by the EU (ERC Stg Grant ARENA, AQUITE Integrating Project, and Initial Training Network COHERENCE), and by Région Île-de-France (LUMAT and Triangle de la Physique).

- [1] J.N. Israelachvili, *Intermolecular And Surface Forces* (Academic, New York, 2010).
- [2] P.C. Hiemenz and R. Rajagopalan, *Principles of Colloid and Surface Chemistry* (Marcel Dekker, New York, 1997).
- [3] R. J. Le Roy and R. B. Bernstein, *J. Chem. Phys.* **52**, 3869 (1970).
- [4] See, e.g., A. Aspect and J. Dalibard, *Séminaire Poincaré* **1**, 67 (2002), and references therein.
- [5] A. Anderson, S. Haroche, E. A. Hinds, W. Jhe, and D. Meschede, *Phys. Rev. A* **37**, 3594 (1988).
- [6] V. Sandoghdar, C. I. Sukenik, E. A. Hinds, and S. Haroche, *Phys. Rev. Lett.* **68**, 3432 (1992).
- [7] D. Jaksch, J. I. Cirac, P. Zoller, R. Côté, and M. D. Lukin, *Phys. Rev. Lett.* **85**, 2208 (2000).

- [8] M.D. Lukin, M. Fleischhauer, and R. Cote, *Phys. Rev. Lett.* **87**, 037901 (2001).
- [9] D. Comparat and P. Pillet, *J. Opt. Soc. Am. B* **27**, A208 (2010).
- [10] K. Singer, M. Reetz-Lamour, T. Amthor, L. G. Marcassa, and M. Weidemüller, *Phys. Rev. Lett.* **93**, 163001 (2004).
- [11] R. Heidemann, U. Raitzsch, V. Bendkowsky, B. Butscher, R. Löw, L. Santos, and T. Pfau, *Phys. Rev. Lett.* **99**, 163601 (2007).
- [12] J. D. Pritchard, D. Maxwell, A. Gauguet, K. J. Weatherill, M. P. A. Jones, and C. S. Adams, *Phys. Rev. Lett.* **105**, 193603 (2010).
- [13] Y. O. Dudin and A. Kuzmich, *Science* **336**, 887 (2012).
- [14] P. Schauss, M. Cheneau, M. Endres, T. Fukuhara, S. Hild, A. Omran, T. Pohl, C. Gross, S. Kuhr, and I. Bloch, *Nature (London)* **491**, 87 (2012).
- [15] E. Urban, T. A. Johnson, T. Henage, L. Isenhower, D. D. Yavuz, T. G. Walker, and M. Saffman, *Nat. Phys.* **5**, 110 (2009).
- [16] A. Gaëtan, Y. Miroshnychenko, T. Wilk, A. Chotia, M. Viteau, D. Comparat, P. Pillet, A. Browaeys, and P. Grangier, *Nat. Phys.* **5**, 115 (2009).
- [17] M. Saffman, T. G. Walker, and K. Mølmer, *Rev. Mod. Phys.* **82**, 2313 (2010).
- [18] H. Weimer, M. Müller, I. Lesanovsky, P. Zoller, and H. P. Büchler, *Nat. Phys.* **6**, 382 (2010).
- [19] N. Schlosser, G. Reymond, I. Protsenko, and P. Grangier, *Nature (London)* **411**, 1024 (2001).
- [20] T. Wilk, A. Gaëtan, C. Evellin, J. Wolters, Y. Miroshnychenko, P. Grangier, and A. Browaeys, *Phys. Rev. Lett.* **104**, 010502 (2010).
- [21] Y. R. P. Sortais *et al.*, *Phys. Rev. A* **75**, 013406 (2007).
- [22] The dispersion in the interatomic distances due to the finite temperature has negligible effects. For $T = 50 \mu\text{K}$, the transverse size in our traps (of radial frequency $\omega_r \sim 2\pi \times 100 \text{ kHz}$) is $\sim 100 \text{ nm}$ (longitudinal size only contributes to second order).
- [23] Y. Miroshnychenko, A. Gaëtan, C. Evellin, P. Grangier, D. Comparat, P. Pillet, T. Wilk, and A. Browaeys, *Phys. Rev. A* **82**, 013405 (2010).
- [24] R. Löw, H. Weimer, J. Nipper, J. B. Balewski, B. Butscher, H. P. Büchler, and T. Pfau, *J. Phys. B* **45**, 113001 (2012).
- [25] T. G. Walker and M. Saffman, *Phys. Rev. A* **77**, 032723 (2008).
- [26] C. Ates, T. Pohl, T. Pattard, and J. M. Rost, *Phys. Rev. A* **76**, 013413 (2007).
- [27] X. L. Zhang, A. T. Gill, L. Isenhower, T. G. Walker, and M. Saffman, *Phys. Rev. A* **85**, 042310 (2012).
- [28] For our data, the best-fit value of $\delta/(2\pi)$ lies in the range $\pm 300 \text{ kHz}$, compatible with observed frequency drifts of the excitation lasers over the acquisition of a full data set (a few hours).
- [29] T. Baluktian, B. Huber, R. Löw and T. Pfau, *Phys. Rev. Lett.* **110**, 123001 (2013).
- [30] W. Li, I. Mourachko, M. W. Noel, and T. F. Gallagher, *Phys. Rev. A* **67**, 052502 (2003).
- [31] M. L. Zimmerman, M. G. Littman, M. M. Kash, and D. Kleppner, *Phys. Rev. A* **20**, 2251 (1979).
- [32] At the large distances used to extract C_6 , only a few tens of states contribute significantly. However, to obtain the correct short-distance behavior, $\sim 10^3$ states are necessary.
- [33] A. Reinhard, T. C. Liebisch, B. Knuffman, and G. Raithel, *Phys. Rev. A* **75**, 032712 (2007).
- [34] W. Li, C. Ates, and I. Lesanovsky, [arXiv:1303.3212](https://arxiv.org/abs/1303.3212).
- [35] T. J. Carroll, K. Claringbould, A. Goodsell, M. J. Lim, and M. W. Noel, *Phys. Rev. Lett.* **93**, 153001 (2004).
- [36] D. Cano and J. Fortágh, *Phys. Rev. A* **86**, 043422 (2012).

Bibliography

- Afrousheh, K., Bohlouli-Zanjani, P., Vagale, D., Mugford, A., Fedorov, M., and Martin, J. D. D., “Spectroscopic observation of resonant electric dipole-dipole interactions between cold rydberg atoms,” *Physical Review Letters* **93**, 233001 (2004).
- Anderlini, M., Lee, P. J., Brown, B. L., Sebby-Strabley, J., Philipps, W. D., and Porto, J. V., “Controlled exchange interaction between pairs of neutral atoms in an optical lattice,” *Nature* **448**, 452–456 (2007).
- Anderson, A., Haroche, S., Hinds, E. A., Jhe, W., and Meschede, D., “Measuring the van der Waals forces between a Rydberg atom and a metallic surface,” *Physical Review A* **37**, 3594–3597 (1988).
- Aspect, A. and Dalibard, J., “Measurement of the Atom-Wall interaction: from London to Casimir-Polder,” in *Séminaire Poincaré* (2002) pp. 67–78.
- Balewski, J. B., Krupp, A. T., Gaj, A., Peter, D., Buchler, H. P., Low, R., Hofferberth, S., and Pfau, T., “Coupling a single electron to a Bose-Einstein condensate,” *Nature* **502**, 664–667 (2013).
- Baluktsian, T., Huber, B., Löw, R., and Pfau, T., “Evidence for strong van der Waals type Rydberg-Rydberg interaction in a thermal vapor,” *Physical Review Letters* **110**, 123001 (2013).
- Barrett, M. D., Sauer, J. A., and Chapman, M. S., “All-optical formation of an atomic Bose-Einstein condensate,” *Physical Review Letters* **87**, 10404 (2001).
- Béguin, L., Vernier, A., Chicireanu, R., Lahaye, T., and Browaeys, A., “Direct measurement of the van der Waals interaction between two Rydberg atoms,” *Physical Review Letters* **110**, 263201 (2013).
- Bennett, C. H. and Brassard, G., “Quantum cryptography: public key distribution and coin tossing,” in *Proceedings of the IEEE International Conference on Computers, Systems and Signal Processing* (IEEE Press, New York, 1984) pp. 175–179.
- Bergamini, S., Darquié, B., Jones, M., Jacubowicz, L., Browaeys, A., and Grangier, P., “Holographic generation of microtrap arrays for single atoms by use of a programmable phase modulator,” *Journal of the Optical Society of America B* **21**, 1889 (2004).
- Beterov, I. I., Ryabtsev, I. I., Tretyakov, D. B., and Entin, V. M., “Quasiclassical calculations of blackbody-radiation-induced depopulation rates and effective lifetimes of Rydberg nS , nP , and nD alkali-metal atoms with $n \leq 80$,” *Physical Review A* **79**, 52504 (2009).

- Beterov, I. I., Tretyakov, D. B., Entin, V. M., Yakshina, E. A., Ryabtsev, I. I., MacCormick, C., and Bergamini, S., “*Deterministic single-atom excitation via adiabatic passage and Rydberg blockade*,” [arXiv:1102.5223v4](https://arxiv.org/abs/1102.5223v4) (2011), [10.1103/PhysRevA.84.023413](https://doi.org/10.1103/PhysRevA.84.023413).
- Beugnon, J., Contrôle de l'état interne d'un atome unique piégé et expériences d'interférences à deux photons : vers l'information quantique avec des atomes neutres, Ph.D. thesis, Université Paris XI (2007).
- Beugnon, J., Jones, M. P. A., Dingjan, J., Darquié, B., Messin, G., Browaeys, A., and Grangier, P., “*Quantum interference between two single photons emitted by independently trapped atoms*,” *Nature* **440**, 779 (2006).
- Bize, S., Sortais, Y., Santos, M. S., Mandache, C., Clairon, A., and Salomon, C., “*High-accuracy measurement of the ^{87}Rb ground-state hyperfine splitting in an atomic fountain*,” *Europhysics Letters* **45**, 558 (1999).
- Black, E. D., “*An introduction to Pound-Drever-Hall laser frequency stabilization*,” *American Journal of Physics* **69**, 79–87 (2001).
- Blatt, R. and Wineland, D., “*Entangled states of trapped atomic ions*,” *Nature* **453**, 1008–1015 (2008).
- Bloch, I., “*Quantum coherence and entanglement with ultracold atoms in optical lattices*,” *Nature* **453**, 1016–1022 (2008).
- Bochmann, J., Mücke, M., Guhl, C., Ritter, S., Rempe, G., and Moehring, D. L., “*Lossless state detection of single neutral atoms*,” *Physical Review Letters* **104**, 203601 (2010).
- Bohlouli-Zanjani, P., Petrus, J. A., and Martin, J. D. D., “*Enhancement of Rydberg atom interactions using ac Stark shifts*,” *Physical Review Letters* **98**, 203005 (2007).
- Bonin, K. D. and McIlrath, T. J., “*Two-photon electric-dipole selection rules*,” *J. Opt. Soc. Am. B* **1**, 52–55 (1984).
- Born, M. and Wolf, E., *Principles of Optics: Electromagnetic Theory of Propagation, Interference and Diffraction of Light*, seventh ed ed. (Cambridge University Press, 2003).
- Briegel, H. J., Browne, D. E., Dur, W., Raussendorf, R., and Van den Nest, M., “*Measurement-based quantum computation*,” *Nature Physics* , 19–26 (2009).
- Carroll, T. J., Claringbould, K., Goodsell, A., Lim, M. J., and Noel, M. W., “*Angular dependence of the dipole-dipole interaction in a nearly one-dimensional sample of Rydberg atoms*,” *Physical Review Letters* **93**, 153001 (2004).
- Chou, C. W., Hume, D. B., Koelemeij, J. C. J., Wineland, D. J., and Rosenband, T., “*Frequency comparison of two high-accuracy Al^+ optical clocks*,” *Physical Review Letters* **104**, 70802 (2010).
- Cohen-Tannoudji, C., Grynberg, G., and Dupont-Roc, J., *Atom-photon interactions: basic processes and applications* (Wiley VCH, 1998).
- Comparat, D. and Pillet, P., “*Dipole blockade in a cold Rydberg atomic sample*,” *Journal of the Optical Society of America B* **27**, A208—A232 (2010).

- Darquié, B., Manipulation d'atomes dans des pièges dipolaires microscopiques et émission contrôlée de photons par un atome unique, Ph.D. thesis, Université Paris XI (2005).
- Darquié, B., Jones, M. P. A., Dingjan, J., Beugnon, J., Bergamini, S., Sortais, Y., Messin, G., Browaeys, A., and Grangier, P., “Controlled single-photon emission from a single trapped two-level atom,” *Science* **309**, 454–456 (2005).
- van Ditzhuijzen, C. S., Koenderink, a. F., Noordam, L. D., and van Linden van den Heuvell, H., “Simultaneous position and state measurement of Rydberg atoms,” *The European Physical Journal D* **40**, 13–17 (2006).
- DiVincenzo, D. P., “Two-bit gates are universal for quantum computation,” *Physical Review A* **51**, 1015–1022 (1995).
- Dudin, Y. O. and Kuzmich, A., “Strongly interacting Rydberg excitations of a cold atomic gas,” *Science* **336**, 887–889 (2012).
- Dumke, R., Volk, M., Müther, T., Buchkremer, F. B. J., Birkl, G., and Ertmer, W., “Micro-optical realization of arrays of selectively addressable dipole traps: A scalable configuration for quantum computation with atomic qubits,” *Physical Review Letters* **89**, 97903 (2002).
- Ebert, M., Gill, A., Gibbons, M., Zhang, X., Saffman, M., and Walker, T. G., “Atomic Fock state preparation using Rydberg blockade,” **1**, 1–5 (2013), [arXiv:1310.7561v1](https://arxiv.org/abs/1310.7561v1).
- Engler, H., Weber, T., Mudrich, M., Grimm, R., and Weidemüller, M., “Very long storage times and evaporative cooling of cesium atoms in a quasidelectrostatic dipole trap,” *Physical Review A* **62**, 31402 (2000).
- Evellin, C., Interactions entre atomes de rubidium dans des états de Rydberg et intrication par blocage de Rydberg, Ph.D. thesis, Université Paris XI (2011).
- Farley, J. W. and Wing, W. H., “Accurate calculation of dynamic Stark shifts and depopulation rates of Rydberg energy levels induced by blackbody radiation. Hydrogen, helium, and alkali-metal atoms,” *Physical Review A* **23**, 2397–2424 (1981).
- Förster, T., “Intermolecular energy migration and fluorescence,” *Annals of Physics* **2**, 55+ (1948).
- Fuhrmanek, A., Bourgain, R., Sortais, Y. R. P., and Browaeys, A., “Free-space lossless state detection of a single trapped atom,” *Physical Review Letters* **106**, 133003 (2011).
- Fuhrmanek, A., Bourgain, R., Sortais, Y. R. P., and Browaeys, A., “Light-assisted collisions between a few cold atoms in a microscopic dipole trap,” *Physical Review A* **85**, 62708 (2012).
- Gabbanini, C., Gozzini, S., and Lucchesini, A., “Photoionization cross section measurement in a Rb vapor cell trap,” *Optics Communications* **141**, 25–28 (1997).
- Gaetan, A., Intrication de deux atomes en utilisant le blocage de Rydberg, Ph.D. thesis, Université Paris XI (2009).
- Gaëtan, A., Miroshnychenko, Y., Wilk, T., Chotia, A., Viteau, M., Comparat, D., Pillet, P., Browaeys, A., and Grangier, P., “Observation of collective excitation of two individual atoms in the Rydberg blockade regime,” *Nature Physics* **5**, 115–118 (2009).

- Gallagher, T. F., *Rydberg Atoms* (Cambridge University Press, 1994).
- Greiner, M., Mandel, O., Esslinger, T., Hansch, T. W., and Bloch, I., “*Quantum phase transition from a superfluid to a Mott insulator in a gas of ultracold atoms*,” *Nature* **415**, 39–44 (2002).
- Grimm, R., Weidemüller, M., and Ovchinnikov, Y., “*Optical dipole traps for neutral atoms*,” *Advances in Atomic, Molecular, and Optical Physics* **42**, 95 (2000).
- Grover, L. K., “*Quantum mechanics helps in searching for a needle in a haystack*,” *Physical Review Letters* **79**, 325–328 (1997).
- Grünzweig, T., Hilliard, A., McGovern, M., and Andersen, M. F., “*Near-deterministic preparation of a single atom in an optical microtrap*,” *Nature Physics* **6**, 951–954 (2010).
- Han, J., Jamil, Y., Norum, D. V. L., Tanner, P. J., and Gallagher, T. F., “*Rb nf quantum defects from millimeter-wave spectroscopy of cold ^{85}Rb Rydberg atoms*,” *Physical Review A* **74**, 54502 (2006).
- Haroche, S. and Raimond, J. M., *Exploring the quantum: atoms, cavities, and photons*, Oxford Graduate Texts (OUP Oxford, 2006).
- He, X., Li, B., Chen, A., and Zhang, C., “*Model-potential calculation of lifetimes of Rydberg states of alkali atoms*,” *Journal of Physics B: Atomic, Molecular and Optical Physics* **23**, 661 (1990).
- Heidemann, R., Raitzsch, U., Bendkowsky, V., Butscher, B., Löw, R., and Pfau, T., “*Rydberg excitation of Bose-Einstein condensates*,” *Physical Review Letters* **100**, 33601 (2008).
- Hiemenz, P. C. and Rajagopalan, R., *Principles of Colloid and Surface Chemistry*, edited by M. Dekker (New York, 1997).
- Hinkley, N., Sherman, J. A., Phillips, N. B., Schioppo, M., Lemke, N. D., Beloy, K., Pizzocaro, M., Oates, C. W., and Ludlow, A. D., “*An atomic clock with 10^{-18} instability*,” *Science* **341**, 1215–1218 (2013).
- Home, J. P., Hanneke, D., Jost, J. D., Amini, J. M., Leibfried, D., and Wineland, D. J., “*Complete methods set for scalable ion trap quantum information processing*,” *Science* **325**, 1227–1230 (2009).
- Isenhower, L., Urban, E., Zhang, X. L., Gill, A. T., Henage, T., Johnson, T. A., Walker, T. G., and Saffman, M., “*Demonstration of a neutral atom controlled-NOT quantum gate*,” *Physical Review Letters* **104**, 10503 (2010).
- Israelachvili, J. N., *Intermolecular and surface forces* (Academic, New York, 2010).
- Jaksch, D., Briegel, H.-J., Cirac, J. I., Gardiner, C. W., and Zoller, P., “*Entanglement of atoms via cold controlled collisions*,” *Physical Review Letters* **82**, 1975–1978 (1999).
- Jaksch, D., Cirac, J. I., Zoller, P., Rolston, S. L., Côté, R., and Lukin, M. D., “*Fast quantum gates for neutral atoms*,” *Physical Review Letters* **85**, 2208–2211 (2000).

- Johnson, T., Urban, E., Henage, T., Isenhower, L., Yavuz, D., Walker, T., and Saffman, M., “*Rabi oscillations between ground and Rydberg states with dipole-dipole atomic interactions*,” *Physical Review Letters* **100**, 113003 (2008).
- Jones, M. P. A., Beugnon, J., Gaëtan, A., Zhang, J., Messin, G., Browaeys, A., and Grangier, P., “*Fast quantum state control of a single trapped neutral atom*,” *Physical Review A* **75**, 40301 (2007).
- Kaufman, A. M., Lester, B. J., and Regal, C. A., “*Cooling a single atom in an optical tweezer to its quantum ground state*,” *Physical Review X* **2**, 041014 (2012).
- Kuhr, S., Alt, W., Schrader, D., Dotsenko, I., Miroschnychnenko, Y., Rosenfeld, W., Khudaverdyan, M., Gomer, V., Rauschenbeutel, A., and Meschede, D., “*Coherence properties and quantum state transportation in an optical conveyor belt*,” *Physical Review Letters* **91**, 213002 (2003).
- Kuhr, S., Alt, W., Schrader, D. M., Müller, M., Gomer, V., and Meschede, D., “*Deterministic delivery of a single atom*,” *Science* **293**, 278 (2001).
- Kuppens, S. J. M., Corwin, K. L., Miller, K. W., Chupp, T. E., and Wieman, C. E., “*Loading an optical dipole trap*,” *Physical Review A* **62**, 13406 (2000).
- LeRoy, R. J. and Bernstein, R. B., “*Dissociation energy and long-range potential of diatomic molecules from vibrational spacings of higher levels*,” *The Journal of Chemical Physics* **52** (1970), 10.1063/1.1673585.
- Lesanovsky, I., “*Many-body spin interactions and the ground state of a dense Rydberg lattice gas*,” *Physical Review Letters* **106**, 25301 (2011).
- Li, W., Ates, C., and Lesanovsky, I., “*Nonadiabatic motional effects and dissipative blockade for Rydberg atoms excited from optical lattices or microtraps*,” *Physical Review Letters* **110**, 213005 (2013).
- Li, W., Mourachko, I., Noel, M. W., and Gallagher, T. F., “*Millimeter-wave spectroscopy of cold Rb Rydberg atoms in a magneto-optical trap: Quantum defects of the ns , np , and nd series*,” *Physical Review A* **67**, 52502 (2003).
- Liebisch, T. C., Reinhard, A., Berman, P. R., and Raithel, G., “*Atom counting statistics in ensembles of interacting Rydberg atoms*,” *Physical Review Letters* **95**, 253002 (2005).
- Loudon, R., *The Quantum Theory of Light (Oxford Science Publications)*, 3rd ed. (Oxford University Press, USA, 2000).
- Löw, R., Weimer, H., Krohn, U., Heidemann, R., Bendkowsky, V., Butscher, B., Büchler, H. P., and Pfau, T., “*Universal scaling in a strongly interacting Rydberg gas*,” *Physical Review A* **80**, 33422 (2009).
- Lukin, M. D., Fleischhauer, M., Cote, R., Duan, L. M., Jaksch, D., Cirac, J. I., and Zoller, P., “*Dipole blockade and quantum information processing in mesoscopic atomic ensembles*,” *Physical Review Letters* **87**, 37901 (2001).
- Lvovsky, A. I., Sanders, B. C., and Tittel, W., “*Optical quantum memory*,” *Nature Photonics* **3**, 706–714 (2009).

- Mandel, O., Greiner, M., Widera, A., Rom, T., Hänsch, T. W., and Bloch, I., “Controlled collisions for multi-particle entanglement of optically trapped atoms,” *Nature* **425**, 937–940 (2003).
- Marinescu, M., Sadeghpour, H. R., and Dalgarno, A., “Dispersion coefficients for alkali-metal dimers,” *Physical Review A* **49**, 982–988 (1994).
- Maxwell, D., Szwer, D. J., Paredes-Barato, D., Busche, H., Pritchard, J. D., Gauguier, A., Weatherill, K. J., Jones, M. P. A., and Adams, C. S., “Storage and control of optical photons using Rydberg polaritons,” *Physical review letters* **110**, 103001 (2013).
- Melde, F., “Ueber die Erregung stehender Wellen eines fadenförmigen Körpers,” *Annalen der Physik* **187**, 513–537 (1860).
- Miroshnychenko, Y., Gaëtan, A., Evellin, C., Grangier, P., Comparat, D., Pillet, P., Wilk, T., and Browaeys, A., “Coherent excitation of a single atom to a Rydberg state,” *Physical Review A* **82**, 13405 (2010).
- Moehring, D. L., Maunz, P., Olmschenk, S., Younge, K. C., Matsukevich, D. N., Duan, L.-M., and Monroe, C., “Entanglement of single-atom quantum bits at a distance.” *Nature* **449**, 68–71 (2007).
- Möller, D., Madsen, L. B., and Mølmer, K., “Quantum gates and multiparticle entanglement by Rydberg excitation blockade and adiabatic passage,” *Physical Review Letters* **100**, 170504 (2008).
- Monz, T., Schindler, P., Barreiro, J. T., Chwalla, M., Nigg, D., Coish, W. A., Harlander, M., Hänsel, W., Hennrich, M., and Blatt, R., “14-qubit entanglement: creation and coherence,” *Physical Review Letters* **106**, 130506 (2011).
- Müller, M., Lesanovsky, I., Weimer, H., Büchler, H. P., and Zoller, P., “Mesoscopic Rydberg gate based on electromagnetically induced transparency,” *Physical Review Letters* **102**, 170502 (2009).
- Nelson, K. D., Li, X., and Weiss, D. S., “Imaging single atoms in a three-dimensional array,” *Nature Physics* **3**, 556 (2007).
- Neukammer, J., Rinneberg, H., Vietzke, K., König, A., Hieronymus, H., Kohl, M., Grabka, H. J., and Wunner, G., “Spectroscopy of Rydberg atoms at $n=500$: observation of quasi-Landau resonances in low magnetic fields,” *Physical Review Letters* **59**, 2947–2950 (1987).
- Nielsen, M. A. and Chuang, I. L., *Quantum computation and quantum information*, Cambridge ed. (2000) p. 676.
- Nipper, J., Balewski, J. B., Krupp, A. T., Butscher, B., Löw, R., and Pfau, T., “Highly resolved measurements of Stark-tuned Förster resonances between Rydberg atoms,” *Physical Review Letters* **108**, 113001 (2012).
- Okoshi, T., Kikuchi, K., and Nakayama, A., “Novel method for high resolution measurement of laser output spectrum,” *Electronics Letters* **16**, 630–631 (1980).
- Peyronel, T., Firstenberg, O., Liang, Q.-Y., Hofferberth, S., Gorshkov, A. V., Pohl, T., Lukin, M. D., and Vuletic, V., “Quantum nonlinear optics with single photons enabled by strongly interacting atoms,” *Nature* **488**, 57–60 (2012).

- Piotrowicz, M. J., Lichtman, M., Maller, K., Li, G., Zhang, S., Isenhower, L., and Saffman, M., “*Two-dimensional lattice of blue-detuned atom traps using a projected Gaussian beam array*,” *Physical Review A* **88**, 013420 (2013).
- Ramsey, N., *Molecular Beams*, Oxford Classic Texts in the Physical Sciences (OUP Oxford, 1956).
- Reinhard, A., Liebisch, T., Knuffman, B., and Raithel, G., “*Level shifts of rubidium Rydberg states due to binary interactions*,” *Physical Review A* **75**, 032712 (2007).
- Reymond, G.-O., Etudes expérimentales d’atomes dans un piège dipolaire microscopique, Ph.D. thesis, Université Paris XI (2002).
- Ryabtsev, I. I., Beterov, I. I., Tretyakov, D. B., Entin, V. M., and Yakshina, E. A., “*Doppler- and recoil-free laser excitation of Rydberg states via three-photon transitions*,” *Physical Review A* **84**, 53409 (2011).
- Saffman, T. G. W. and Molmer, K., “*Quantum information with Rydberg atoms*,” *Reviews of Modern Physics* **82**, 2313 (2010).
- Sandoghdar, V., Sukenik, C. I., Hinds, E. A., and Haroche, S., “*Direct measurement of the van der Waals interaction between an atom and its images in a micron-sized cavity*,” *Physical Review Letters* **68**, 3432–3435 (1992).
- Savard, T. A., O’Hara, K. M., and Thomas, J. E., “*Laser-noise-induced heating in far-off resonance optical traps*,” *Physical Review A* **56**, R1095—R1098 (1997).
- Schauss, P., Cheneau, M., Endres, M., Fukuhara, T., Hild, S., Omran, A., Pohl, T., Gross, C., Kuhr, S., and Bloch, I., “*Observation of spatially ordered structures in a two-dimensional Rydberg gas*,” *Nature* **491**, 87–91 (2012).
- Schlosser, N., Etude et réalisation de micro-pièges dipolaires optiques pour atomes neutres, Ph.D. thesis, Université Paris XI (2001).
- Schlosser, N., Reymond, G., and Grangier, P., “*Collisional blockade in microscopic optical dipole traps*,” *Physical Review Letters* **89**, 023005 (2002).
- Schlosser, N., Reymond, G., Protsenko, I., and Grangier, P., “*Sub-poissonian loading of single atoms in a microscopic dipole trap*,” *Nature* **411**, 1024 (2001).
- Shor, P., “*Algorithms for quantum computation: discrete logarithms and factoring*,” in *Proceedings of the 35th Annual Symposium on Foundations of Computer Science* (IEEE Computer Society Press, Los Alamitos, CA, 1994) pp. 116–123.
- Singer, K., Reetz-Lamour, M., Amthor, T., Marcassa, L. G., and Weidemüller, M., “*Suppression of excitation and spectral broadening induced by interactions in a cold gas of rydberg atoms*,” *Physical Review Letters* **93**, 163001 (2004).
- Singer, K., Stanojevic, J., Weidemüller, M., and Côté, R., “*Long range interactions between alkali rydberg atom pairs correlated to the ns ns, np np and nd nd asymptotes*,” *Journal of Physics B: Atomic and Molecular Physics* , 295–307 (2005).

- Sortais, Y. R. P., Marion, H., Tuchendler, C., Lance, A. M., Lamare, M., Fournet, P., Armellin, C., Mercier, R., Messin, G., Browaeys, A., and Grangier, P., “*Diffraction-limited optics for single-atom manipulation*,” *Physical Review A* **75**, 13406 (2007).
- Spencer, W. P., Vaidyanathan, A. G., Kleppner, D., and Ducas, T. W., “*Measurements of lifetimes of sodium Rydberg states in a cooled environment*,” *Physical Review A* **24**, 2513–2517 (1981).
- Steck, D. A., “*Rubidium 87 D Line Data*,” available online at <http://steck.us/alkalidata> (2008).
- Tauschinsky, A., Thijssen, R. M. T., Whitlock, S., van Linden van den Heuvell, H. B., and Spreeuw, R. J. C., “*Spatially resolved excitation of Rydberg atoms and surface effects on an atom chip*,” *Physical Review A* **81**, 063411 (2010).
- Theodosiou, C. E., “*Lifetimes of alkali-metal-atom Rydberg states*,” *Physical Review A* **30**, 2881–2909 (1984).
- Tong, D., Farooqi, S. M., Stanojevic, J., Krishnan, S., Zhang, Y. P., Côté, R., Eyler, E. E., and Gould, P. L., “*Local blockade of rydberg excitation in an ultracold gas*,” *Physical Review Letters* **93**, 63001 (2004).
- Tuchendler, C., Lance, A. M., Browaeys, A., Sortais, Y. R. P., and Grangier, P., “*Energy distribution and cooling of a single atom in an optical tweezer*,” *Physical Review A* **78**, 33425 (2008).
- Urban, E., Johnson, T. A., Henage, T., Isenhower, L., Yavuz, T. G., Walker, T. G., and Saffman, M., “*Observation of Rydberg blockade between two atoms*,” *Nature Physics* **5**, 110–114 (2009).
- Vedral, V., “*Quantifying entanglement in macroscopic systems*,” *Nature* , 1004 (2008).
- Viteau, M., Bason, M. G., Radogostowicz, J., Malossi, N., Ciampini, D., Morsch, O., and Arimondo, E., “*Rydberg excitations in Bose-Einstein condensates in quasi-one-dimensional potentials and optical lattices*,” *Physical Review Letters* **107**, 60402 (2011).
- Vogt, T., Viteau, M., Chotia, A., Zhao, J., Comparat, D., and Pillet, P., “*Electric-field induced dipole blockade with Rydberg atoms*,” *Physical Review Letters* **99**, 73002 (2007).
- Volz, J., Weber, M., Schlenk, D., Rosenfeld, W., Vrana, J., Saucke, K., Kurtsiefer, C., and Weinfurter, H., “*Observation of entanglement of a single photon with a trapped atom*,” *Physical Review Letters* **96**, 030404 (2006).
- Walker, T. G. and Saffman, M., “*Consequences of Zeeman degeneracy for the van der Waals blockade between Rydberg atoms*,” *Physical Review A* **77**, 32723 (2008).
- Walther, A., Ziesel, F., Ruster, T., Dawkins, S. T., Ott, K., Hettrich, M., Singer, K., Schmidt-Kaler, F., and Poschinger, U., “*Controlling fast transport of cold trapped ions*,” *Physical Review Letters* **109**, 80501 (2012).
- Weatherill, K. J. and Adams, C. S., “*Nonlinear optics using cold Rydberg atoms*,” *Annual Review of Cold Atoms and Molecules* **1**, 301 (2012).

- Weber, M., Volz, J., Saucke, K., Kurtsiefer, C., and Weinfurter, H., “*Analysis of a single-atom dipole trap*,” *Physical Review A* **73**, 43406 (2006).
- Weissbluth, M., *Atoms and molecules* (Academic Press, 1978).
- Wilk, T., Gaëtan, A., Evellin, C., Wolters, J., Miroshnychenko, Y., Grangier, P., and Browaeys, A., “*Entanglement of two individual neutral atoms using Rydberg blockade*,” *Physical Review Letters* **104**, 010502 (2010).
- Yavuz, D. D., Kulatunga, P. B., Urban, E., Johnson, T. A., Proite, N., Henage, T., Walker, T. G., and Saffman, M., “*Fast ground state manipulation of neutral atoms in microscopic optical traps*,” *Physical Review Letters* **96**, 63001 (2006).
- Zimmerman, M. L., Littman, M. G., Kash, M. M., and Kleppner, D., “*Stark structure of the Rydberg states of alkali-metal atoms*,” *Physical Review A* **20**, 2251–2275 (1979).
- Zurek, W. H., “*Decoherence and the transition from quantum to classical*,” *Physics Today* **44**, 36 (1991).
- Zürn, G., Serwane, F., Lompe, T., Wenz, A. N., Ries, M. G., Bohn, J. E., and Jochim, S., “*Fermionization of two distinguishable fermions*,” *Physical Review Letters* **108**, 75303 (2012).

Résumé

Les atomes neutres sont des candidats prometteurs pour la réalisation et l'étude d'états intriqués à quelques dizaines de particules. Pour générer de tels états, une approche consiste à utiliser le mécanisme de blocage dipolaire résultant des fortes interactions dipôle-dipôle entre atomes de Rydberg.

Suivant cette approche, cette thèse présente la conception et la caractérisation d'un dispositif expérimental permettant de manipuler des atomes de ^{87}Rb individuels piégés dans des pinces optiques microscopiques, et à les exciter vers des états de Rydberg. Un environnement électrostatique stable et des électrodes de contrôle permettent une manipulation fine de ces états. Avec deux pinces optiques séparées de quelques microns, nous démontrons le blocage de Rydberg entre deux atomes, et nous observons leur excitation collective.

Enfin, en opérant en régime de blocage partiel, nous développons une méthode permettant de mesurer l'interaction de van der Waals $\Delta E = C_6/R^6$ entre deux atomes séparés par une distance R contrôlée. Les coefficients C_6 obtenus pour différents états de Rydberg sont en bon accord avec des calculs théoriques *ab initio*, et nous observons l'augmentation spectaculaire de l'interaction en fonction du nombre quantique principal n de l'état de Rydberg.

Mots-clés: simulation quantique, atomes uniques, pinces optiques, atomes de Rydberg, interaction dipôle-dipôle, interaction de van der Waals, blocage de Rydberg, intrication.

Summary

Neutral atoms are promising candidates for the realization of entangled states involving up to a few tens of particles. To generate such states, one approach consists in using the dipole blockade mechanism which results from the strong dipole-dipole interactions between Rydberg atoms.

Following this approach, this thesis describes the design and the characterization of an experimental apparatus allowing to manipulate single ^{87}Rb atoms trapped in microscopic optical tweezers, and to excite them towards Rydberg states. A stable electrostatic environment and controlled electrodes enable the fine manipulation of these states. Using two optical tweezers separated by a few microns, we demonstrate the Rydberg blockade between two single atoms, and we observe their collective excitation.

Finally, by operating in the partial blockade regime, we develop a method allowing to measure the van der Waals interaction $\Delta E = C_6/R^6$ between two atoms separated by a controlled distance R . The C_6 coefficients obtained for various Rydberg states agree well with *ab initio* theoretical calculations, and we observe the dramatic increase of the interaction with the principal quantum number n of the Rydberg state.

Key words: quantum simulation, single atoms, optical tweezers, Rydberg atoms, dipole-dipole interaction, van der Waals interaction, Rydberg blockade, entanglement.

